RATIONAL REDUCTION OF REACTIVE FLOW MODELS AND EFFICIENT COMPUTATION OF THEIR SOLUTIONS

A Dissertation

Submitted to the Graduate School
of the University of Notre Dame
in Partial Fulfillment of the Requirements
for the Degree of

Doctor of Philosophy

by

Sandeep Singh, B.Tech., M.S.

Joseph M. Powers, Director

Department of Aerospace and Mechanical Engineering
Notre Dame, Indiana
March 2003

RATIONAL REDUCTION OF REACTIVE FLOW MODELS AND EFFICIENT COMPUTATION OF THEIR SOLUTIONS

Abstract

by

Sandeep Singh

This study will focus on the development of methods for rational reduction of model equations of reactive systems and their efficient numerical simulations. The method of Intrinsic Low-Dimensional Manifold (ILDM), which is used to obtain reduced model equations for spatially homogeneous reactive systems modeled by a system of stiff ordinary differential equation (ODEs), is described in detail. A less stiff reduced system of ODEs is obtained using the ILDM method by equilibrating the fast time scale chemical processes and resolving only the slow time scale chemical processes. The accuracy of the standard ILDM approximation is clarified, and it is shown that the ILDM is a good approximation of the Slow Invariant Manifold (SIM) for stiff ODEs and small manifold curvature. Efficient construction of multi-dimensional ILDMs in a polar parametric space is also presented. Subsequently, an operator splitting method is used to extend the use of the ILDM method to spatially inhomogeneous reactive systems or reactive flow systems modeled by a system of partial differential equations (PDEs). This procedure is implemented on a one-dimensional viscous detonation problem for a mixture of hydrogen-oxygen-argon in a shocktube. The operator splitting method allows each spatial point to be treated as a spatially homogeneous premixed reactor in the reaction step, so that the ILDM method can be implemented. The Wavelet Adaptive Multilevel Representation

(WAMR) is used in the convection diffusion step for efficient resolution of the fine spatial structures in the flow. In this problem, the ILDM and WAMR methods, together, allow for a numerical simulation which is three times faster than the numerical simulation of the full model equations. The construction of slow manifolds for PDEs modeling the reactive flow systems is also addressed. An improved extension of the standard ILDM method to reactive flow systems is given. Reduced model equations are obtained by equilibrating the fast dynamics of a closely coupled reaction/convection/diffusion system and resolving only the slow dynamics of the same in order to reduce computational costs, while maintaining a desired level of accuracy. The improvement is realized through formulation of an elliptic system of partial differential equations which describe the infinite-dimensional Approximate Slow Invariant Manifold (ASIM) for the reactive flow system. This is demonstrated on a simple reaction diffusion system, where it is shown that the error incurred when using the ASIM is less than that incurred by use of Mass-Pope Projection (MPP) of the diffusion effects onto the ILDM. This comparison is further done for ozone decomposition in a premixed laminar flame where an error analysis shows a similar trend.

This dissertation is dedicated to my parents Saroj and Mahipal Singh.

CONTENTS

TABLES v

FIGURES vi

ACKNOWLEDGEMENTS x

CHAPTER 1: INTRODUCTION 1
1.1 Motivation and objectives 1
1.2 Background 4
1.3 Organization of dissertation 20

CHAPTER 2: INTRINSIC LOW DIMENSIONAL MANIFOLDS FOR A CLOSED ADIABATIC SPATIALLY HOMOGENEOUS PREMIXED REACTOR 23
2.1 Closed adiabatic spatially homogeneous premixed reactor 23
2.1.1 Energy conservation equation for the isochoric CASHPR . . . 26
2.1.2 Energy conservation equation for the isobaric CASHPR 28
2.1.3 Summary 30
2.2 Intrinsic low-dimensional manifolds 32
2.3 SIM *vs.* ILDM 40
2.4 ILDM computation 44
2.4.1 The $L + 2$ parametric equations associated with the $L + 2$ conserved quantities 53
2.4.2 The m_d parametric equations associated with the m_d-dimensional ILDM 63
2.4.3 Final form of the $m = m_d + L + 2$ parametric equations 64
2.4.4 Predictor corrector method of computing the ILDM 67
2.5 Examples 71
2.5.1 Ozone decomposition reaction mechanism 71
2.5.2 Syngas combustion reaction mechanism 76
2.5.3 $H_2/O_2/Ar$ reaction mechanism 83
2.5.4 Methane combustion reaction mechanism 93

CHAPTER 3: VISCOUS DETONATION IN A REACTIVE MIXTURE OF $H_2/O_2/Ar$ . . . 100
3.1 Problem description . . . 101
3.2 Governing equations . . . 103
3.3 Operator splitting . . . 110
3.3.1 Reaction step . . . 111
3.3.2 Convection diffusion step . . . 113
3.4 ILDM for the reaction step . . . 114
3.5 Results . . . 120

CHAPTER 4: APPROXIMATE SLOW INVARIANT MANIFOLD FOR REACTIVE FLOW SYSTEMS . . . 129
4.1 Reactive flow equations . . . 129
4.2 Simple example . . . 133
4.3 Premixed laminar flame for ozone decomposition . . . 141

CHAPTER 5: CONCLUSIONS AND FUTURE WORK . . . 151

APPENDIX A: REACTION MECHANISMS . . . 155

APPENDIX B: MIXTURE FRACTION . . . 162

APPENDIX C: ELEMENT CONSERVATION IN THE CASHPR . . . 167

BIBLIOGRAPHY . . . 169

TABLES

A.1 OZONE DECOMPOSITION REACTION MECHANISM 156

A.2 SYNGAS COMBUSTION REACTION MECHANISM 157

A.3 HYDROGEN COMBUSTION REACTION MECHANISM 159

A.4 METHANE COMBUSTION REACTION MECHANISM 160

FIGURES

1.1 Phase space of a three-dimensional dynamical system modeling the SHPR, depicting the slow manifolds and the behavior of the phase space trajectories. 14

2.1 Isochoric CASHPR 26

2.2 Isobaric CASHPR 28

2.3 Graphical representation of the ILDM for a two-dimensional dynamical system, depicting that the ILDM is a set of points in the phase space where the vector $\mathbf{V}_s$ has the same orientation as the vector $\mathbf{f}$, and that $\mathbf{f}$ is not tangent to the ILDM which is required for the ILDM to be a phase space trajectory and the SIM. 39

2.4 One-dimensional ILDM with fixed conserved quantities for ozone decomposition in the isobaric CASHPR for a reactive mixture of composition $Y_{O_0} = 0$, $Y_{O_{2_0}} = 0.6667$, $Y_{O_{3_0}} = 0.3333$ at a temperature $T_0 = 300$ K and pressure $p_0 = 0.832 \times 10^6$ dynes cm^{-2}. 74

2.5 One-dimensional ILDM for combustion of a syngas fuel mixture A (Y^A_{CO} / $Y^A_{H_2}$ / $Y^A_{N_2} = 0.4517$ / 0.0300 / 0.5543) reacting with an oxidizer mixture B ($Y^B_{O_2}/Y^B_{N_2} = 0.2329/0.7671$), for mixture fractions of $\chi = 0.70, 0.75$, in the isobaric CASHPR at temperature $T_0 = 298$ K and pressure $p_0 = 1 \times 10^6$ dynes cm^{-2}. 78

2.6 Two-dimensional ILDM for combustion of a syngas fuel mixture A (Y^A_{CO} / $Y^A_{H_2}$ / $Y^A_{N_2} = 0.4517$ / 0.0300 / 0.5543) reacting with an oxidizer mixture B ($Y^B_{O_2}/Y^B_{N_2} = 0.2329/0.7671$), for a mixture fraction of $\chi = 0.70$, in the isobaric CASHPR at temperature $T_0 = 298$ K and pressure $p_0 = 1 \times 10^6$ dynes cm^{-2}. 81

2.7 Parametric space associated with the two-dimensional ILDM in Figure 2.6 for syngas combustion. 82

2.8 One-dimensional ILDM with fixed conserved quantities for $H_2/O_2/Ar$ reaction mechanism in the isochoric CASHPR for a reactive mixture of composition $Y_{H_{2_0}} = 0.01277$, $Y_{O_{2_0}} = 0.10137$, $Y_{Ar_0} = 0.88586$ at a constant mixture density of $\rho_0 = 0.5 \times 10^{-3}$ g cm^{-3} and a constant mixture internal energy per unit mass of $e_0 = 8 \times 10^9$ ergs g^{-1} (fixed parameterization). 85

2.9 One-dimensional ILDM with fixed conserved quantities for $H_2/O_2/Ar$ reaction mechanism in the isochoric CASHPR for a reactive mixture of composition $Y_{H_{2_0}} = 0.01277$, $Y_{O_{2_0}} = 0.10137$, $Y_{Ar_0} = 0.88586$ at a constant mixture density of $\rho_0 = 0.5 \times 10^{-3}$ g cm^{-3} and a constant mixture internal energy per unit mass of $e_0 = 8 \times 10^9$ ergs g^{-1} (adaptive parameterization). 86

2.10 Two-dimensional ILDM with fixed conserved quantities for $H_2/O_2/Ar$ reaction mechanism in the isochoric CASHPR for a reactive mixture of composition $Y_{H_{2_0}} = 0.01277$, $Y_{O_{2_0}} = 0.10137$, $Y_{Ar_0} = 0.88586$ at a constant mixture density of $\rho_0 = 0.5 \times 10^{-3}$ g cm^{-3} and a constant mixture internal energy per unit mass of $e_0 = 8 \times 10^9$ ergs g^{-1}. 89

2.11 Parametric space associated with the two-dimensional ILDM in Figure 2.10 for $H_2/O_2/Ar$ reaction mechanism. 90

2.12 One-dimensional ILDM for $H_2/O_2/Ar$ reaction mechanism in the isochoric CASHPR for a reactive mixture of composition $Y_{H_{2_0}} = 0.01277$, $Y_{O_{2_0}} = 0.10137$, $Y_{Ar_0} = 0.88586$ for constant element mass fractions and constant mixture density of $\rho_0 = 0.5 \times 10^{-3}$ g cm^{-3} but a varying mixture internal energy per unit mass of $e \in [e_{min}, e_{max}] = [1 \times 10^9, 10 \times 10^9]$ ergs g^{-1}. 92

2.13 Parametric space associated with the one-dimensional ILDM in Figure 2.12 for $H_2/O_2/Ar$ reaction mechanism. 93

2.14 One-dimensional ILDM with fixed conserved quantities for methane combustion in the isobaric CASHPR for a reactive mixture of composition $Y_{CH_{4_0}}/Y_{O_{2_0}}/Y_{N_{2_0}} = 0.05515/0.22002/0.72483$ at a temperature $T_0 = 298K$ and pressure 1.01325×10^6 dynes cm^{-2}. 96

2.15 Two-dimensional ILDM with fixed conserved quantities for methane combustion in the isobaric CASHPR for a reactive mixture of composition $Y_{CH_{4_0}}/Y_{O_{2_0}}/Y_{N_{2_0}} = 0.05515/0.22002/0.72483$ at a temperature $T_0 = 298K$ and pressure 1.01325×10^6 dynes cm^{-2}. 98

2.16 Parametric space associated with the one-dimensional ILDM in Figure 2.15 for methane combustion. 99

3.1 ILDM projection for 9 species 37 step reaction mechanism of $H_2/O_2/Ar$ combustion as function of Y_{H_2O} at constant values of $\rho = 0.5 \times 10^{-3}$ g cm^{-3}, $e = 8.0 \times 10^9$ erg g^{-1}. Element mass fractions fixed at $\hat{Y}_H = 0.01277$, $\hat{Y}_O = 0.10137$, $\hat{Y}_{Ar} = 0.88586$. Also plotted are trajectories from full time integration showing relaxation to the ILDM and equilibrium. The symbol 'x' denotes equally spaced 0.10 μs time intervals. Total time to relax to equilibrium is near 0.1 ms. 116

3.2 ILDM projection for 9 species 37 step mechanism of $H_2/O_2/Ar$ combustion giving $Y_{H_2O_2}$ as a function of Y_{H_2O} and e for constant $\rho = 0.5 \times 10^{-3}$ g cm^{-3}. Element mass fractions fixed at $\hat{Y}_H = 0.01277$, $\hat{Y}_O = 0.10137$, $\hat{Y}_{Ar} = 0.88586$. 117

3.3 Sketch of projection back to the ILDM of new energy and density levels following perturbation due to convection and diffusion. 119

3.4 Predictions of temperature, velocity, pressure, and density vs. distance at $t = 195$ μs using a maximum of 300 collocation points, 15 wavelet scale levels for full chemical kinetics (solid lines) and ILDM kinetics (dots) for viscous $H_2/O_2/Ar$ detonation. 120

3.5 Predictions of species mass fractions vs. distance at $t = 195$ μs using a maximum of 300 collocation points, 15 wavelet scale levels for full chemical kinetics (solid lines) and ILDM kinetics (dots) for viscous $H_2/O_2/Ar$ detonation. 122

3.6 Spatial distribution of collocation points and wavelet levels at $t = 180$ μs (two shock structure), and $t = 230$ μs (single shock structure) demonstrating grid adaption. 123

3.7 Predictions of pressure vs. distance at $t = 230$ μs on a coarse and fine length scales demonstrating the spatial resolution of viscous and induction zone structures. 124

3.8 Predictions of temperature, velocity, pressure, and density vs. distance before commencement of significant reaction but after shock reflection using a reactive Navier-Stokes model ($t = 177$ μs). 125

3.9 Close-up view of predictions of temperature, velocity, pressure, and density vs. distance before commencement of significant reaction but just after shock reflection ($t = 174$ μs) and slightly later ($t = 177$ μs). 126

4.1 Comparison of solution of the full PDEs at $t = 5$ with the ILDM, for $\gamma = 10$ and $\mathcal{D} = 0.01$, 0.1, for Davis and Skodje's [36] model problem extended to include diffusion. 134

4.2 Maximum error ($\mathbf{L}_\infty[0,1]$) between solution of the full PDEs at $t = 5$ and the ILDM, for fixed $\gamma = 10$ and varying $\mathcal{D}$, for Davis and Skodje's [36] model problem extended to include diffusion. Stars indicate the values of $\mathcal{D}$ for which the computations were done. 135

4.3 Comparison of solution of the full PDEs at $t = 5$ with the ILDM, for $\gamma = 100$ and $\mathcal{D} = 0.1$, for Davis and Skodje's [36] model problem extended to include diffusion. 136

4.4 Maximum error ($\mathbf{L}_\infty[0,1]$) between solution of the full PDEs at $t = 5$ and the ILDM, for varying γ and fixed $\mathcal{D} = 0.1$, for Davis and Skodje's [36] model problem extended to include diffusion. Stars indicate the values of γ for which the computations were done. 137

4.5 Comparison of errors incurred by the three methods at a resolution of 100 grid points relative to a baseline solution of full integration at a resolution of 10000 grid points, for $\gamma = 10$ and $\mathcal{D} = 0.1$, for Davis and Skodje's [36] model problem extended to include diffusion. 139

4.6 Comparison of solutions obtained by full integration, using the ASIM and the MPP method at $t = 5$, for $\gamma = 10$ and $\mathcal{D} = 0.1$, for a case where the boundary condition at $x = 1$ does not lie on the ILDM. . . 141

4.7 Comparison of the steady state solution of the full PDEs with the ILDM in the phase space for ozone decomposition laminar flame: a) global view b) close-up view. 146

4.8 Ozone decomposition flame profile at $t^* = 70000$ for a) temperature, and b) species mass fractions. 147

4.9 The phase error δ incurred in computations of the premixed laminar flame of ozone decomposition with the three methods, at a resolution of 1000 points, relative to computations using full integration at a resolution of 10000 points. 148

ACKNOWLEDGEMENTS

I would like to acknowledge several people who have contributed in various ways to this work. My advisor, Dr. Joseph M. Powers, has provided invaluable guidance, discussions and technical insights throughout my graduate studies. He has also been helpful in improving my technical writing skills. All his contributions towards my education are most gratefully acknowledged. I also gratefully acknowledge Dr. Samuel Paolucci for useful inputs and discussions during our group meetings. I would also like to acknowledge the members of my doctoral committee, Dr. Samuel Paolucci, Dr. Hsueh-Chia Chang, and Dr. Mark Alber, for reviewing this dissertation.

I acknowledge my colleague Dr. Yevgenii Rastigejev for collaborating with me in combining of his WAMR and my ILDM codes for reactive flow computations which were published in Singh *et al.* [40]. I thank all the faculty and staff of the Department of Aerospace and Mechanical Engineering, University of Notre Dame, for providing an excellent environment and facilities during my graduate education.

This research has been funded by the National Science Foundation, the Air Force Office of Scientific Research and the Los Alamos National Laboratory.

I thank all my friends at Notre Dame who have made my stay here enjoyable. I also thank all the graduate students who shared the 300 Cushing offices with me, and made it a fun and intellectually stimulating place to work at. Finally, I thank my family in India for always supporting and encouraging me to follow my dreams.

LIST OF SYMBOLS

(Equation) Page

Greek Symbols

α_j Kinetic rate constant of elementary reaction j ..... (2.6) 24

β_j Temperature dependence exponent of elementary reaction j ..... (2.6) 24

χ Mixture fraction, $\chi \in [0, 1]$ ..... (2.96) 57

χ^e Mixture fraction at the chemical equilibrium state $\mathbf{y}^e$ ..... (2.105) 59

δ_{ij} Kronecker delta; $\delta_{ij} = 1$ for $i = j$ and $\delta_{ij} = 0$ for $i \neq j$ ..... (1.15) 12

ϵ Small parameter ..... (1.21) 16

$\mathbf{\Gamma}$ Matrix defined in ..... (2.101) 58

$\mathbf{\Gamma}^{\perp}$ Orthogonal complement of the matrix $\mathbf{\Gamma}$ 58

$\mathbf{\Upsilon}$ Matrix composed of the column vectors of the matrices $\mathbf{\Gamma}^{\perp}$ and $\mathbf{\Gamma}$, respectively 58

γ Stiffness parameter for the simple dynamical system in ..... (2.64) 42

$\mathbf{\Lambda}$ Diagonal matrix with eigenvalues of $\mathbf{J}$ along its diagonal ..... (2.51) 34

$\mathbf{\Lambda}_{(f)}$ Diagonal matrix with the fast set of eigenvalues, $\lambda_{(m+1)}, \ldots, \lambda_{(n)}$, along its diagonal ..... (2.51) 34

$\mathbf{\Lambda}_{(s)}$ Diagonal matrix with the slow set of eigenvalues, $\lambda_{(1)}, \ldots, \lambda_{(m)}$, along its diagonal ..... (2.51) 34

$\lambda_{(i)}$ Eigenvalues of $\mathbf{J}$ ..... (2.51) 34

μ Dynamic viscosity ..... (3.6) 103

ν''_{ij} Stoichiometric coefficient of species i on the product side of elementary reaction j ..... (2.3) 24

ν'_{ij} Stoichiometric coefficient of species i on the reactant side of elementary reaction j ..... (2.3) 24

$\mathbf{\Omega}$ Constant vector ..... (2.93) 55

$\dot{\omega}_i$ Molar rate of evolution per unit volume of species i ..... (2.2) 23

$\mathbf{\Phi}$ Matrix with elements ϕ_{il} ..... (2.90) 55

ϕ_{il} Defined in 55

φ_{il} Number of atoms of element l in a molecule of species i ..... (2.9) 25

ψ Lagrangian coordinate ..... (4.21) 142

$\mathbf{\Psi}$ Vector of conserved parameters ..... (2.93) 55

$\mathbf{\Psi}^e$ Vector of conserved parameters associated with $\mathbf{y}^e$ ..... (2.94) 56

$\mathbf{\Psi}^A$ Vector of conserved parameters associated with $\mathbf{y}^A$ ..... (2.97) 57

$\mathbf{\Psi}^B$ Vector of conserved parameters associated with $\mathbf{y}^B$ ..... (2.97) 57

ψ_l Conserved parameters ..... (2.86) 53

ψ_l^e Conserved parameters associated with chemical equilibrium state ..... (2.106) 59

ψ_l^A Conserved parameters associated with the mixture A ..... (2.99) 57

ψ_l^B Conserved parameters associated with the mixture B ..... (2.99) 57

ρ Density ..... (2.7) 24

ρ_0 Density at time $t = 0$ ..... (2.38) 30

ρ_{max} Maximum limit of the range of ρ for which the ILDM is constructed ... 83

ρ_{min} Minimum limit of the range of ρ for which the ILDM is constructed ... 83

$\mathbf{\Sigma}$ Diagonal matrix obtained by singular value decomposition of the matrix $\mathbf{\Gamma}$ ..... (2.102) 58

τ Viscous stress ..... (3.2) 103

$\mathbf{\Theta}$ Vector of polar angles 66

θ_l Polar angles in the parametric space of the ILDM ..... (2.127) 66

$\mathbf{\Xi}_{(1)}$ Vector defined in ..... (2.107) 59

$\mathbf{\Xi}^e_{(1)}$ Vector defined in ..... (2.107) 59

$\mathbf{\Xi}_{(2)}$ Vector defined in ..... (2.118) 62

$\mathbf{\Xi}^e_{(2)}$ Vector defined in ..... (2.118) 62

ζ Pseudo-time variable used in the corrector step ..... (2.138) 69

Roman Symbols

B Small parameter; a species is eliminated from the reaction mechanism via sensitivity analysis if $B_i < B$ 7

B_i Relative sensitivity of the dynamics of the reactive system for changes in concentration of species i ..... (1.5) 6

c_k k-th coefficient in the polynomial approximation of the SIM ..... (2.71) 43

c_p Mass averaged specific heat at constant pressure ..... (2.32) 29

c_{pi} Specific heat at constant pressure of species i ..... (2.29) 29

c_v Mass averaged specific heat at constant volume ..... (2.20) 27

c_{vi} Specific heat at constant volume of species i ..... (2.17) 27

$\mathcal{D}$ Diffusion parameter in the simple example ..... (4.8) 133

$\mathbb{D}$ Domain of the parametric space 65

$\mathcal{D}_{ij}$ Multicomponent mass diffusion coefficient of species i in species j ..... (3.8) 103

$\mathcal{D}_k$ Diffusion coefficient of species k in the fluid mixture ..... (4.20) 142

$\mathcal{D}_i^T$ Soret/DuFour thermal diffusion coefficient of species i ..... (3.7) 103

$\mathbf{d}$ Vector of free parameters associated with the ILDM ..... (2.123) 64

d_l Elements of vector $\mathbf{d}$ 64

E_j Activation energy of elementary reaction j ..... (2.6) 24

e Mixture internal energy per unit mass ..... (2.13) 26

e_0 Mixture internal energy per unit mass at time $t = 0$ ..... (2.42) 31

e_i Internal energy per unit mass of species i ..... (2.14) 27

$\mathbf{e}_i$ Standard unit normal vector 39

e_{max} Maximum limit of the range of e for which the ILDM is constructed ... 83

e_{min} Minimum limit of the range of e for which the ILDM is constructed ... 83

e_r Minimum error between the full model equations and the reduced model equations obtained by optimization technique ..... (1.9) 8

F Forcing function in the two-point boundary value problem ..... (4.14) 138

$\mathbf{F}$ Rate sensitivity Jacobian matrix with elements F_{ij} ..... (1.8) 7

$\mathbf{f}(\mathbf{y})$ Nonlinear vector function of $\mathbf{y}$ or the reaction source term ..... (2.50) 33

$\bar{\mathbf{f}}$ Forcing function for lumped variables ..... (1.12) 9

$\mathbf{f}_f$ Forcing function for fast variables ..... (1.21) 16

f_i Elements of vector $\mathbf{f}$ ..... (2.62) 41

$\mathbf{f}_d$ Functional mapping for the ILDM from the parametric space to the phase space ..... (2.125) 65

$\mathbf{f}_r$ Functional mapping for the ILDM from the polar parametric space to the phase space ..... (2.130) 67

$\mathbf{f}_s$ Forcing function for slow variables ..... (1.21) 16

G Green's function ..... (4.16) 138

$\mathcal{G}_i$ Implicit function solved by functional iteration for computation of the SIM, $(i = m+1, \ldots, n)$ ..... (2.63) 41

g_i Amplitude of the i-th mode in the CSP method ..... (1.14) 12

$\mathbf{g}$ Nonlinear part of $\mathbf{f}$ ..... (2.52) 35

$\mathbb{H}$ Domain of the parametric space for which the SIM is computed 41

h Mixture enthalpy per unit mass ..... (2.25) 29

h_0 Mixture enthalpy per unit mass at time $t = 0$ ..... (2.48) 32

h°_{fi} Enthalpy of formation of species i at standard temperature of $T_s = 298$ K ..... (2.36) 30

h_i Enthalpy per unit mass of species i ..... (2.26) 29

h_{max} Maximum limit of the range of h for which the ILDM is constructed ..... (2.86) 53

h_{min} Minimum limit of the range of h for which the ILDM is constructed ..... (2.86) 53

h^A Enthalpy per unit mass of the mixture A ..... (2.108) 60

h^B Enthalpy per unit mass of the mixture B ..... (2.108) 60

$\mathbf{h}(\mathbf{y})$ Tensor function representing the convective and diffusive fluxes .... (1.1) 1

$\mathbf{h}_\epsilon(\mathbf{y}_s)$ Asymptotic expansion for the SIM ..... (1.22) 16

$\mathbf{h}_0(\mathbf{y}_s)$ Coefficient of the $\mathcal{O}(\epsilon^0)$ term in the asymptotic expansion for the SIM ..... (1.22) 16

$\mathbf{h}^{(i)}(\mathbf{y}_s)$ Coefficient of the $\mathcal{O}(\epsilon^i)$ term in the asymptotic expansion for the SIM ..... (1.22) 16

$\mathbf{h}'(\mathbf{y}_s)$ Algebraic inertial manifold approximation for the SIM ..... (1.23) 17

J Total number of reactions in a reaction mechanism ..... (2.3) 24

$\mathbf{J}$ Jacobian matrix $\frac{\partial \mathbf{f}}{\partial \mathbf{y}}$ ..... (2.51) 34

J_i^m Diffusive mass flux of species i ..... (3.5) 103

$\hat{J}_l^m$ Diffusive mass flux of element l ..... (3.4) 103

J^q Diffusive energy flux ..... (3.3) 103

$K(\boldsymbol{\Theta})$ Number of points along a one-dimensional ILDM slice, for a fixed $\boldsymbol{\Theta}$ in the parametric space, before it cuts the boundary of the subspace $\mathbb{S} \in \mathbb{R}^n$ ..... (2.132) 68

k Thermal conductivity ..... (3.7) 103

k_d Number of dormant modes while using the CSP method ..... (1.17) 13

k_e Number of exhausted modes while using the CSP method ..... (1.17) 13

k_j Temperature dependent rate constant for elementary reaction j ... (2.5) 24

k_r Number of elementary reactions in the reduced reaction mechanism obtained by optimization technique ..... (1.9) 8

k_{s1} Minimum number of species in the reduced reaction mechanism obtained by optimization technique ..... (1.10) 8

k_{s2} Maximum number of species in the reduced reaction mechanism obtained by optimization technique ..... (1.10) 8

L Total number of elements in a reaction mechanism ..... (2.9) 25

$\mathbf{L}$ Linear operator ..... (4.13) 138

$\mathbf{L}(\mathbf{Y})$ Lumping transformation vector function ..... (1.11) 9

l_1 Length of the null vector given by $m - l_2$ 64

l_2 Dimension of the parametric space associated with the ILDM 64

M Multicomponent mean molecular mass ..... (3.9) 104

$\mathbb{M}_i$ i-dimensional ILDM in the phase space, $(i = 1, \ldots, N - L)$ ..... (2.79) 48

M_i Molecular mass of species i ..... (2.7) 24

$\hat{M}_l$ Atomic mass of element l ..... (2.10) 25

m Number of slow time scales ($m < n$) 35

$\mathsf{m}_\circ$ Total mass of a reacting mixture ..... (2.1) 23

m_d Dimension of the ILDM 48

m_i Mass of species i ..... (2.1) 23

$\hat{\mathsf{m}}_l$ Mass of element l 25

$\dot{m}_0$ Inlet mass flow rate ..... (4.22) 142

N Total number of species in a reaction mechanism ..... (2.1) 23

$\mathcal{N}_i$ Number of moles of species i ..... (2.2) 23

$\hat{\mathcal{N}}_l$ Number of moles of element l ..... (2.9) 25

$\mathbf{N}_f$ Upper-triangular matrix, obtained from real Schur decomposition of $\mathbf{J}$, with the fast set of eigenvalues along its main diagonal ..... (2.80) 50

$\mathbf{N}_s$ Upper-triangular matrix, obtained from real Schur decomposition of $\mathbf{J}$, with the slow set of eigenvalues along its main diagonal .... (2.80) 50

$\mathbf{N}_{sf}$ Full matrix, obtained from real Schur decomposition of $\mathbf{J}$ ..... (2.80) 50

n Dimension of the phase space associated with the dynamical system modeling the CASHPR ..... (2.50) 33

$\mathcal{O}(\ )$ Order ( ) ..... (2.70) 43

$\mathbf{P}_c$ Matrix defined in ..... (2.88) 54

$\mathbf{P}_d$ Matrix defined in ..... (2.123) 64

$\mathbf{P}_p$ Matrix defined in ..... (2.90) 55

$\mathbf{P}_r$ Matrix defined in ..... (2.131) 67

$\mathbf{P}_s$ User specified parametric matrix associated with the m_d-dimensional ILDM ..... (2.122) 63

$\mathbf{P}_z$ Matrix defined in ..... (2.93) 55

$\mathbf{P}_\chi^{(1)}$ Matrix defined in ..... (2.104) 59

$\mathbf{P}_\chi^{(2)}$ Matrix defined in ..... (2.115) 62

p Pressure ..... (2.8) 25

p_0 Pressure at time $t = 0$ ..... (2.46) 32

p_{max} Maximum limit of the range of p for which the ILDM is constructed ..... (2.86) 53

p_{min} Minimum limit of the range of p for which the ILDM is constructed ..... (2.86) 53

$\mathbf{p}_r$ Vector function for transformation of polar coordinate system to Cartesian coordinate system ..... (2.129) 67

$\mathbf{Q}_f$ Matrix with orthogonal column vectors as the real Schur vectors associated with the fast set of eigenvalues ..... (2.80) 50

$\mathbf{Q}_s$ Matrix with orthogonal column vectors as the real Schur vectors associated with the slow set of eigenvalues ..... (2.80) 50

q_j 1 or 0 depending on whether or not elementary reaction j is part of the reduced reaction mechanism obtained by optimization technique ..... (1.9) 8

$\mathbf{R}_{l_2 \times l_2}$ l_2-dimensional rotation matrix ..... (2.126) 65

R_{ij} Elements of matrix $\mathbf{R}_{l_2 \times l_2}$ ..... (2.127) 66

$\Re$ Universal gas constant ..... (2.6) 24

$\mathbb{R}^{l_2}$ l_2-dimensional real parametric space 65

$\mathbb{R}^n$ n-dimensional real phase space 33

r Radial distance from the chemical equilibrium state, $\mathbf{d} = \mathbf{0}$, in the parametric space ..... (2.126) 65

$\mathbf{r}$ Vector defined in 66

r_p Distance between two consecutive points along a one-dimensional ILDM slice for a fixed $\boldsymbol{\Theta}$ in the parametric space ..... (2.134) 69

$\mathbf{r}_p$ Vector defined in ..... (2.134) 69

r_j Rate of elementary reaction j ..... (2.5) 24

S'_j Set of indices of those species which appear in reaction j ..... (1.10) 8

S_i Symbol for species i ..... (2.3) 24

$\mathbb{S}$ Physically accessible subspace of the phase space $\mathbb{R}^n$ ..... (2.78) 47

$\mathbb{S}'$ Invariant manifold subspace in $\mathbb{R}^n$ 38

$\mathbf{s}$ Parametric vector associated with the m_d-dimensional ILDM ... (2.122) 63

$\mathbf{s}^e$ Parametric vector associated with the chemical equilibrium state ..... (2.122) 63

s_l Elements of vector $\mathbf{s}$ 63

T Temperature ..... (2.6) 24

T_s Standard temperature 298 K ..... (2.36) 30

T_0 Temperature at time $t = 0$ 71

T' Certain fixed time > 0 38

$\mathbf{T}_t$ Tangent space to the ILDM 38

t Time ..... (2.2) 23

t_i Induction time 108

$\mathbf{U}$ Orthogonal matrix obtained by singular value decomposition of the matrix $\mathbf{\Gamma}$, with columns as the eigenvectors of the matrix $\mathbf{\Gamma}\mathbf{\Gamma}^T$ ..... (2.102) 58

u Mass averaged velocity ..... (3.1) 103

V Volume ..... (2.2) 23

$\mathbf{V}$ Right eigenvector matrix of $\mathbf{J}$ ..... (2.51) 34

$\tilde{\mathbf{V}}$ Left eigenvector matrix of $\mathbf{J}$ ..... (2.51) 34

$\mathbf{V}_f$ Matrix with column vectors which form the local fast basis ..... (2.51) 34

$\tilde{\mathbf{V}}_f$ Matrix with row vectors which form the local reciprocal fast basis ..... (2.51) 34

$\mathbf{V}_s$ Matrix with column vectors which form the local slow basis ..... (2.51) 34

$\tilde{\mathbf{V}}_s$ Matrix with row vectors which form the local reciprocal slow basis ..... (2.51) 34

v Specific volume ..... (2.23) 28

$\mathbf{v}_i$ Right eigenvectors of $\mathbf{J}$ ..... (2.51) 34

$\tilde{\mathbf{v}}_i$ Left eigenvectors of $\mathbf{J}$ ..... (2.51) 34

$\mathbf{W}$ Orthogonal matrix obtained by singular value decomposition of the matrix $\mathbf{\Gamma}$, with columns as the eigenvectors of the matrix $\mathbf{\Gamma}^T\mathbf{\Gamma}$ ..... (2.102) 58

w_i 1 or 0 depending on whether or not species i is part of the reduced reaction mechanism obtained by optimization technique ..... (1.10) 8

$\mathbf{X}$ Solution matrix of the Sylvester equation ..... (2.81) 51

$[X_i]$ Molar concentration of species i ..... (2.5) 24

X_i Mole fraction of species i ..... (3.7) 103

$\mathbf{Y}$ Vector of species mass fractions ..... (1.4) 5

$\bar{\mathbf{Y}}$ Vector of lumped variables ..... (1.11) 9

Y_i' Mass fraction of species i in the reduced model equations obtained by optimization technique ..... (1.9) 8

Y_i Mass fraction of species i ..... (2.7) 24

Y_{i_0} Mass fraction of species i at time $t = 0$ ..... (2.12) 26

Y_i^A Mass fraction of species i in the mixture A 56

Y_i^B Mass fraction of species i in the mixture B 56

$\hat{Y}_l$ Mass fraction of element l ..... (2.10) 25

$\hat{Y}_{l_0}$ Mass fraction of element l at time $t = 0$ ..... (2.12) 26

$\hat{Y}_l^A$ Mass fraction of element l in the mixture A ..... (2.96) 57

$\hat{Y}_l^B$ Mass fraction of element l in the mixture B ..... (2.96) 57

$\mathbf{y}$ Vector representing the state of a reactive mixture in the phase space ..... (2.50) 33

$\mathbf{y}_{c_k}$ A point along a one-dimensional ILDM slice for a fixed $\mathbf{\Theta}$ and a radial distance of kr_p from the origin in the parametric space ..... (2.132) 68

$\mathbf{y}^e$ Chemical equilibrium state in the phase space ..... (2.94) 56

$\mathbf{y}^A$ Fuel mixture state in the phase space ..... (2.97) 57

$\mathbf{y}^B$ Oxidizer mixture state in the phase space ..... (2.97) 57

$\mathbf{y}_f$ Vector of fast variables ..... (1.21) 16

y_i Elements of vector $\mathbf{y}$ ..... (2.60) 40

y_i^k k-th functional iterate for computation of the SIM ..... (2.63) 41

$\mathbf{y}_{p_k}$ Prediction or initial guess for computation of $\mathbf{y}_{c_k}$ by Newton's method ..... (2.132) 68

$\mathbf{y}_s$ Vector of slow variables ..... (1.21) 16

$\bar{\mathbf{y}}$ Vector of conserved quantities ..... (2.86) 53

$\bar{y}_l$ Elements of vector $\bar{\mathbf{y}}$ ..... (2.86) 53

$\mathbf{Z}_f$ Matrix with column vectors which form the local fast basis ..... (2.83) 51

$\tilde{\mathbf{Z}}_f$ Matrix with row vectors which form the local reciprocal fast basis ..... (2.83) 51

$\mathbf{Z}_s$ Matrix with column vectors which form the local slow basis ..... (2.83) 51

$\tilde{\mathbf{Z}}_s$ Matrix with row vectors which form the local reciprocal slow basis ..... (2.83) 51

$\mathbf{Z}_{f_k}$ Local fast basis at $\mathbf{y}_{c_k}$ 68

$\tilde{\mathbf{Z}}_{f_k}$ Local reciprocal fast basis at $\mathbf{y}_{c_k}$ 68

$\mathbf{Z}_{s_k}$ Local slow basis at $\mathbf{y}_{c_k}$ 68

$\tilde{\mathbf{Z}}_{s_k}$ Local reciprocal slow basis at $\mathbf{y}_{c_k}$ 68

$\mathbf{z}$ Nonlinear transformation of $\mathbf{y}$ defined in 35

z_i Elements of vector $\mathbf{z}$.....(2.55) 35

CHAPTER 1

INTRODUCTION

1.1 Motivation and objectives

This study will focus on development of algorithms which enable efficient computational simulations of combustion processes. Some applications in combustion science are candle flames, atmospheric chemistry, internal combustion engines and gas turbine engines. However, the algorithms developed in this work will be applied and tested in the framework of some basic combustion processes such as detonation and laminar flames, which are intrinsic to the more complicated applications. All these combustion processes involve a large number of elementary chemical reactions occurring simultaneously within a complex flow field. This reactive flow phenomenon is modeled by a large number of partial differential equations (PDEs) representing the evolution of numerous reactive chemical species, coupled with the full Navier-Stokes equations. The PDEs are usually of the form

$$\frac{\partial \mathbf{y}}{\partial t} = \mathbf{f}(\mathbf{y}) - \nabla \cdot \mathbf{h}(\mathbf{y}), \tag{1.1}$$

where the vector $\mathbf{y} \in \mathbb{R}^n$ represents a set of dependent variables which typically include the species mass fractions, thermodynamic state variables such as temperature, density and pressure, and fluid velocity vector field. The number of PDEs, n, is usually large due to the large number of chemical species involved in combustion processes. The reaction source term is represented by the vector function $\mathbf{f}(\mathbf{y})$, while the convective and diffusive fluxes are represented by the tensor function

$\mathbf{h}(\mathbf{y})$. The time variable is represented by t. Fully resolved numerical solutions of these model equations, incorporating detailed finite rate chemical kinetics in $\mathbf{f}$, along with the initial and boundary conditions, often require a prohibitive amount of computational resources. Hence, there is a need to develop methods which rationally reduce the model equations such that numerical simulations can be accomplished in a reasonable amount of computational time, but also in a way which maintains essential fidelity of the reduced model equations to the underlying full equations.

Combustion of a typical hydrocarbon may involve hundreds of chemical species which may be reactants, products or intermediate species. These chemical species may react in thousands of elementary reaction steps, which constitute a reaction mechanism. The number of model equations for combustion processes associated with such large reaction mechanisms is of the order of the number of reacting chemical species. The computational expense for numerical simulations increases with both the number of species and the number of elementary reactions involved. The elementary chemical reactions occur over a wide range of time scales which is manifested as stiffness in the model equations. This is a more serious problem as it is computationally expensive to solve stiff differential equations. In order to alleviate these problems and achieve computational efficiency, several methods have been developed to reduce the complexity associated with large reaction mechanisms. In this study the method of Intrinsic Low-Dimensional Manifolds (ILDM) [1] will be employed and extended for this purpose. A code, based on an algorithm associated with the ILDM method, with new features, was developed and used for various reaction mechanisms. In this work the accuracy of the standard ILDM method will also be clarified.

Some of the recent methods reduce the stiffness in the model equations by systematically equilibrating the chemical processes which occur at fast time scales

and by resolving only those chemical processes which occur at relevant slow time scales. The time scales at which the reactive processes occur usually overlap the time scales at which the flow or mixing processes occur due to convection and diffusion effects. Hence, it is important that the reduced model equations maintain the coupling of the flow processes with those chemical processes which occur at similar time scales. Often reduced reaction mechanisms are developed based on chemistry alone and then used in reactive flow scenarios, in which case this coupling may not be maintained. In this work it will also be illustrated how the coupling of fluid and chemical processes can be maintained such that an approximate and less expensive numerical solution of the reduced model equations is consistent with the more accurate and expensive numerical solution of the full model equations.

Some of the original contributions of this dissertation include a clarification of the accuracy of the ILDM approximation of the Slow Invariant Manifold (SIM) for a dynamical system which models a spatially homogeneous reactive system. A new algorithm for computing the multi-dimensional ILDM in a polar parametric space has been developed and the associated parametric equations have been derived. A FORTRAN code based on the new algorithm was also developed. An operator splitting method was used to extend the use of the ILDM method for efficient numerical simulation of one-dimensional viscous detonation in a reactive mixture of $H_2/O_2/Ar$, which is a reactive flow system. This was a first application of the ILDM method in supersonic reactive flow. Also, a new infinite-dimensional Approximate Slow Invariant Manifold (ASIM) was developed for reactive flow systems in which reactive, convective and diffusive effects are closely coupled.

1.2 Background

Over the years several strategies have been used for efficient simulation of reactive flows. For completeness, the strategy of the frozen flow assumption, which can be applied on an *ad hoc* basis to cold regions of the flow, is mentioned. The method of frozen flow assumes that all chemical reactions are inhibited ($\mathbf{f} \sim \mathbf{0}$) and only mixing of chemical species occurs due to convection and diffusion. The following PDEs are then solved for the multicomponent system

$$\frac{\partial \mathbf{y}}{\partial t} = -\nabla \cdot \mathbf{h}(\mathbf{y}). \tag{1.2}$$

This strategy only works well in cold regions of the flow where the temperatures are too low to initiate any reactions and is not viable to predict reactive flows. Another approach of equilibrium flow assumes all chemical species to be in local chemical equilibrium, everywhere in the changing flow field. This is equivalent to the assumption that all chemical processes equilibrate at an infinitely fast time scale. In this approach the numerical simulation is performed in two steps. In the first step, the thermodynamic state and the composition of the chemical species are adjusted at each location in the flow field to a chemical equilibrium obtained by solving the nonlinear algebraic equations

$$\mathbf{f}(\mathbf{y}) = \mathbf{0}. \tag{1.3}$$

The local chemical equilibria vary throughout the flow field as they depend on the thermodynamic state and the chemical composition at each location in the flow field, just before Equation (1.3) is solved. These local chemical equilibria can also be obtained, alternatively and more efficiently, by using a minimum potential method of the code STANJAN [2]. In the second step, the convection and diffusion of various chemical species are accounted for by numerically integrating the less

stiff Equation (1.2) for a small time step. The two steps are repeated for several time steps to predict a solution at a future time. This strategy only works well in hot regions of the flow where the chemical species quickly relax to local chemical equilibria, while they continue to mix due to convection and diffusion effects. The method of equilibrium flow is also less expensive than a numerical integration of the full model Equation (1.1). However, these approaches of frozen flow and equilibrium flow, discussed in detail by Vincenti and Kruger [3], are not very accurate for many flows as they do not capture any reaction time scales and hence, miss the coupling between flow and chemical processes.

Some other strategies are based on *a priori* reduction of detailed chemical kinetics associated with a reaction mechanism, before using it with a computational fluid dynamics (CFD) code for reactive flow simulations. In order to do so, a reactive system often studied is a spatially homogeneous premixed reactor (SHPR), which is modeled by a system of ordinary differential equations (ODEs) in the absence of any transport processes such as convection and diffusion ($\mathbf{h} = \mathbf{0}$)

$$\frac{d\mathbf{y}}{dt} = \mathbf{f}(\mathbf{y}). \tag{1.4}$$

These model equations depend on chemical kinetics alone and are useful for analyzing the reaction mechanism as a dynamical system. Unlike in Equation (1.1), the vector $\mathbf{y}$ in Equation (1.4) represents a vector of species mass fractions only, with $\mathbf{y} = \mathbf{Y} = (Y_1, \ldots, Y_N)^T$, where Y_i is the mass fraction of species i, and $n = N$ is the total number of species. Due to spatial homogeneity, the thermodynamic state of the reactive mixture in the SHPR at a certain time can be obtained from the algebraic thermal and caloric equations of state. The behavior of the SHPR can be described by trajectories in composition space or phase space $\mathbb{R}^n$, starting from an initial condition and relaxing to a chemical equilibrium. Numerical integration of Equation (1.4), which represents a large number of stiff

ODEs, is expensive. However, numerical integration of Equation (1.1), which after discretization represents a much larger number of stiff ODEs, is much more expensive as it is equivalent to solving stiff Equation (1.4) at every location in an inhomogeneous flow field. The review articles by Griffiths [4] and Okino and Mavrovouinotis [5] discuss in detail several strategies to obtain reduced model equations for the SHPR.

One simple and often useful method, which may capture some of the reaction time scales, consists of replacing hundreds of elementary reaction steps by explicit one- or two-step reaction models [6, 7, 8, 9]. Typically, only the important reactant and product species of the full reaction mechanism are retained in the reduced reaction mechanism, while most of the intermediate species are eliminated. This method is *ad hoc* and is used to obtain simplified kinetics which has some characteristics of the detailed kinetics. It requires curve fitting of reaction rate parameters of the reduced reaction mechanism. This is done such that the dynamics of the SHPR, when the reduced reaction mechanism is used, is similar to some approximation to the dynamics of the SHPR, when the original detailed reaction mechanism is used.

Sensitivity analysis is often used to obtain a reduced reaction mechanism by identifying the unimportant species and redundant elementary reactions in a reaction mechanism. A species can be eliminated from a reaction mechanism, if changes in its concentration have only a negligible effect on the dynamics of the reactive system modeled by Equation (1.4). The relative sensitivity, B_i, of species i with respect to the other species is given by following [10]

$$B_i = \sum_{j=1}^{N} \left(\frac{\partial \ln \dot{\omega}_j}{\partial \ln[X_i]} \right)^2, \qquad (i = 1, \ldots, N), \tag{1.5}$$

where $\dot{\omega}_i = \frac{\rho}{M_i} f_i$ is the molar rate of evolution per unit volume of species i, M_i is

the molecular mass of species i, ρ is the reactive mixture density and $[X_i] = \frac{\rho}{M_i} Y_i$ is the moles per unit volume of species i. Species i can be eliminated if $B_i < B$, where B is a small parameter. Typically, eliminating a species from a reaction mechanism means that it does not take part in the reactive process and its concentration remains constant at its initial condition value. All the elementary reactions in which the eliminated species take part are also removed from the original reaction mechanism. By eliminating the unimportant species, the number of ODEs modeling the SHPR are reduced. The molar rate of evolution per unit volume of species i is given by

$$\dot{\omega}_i = \sum_{j=1}^{J} (\nu''_{ij} - \nu'_{ij}) r_j, \qquad (i = 1, \ldots, N), \tag{1.6}$$

where ν'_{ij} and ν''_{ij} are the stoichiometric coefficients of species i on the reactants and products side of elementary reaction j, respectively, r_j is the rate of elementary reaction j, and J is the number of elementary reactions in the reaction mechanism. The rate of an elementary reaction, using law of mass action, is given by

$$r_j = k_j \prod_{i=1}^{N} [X_i]^{\nu'_{ij}}, \qquad (j = 1, \ldots, J), \tag{1.7}$$

where k_j is the rate constant of elementary reaction j. An elementary reaction can be eliminated from a reaction mechanism via sensitivity analysis if perturbations in its rate constant have only a negligible effect on the dynamics of the reactive system modeled by Equation (1.4). The redundant elementary reactions can be determined by a principal component analysis [11] of the rate sensitivity Jacobian matrix, $\mathbf{F}$, which has elements obtained by differentiating Equation (1.6)

$$F_{ij} = \frac{\partial \ln \dot{\omega}_i}{\partial \ln k_j} = \frac{(\nu''_{ij} - \nu'_{ij}) r_j}{\dot{\omega}_i}, \qquad (i = 1, \ldots, N), \ (j = 1, \ldots, J). \tag{1.8}$$

An elementary reaction can be eliminated from a reaction mechanism if the corresponding reaction vector, $(\nu''_{1j} - \nu'_{1j}, \ldots, \nu''_{Nj} - \nu'_{Nj})^T$, has a negligible component in the basis spanned by the eigenvectors of the matrix $\mathbf{F}\mathbf{F}^T$.

Optimization approaches [12, 13, 14] have also been used to derive a reduced reaction mechanism from the full reaction mechanism by eliminating some species and elementary reactions. Petzold and Zhu [12] find the optimum reduced reaction mechanism with reduced number of elementary reactions by solving the following discrete constrained optimization problem

$$e_r = \min||\mathbf{Y} - \mathbf{Y}'||, \tag{1.9a}$$

subject to

$$\frac{dY_i}{dt} = \frac{M_i}{\rho}\sum_{j=1}^{J}(\nu''_{ij} - \nu'_{ij})r_j, \qquad Y_i(0) = Y_{i_0}, \qquad (i = 1, \ldots, N), \tag{1.9b}$$

$$\frac{dY'_i}{dt} = \frac{M_i}{\rho}\sum_{j=1}^{J}(\nu''_{ij} - \nu'_{ij})q_j r_j, \qquad Y'_i(0) = Y_{i_0}, \qquad (i = 1, \ldots, N), \tag{1.9c}$$

$$\sum_{j=1}^{J} q_j = k_r, \qquad q_j = 1 \text{ or } 0, \tag{1.9d}$$

where Y'_i represents the mass fraction of species i in the reduced model equations (1.9c). The minimum e_r is over $q_1, \ldots, q_J$, where each q_j can take the value 1 or 0 depending on whether or not elementary reaction j is part of the reduced reaction mechanism. Equation (1.9b) is same as the original model Equation (1.4) for the SHPR, while Equation(1.9c) is the reduced model equation. The number of elementary reactions k_r, in the reduced reaction mechanism, is user specified with $k_r << J$. Similarly, the optimum reduced reaction mechanism with reduced number of species is obtained by solving the discrete constrained optimization problem in Equation (1.9) with Equation (1.9d) replaced by the following

$$q_j = \prod_{i \in S'_j} w_i, \qquad k_{s1} \leq \sum_{i=1}^{N} w_i \leq k_{s2}, \qquad w_i = 1 \text{ or } 0, \tag{1.10}$$

where the minimum e_r is now over $w_1, \ldots, w_N$, where each w_i can take the value 1 or 0 depending on whether or not species i is part of the reduced reaction mechanism. The set of indices of those species which appear in elementary reaction

j is represented by S'_j. It is evident from Equations (1.9c) and (1.10) that all the elementary reactions in which the eliminated species take part are also eliminated from the reaction mechanism. The mass fraction of the eliminated species remains constant at its initial condition value. The minimum number of species, k_{s1}, and the maximum number of species, k_{s2}, in the reduced reaction mechanism, are user specified with $k_{s1} < k_{s2} < N$. The discrete constrained optimization problem for species reduction is highly nonlinear and more difficult to solve than that for elementary reaction reduction. The error in the thermodynamic state of the reactive system, when using the reduced model in Equation (1.9c), should also be included in the error norm e_r. Also, the discrete optimization problem is converted to a continuous optimization problem to reduce the computational costs.

Some methods have been developed to reduce the ODEs in Equation (1.4) and their stiffness, instead of actually generating reduced reaction mechanisms by eliminating some species and elementary reactions. One such method is the lumping method [15, 16], where the mass fractions of the chemical species are lumped into reduced number of variables using the following transformation

$$\bar{\mathbf{Y}} = \mathbf{L}(\mathbf{Y}), \qquad (m \text{ algebraic equations}), \tag{1.11}$$

where $\mathbf{L} : \mathbb{R}^n \rightarrow \mathbb{R}^m$ $(m < n)$ is the lumping transformation function, and $\bar{\mathbf{Y}}$ represents the transformed dependent variable. For linear lumping, $\mathbf{L}(\mathbf{Y})$ is a linear function, while for nonlinear lumping, $\mathbf{L}(\mathbf{Y})$ is a nonlinear function. The reduced model equations for the SHPR, using the lumping method, are given by

$$\frac{d\bar{\mathbf{Y}}}{dt} = \bar{\mathbf{f}}(\bar{\mathbf{Y}}), \qquad (m \text{ ODEs}). \tag{1.12}$$

The main challenge of the lumping method is to identify the lumping and inverse lumping transformation functions. Nonlinear lumping techniques [17, 18] have been developed using singular perturbation methods, which exploit the inherent

separation in time scales of reactive processes. In such techniques $\bar{\mathbf{Y}}$ represents the slow variables and Equation (1.12) describes only the slow dynamics of the reactive system. Hence, the reduced model equations are less stiff. However, this method has been restricted to simple reactive systems where a constant small singular perturbation parameter, which quantifies the separation in slow and fast time scales, can be easily identified.

To reduce the model equations (1.4) and their stiffness, quasi steady state assumptions (QSSA) are commonly applied for those chemical species which react at fast time scales and reach a stationary state with respect to the other species in the reactive system. The reduced model equations, which are a system of differential algebraic equations (DAEs), are given by

$$\frac{dY_i}{dt} = f_i(Y_1, \ldots, Y_n), \qquad (i = 1, \ldots, m), \tag{1.13a}$$

$$0 = f_i(Y_1, \ldots, Y_n), \qquad (i = m+1, \ldots, n), \tag{1.13b}$$

where species $m+1, \ldots, n$, are assumed to be in quasi steady state, resulting into the algebraic Equations (1.13b). The concentration of these quasi steady state species is not constant and can be obtained from the algebraic Equations (1.13b). The DAEs obtained by the QSSA method can be further simplified by assuming partial equilibrium for some fast elementary reactions. The algebraic equations obtained by QSSA and partial equilibrium assumptions can sometimes be substituted into Equation (1.13a) to simply obtain a set of reduced number of ODEs as in Equation (1.12), but with $\bar{\mathbf{Y}} = (Y_1, \ldots, Y_m)^T$. Often, a reduced reaction mechanism associated with these reduced set of ODEs can be written explicitly. More details on this procedure can be found in [19, 20]. However, this method requires substantial amounts of fallible human intuition and human time. A knowledge of chemistry and a careful analysis of the large number of reaction rate parameters is required

to decide which species can be in quasi steady state and which elementary reaction can be in partial equilibrium.

Of the reduction methods discussed thus far, the one- or two-step reduced reaction models, the method of sensitivity analysis, and the optimization technique, none attempt to systematically reduce the stiffness associated with the full reaction mechanism. Instead, these methods rely on elimination, by analysis, of unimportant species and elementary reactions to generate a reduced reaction mechanism. Even though the lumping method, QSSA and partial equilibrium assumptions somewhat reduce the stiffness, besides reducing the model equations, they do not do so by a rational analysis of the time scales involved. Hence, the reduced model equations, derived using these methods, may still be considerably stiff. Another problem with all the approaches discussed until now is that while the resulting reduced models may be useful for a certain range of thermodynamic states and compositions of chemical species for which they have been calibrated, it is often easy to find scenarios where they do not do a good job of approximating the full model. Hence, these methods should be applied for an extensive range of operating conditions before generating the final reduced model.

The methods of Intrinsic Low Dimensional Manifolds (ILDM) [1] and Computational Singular Perturbation (CSP) [21, 22] use a dynamical systems approach of time scale analysis to systematically reduce the stiffness in the model equations. Also, these methods are based on a local analysis of the slow and fast time scales in phase space, and hence, adapt for appropriate reduced description of chemical kinetics in different regions of phase space.

The CSP method identifies and eliminates, what have been named by Lam [22], the local exhausted and dormant modes, while retaining only the local slow active modes at a certain time along the phase space trajectory of the dynamical system

in Equation (1.4), thereby reducing the stiffness. The exhausted and dormant modes are associated with equilibrated and temporarily inactive reactive processes, respectively. The vector $\mathbf{f}$, which represents the reaction source term, is locally partitioned into various modes, using n linearly independent basis vectors $\mathbf{v}_i$

$$\mathbf{f}(\mathbf{y}) = \sum_{i=1}^{n} g_i(\mathbf{y})\mathbf{v}_i(\mathbf{y}), \tag{1.14}$$

where g_i is the amplitude of the i-th mode and is given by

$$g_i(\mathbf{y}) = \tilde{\mathbf{v}}_i(\mathbf{y}) \cdot \mathbf{f}(\mathbf{y}), \qquad \text{with} \qquad \tilde{\mathbf{v}}_i(\mathbf{y}) \cdot \mathbf{v}_j(\mathbf{y}) = \delta_{ij}, \tag{1.15}$$

where the n vectors $\tilde{\mathbf{v}}_i$ form the reciprocal basis of the basis formed by the n vectors $\mathbf{v}_i$, and δ_{ij} is the Kronecker delta ($\delta_{ij} = 1$ for $i = j$ and $\delta_{ij} = 0$ for $i \neq j$). The basis vectors $\mathbf{v}_i$ are local and vary in phase space, and they are ordered such that the corresponding modes g_i are associated with time scales which are ordered from the slowest to fastest. The local time scales are given by the inverse of the absolute value of the real part of eigenvalues of the Jacobian $\mathbf{J} = \frac{\partial \mathbf{f}}{\partial \mathbf{y}}$. Hence, the slowest time scales are associated with the eigenvalues which have the least negative real part, while the fastest time scales are associated with the eigenvalues which have the most negative real parts. For linear dynamical systems the basis vectors are simply the constant eigenvectors of the Jacobian. However, for nonlinear dynamical systems the basis vectors are obtained by a two step iteration procedure [22] and they are closely related to the local eigenvectors of the Jacobian. The less stiff reduced model equations, which approximately describe the dynamics of the local slow active modes, are given by

$$\frac{d\mathbf{y}}{dt} \approx \sum_{i=(k_d+1)}^{(n-k_e)} g_i(\mathbf{y})\mathbf{v}_i(\mathbf{y}), \tag{1.16}$$

with the algebraic equations

$$g_i(\mathbf{y}) \approx 0, \qquad (i = 1, \ldots, k_d), \tag{1.17}$$

approximately describing the k_d dormant modes, and the algebraic equations

$$g_i(\mathbf{y}) \approx 0, \qquad (i = n - k_e + 1, \ldots, n), \tag{1.18}$$

approximately describing the k_e exhausted modes. Hence, there are $(n - k_d - k_e)$ active modes. The number of dormant, active and exhausted modes change with time along the phase space trajectory. Computing the appropriate basis vectors along the phase space trajectory is the computationally most expensive part of the CSP method.

The dynamics of a three-dimensional ($n = 3$) dynamical system in Equation (1.4), modeling the SHPR, is depicted in Figure 1.1. The phase space trajectories, in the three-dimensional phase space, start from an initial condition and quickly relax to a two-dimensional subspace or manifold as the time progresses. Then the phase space trajectories move slowly along the two-dimensional manifold and relax to a one-dimensional subspace or manifold. Finally the phase space trajectories move much more slowly along the one-dimensional manifold and relax to a zero-dimensional subspace or the equilibrium point. This behavior is typical for gas phase combustion of several species in which reactive processes occur at varying time scales. Relaxation of the phase space trajectories from a higher dimensional manifold to a lower dimensional manifold occurs exponentially, and is equivalent to the equilibration of some fast chemical processes. On the other hand the slower chemical processes evolve along the low-dimensional manifolds.

The ILDM method identifies *ab initio* a low-dimensional subspace, known as the ILDM, within phase space $\mathbb{R}^n$, which closely approximates the low-dimensional manifold depicted in Figure 1.1. For an n-dimensional dynamical system in Equation (1.4), an m-dimensional ($m < n$) ILDM, in the n-dimensional phase space, is identified by a local eigenvalue-eigenvector analysis, and is described by

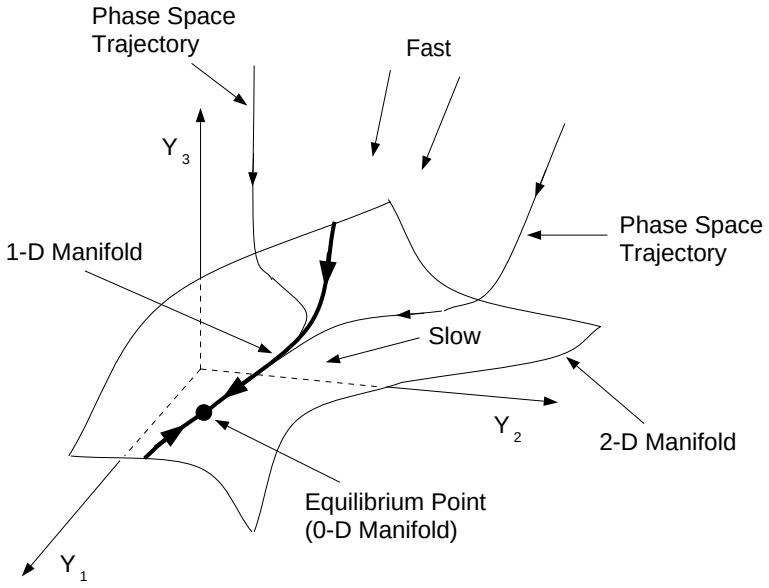

Figure 1.1. Phase space of a three-dimensional dynamical system modeling the SHPR, depicting the slow manifolds and the behavior of the phase space trajectories.

the following nonlinear algebraic equations

$$\tilde{\mathbf{V}}_f \mathbf{f}(\mathbf{y}) = \mathbf{0}, \qquad (n-m \text{ algebraic equations}), \tag{1.19}$$

where $\tilde{\mathbf{V}}_f$ is a matrix of dimensions $(n-m)\times n$, with row vectors which are the $n-m$ left eigenvectors, of the Jacobian $\mathbf{J} = \frac{\partial \mathbf{f}}{\partial \mathbf{y}}$, associated with the $n-m$ eigenvalues with the most negative real part. If the chemical processes associated with $n-m$ fast time scales are equilibrated, then the chemical processes associated with m slow time scales occur close to the m-dimensional ILDM in phase space. On the m-dimensional ILDM, m ODEs with reduced stiffness are required to be integrated coupled with $n-m$ non-linear algebraic equations describing the ILDM. The slow dynamics of the reactive system is described by the following reduced model equations, which are a system of DAEs

$$\tilde{\mathbf{V}}_s \frac{d\mathbf{y}}{dt} = \tilde{\mathbf{V}}_s \mathbf{f}(\mathbf{y}), \qquad (m \text{ ODEs}), \tag{1.20a}$$

$$\mathbf{0} = \tilde{\mathbf{V}}_f \mathbf{f}(\mathbf{y}), \qquad (n-m \text{ algebraic equations}), \tag{1.20b}$$

where $\tilde{\mathbf{V}}_s$ is a matrix of dimensions $m \times n$, with row vectors which are the m left eigenvectors, of the Jacobian $\mathbf{J}$, associated with the m eigenvalues with the least negative real part. The reduced model equations obtained by the ILDM method can be used after the phase space trajectories, which start from the initial condition, have relaxed onto the ILDM. This is acceptable under the assumption that fast time scale processes can be neglected. A proper projection is required from the initial condition to the ILDM such that there is at most a small temporal phase error between the solution obtained using the ILDM method and the solution of the full system of ODEs. The m-dimensional ILDM can be computed *a priori* in phase space by solving Equation (1.19) coupled with m parametric equations, and can then be stored in a table. This table can then be used while integrating Equation (1.20a) to obtain the slow dynamics of the system. Hence, the ILDM method has a significant computational advantage over the CSP method, as the expensive computation of local eigenvalues and eigenvectors is not required during the actual computations with the reduced model equations. Another advantage of the ILDM method is that the same table can be reused for several different computations. The reduced model equations obtained by both, the ILDM method and the QSSA method, are DAEs (1.20) and (1.13), respectively. However, the QSSA method, coupled with partial equilibrium assumptions, attempts to equilibrate fast time scale processes by an *ad hoc* method, while the ILDM method systematically does the same and resolves only the slow time scale processes without requiring an extensive knowledge of chemistry. Unlike some of the approaches discussed earlier, the reduced model equations obtained by the ILDM method are valid for a large domain of phase space which is also known *a priori* from the computation of the ILDM. A number of studies have appeared in recent years advancing the ILDM method and some variants, such as Blasenbrey, *et al.* [23], Eggels, *et al.* [24], Schmidt, *et al.* [25], Yang and Pope

[26], Rhodes, *et al.* [27], Lowe and Tomlin [28], Gicquel, *et al.* [29], and Correa, *et al.* [30].

The ILDM is only an approximation of the manifolds depicted in Figure 1.1 which are referred to as the Slow Invariant Manifolds (SIM). Slow indicates that the SIM is associated with slow time scale processes, and invariant indicates that if the initial condition lies on the SIM, the phase space trajectory lies completely within the SIM for all future times. Relative to the more fundamental SIM, the ILDM contains an intrinsic error which decreases as the spectral gap between the slow and fast time scales increases. Consequently, it will be shown in this work that the contention of Rhodes, *et al.* [27] that the Maas and Pope algorithm identifies a SIM is in error. The SIM can be obtained analytically by perturbation analysis [31] for simple systems, for which Equation (1.4) can be transformed to the following

$$\frac{d\mathbf{y}_s}{dt} = \mathbf{f}_s(\mathbf{y}_s, \mathbf{y}_f, \epsilon), \qquad (m \text{ ODEs}), \tag{1.21a}$$

$$\epsilon\frac{d\mathbf{y}_f}{dt} = \mathbf{f}_f(\mathbf{y}_s, \mathbf{y}_f, \epsilon), \qquad (n-m \text{ ODEs}), \tag{1.21b}$$

where $0 < \epsilon << 1$ is a small parameter, and $\mathbf{y}_s$, a vector of length m, represents the slow variables, and $\mathbf{y}_f$, a vector of length $n-m$, represents the fast variables. Each of the slow and fast variables can be a combination of the dependent variables, in vector $\mathbf{y}$, of the original system of Equations (1.4). Using Fenichel's theorem [32], an asymptotic expansion of the SIM, for the system in Equation (1.21), can be written as following

$$\mathbf{y}_f = \mathbf{h}_\epsilon(\mathbf{y}_s) = \mathbf{h}_0(\mathbf{y}_s) + \epsilon\mathbf{h}^{(1)}(\mathbf{y}_s) + \epsilon^2\mathbf{h}^{(2)}(\mathbf{y}_s) + \ldots, \tag{1.22}$$

where $\mathbf{f}_f(\mathbf{y}_s, \mathbf{h}_0(\mathbf{y}_s), 0) = 0$, and the coefficients $\mathbf{h}^{(i)}(\mathbf{y}_s)$, $(i = 1, 2, \ldots)$, can be found recursively using Fenichel's theorem. It has been shown by Kaper and Kaper [31], for systems similar to the one in Equation (1.21), that the ILDM approximation of the SIM is $\mathcal{O}(\epsilon)$ accurate. Equation (1.22) can be substituted in Equation (1.21a)

to obtain the following less stiff reduced model equations which describe the slow dynamics of the dynamical system

$$\frac{d\mathbf{y}_s}{dt} = \mathbf{f}_s(\mathbf{y}_s, \mathbf{h}_\epsilon(\mathbf{y}_s), \epsilon), \qquad (m \text{ ODEs}). \tag{1.23}$$

Another method of inertial manifolds [33] is also used to to find an algebraic approximation, $\mathbf{y}_f = \mathbf{h}'(\mathbf{y}_s)$, for the SIM. However, this method has also been only applied for simpler systems as in Equation (1.21). It is difficult to apply the methods of asymptotic expansion and inertial manifolds to combustion systems as it is difficult to find a constant small parameter ϵ from the large number of reaction rate parameters associated with a reaction mechanism. Also, the membership of the slow and fast sets of variables changes in phase space and in different ranges of thermodynamic states.

The SIM can be approximated by another method of algebraic functional iteration [34, 35], for systems which are not amenable to a transformation to the form in Equation (1.21). Kaper and Kaper [31] have shown for simple systems that the order of accuracy of the SIM obtained by this method improves, by one order, with each iteration. For more complex combustion systems, it is more suitable to compute the SIM using a slightly variant method of numerical functional iteration [36]. However, provided that a spectral gap condition is satisfied, the ILDM does a good job of approximating the SIM, and in our experience, computation of high dimensional ILDMs appears to be more tractable than that of high dimensional SIMs.

Most of the methods discussed until now achieve computational efficiency for the SHPR modeled by a system of ODEs in Equation (1.4). However, in more realistic scenarios it is important to achieve similar computational efficiency for simulating spatially inhomogeneous reactive systems or reactive flow systems which are modeled by PDEs in Equation (1.1). Hadjinicolaou and Goussis [37] have extended the CSP

method to reaction diffusion equations. Yannacopolous, *et al.* [33] illustrate, using inertial manifolds, infinite-dimensionality of slow manifolds associated with PDEs when compared to finite-dimensionality of slow manifolds associated with ODEs. The algebraic approximation of these infinite-dimensional inertial manifolds is only suitable for simpler systems where a fixed segregation of slow and fast variables can be easily found. However, it is important to note that the slow manifolds associated with the PDEs have infinite-dimensionality.

Maas and Pope have proposed an extension of the ILDM method for reactive flow systems described by PDEs [38]. They assume that if flow processes occur at time scales of the order of the m slow chemical time scales associated with the m-dimensional reaction ILDM, then the flow processes only perturb the system slightly off the ILDM, while the fast chemical processes rapidly relax the system back onto the ILDM. Therefore, in the Maas and Pope Projection (MPP), convection-diffusion terms in reactive flow PDEs are projected onto the finite-dimensional tangent subspace of the ILDM, signifying that the reactive system never leaves the ILDM in phase space. The reduced PDEs can then be integrated, coupled with the m-dimensional ILDM Equation (1.19) or its tabular form, to obtain the slow dynamics of the reactive flow system. These reduced partial differential algebraic equations are also less stiff than the original reactive flow PDEs (1.1). The dimension of the ILDM to be used is determined by prescribing a cutoff for the chemical time scales, based on the fastest flow time scales. If the flow time scales are faster than any of the chemical time scales associated with an ILDM of a certain dimension, then a higher dimensional ILDM is required, which is essential to maintain full coupling of the flow and chemical processes. Hence, a different dimensional ILDM is often required at different locations in physical space as the flow time scales vary in physical space and the chemical time scales vary in both physical and phase spaces.

This amounts to solving a different number of reduced PDEs at different locations in physical space. It is also difficult to determine *a priori* the magnitude of the flow time scales which control the dimension of the ILDM to be used.

One way to overcome these problems is to use Strang operator splitting [39] between the reaction source terms and the convection-diffusion terms when solving the reactive flow model PDEs [40]. In the first step, each point in physical space is treated as a spatially homogeneous premixed reactor with convection-diffusion suppressed, and the resulting ODEs for the reaction part are solved using the standard ILDM method. This allows use of the ILDMs of different dimensions at different locations in physical space. If the chemical composition at a certain location in the physical space does not lie near the ILDM, implicit integration of the full equations is used in the reaction step, until the chemical composition relaxes to the ILDM. In the second step, the reaction part of the reactive flow equations is suppressed, and the resulting PDEs for the convection-diffusion part are solved using standard discretization techniques for inert flows. The second step perturbs the reactive system off the ILDM; it is then projected back onto the ILDM along the direction, in phase space $\mathbb{R}^n$, of the fast local eigenvectors of the Jacobian of the reaction source term in the reactive flow PDEs. Even though the ILDM method reduces the number of ODEs to be solved in the first step, the number of PDEs to be solved in the second step is same as the number of original model equations. Another disadvantage of this method is that errors are incurred due to operator splitting. Strang splitting has second order accuracy in time provided both steps have second order accuracy in time. If the chemical time scales are highly disparate from the flow times scales, the operator splitting method will induce errors in wave speeds. These errors can be minimized by resolving the spatial and temporal scales in the thin reaction zones using adaptive mesh refinement methods [41].

In this work we propose a more systematic approach to preserve the coupling between chemistry and flow physics. The full model equations are projected onto the fast and slow basis vectors of the Jacobian of the reactive source term in the reactive flow PDE. A set of elliptic PDEs is obtained by equilibrating the fast dynamics. The elliptic PDEs approximately describe the infinite-dimensional Approximate Slow Invariant Manifold (ASIM) analogous to the algebraic equations which describe the ILDM. The reactive flow system relaxes to the ASIM before reaching steady state. Unlike the ILDM, the ASIM accounts for the effects of convection and diffusion in the reactive flow system. When using the ASIM, a set of elliptic PDEs, coupled with time-dependent less stiff reduced PDEs describing the slow dynamics, are solved in physical space.

1.3 Organization of dissertation

This dissertation is organized as follows. In Chapter 2 the model equations for a closed adiabatic spatially homogeneous premixed reactor (CASHPR) are described. These model equations include ODEs which describe the evolution of species mass fractions in time, due to reactive processes within the CASHPR, based on Arrhenius kinetics and law of mass action. It is demonstrated that the atoms or elements, which compose various chemical species, remain conserved within the CASHPR. The energy conservation equations are derived for the isochoric CASHPR and the isobaric CASHPR and are presented as an ODE for temperature evolution and also as a nonlinear algebraic equation. The ideal gas equation of state is used with the model equations to close the system. Next, a detailed description of the ILDM method is given along with a derivation of the resulting reduced model equations obtained for the dynamical system modeling the CASHPR. A geometrical description of the nonlinear algebraic equations describing an m-dimensional ILDM

in an n-dimensional phase space is given. Next, the ILDM is compared with the SIM, and it is shown for a general case that there exists a small intrinsic error in the ILDM approximation which increases as the spectral gap between the slow and fast time scales decreases and as the curvature of the manifold increases. Finally, a detailed description of an efficient algorithm for *a priori* computation of the ILDM in phase space is given. The m parametric equations, which are required while computing the m-dimensional ILDM using the $n - m$ algebraic equations (1.19), are also derived. Several examples of *a priori* computation of the ILDM for various reaction mechanisms are given.

In Chapter 3 a standard ignition delay problem for a mixture of hydrogen-oxygen-argon in a shock tube is solved using the ILDM method coupled with a wavelet adaptive multilevel representation (WAMR) spatial discretization technique. The governing equations, initial and boundary conditions are described for this reactive flow problem. An operator splitting technique, which is used to split the reaction part from the convection diffusion part, is described, such that the governing equations can be solved in two steps. In the reaction step a system of ODEs at each spatial point is integrated, which is computationally the most expensive part of the numerical simulation. It is shown how the ILDM method, which is developed for a CASHPR in Chapter 2, can be naturally used to reduce the computational expense of solving the ODEs in the reaction step. A brief review of the WAMR technique is given, which is used to solve the PDEs in the convection diffusion step of the numerical simulation. The table generated for the ILDM for the H_2-O_2-Ar reaction mechanism is described. Next, the projection onto the ILDM is described, which is required after the convection diffusion step results in a perturbation of the reactive system off the ILDM. Finally, detailed results are given for the shock tube test problem, and conclusions are presented.

In Chapter 4 the construction of slow manifolds for reactive flow systems is addressed. A theoretical development of the Approximate Slow Invariant Manifold (ASIM), associated with a spatially inhomogeneous reactive system, as an improved extension for the standard ILDM method, is given. The improvement is realized through formulation of an elliptic system of partial differential equations which describe the ASIM for the reactive flow system in which reactive processes couple with convection and diffusion processes at similar time scales. This is demonstrated on a simple reaction diffusion system, where it is shown that the error incurred when using the ASIM is less than the error incurred when using the Mass-Pope projection (MPP) of the diffusion effects onto the ILDM. This comparison is also done for ozone decomposition in a premixed laminar flame where an error analysis shows a similar trend. The governing equations along with the initial and boundary conditions are described for the ozone decomposition premixed laminar flame problem. Finally, detailed results and conclusions are given for the comparisons of the use of the ASIM and the MPP method for the laminar flame problem.

In Chapter 5 the final conclusions and suggestions for future work are given.

CHAPTER 2

INTRINSIC LOW DIMENSIONAL MANIFOLDS FOR A CLOSED ADIABATIC SPATIALLY HOMOGENEOUS PREMIXED REACTOR

2.1 Closed adiabatic spatially homogeneous premixed reactor

A closed adiabatic spatially homogeneous premixed reactor (CASHPR) is a closed system consisting of a homogeneous mixture of reacting chemical species. It is treated as a closed adiabatic system as there is no mass and heat transfer to or from the reactor. The total mass of the reacting mixture remains constant and is given by

$$\mathsf{m}_\circ = \sum_{i=1}^{N} \mathsf{m}_i, \tag{2.1}$$

where $\mathsf{m}_\circ$ is the total mass, m_i is the mass of species i, and N is the total number of species. The rate of evolution of chemical species is given by

$$\frac{d\mathcal{N}_i}{dt} = V\dot{\omega}_i, \qquad (i = 1, \ldots, N), \tag{2.2}$$

where $\mathcal{N}_i$ is the number of moles of species i, $\dot{\omega}_i$ is the molar rate of evolution per unit volume of species i due to the reactive processes, V is the mixture volume, and t is time.

A typical reaction mechanism consists of several elementary reaction steps involving many chemical species. A compact notation for such a reaction mechanism is given by

$$\sum_{i=1}^{N} \nu'_{ij} S_i \Rightarrow \sum_{i=1}^{N} \nu''_{ij} S_i, \qquad (j = 1, \ldots, J), \tag{2.3}$$

where S_i represents the symbol for species i, J is the number of elementary reaction steps and ν'_{ij} and ν''_{ij} are the stoichiometric coefficients of species i, on the reactants and products side of elementary reaction j, respectively. Each of the reversible reactions in the reaction mechanism are treated as two irreversible reactions; first having the forward reaction rate and second having the backward reaction rate of the corresponding reversible reaction. The molar rate of evolution per unit volume of species i in the multi-step reaction mechanism is given by

$$\dot{\omega}_i = \sum_{j=1}^{J} \left(\nu''_{ij} - \nu'_{ij}\right) r_j, \qquad (i = 1, \ldots, N), \tag{2.4}$$

where r_j is the rate of elementary reaction j given by law of mass action

$$r_j = k_j \prod_{i=1}^{N} [X_i]^{\nu'_{ij}}, \qquad (j = 1, \ldots, J), \tag{2.5}$$

where $[X_i] = \frac{\mathcal{N}_i}{V}$ is the molar concentration of species i, and k_j is the temperature dependent rate constant for reaction j given by Arrhenius kinetics

$$k_j = \alpha_j T^{\beta_j} \exp\left(\frac{-E_j}{\Re T}\right), \qquad (j = 1, \ldots, J), \tag{2.6}$$

where the constant parameters α_j, β_j, E_j and $\Re$ represent the kinetic rate constant of reaction j, the temperature dependence exponent of reaction j, the activation energy of reaction j, and the universal gas constant ($\Re = 8.31441 \times 10^7$ erg mol^{-1} K^{-1}), respectively, and T is the mixture temperature.

The species evolution Equation (2.2) can be rewritten in terms of species mass fractions as

$$\frac{dY_i}{dt} = \frac{\dot{\omega}_i M_i}{\rho}, \qquad (i = 1, \ldots, N), \tag{2.7}$$

where $Y_i = \frac{\mathcal{N}_i M_i}{\mathsf{m}_\circ} = \frac{[X_i] M_i}{\rho} = \frac{\mathsf{m}_i}{\mathsf{m}_\circ}$ is the mass fraction of species i, M_i is the molecular mass of species i, and $\rho = \frac{\mathsf{m}_\circ}{V}$ is the mixture density.

The thermal equation of state used for the mixture of chemical species in gas phase is that of an ideal gas and is given by

$$p = \rho \left(\sum_{i=1}^{N} \frac{Y_i}{M_i} \right) \Re T, \tag{2.8}$$

where p is the mixture pressure.

Each molecule of chemical species is composed of certain number of atomic elements connected by chemical bonds. If the number of atoms of element l in the molecule of species i is represented by φ_{il}, then the total number of moles of element l in the mixture is given by

$$\hat{\mathcal{N}}_l = \sum_{i=1}^{N} \varphi_{il} \mathcal{N}_i, \qquad (l = 1, \ldots, L), \tag{2.9}$$

where $\hat{\mathcal{N}}_l$ is the number of moles of element l, and L is the total number of elements. Similarly the mass fraction of each element in the mixture is given by

$$\hat{Y}_l = \hat{M}_l \sum_{i=1}^{N} \varphi_{il} \frac{Y_i}{M_i}, \qquad (l = 1, \ldots, L), \tag{2.10}$$

where $\hat{Y}_l = \frac{\hat{\mathsf{m}}_l}{\mathsf{m}_\circ}$ is the mass fraction, $\hat{\mathsf{m}}_l$ is the mass and $\hat{M}_l$ is the atomic mass of element l. The sums of both species mass fractions and element mass fractions are unity ($\sum_{i=1}^{N} Y_i = 1$; $\sum_{l=1}^{L} \hat{Y}_l = 1$), and the molecular mass of species i is also given by $M_i = \sum_{l=1}^{L} \varphi_{il} \hat{M}_l$. Using Equation (2.7) with Equations (2.4) and (2.10), and enforcing the stoichiometric balances for reaction j, $\sum_{i=1}^{N} \nu'_{ij} \varphi_{il} = \sum_{i=1}^{N} \nu''_{ij} \varphi_{il}$ for $(l = 1, \ldots, L)$, it can be shown that for the CASHPR (see Appendix C)

$$\frac{d\hat{Y}_l}{dt} = 0, \qquad (l = 1, \ldots, L). \tag{2.11}$$

Hence, the element mass fractions in the CASHPR remain constant constant for all times and only $N - L$ species evolution Equations (2.7) are required to be integrated in conjunction with the following linear algebraic equations, representing

the conservation of atoms in absence of nuclear reactions,

$$\sum_{i=1}^{N} \varphi_{il} \frac{Y_i}{M_i} = \sum_{i=1}^{N} \varphi_{il} \frac{Y_{i_0}}{M_i} = \frac{\hat{Y}_{l_0}}{\hat{M}_l}, \qquad (l = 1, \ldots, L), \tag{2.12}$$

where Y_{i_0} is the mass fraction of species i and $\hat{Y}_{l_0}$ is the mass fraction of element l at time $t = 0$.

2.1.1 Energy conservation equation for the isochoric CASHPR

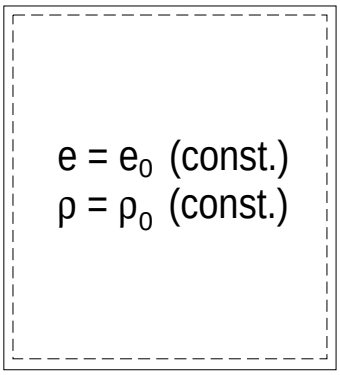

Figure 2.1. Isochoric CASHPR

Figure 2.1 depicts the isochoric CASHPR which has a fixed mass of reacting chemical species and has no heat exchange with the surroundings. For an adiabatic system which has no work interaction with the surroundings, the differential form of the first law of thermodynamics, neglecting changes in kinetic and potential energy, is given by

$$\frac{de}{dt} = \underbrace{\frac{dq}{dt}}_{=0} - \underbrace{\frac{dw}{dt}}_{=0} = 0, \tag{2.13}$$

where e is the internal energy per unit mass of the reactive mixture, q is the heat transfer per unit mass, and w is the work per unit mass. The mass averaged mixture internal energy per unit mass, e, is given by

$$e = \sum_{i=1}^{N} e_i Y_i, \tag{2.14}$$

where e_i is the internal energy per unit mass of species i. Differentiating Equation (2.14) and using Equation (2.13) gives

$$\frac{de}{dt} = \sum_{i=1}^{N} Y_i \frac{de_i}{dt} + \sum_{i=1}^{N} e_i \frac{dY_i}{dt} = 0. \tag{2.15}$$

It is assumed that all chemical species are thermally perfect, so that their internal energy and specific heat at constant volume are functions of at most temperature only. Hence,

$$e_i = e_i(T), \quad c_{vi} = c_{vi}(T), \tag{2.16}$$

where c_{vi} is the specific heat at constant volume for species i. In general c_{vi} is given by

$$c_{vi} = \left.\frac{\partial e_i}{\partial T}\right|_v; \tag{2.17}$$

however, for the thermally perfect species i, c_{vi} is given by

$$c_{vi} = \frac{de_i}{dT}, \qquad \text{hence,} \qquad \frac{de_i}{dt} = c_{vi}\frac{dT}{dt}. \tag{2.18}$$

Substituting the expression for $\frac{de_i}{dt}$ from Equation (2.18) into Equation (2.15) gives

$$\frac{de}{dt} = \sum_{i=1}^{N} c_{vi} Y_i \frac{dT}{dt} + \sum_{i=1}^{N} e_i \frac{dY_i}{dt} = 0. \tag{2.19}$$

The mass averaged specific heat at constant volume, c_v, for the mixture is given by

$$c_v = \sum_{i=1}^{N} c_{vi} Y_i. \tag{2.20}$$

Hence, Equation (2.19) can be rewritten as

$$\frac{de}{dt} = c_v \frac{dT}{dt} + \sum_{i=1}^{N} e_i \frac{dY_i}{dt} = 0. \tag{2.21}$$

By substituting the expression for the evolution of species mass fraction, $\frac{dY_i}{dt}$, from Equation (2.7) into Equation (2.21), the energy conservation equation for the isochoric CASHPR can be written as

$$\frac{dT}{dt} = -\frac{1}{\rho c_v} \sum_{i=1}^{N} e_i \dot{\omega}_i M_i. \tag{2.22}$$

2.1.2 Energy conservation equation for the isobaric CASHPR

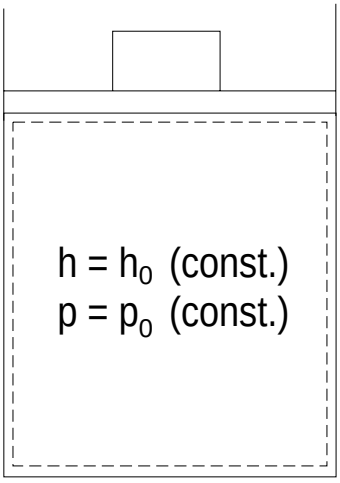

Figure 2.2. Isobaric CASHPR

Figure 2.2 depicts the isobaric CASHPR which has a fixed mass of reacting chemical species and has no heat exchange with the surroundings. It is assumed that there is only volumetric work due to the piston and that there is no friction between the piston and the cylinder walls. For an adiabatic system with only volumetric work done by the system, the differential form of the first law of thermodynamics, neglecting changes in kinetic and potential energy, is given by

$$\frac{de}{dt} = \underbrace{\frac{dq}{dt}}_{=0} - \underbrace{\frac{dw}{dt}}_{=p\frac{dv}{dt}}, \qquad \text{hence,} \qquad \frac{de}{dt} + p\frac{dv}{dt} = 0, \tag{2.23}$$

where $v = \frac{1}{\rho} = \frac{V}{\mathsf{m}_\circ}$ is the specific volume of the mixture of chemical species. The mixture enthalpy per unit mass, h, is given by

$$h = e + pv. \tag{2.24}$$

Differentiating Equation (2.24) and using Equation (2.23), the following is obtained for an isobaric closed adiabatic system

$$\frac{dh}{dt} = \underbrace{\frac{de}{dt} + p\frac{dv}{dt}}_{=0} + \underbrace{v\frac{dp}{dt}}_{=0} = 0. \tag{2.25}$$

The mass averaged mixture enthalpy per unit mass is given by

$$h = \sum_{i=1}^{N} h_i Y_i, \tag{2.26}$$

where h_i is the enthalpy per unit mass of species i. Differentiating Equation (2.26) and using Equation (2.25) gives

$$\frac{dh}{dt} = \sum_{i=1}^{N} Y_i \frac{dh_i}{dt} + \sum_{i=1}^{N} h_i \frac{dY_i}{dt} = 0. \tag{2.27}$$

Again it is assumed that all chemical species are thermally perfect, so that their enthalpy and specific heat at constant pressure are functions of at most temperature only. Hence,

$$h_i = h_i(T), \quad c_{pi} = c_{pi}(T), \tag{2.28}$$

where c_{pi} is the specific heat at constant pressure of species i. In general c_{pi} is given by

$$c_{pi} = \left.\frac{\partial h_i}{\partial T}\right|_p; \tag{2.29}$$

however, for the thermally perfect species i, c_{pi} is given by

$$c_{pi} = \frac{dh_i}{dT}, \qquad \text{hence,} \qquad \frac{dh_i}{dt} = c_{pi}\frac{dT}{dt}. \tag{2.30}$$

Substituting the expression for $\frac{dh_i}{dt}$ from Equation (2.30) into Equation (2.27) gives

$$\frac{dh}{dt} = \sum_{i=1}^{N} c_{pi} Y_i \frac{dT}{dt} + \sum_{i=1}^{N} h_i \frac{dY_i}{dt} = 0. \tag{2.31}$$

The mass averaged specific heat at constant pressure, c_p, for the mixture is given by

$$c_p = \sum_{i=1}^{N} c_{pi} Y_i. \tag{2.32}$$

Hence, Equation (2.31) can be rewritten as

$$\frac{dh}{dt} = c_p \frac{dT}{dt} + \sum_{i=1}^{N} h_i \frac{dY_i}{dt} = 0. \tag{2.33}$$

By substituting the expression for the evolution of species mass fraction, $\frac{dY_i}{dt}$, from Equation (2.7) into Equation (2.33), the energy conservation equation for the isobaric CASHPR can be written as

$$\frac{dT}{dt} = -\frac{1}{\rho c_p} \sum_{i=1}^{N} h_i \dot{\omega}_i M_i. \tag{2.34}$$

In energy conservation Equations (2.22) and (2.34) the species internal energy per unit mass, e_i, and the species enthalpy per unit mass, h_i, are evaluated using the following relations valid for an ideal gas

$$h_i = h_{fi}^{\circ} + \int_{T_s}^{T} c_{pi}(T) dT, \tag{2.35}$$

$$e_i = h_i - \frac{\Re}{M_i} T, \tag{2.36}$$

where h_{fi}° is the enthalpy of formation of species i at the standard temperature of $T_s = 298\ K$. The CHEMKIN [42] package has a thermodynamic database for various chemical species, which is used to evaluate $c_{pi}(T)$ from polynomial fits of empirical data and also to obtain h_{fi}°. Finally, c_{vi} can be evaluated using the following relation

$$c_{vi} = c_{pi} - \frac{\Re}{M_i}. \tag{2.37}$$

2.1.3 Summary

The isochoric CASHPR can be modeled by the following set of equations which include the species evolution equations

$$\frac{dY_i}{dt} = \frac{\dot{\omega}_i M_i}{\rho_0}, \qquad (i = 1, \ldots, N - L), \tag{2.38}$$

the conservation equations for atoms

$$\sum_{i=1}^{N} \varphi_{il} \frac{Y_i}{M_i} = \frac{\hat{Y}_{l_0}}{\hat{M}_l}, \qquad (l = 1, \ldots, L), \tag{2.39}$$

the equation of state

$$p = \rho_0 \left(\sum_{i=1}^{N} \frac{Y_i}{M_i} \right) \Re T, \tag{2.40}$$

and the energy conservation equation either as an ODE for temperature evolution

$$\frac{dT}{dt} = -\frac{1}{\rho_0 c_v} \sum_{i=1}^{N} e_i \dot{\omega}_i M_i, \tag{2.41}$$

or as a nonlinear algebraic conservation equation for mixture internal energy per unit mass

$$\sum_{i=1}^{N} e_i(T) Y_i = e_0. \tag{2.42}$$

If the algebraic form of the energy conservation equation is used, then the model equations for the isochoric CASHPR can be represented by the following set of autonomous, nonlinear, ordinary differential equations of the form

$$\frac{d\mathbf{Y}}{dt} = \mathbf{f}(\mathbf{Y}), \tag{2.43}$$

where $\mathbf{Y} = (Y_1, \ldots, Y_{N-L})^T$ and $\mathbf{f} = \mathbf{f}(Y_1, \ldots, Y_{N-L}; \rho_0, e_0, \hat{Y}_{1_0}, \ldots, \hat{Y}_{L_0})$. The element mass fractions, $\hat{Y}_{1_0}, \ldots, \hat{Y}_{L_0}$, the mixture density, ρ_0, and the mixture internal energy per unit mass, e_0, represent their respective values at time $t = 0$, which remain constant. Similar equations are required to be solved in the reaction step when operator splitting is used to solve the model equations for viscous detonation in a reactive mixture of $H_2/O_2/Ar$.

The isobaric CASHPR can be modeled by the following set of equations which include the species evolution equations

$$\frac{dY_i}{dt} = \frac{\dot{\omega}_i M_i}{\rho}, \qquad (i = 1, \ldots, N - L). \tag{2.44}$$

the linear conservation equations for atoms

$$\sum_{i=1}^{N} \varphi_{il} \frac{Y_i}{M_i} = \frac{\hat{Y}_{l_0}}{\hat{M}_l}, \qquad (l = 1, \ldots, L). \tag{2.45}$$

the equation of state

$$p_0 = \rho \left(\sum_{i=1}^{N} \frac{Y_i}{M_i} \right) \Re T, \tag{2.46}$$

and the energy conservation equation either as an ODE for temperature evolution

$$\frac{dT}{dt} = -\frac{1}{\rho c_p} \sum_{i=1}^{N} h_i \dot{\omega}_i M_i, \tag{2.47}$$

or as a nonlinear algebraic conservation equation for mixture enthalpy per unit mass

$$\sum_{i=1}^{N} h_i(T) Y_i = h_0. \tag{2.48}$$

If the nonlinear algebraic form of the energy conservation equation is used, then the model equations for the isobaric CASHPR can be represented by the following set of autonomous, nonlinear, ordinary differential equations of the form

$$\frac{d\mathbf{Y}}{dt} = \mathbf{f}(\mathbf{Y}), \tag{2.49}$$

where $\mathbf{Y} = (Y_1, \ldots, Y_{N-L})^T$ and $\mathbf{f} = \mathbf{f}(Y_1, \ldots, Y_{N-L}; p_0, h_0, \hat{Y}_{1_0}, \ldots, \hat{Y}_{L_0})$. The element mass fractions, $\hat{Y}_{1_0}, \ldots, \hat{Y}_{L_0}$, the mixture pressure, p_0, and the mixture enthalpy per unit mass, h_0, represent their respective values at time $t = 0$, which remain constant. Similar equations are required to be solved in the reaction step when operator splitting is used to solve the model equations for constant pressure adiabatic laminar premixed flames.

2.2 Intrinsic low-dimensional manifolds

The method of Intrinsic Low-Dimensional Manifolds (ILDM) by Maas and Pope [1] is applied to the CASHPR which is modeled by a set of ordinary differential equations of the form

$$\frac{d\mathbf{y}}{dt} = \mathbf{f}(\mathbf{y}), \qquad \mathbf{y}(t=0) = \mathbf{y}_0, \tag{2.50}$$

where $\mathbf{y} \in \mathbb{R}^n$ represents a set of dependent variables or a vector of species mass fractions for the CASHPR, $\mathbf{f}(\mathbf{y})$ is the forcing function or the reaction source term for the CASHPR, and t is the independent time variable. Equation (2.50) is identical to Equations (2.43) or (2.49) modeling the CASHPR with $n = N - L$. Without loss of generality, the origin is translated to the chemical equilibrium point for the system in Equation (2.50), such that $\mathbf{f}(\mathbf{0}) = \mathbf{0}$. The nonlinear reaction source term typically induces severe stiffness in Equation (2.50) and makes it computationally expensive to solve. The stiffness is due to the widely disparate time scales over which different chemical reactions occur. The eigenvalues of the Jacobian $\frac{\partial \mathbf{f}}{\partial \mathbf{y}} = \mathbf{J}$ identify the local time scales associated with the reactive system. The eigenvectors of $\mathbf{J}$ identify the local directions associated with the corresponding time scales in the n-dimensional phase space. It is ensured that there are no zero eigenvalues by eliminating all the conserved quantities from Equation (2.50). These conserved quantities can arise, for example, due to the conservation of atoms in the CASHPR, and can be described by linear algebraic equations. The eigenvalues and eigenvectors can be obtained by

the following decomposition of $\mathbf{J}$, with $\tilde{\mathbf{V}} = \mathbf{V}^{-1}$:

$$\mathbf{J} = \mathbf{V}\mathbf{\Lambda}\tilde{\mathbf{V}}, \tag{2.51a}$$

$$\mathbf{V} = \left(\begin{array}{ccc:ccc} | & & | & | & & | \\ \mathbf{v}_1 & \cdots & \mathbf{v}_m & \mathbf{v}_{m+1} & \cdots & \mathbf{v}_n \\ | & & | & | & & | \end{array}\right) = \left(\begin{array}{c:c} \mathbf{V}_s & \mathbf{V}_f \end{array}\right), \tag{2.51b}$$

$$\mathbf{\Lambda} = \left(\begin{array}{ccc:ccc} \lambda_{(1)} & & 0 & & & \\ & \ddots & & & 0 & \\ 0 & & \lambda_{(m)} & & & \\ \hdashline & & & \lambda_{(m+1)} & & 0 \\ & 0 & & & \ddots & \\ & & & 0 & & \lambda_{(n)} \end{array}\right) = \left(\begin{array}{c:c} \mathbf{\Lambda}_{(s)} & 0 \\ \hdashline 0 & \mathbf{\Lambda}_{(f)} \end{array}\right), \tag{2.51c}$$

$$\tilde{\mathbf{V}} = \left(\begin{array}{ccc} - & \tilde{\mathbf{v}}_1 & - \\ & \vdots & \\ - & \tilde{\mathbf{v}}_m & - \\ \hdashline - & \tilde{\mathbf{v}}_{m+1} & - \\ & \vdots & \\ - & \tilde{\mathbf{v}}_n & - \end{array}\right) = \left(\begin{array}{c} \tilde{\mathbf{V}}_s \\ \hdashline \tilde{\mathbf{V}}_f \end{array}\right). \tag{2.51d}$$

Here $\mathbf{v}_1, \ldots, \mathbf{v}_n$ represent the right eigenvectors of $\mathbf{J}$ and form the column vectors of the $n \times n$ right eigenvector matrix $\mathbf{V}$. The diagonal matrix $\mathbf{\Lambda}$, also of dimension $n \times n$, contains the eigenvalues, $\lambda_{(1)}, \ldots, \lambda_{(n)}$, of $\mathbf{J}$ along its main diagonal, with their real parts ordered from least negative to most negative. Sufficiently close to the chemical equilibrium point, all the eigenvalues are real and negative. Thus, for the following discussion in this section, it will be assumed that all eigenvalues are real and negative. The reciprocal vectors to the right eigenvectors are represented by $\tilde{\mathbf{v}}_1, \ldots, \tilde{\mathbf{v}}_n$, which form the row vectors of the inverse right eigenvector matrix $\tilde{\mathbf{V}}$.

The local time scales in the phase space are given by the inverse of the magnitudes of the eigenvalues, $\frac{1}{|\lambda_{(1)}|}, \ldots, \frac{1}{|\lambda_{(n)}|}$, and are ordered from slowest to fastest.

Defining $\mathbf{g}$ as

$$\mathbf{g} = \mathbf{f} - \mathbf{J}\mathbf{y}, \tag{2.52}$$

Equation (2.50) can be rewritten as

$$\frac{d\mathbf{y}}{dt} = \mathbf{J}\mathbf{y} + \mathbf{g}. \tag{2.53}$$

A new set of variables defined by $\mathbf{z} = \tilde{\mathbf{V}}\mathbf{y}$, is used with Equation (2.53) to obtain

$$\frac{d\mathbf{z}}{dt} + \tilde{\mathbf{V}}\frac{d\mathbf{V}}{dt}\mathbf{z} = \mathbf{\Lambda}\mathbf{z} + \tilde{\mathbf{V}}\mathbf{g}. \tag{2.54}$$

Hence, the time evolution of processes associated with the i-th time scale is approximately given, in Einstein notation, by

$$\frac{1}{\lambda_{(i)}}\left(\frac{dz_i}{dt} + \tilde{\mathbf{v}}_i \sum_{j=1}^{n} \frac{d\mathbf{v}_j}{dt} z_j\right) = z_i + \frac{1}{\lambda_{(i)}}\left(\tilde{\mathbf{v}}_i \mathbf{g}\right), \quad (i = 1, \ldots, n). \tag{2.55}$$

Even though Equation (2.55) is not a decoupled set of ODEs, it represents a decoupled set of ODEs in a local linear sense if the nonlinear terms on both sides of the equation are neglected.

It is assumed that the dynamics of the processes which occur at time scales of $\mathcal{O}\left(\frac{1}{|\lambda_{(m+1)}|}\right)$ or faster are not important, and that there are m $(m < n)$ slow time scales and $n - m$ fast time scales. The transients of fast processes equilibrate before the transients of slow processes, and fast processes are associated with eigenvalues which are negative and large in magnitude. Equation (2.55) represents the dynamical system in Equation (2.50), in a form equivalent to that of a singularly perturbed system [43], with $\frac{1}{|\lambda_{(m+1)}|}, \ldots, \frac{1}{|\lambda_{(n)}|}$ as the small parameters multiplying the time derivatives on the left-hand side of the equations.

If the right eigenvectors $\mathbf{v}_i$ are normalized, then both $\mathbf{v}_i$ and the left eigenvectors $\tilde{\mathbf{v}}_i$ are $\mathcal{O}(1)$ as $\tilde{\mathbf{v}}_i \mathbf{v}_j = \delta_{ij}$, where δ_{ij} is the Kronecker delta. Hence, sufficiently close

to the equilibrium $\mathbf{y} = \mathbf{0}$, the left-hand side of Equation (2.55) is $\mathcal{O}\left(\frac{1}{|\lambda_{(m+1)}|}\right)$ for $(i = m+1, \ldots, n)$, while the right-hand side of Equation (2.55) is $\mathcal{O}(1)$. By neglecting all the terms of $\mathcal{O}\left(\frac{1}{|\lambda_{(m+1)}|}\right)$ from the left hand side of Equation (2.55), the fast processes are effectively equilibrated, and the slow dynamics of the system can be approximated by the following set of differential algebraic equations

$$\frac{1}{\lambda_{(i)}}\left(\frac{dz_i}{dt} + \tilde{\mathbf{v}}_i \sum_{j=1}^{n} \frac{d\mathbf{v}_j}{dt} z_j\right) = z_i + \frac{1}{\lambda_{(i)}}\left(\tilde{\mathbf{v}}_i \mathbf{g}\right), \qquad (i = 1, \ldots, m), \tag{2.56a}$$

$$0 = z_i + \frac{1}{\lambda_{(i)}}\left(\tilde{\mathbf{v}}_i \mathbf{g}\right), \qquad (i = m+1, \ldots, n). \tag{2.56b}$$

This is expected to be a good approximation if a significant spectral gap exists between $\left|\lambda_{(m)}\right|$ and $\left|\lambda_{(m+1)}\right|$. In writing Equation (2.56b), it is assumed that $\|\mathbf{g}\|$ can be $\mathcal{O}\left(|\lambda_{(m+1)}|\right)$ or greater, and hence, the second term is not neglected. A direct substitution of Equations (2.51), (2.52), and the definition of $\mathbf{z}$ is used to rewrite Equation (2.56) as

$$\tilde{\mathbf{V}}_s \frac{d\mathbf{y}}{dt} = \tilde{\mathbf{V}}_s \mathbf{f}, \qquad (m \text{ ODEs}) \tag{2.57a}$$

$$\mathbf{0} = \tilde{\mathbf{V}}_f \mathbf{f}, \qquad (n - m \text{ algebraic equations}) \tag{2.57b}$$

where the matrix $\tilde{\mathbf{V}}_s$ has dimensions $m \times n$, and its row vectors contain the left eigenvectors associated with the m slow time scales, while the matrix $\tilde{\mathbf{V}}_f$ has dimensions $(n-m) \times n$, and its row vectors contain the left eigenvectors associated with the $n - m$ fast time scales.

The algebraic equation for the ILDM, as obtained by Maas and Pope [1], and derived here alternatively, is given by

$$\tilde{\mathbf{V}}_f \mathbf{f} = \mathbf{0}. \tag{2.58}$$

The ILDM is an approximation of an m-dimensional subspace within an n-dimensional phase space along which processes associated with slow time scales

occur. The fast time scale processes, prior to equilibration, rapidly approach the ILDM. Once the fast time scale processes have equilibrated, the slow dynamics for Equation (2.50) can be approximated by Equation (2.57).

The differential algebraic equations (2.57) have reduced stiffness compared to the original equation (2.50), and the number of ODEs to be integrated has also been reduced to m from n. The reduction in stiffness allows for larger time steps when integrating Equations (2.57) than when integrating the original Equation (2.50) with explicit numerical methods, thereby reducing the computational time. Moreover, because matrix inversions are not necessary, the method is faster than implicit methods as well. To further reduce computational time, the algebraic Equation (2.57b) is solved *a priori* in a pre-determined domain of the n-dimensional phase space. The ILDM, obtained by the numerical solution of the Equation (2.57b), can then be stored in a table parameterized by m variables. The table can then be used during the integration of Equation (2.57a), instead of solving the differential algebraic system of Equations (2.57). Another advantage of storing the ILDM in tabular form is that the table can be reused for different sets of computations involving the same reaction kinetics. Details of this procedure and the computation of the ILDM in the phase space will be described later in this chapter.

Outside the subspace of the ILDM, Equation (2.57) does not apply. In general, initial conditions may not lie on the ILDM or satisfy Equation (2.57b), though the trajectory starting from an arbitrary initial condition in the phase space will rapidly approach the ILDM as the fast time scale processes equilibrate. The projection of the initial condition onto the ILDM has to be done carefully in order to avoid a large phase error in the time-dependent solution of the differential algebraic system of Equations (2.57). An accurate method, although computationally expensive,

is to use implicit integration of the full system of Equations (2.50), until the trajectory is close to the ILDM, and then integrate the differential algebraic system of Equations (2.57) [40]. A more efficient approach remains an outstanding problem.

Based on Equation (2.58), the ILDM can also be defined as a subspace of the phase space where the vector $\mathbf{f}$ lies completely within the local linear subspace spanned by the eigenvectors associated with the slow time scales. This is illustrated in Figure 2.3 for a two-dimensional system. For $n = 2$, $\mathbf{V}_s = \mathbf{v}_1$ and $\mathbf{V}_f = \mathbf{v}_2$ are the eigenvectors associated with slow and fast time scales, respectively. The corresponding reciprocal bases are given by the vectors $\tilde{\mathbf{V}}_s = \tilde{\mathbf{v}}_1$ and $\tilde{\mathbf{V}}_f = \tilde{\mathbf{v}}_2$. Figure 2.3 gives a graphical representation of Equation (2.58) describing the ILDM. The ILDM consists of the set of points in phase space where the vector $\mathbf{f}$ has the same orientation as the slow eigenvector $\mathbf{V}_s$. This does not ensure that the vector $\mathbf{f}$ is tangent to the ILDM. The tangent to the ILDM ($\tilde{\mathbf{V}}_f\mathbf{f} = \mathbf{0}$) is denoted by $\mathbf{T}_t$, while the normal to the ILDM is given by the gradient $\nabla(\tilde{\mathbf{V}}_f\mathbf{f})$ and is denoted by the same. By definition an invariant manifold is a subspace $\mathbb{S}' \subset \mathbb{R}^n$, if for any solution $\mathbf{y}(t)$, $\mathbf{y}(0) \in \mathbb{S}'$, of Equation (2.50), implies that for some $T' > 0$, $\mathbf{y}(t) \in \mathbb{S}'$ for all $t \in [0, T']$ [43]. The ILDM is an approximation for the exact slow invariant manifold (SIM). Like all invariant manifolds the SIM is also a trajectory in the phase space, and the vector $\mathbf{f}$ must be tangent to it.

It is easily shown that the ILDM is not a trajectory in the phase space; instead, it is only an approximation of the SIM. Using Equations (2.58) and (2.51), the normal vector space to the ILDM is given by

$$\begin{aligned} \nabla(\tilde{\mathbf{V}}_f\mathbf{f}) &= \tilde{\mathbf{V}}_f\nabla\mathbf{f} + (\nabla\tilde{\mathbf{V}}_f)\mathbf{f} \\ &= \tilde{\mathbf{V}}_f\mathbf{J} + (\nabla\tilde{\mathbf{V}}_f)\mathbf{f} \\ &= \mathbf{\Lambda}_{(f)}\tilde{\mathbf{V}}_f + (\nabla\tilde{\mathbf{V}}_f)\mathbf{f}, \end{aligned} \tag{2.59}$$

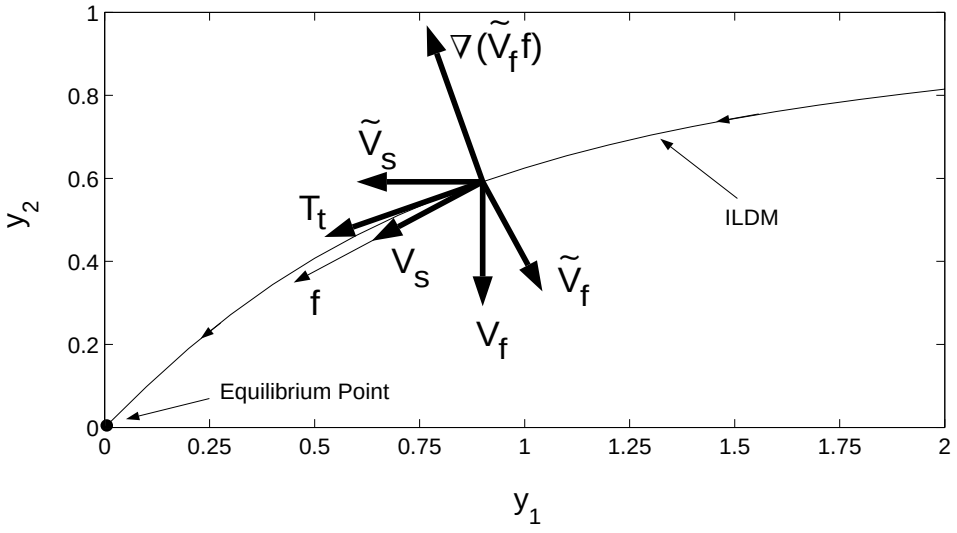

Figure 2.3. Graphical representation of the ILDM for a two-dimensional dynamical system, depicting that the ILDM is a set of points in the phase space where the vector $\mathbf{V}_s$ has the same orientation as the vector $\mathbf{f}$, and that $\mathbf{f}$ is not tangent to the ILDM which is required for the ILDM to be a phase space trajectory and the SIM.

where $\nabla = \sum_{i=1}^{n} \left(\frac{\partial}{\partial y_i}\right) \mathbf{e}_i$, and $\mathbf{e}_i$, $(i = 1, \ldots, n)$, are the unit normal vectors which form the standard basis for $\mathbb{R}^n$. The row vectors of the resultant matrix $\nabla(\tilde{\mathbf{V}}_f \mathbf{f})$ of dimensions $(n - m) \times n$, form the local $(n - m)$-dimensional normal space to the ILDM. The corresponding local m-dimensional tangent space to the ILDM is orthogonal to these row vectors. If $\mathbf{f}$ is linear in $\mathbf{y}$, the eigenvectors in the phase space are constant, and $\nabla \tilde{\mathbf{V}}_f = \mathbf{0}$. Then from Equation (2.59) it is evident that the normal space to the ILDM is same as the subspace spanned by the row vectors of the matrix $\tilde{\mathbf{V}}_f$. Hence, for a linear system, the vector $\mathbf{f}$ lies within the tangent space of the ILDM, making the ILDM a phase space trajectory as well as the SIM. In two dimensions $(n = 2)$, for a linear system, the vectors $\mathbf{f}$ and $\mathbf{T}_t$, in Figure 2.3, will be aligned and the vectors $\nabla(\tilde{\mathbf{V}}_f \mathbf{f})$ and $\mathbf{V}_f$ will also be aligned. To summarize, for a linear system, the ILDM is a linear subspace of the phase space given by $\mathbf{z}_f = \tilde{\mathbf{V}}_f \mathbf{y} = \mathbf{0}$, as obtained from Equation (2.56b). For a nonlinear system, the second term on the right hand side of Equation (2.59) is non-zero; consequently,

the normal space to the ILDM is not same as the subspace spanned by the row vectors of the matrix $\tilde{\mathbf{V}}_f$, nor does the vector $\mathbf{f}$ lies within the tangent space to the ILDM. The two-dimensional ($n = 2$) nonlinear case is depicted in Figure 2.3. To summarize, for a nonlinear system, the ILDM is not a trajectory in the phase space, but, as long as a spectral gap exists, it can be deduced from Equation (2.59) that in the limit of large $\|\mathbf{\Lambda}_{(f)}\|$, the deviation of the ILDM from the phase space trajectory and the SIM becomes small. Similar conclusions were obtained independently by Kaper and Kaper [31], in a more rigorous fashion, but for a simpler system in which the segregation of slow and fast variables is fixed for all times throughout the phase space, which is not the case for chemically reactive systems modeled by Equation (2.50). They also showed that as the curvature of the manifold increases, the error in the ILDM approximation of the SIM increases. This phenomenon is also indicated by Equation (2.59), where, as the second term, which corresponds to a local measure of the curvature of the manifold, becomes larger in magnitude, $\mathbf{f}$ becomes less tangent to the ILDM.

2.3 SIM *vs.* ILDM

If one assumes the existence of an m-dimensional SIM in an n-dimensional phase space, it can be described as

$$y_i = y_i(y_1, \ldots, y_m), \quad (i = m+1, \ldots, n), \tag{2.60}$$

where $y_1, \ldots, y_m$ are the independent state variables chosen to parameterize the SIM, and $y_{m+1}, \ldots, y_n$ are the dependent state variables. The assumed form of the SIM is then differentiated to obtain

$$\frac{dy_i}{dt} = \sum_{j=1}^{m} \frac{\partial y_i}{\partial y_j} \frac{dy_j}{dt}, \quad (i = m+1, \ldots, n). \tag{2.61}$$

All trajectories in the phase space, including the SIM defined by Equation (2.60), satisfy the following equation, which is obtained by eliminating time derivatives from Equation (2.61) with the use of Equation (2.50),

$$f_i(y_{m+1},\ldots,y_n;y_1,\ldots,y_m) = \sum_{j=1}^{m} f_j(y_{m+1},\ldots,y_n;y_1,\ldots,y_m)\frac{\partial y_i(y_1,y_2,\ldots,y_m)}{\partial y_j}, \quad (i=m+1,\ldots,n). \tag{2.62}$$

Fraser and Roussel [34, 35] have used functional iteration to solve Equation (2.62). For each y_i, $(i = m+1,\ldots,n)$, an initial function of the form $y_i = y_i^0(y_1,\ldots,y_m)$ is chosen. Functional iteration is then performed on the following equations, which are obtained by re-writing Equation (2.62),

$$\mathcal{G}_i\left(y_{m+1}^{k+1},\ldots,y_n^{k+1},\frac{\partial y_i^k}{\partial y_1},\ldots,\frac{\partial y_i^k}{\partial y_m};y_1,\ldots,y_m\right)=0, \quad (i=m+1,\ldots,n), \tag{2.63}$$

where the superscript indicates the iteration number starting from $k=0$. One can use computer algebra to perform functional iteration. For high dimensional systems and for systems where Equation (2.63) is not explicit in y_i^{k+1}, $(i=m+1,\ldots,n)$, it is more convenient to use the modified method of Davis and Skodje [36], which uses numerical functional iteration. A discrete form of initial functions $y_i^0(y_1,\ldots,y_m)$, $(i=m+1,\ldots,n)$, are now chosen in a domain $\mathbb{H}$ where the SIM is to be estimated, such that $(y_1,\ldots,y_m)\in\mathbb{H}$. For numerical computations, the domain $\mathbb{H}$ is discretized into a finite number of points, and partial derivatives in Equation (2.63) are approximated by finite differences. Numerical functional iteration is then performed on the resulting implicit algebraic equations. The choice of state variables used for parameterization of the SIM in Equation (2.60) may be arbitrary, though it is essential that these variables be chosen in such a way that the manifold functions given in Equation (2.60) are single-valued. A proper choice of parametric state variables makes numerical computations of the SIM easier. The functional iteration

is expected to converge to the SIM if a) the initial functional guess is good, b) the initial guess does not correspond to a phase space trajectory, and c) there exists an attractive SIM in the phase space as assumed. Both Davis and Skodje [36], Roussel [44], and Roussel and Fraser [45] have suggested methods to enhance the stability of the numerical and algebraic functional iterations, respectively.

Davis and Skodje [36], using a simple example, have illustrated the difference between the ILDM and the SIM. Their two-dimensional system is analogous to the system of Equation (2.50) modeling the CASHPR and is given by

$$\frac{d}{dt}\begin{pmatrix} y_1 \\ y_2 \end{pmatrix} = \begin{pmatrix} -y_1 \\ -\gamma y_2 + \frac{(\gamma-1)y_1+\gamma y_1^2}{(1+y_1)^2} \end{pmatrix}, \tag{2.64}$$

where $\gamma > 1$ gives a measure of stiffness for the system. If γ is increased, stiffness will increase. The Jacobian of the right-hand side is

$$\mathbf{J} = \begin{pmatrix} -1 & 0 \\ \frac{\gamma-1+(\gamma+1)y_1}{(1+y_1)^3} & -\gamma \end{pmatrix}, \tag{2.65}$$

and has eigenvalues $(\lambda_{(1)}, \lambda_{(2)}) = (-1, -\gamma)$. The right and left eigenvectors and are given by

$$\mathbf{V} = \left(\begin{array}{c:c} \mathbf{V}_s & \mathbf{V}_f \end{array}\right) = \left(\begin{array}{c:c} \mathbf{v}_1 & \mathbf{v}_2 \end{array}\right) = \left(\begin{array}{c:c} 1 & 0 \\ \frac{\gamma-1+(\gamma+1)y_1}{(\gamma-1)(1+y_1)^3} & 1 \end{array}\right), \tag{2.66}$$

$$\tilde{\mathbf{V}} = \begin{pmatrix} \tilde{\mathbf{V}}_s \\ \hdashline \tilde{\mathbf{V}}_f \end{pmatrix} = \begin{pmatrix} \tilde{\mathbf{v}}_1 \\ \hdashline \tilde{\mathbf{v}}_2 \end{pmatrix} = \left(\begin{array}{cc} 1 & 0 \\ \hdashline -\frac{\gamma-1+(\gamma+1)y_1}{(\gamma-1)(1+y_1)^3} & 1 \end{array}\right). \tag{2.67}$$

Note that in this case, the eigenvectors are $\mathcal{O}(1)$ even when the right eigenvectors are not normalized. Equation (2.58) is used to determine the one-dimensional ILDM for this system, which can be written in closed form:

$$y_2 = \frac{y_1}{1+y_1} + \frac{2y_1^2}{\gamma(\gamma-1)(1+y_1)^3}. \tag{2.68}$$

The slow, $\tilde{\mathbf{V}}_s \frac{d\mathbf{y}}{dt} = \tilde{\mathbf{V}}_s \mathbf{f}$, and fast, $\tilde{\mathbf{V}}_f \frac{d\mathbf{y}}{dt} = \tilde{\mathbf{V}}_f \mathbf{f}$, equations for this example are given by

$$\frac{dy_1}{dt} = -y_1, \tag{2.69a}$$

$$\frac{1}{\gamma}\left(-\frac{\gamma - 1 + (\gamma+1)y_1}{(\gamma-1)(1+y_1)^3}\frac{dy_1}{dt} + \frac{dy_2}{dt}\right) = -y_2 + \frac{y_1}{1+y_1} + \frac{2y_1^2}{\gamma(\gamma-1)(1+y_1)^3}, \tag{2.69b}$$

respectively. In this case, $\mathbf{g} = \left(0, \frac{((1+y_1)\gamma - 2)y_1^2}{(1+y_1)^3}\right)^T$, hence, the second term, $\frac{1}{\gamma}(\tilde{\mathbf{v}}_2 \mathbf{g})$, in Equation (2.56b) cannot be neglected as it is $\mathcal{O}(1)$. The order of the terms on both sides of Equation (2.69b) can be represented by

$$\mathcal{O}\left(\gamma^{-1}\right) + \mathcal{O}\left(\gamma^{-2}\right) + \ldots = \mathcal{O}(1) + \mathcal{O}\left(\gamma^{-1}\right) + \mathcal{O}\left(\gamma^{-2}\right) + \ldots \tag{2.70}$$

The standard ILDM approximation neglects all terms on the left hand side of the fast equation while retaining all terms on the right hand side. This makes the ILDM an inconsistent approximation to the SIM. On the other hand a systematic matching of terms of all orders will correctly lead to the SIM. This is demonstrated by Kaper and Kaper [31]. However, it is not clear how to implement a systematic perturbation analysis for a system where small parameters such as γ^{-1} are difficult to identify explicitly and globally in the phase space. This is the case in complex systems of chemical kinetics. In such systems, the order of eigenvalues and their membership in the slow and fast sets change with time.

Here Equation (2.62) is solved using an approach often used in center manifold theory [43]. The SIM is assumed to exist and have the following polynomial form

$$y_2 = y_2(y_1) = \sum_{k=0}^{\infty} c_k y_1^k, \tag{2.71}$$

where c_k are constant coefficients. Equation (2.62), in this case, is given by

$$-\gamma y_2 + \frac{(\gamma-1)y_1 + \gamma y_1^2}{(1+y_1)^2} = \frac{dy_2}{dy_1}(-y_1). \tag{2.72}$$

Substituting Equation (2.71) into Equation (2.72), the following values of the coefficients for the SIM are obtained

$$c_0 = 0, \quad c_k = (-1)^{k+1}, \quad k = 1, \ldots, \infty. \tag{2.73}$$

Hence, the SIM is given by

$$y_2 = y_1(1 - y_1 + y_1^2 - y_1^3 + y_1^4 + \ldots) = \frac{y_1}{1 + y_1}. \tag{2.74}$$

When the ILDM in Equation (2.68) is compared with the SIM in Equation (2.74) for this simple system, it is obvious that 1) the ILDM is *not* a SIM, and 2) the error in the ILDM approximation decreases as γ increases. Though the assumption for the SIM to be of polynomial form, as in Equation (2.71), works well in this example, it may not work for more complex systems. This is primarily because such a representation of the SIM is a good approximation sufficiently close to the equilibrium point, and in general, diverges rapidly away from it. To find the global SIM for complex systems, numerical computations are used such as those proposed by Davis and Skodje [36].

The inconsistency in the ILDM procedure in matching of terms of similar orders, leads to errors as shown in this simple system. It is emphasized that the error in the ILDM approximation is small for systems in which the spectral gap condition $|\lambda_{(m)}|/|\lambda_{(m+1)}| << 1$ is valid. Fortunately this situation arises frequently in complex dynamical systems associated with chemical kinetics. Also, in practice, it was found that the numerical computation of the ILDM is more tractable in its implementation than the numerical computation of the SIM.

2.4 ILDM computation

The algebraic equations describing the ILDM are highly nonlinear and several difficulties may arise while numerically computing the ILDM in a certain domain of

the phase space. In Section 2.2 the algebraic Equation (2.58) describing the ILDM was derived for the CASHPR modeled by a system of $n = N - L$ ODEs given in Equations (2.43) or (2.49). The CASHPR, which consists of N chemically reactive species, is modeled by $N - L$ ODEs, when there are L conserved elements in the system. The isochoric CASHPR has two other conserved quantities, namely density and mixture internal energy per unit mass, associated with the thermodynamic state of the system. Similarly, the isobaric CASHPR has two other conserved quantities, namely pressure and mixture enthalpy per unit mass, associated with the thermodynamic state of the system. In some cases, though uncommon and hence, ignored here, there might be an additional conserved quantity associated with the conservation of molecules in the CASHPR, if the number of molecules are conserved within the reaction network in Equation (2.3). Hence, there are typically $L + 2$ conserved quantities associated with the CASHPR: 1)$(\hat{Y}_{1_0}, \ldots, \hat{Y}_{L_0}, \rho_0, e_0)$ for the isochoric CASHPR, 2)$(\hat{Y}_{1_0}, \ldots, \hat{Y}_{L_0}, p_0, h_0)$ for the isobaric CASHPR. Associated with each set of conserved quantities, there exists, within the physically accessible region of the phase space, a stable physical chemical equilibrium point which is a zero-dimensional ILDM, a one-dimensional ILDM, a two-dimensional ILDM, and so on until $(N - L)$-dimensional ILDM which is the complete physically accessible region of the phase space. Each ILDM is associated with $L + 2$ additional constant parameters. A systematic procedure to compute the ILDM for varying values of conserved parameters will be outlined in this section.

In the following discussion the CASHPR will be modeled by $n = N + 2$ ODEs without eliminating the $L + 2$ conserved quantities. For the isochoric CASHPR

these $N+2$ ODEs are

$$\frac{de}{dt} = 0, \qquad e(t=0) = e_0, \tag{2.75a}$$

$$\frac{d\rho}{dt} = 0, \qquad \rho(t=0) = \rho_0, \tag{2.75b}$$

$$\frac{dY_i}{dt} = \frac{\dot{\omega}_i M_i}{\rho_0}, \qquad Y_i(t=0) = Y_{i_0}, \qquad (i = 1, \ldots, N), \tag{2.75c}$$

where Equation (2.75a) is obtained from Equation (2.21), Equation (2.75b) holds because it is an isochoric and constant mass system, and Equation (2.75c) is the constant density version of Equation (2.7). The temperature T, which is required for the evaluation of $\dot{\omega}_i$ (see Equations (2.4-2.6), can be obtained by solving the nonlinear algebraic energy conservation equation (2.42) which is implicit in T. During numerical computations, Equation (2.42) can be easily solved using Newton-Raphson method as the left hand side is a polynomial function of temperature T for a given set of values of species mass fractions Y_i, $(i = 1, \ldots, N)$, and the right hand side is the constant mixture internal energy per unit mass e_0. The pressure p is evaluated using the equation of state (2.40). Similarly, the isobaric CASHPR is modeled by the following $n = N + 2$ ODEs

$$\frac{dh}{dt} = 0, \qquad h(t=0) = h_0, \tag{2.76a}$$

$$\frac{dp}{dt} = 0, \qquad p(t=0) = p_0, \tag{2.76b}$$

$$\frac{dY_i}{dt} = \frac{\dot{\omega}_i M_i}{\rho}, \qquad Y_i(t=0) = Y_{i_0}, \qquad (i = 1, \ldots, N), \tag{2.76c}$$

where Equation (2.76a) is obtained from Equation (2.33), Equation (2.76b) holds because it is an isobaric system, and Equation (2.76c) is the constant pressure version of Equation (2.7). The temperature T, which is required for the evaluation of $\dot{\omega}_i$, can be obtained by solving the nonlinear algebraic energy conservation equation (2.48) which is implicit in T. The density ρ is evaluated using the equation of state (2.46).

Equations (2.75) and (2.76) can be rewritten in a succinct form as in Equa-

tion (2.50)

$$\frac{d\mathbf{y}}{dt} = \mathbf{f}, \qquad \mathbf{y}(t=0) = \mathbf{y}_0, \tag{2.77}$$

where $\mathbf{y} = (h, p, Y_1, \ldots, Y_N)^T$ and $\mathbf{f} = \left(0, 0, \frac{\dot{\omega_1} M_1}{\rho}, \ldots, \frac{\dot{\omega_N} M_N}{\rho}\right)^T$ for the isobaric CASHPR. Here onwards only the isobaric CASHPR will be considered. Construction of the ILDM for the isochoric CASHPR is analogous. The complete phase space or the composition space associated with the dynamical system in Equation (2.77), is represented by the n-dimensional real space $\mathbb{R}^n$. But the physically accessible region of the phase space is restricted to the following subspace

$$\mathbb{S} = \left\{ \mathbf{y} \in \mathbb{R}^n \;\middle|\; \begin{array}{l} p = p_0 > 0, \\ T > 0, \\ 0 \leq Y_1, \ldots, Y_N \leq 1, \\ \sum_{i=1}^{N} Y_i = 1, \\ \sum_{i=1}^{N} h_i(T) Y_i = h = h_0, \\ \sum_{i=1}^{N} \varphi_{il} \frac{Y_i}{M_i} = \sum_{i=1}^{N} \varphi_{il} \frac{Y_{i_0}}{M_i}, l = 1, \ldots, L. \end{array} \right\}, \tag{2.78}$$

because the constant pressure and the temperature of the reactive mixture cannot be negative or zero, the species mass fractions can only take values from zero to unity and their sum is always unity, and the mixture enthalpy per unit mass and the element mass fractions remain constant in the isobaric CASHPR.

A more practical and restrictive constraint for $\mathbb{S}$ is because the Arrhenius kinetics rate constants in Equation (2.6) and the database of thermodynamic properties for chemical species are usually valid for a restricted temperature range (often 300 K $< T <$ 3000 K). But mathematically, a certain initial condition in $\mathbb{S}$ with temperature in the range 300 K $< T <$ 3000 K, can result in a temperature at a future time along the phase space trajectory, which does not lie within the same range. Typically for a physical initial condition $\mathbf{y}_0$ which lies within $\mathbb{S}$, the complete phase space trajectory and the chemical equilibrium point lie within $\mathbb{S}$.

The subspace $\mathbb{S}$, itself, is the $(N-L)$-dimensional ILDM which is the highest dimensional ILDM for an $(n = N+2)$-dimensional system with $L+2$ conserved quantities. Each ILDM of a certain dimension is a subspace of the ILDMs of higher dimension than itself. If the zero-dimensional ILDM, which is the chemical equilibrium point, is represented by $\mathbb{M}_0$ and ILDM of dimensionality i is represented by $\mathbb{M}_i$ then the following is true

$$\mathbb{M}_0 \subset \mathbb{M}_1 \subset \ldots \subset \mathbb{M}_{N-L} = \mathbb{S} \subset \mathbb{R}^n. \tag{2.79}$$

The difference between the system of ODEs in Equation (2.77) and the system of ODEs in Equation (2.50), both modeling the CASHPR, is that the conserved quantities have not been eliminated from the former. The Jacobian, $\mathbf{J} = \frac{\partial \mathbf{f}}{\partial \mathbf{y}}$, for $\mathbf{f}$ in Equation (2.77), can be decomposed to obtain the local eigenvalues and eigenvectors as done in Equation (2.51). However, if the local time scales are partitioned into m slow time scales and $n-m$ fast time scales, then out of the eigenvalues $\lambda_{(1)}, \ldots, \lambda_{(m)}$ associated with m slow time scales as shown in Equation (2.51c), the first $L+2$ eigenvalues are identically zero with $m > L+2$. The $L+2$ zero eigenvalues appear because the $L+2$ conserved quantities are not eliminated from the system of ODEs in Equation (2.77). These $L+2$ conserved quantities do not change along the ILDM. Hence, the actual dimensionality of the ILDM associated with m slow time scales, is only $m_d = m - L - 2$. For example, a one-dimensional ILDM has $m_d = 1$ with $m = L+3$ used to determine the partitioning of the eigenvalues into slow and fast sets. The m_d-dimensional ILDM is associated with reactive processes evolving at m_d *finitely* slow time scales. While deriving the nonlinear algebraic Equation (2.58) describing the ILDM, it was assumed for convenience that all nonzero eigenvalues are real and negative. In that case, since, the eigenvalues in Equation (2.51c) are ordered from least negative to most negative, the $m_d = m-L-2$ nonzero eigenvalues,

in the slow set of eigenvalues $\lambda_{(1)}, \ldots, \lambda_{(m)}$, are the eigenvalues $\lambda_{(L+3)}, \ldots, \lambda_{(m)}$. However, the eigenvalues are real and negative only when sufficiently close to the chemical equilibrium point $\mathbb{M}_0$, and the derivation in Section 2.2 is not a rigorous mathematical proof for the existence of the ILDM. In practice it is found that the ILDM is at times a good approximation of the SIM even if some of the eigenvalues are complex or some of the eigenvalues in the slow set of eigenvalues have positive real part. In that case it is not necessary that the first $L + 2$ eigenvalues are zero in the slow set of eigenvalues. However, it is required, for the construction of the ILDM, that the zero eigenvalues associated with the conserved quantities always lie within the slow set of eigenvalues, or in other words it is required that $m \geq L + 2$.

The complex eigenvalues always appear in pairs of complex conjugates. An ILDM, associated with m slow time scales, will become discontinuous in that region of the phase space where the eigenvalues $\lambda_{(m)}$ and $\lambda_{(m+1)}$ become a complex conjugate pair or where they become equal ($\lambda_{(m)} = \lambda_{(m+1)}$). The ILDM ceases to exist in such regions of the phase space because the local linear slow and fast basis cannot be decoupled. However, if these complex conjugate pairs or equal pairs of eigenvalues appear within the slow set of eigenvalues, $\lambda_{(1)}, \ldots, \lambda_{(m)}$, or within the fast set of eigenvalues, $\lambda_{(m+1)}, \ldots, \lambda_{(n)}$, the ILDM will exist. Here onwards the set of eigenvalues $\lambda_{(1)}, \ldots, \lambda_{(m)}$ will be referred to as the slow set of eigenvalues, while the set of eigenvalues $\lambda_{(m+1)}, \ldots, \lambda_{(n)}$ will be referred to as the fast set of eigenvalues. In some regions of the phase space where $\left(\frac{\lambda_{(m)}}{\lambda_{(m+1)}}\right) \sim \mathcal{O}(1)$ or in other words the spectral gap between the slow and fast time scales is not large, the ILDM does not approximate the SIM well. Close to the chemical equilibrium point $\mathbb{M}_0$, the eigenvalues have mostly negative real parts. However, the eigenvalues might have a positive real part far from $\mathbb{M}_0$ but within the physically accessible subspace $\mathbb{S}$ of the phase space. For the ILDM to be attractive, all the eigenvalues in the fast set

of eigenvalues should have a negative real part. In practice, in most of the reactive systems studied, only one or two positive eigenvalues were encountered far from $\mathbb{M}_0$ while computing the ILDM. Some of these peculiar cases associated with the computation of the ILDM will be demonstrated by examples.

The eigenvectors of the Jacobian $\mathbf{J}$, associated with the system of ODEs in Equation (2.77), may be difficult to evaluate as $\mathbf{J}$ will have multiple zero eigenvalues and it may also have nonzero eigenvalues with multiplicity more than one. Numerical difficulties may also arise due to the presence of nearly equal eigenvalues or the presence of very small, near zero physical eigenvalues which can be confused with the actual zero eigenvalues. In the presence of complex eigenvalues, the eigenvectors will be complex. However, it is more convenient to work with a real representation of the local slow and fast basis vectors, instead of $\mathbf{V}_s$ and $\mathbf{V}_f$ which can be complex, as the behavior of the dynamical system model for the CASHPR is described in the real phase space $\mathbb{R}^n$ Hence, instead of an eigenvalue eigenvector decomposition of $\mathbf{J}$ as in Equation (2.51), the real representation of the local slow and fast basis is obtained as following, starting with a real Schur decomposition of $\mathbf{J}$

$$\mathbf{J} = \begin{pmatrix} \mathbf{Q}_s & \mathbf{Q}_f \end{pmatrix} \begin{pmatrix} \mathbf{N}_s & \mathbf{N}_{sf} \\ 0 & \mathbf{N}_f \end{pmatrix} \begin{pmatrix} \mathbf{Q}_s^T \\ \mathbf{Q}_f^T \end{pmatrix}, \qquad \text{with} \qquad \begin{pmatrix} \mathbf{Q}_s^T \\ \mathbf{Q}_f^T \end{pmatrix} = \begin{pmatrix} \mathbf{Q}_s & \mathbf{Q}_f \end{pmatrix}^{-1}, \tag{2.80}$$

where the real matrix $\mathbf{Q}_s$ has dimensions $n \times m$ and the real matrix $\mathbf{Q}_f$ has dimensions $n \times (n-m)$. It is obvious from Equation (2.80) that the matrix $\begin{pmatrix} \mathbf{Q}_s & \mathbf{Q}_f \end{pmatrix}$ has orthonormal column vectors. The real matrix $\mathbf{N}_s$ is upper triangular, with dimensions $m \times m$, and has the eigenvalues $\lambda_{(1)}, \ldots, \lambda_{(m)}$, the m eigenvalues of $\mathbf{J}$ with the least negative real parts, along its main diagonal. The real matrix $\mathbf{N}_f$ is also upper triangular, with dimensions $(n-m) \times (n-m)$, and has the eigenvalues $\lambda_{(m+1)}, \ldots, \lambda_{(n)}$, the $n-m$ eigenvalues of $\mathbf{J}$ with the most negative

real parts, along its main diagonal. If complex conjugate pairs of eigenvalues exist in either the slow or fast sets of eigenvalues, then the real matrices $\mathbf{N}_s$ and $\mathbf{N}_f$ are not strictly upper triangular. Instead, the complex conjugate pairs of eigenvalues exist as two by two blocks along the main diagonal of $\mathbf{N}_s$ and $\mathbf{N}_f$, with the real part of the complex conjugate eigenvalues appearing along the main diagonal of the two by two block and the complex part of the eigenvalues appearing at the other two entries of the two by two block. Hence, the first sub-diagonal in the real matrices $\mathbf{N}_s$ and $\mathbf{N}_f$ may have some non-zero entries in the presence of complex eigenvalues. Finally, the real matrix $\mathbf{N}_{sf}$ is full and has dimensions $m \times (n-m)$.

The real Schur decomposition of $\mathbf{J}$ is followed by a solution of the Sylvester equation for the unknown matrix $\mathbf{X}$

$$\mathbf{N}_s\mathbf{X} - \mathbf{X}\mathbf{N}_f = -\mathbf{N}_{sf}, \tag{2.81}$$

where the real matrix $\mathbf{X}$ has dimensions $m \times (n-m)$. Finally, the local slow and fast basis, now represented by the real matrices $\mathbf{Z}_s$ and $\mathbf{Z}_f$, respectively, are evaluated using the following matrix multiplications

$$\begin{pmatrix} \mathbf{Z}_s & \mathbf{Z}_f \end{pmatrix} = \begin{pmatrix} \mathbf{Q}_s & \mathbf{Q}_f \end{pmatrix} \begin{pmatrix} \mathbf{I} & \mathbf{X} \\ 0 & \mathbf{I} \end{pmatrix}, \tag{2.82}$$

$$\begin{pmatrix} \tilde{\mathbf{Z}}_s \\ \tilde{\mathbf{Z}}_f \end{pmatrix} = \begin{pmatrix} \mathbf{I} & -\mathbf{X} \\ 0 & \mathbf{I} \end{pmatrix} \begin{pmatrix} \mathbf{Q}_s^T \\ \mathbf{Q}_f^T \end{pmatrix}, \tag{2.83}$$

where the real matrix $\mathbf{Z}_s$ has dimensions $n \times m$, the real matrix $\mathbf{Z}_f$ has dimensions $n \times (n-m)$, the real matrix $\tilde{\mathbf{Z}}_s$ has dimensions $m \times n$ and the real matrix $\tilde{\mathbf{Z}}_f$ has dimensions $(n-m) \times n$. Equations (2.82) and (2.83) are used with Equation (2.80) to obtain the following decomposition of $\mathbf{J}$

$$\mathbf{J} = \begin{pmatrix} \mathbf{Z}_s & \mathbf{Z}_f \end{pmatrix} \begin{pmatrix} \mathbf{N}_s & 0 \\ 0 & \mathbf{N}_f \end{pmatrix} \begin{pmatrix} \tilde{\mathbf{Z}}_s \\ \tilde{\mathbf{Z}}_f \end{pmatrix}, \qquad \text{with} \qquad \begin{pmatrix} \tilde{\mathbf{Z}}_s \\ \tilde{\mathbf{Z}}_f \end{pmatrix} = \begin{pmatrix} \mathbf{Z}_s & \mathbf{Z}_f \end{pmatrix}^{-1}. \tag{2.84}$$

The decomposition in Equation (2.84) can be done for any real square matrix, such as $\mathbf{J}$, using the steps in Equations (2.80-2.83), all of which can be implemented using the subroutines available in the linear algebra package LAPACK [46]. This decomposition of $\mathbf{J}$ was outlined by Maas [47] following the general theory given by Golub and Van Loan [48]. The column vectors of the real matrix $\mathbf{Z}_s$ form the local basis associated with the m slow time scales, while the column vectors of the real matrix $\mathbf{Z}_f$ form the local basis associated with the remaining $n-m$ fast time scales. The two basis are fully decoupled. The row vectors of the real matrices $\tilde{\mathbf{Z}}_s$ and $\tilde{\mathbf{Z}}_f$ form the reciprocal slow and fast basis, respectively. The decomposition of $\mathbf{J}$ in Equation (2.84) is advantageous as it is not associated with the numerical difficulties associated with the eigenvalue eigenvector decomposition in Equation (2.51) and it also gives a real representation of the local slow and fast basis. The column vectors of the matrices $\mathbf{V}_s$, $\mathbf{Z}_s$ and $\mathbf{Q}_s$ ($\mathbf{Z}_s = \mathbf{Q}_s$) span the same local slow basis, while the row vectors of the matrices $\tilde{\mathbf{V}}_s$ and $\tilde{\mathbf{Z}}_s$ span the same reciprocal slow basis. The column vectors of the matrices $\mathbf{V}_f$ and $\mathbf{Z}_f$ span the same local fast basis, while the row vectors of the matrices $\tilde{\mathbf{V}}_f$ and $\tilde{\mathbf{Z}}_f$ and the column vectors of the matrix $\mathbf{Q}_f$ ($\tilde{\mathbf{Z}}_f = \mathbf{Q}_f^T$) span the same reciprocal fast basis. Hence, as in Equation (2.58), the ILDM can be identically represented by the following nonlinear algebraic Equations

$$\tilde{\mathbf{Z}}_f \mathbf{f}(\mathbf{y}) = \mathbf{0}. \tag{2.85}$$

There are $n-m$ nonlinear algebraic Equations (2.85), in n unknowns, describing the ILDM. Hence, $m = m_d + L + 2$ supplemental parametric equations are required to close the system of equations for *a priori* computation of the ILDM in the phase space.

2.4.1 The $L+2$ parametric equations associated with the $L+2$ conserved quantities

The $L+2$ parametric equations associated with the conserved quantities are derived first. The conserved quantities for the isobaric CASHPR are represented by a vector $\bar{\mathbf{y}}$, with $\bar{y}_1 = \hat{Y}_1, \ldots, \bar{y}_L = \hat{Y}_L$, $\bar{y}_{L+1} = p$ and $\bar{y}_{L+2} = h$, and can be written in a vector form as following

$$\bar{\mathbf{y}} = \begin{pmatrix} \bar{y}_1 \\ \vdots \\ \bar{y}_{L+2} \end{pmatrix} = \begin{pmatrix} \hat{Y}_1 \\ \vdots \\ \hat{Y}_L \\ p \\ h \end{pmatrix} = \begin{pmatrix} 1 - \sum_{l=2}^{L} \psi_l \\ \psi_2 \\ \vdots \\ \psi_L \\ p_{min} + \psi_{L+1}(p_{max} - p_{min}) \\ h_{min} + \psi_{L+2}(h_{max} - h_{min}) \end{pmatrix}, \tag{2.86}$$

where $\psi_l \in [0,1]$, $(l = 1, \ldots, L)$, as the conserved element mass fractions, $\hat{Y}_1, \ldots, \hat{Y}_L$, can only have values from zero to unity, and $\psi_l \in [0,1]$, $(l = L+1, L+2)$, as the ILDM is computed for range of values of the two conserved quantities p and h given by $p \in [p_{min}, p_{max}]$ and $h \in [h_{min}, h_{max}]$. Since, the sum of the element mass fractions is unity, $\sum_{l=1}^{L} \psi_l = 1$. Equation (2.86) can be rewritten as following

$$\bar{\mathbf{y}} = \begin{pmatrix} 1 \\ \mathbf{0}_{(L-1)\times 1} \\ p_{min} \\ h_{min} \end{pmatrix} + \mathbf{P}_c \begin{pmatrix} 0 \\ \psi_2 \\ \vdots \\ \psi_{L+2} \end{pmatrix}, \tag{2.87}$$

where the matrix $\mathbf{P}_c$ has dimensions $(L+2) \times (L+2)$, while the remaining two vectors on the right hand side are of length $L+2$ each. A null matrix of dimensions

$i \times j$ is represented by $\mathbf{0}_{i\times j}$. The elements of the matrix $\mathbf{P}_c$ are given as following

$$\mathbf{P}_c = \left(\begin{array}{c|ccc|cc} 1 & -1 & \cdots & -1 & \multicolumn{2}{c}{\mathbf{0}_{1\times 2}} \\ \hline 1 & & & & & \\ \vdots & \multicolumn{3}{c|}{\mathbf{I}_{(L-1)\times(L-1)}} & \multicolumn{2}{c}{\mathbf{0}_{(L-1)\times 2}} \\ 1 & & & & & \\ \hline & & & & p_{max}-p_{min} & 0 \\ \mathbf{0}_{2\times 1} & \multicolumn{3}{c|}{\mathbf{0}_{2\times(L-1)}} & & \\ & & & & 0 & h_{max}-h_{min} \end{array}\right), \quad (2.88)$$

where $\mathbf{I}_{i\times j}$ represents an identity matrix of dimensions $i \times j$. Note that the first column vector of the matrix $\mathbf{P}_c$ can be any vector with first element unity for Equation (2.87) to be consistent with Equation (2.86). However, the first column vector of the matrix $\mathbf{P}_c$ is chosen to be orthogonal to all other linearly independent column vectors of the matrix $\mathbf{P}_c$. This choice ensures that all column vectors of the matrix $\mathbf{P}_c$ are linearly independent and hence, the inverse of the matrix $\mathbf{P}_c$ exists.

The conserved quantities can also be expressed as a linear combination of the dependent variables in Equation (2.77), which models the isobaric CASHPR, as following

$$\bar{\mathbf{y}} = \mathbf{P}_p \mathbf{y}, \quad (2.89)$$

where the matrix $\mathbf{P}_p$ has dimensions $(L+2) \times (N+2)$ and is given by

$$\mathbf{P}_p = \left(\begin{array}{cc|c} & & \\ \mathbf{0}_{L\times 2} & & \mathbf{\Phi} \\ & & \\ \hline 0 & 1 & \\ & & \mathbf{0}_{2\times N} \\ 1 & 0 & \end{array}\right). \quad (2.90)$$

The matrix $\mathbf{\Phi}$ has dimensions $L \times N$ and has elements $\phi_{il} = \varphi_{il}\frac{\hat{M}_l}{M_i}$ (with no summation over repeated indices) which are obtained using Equation (2.12) which relates the conserved element mass fractions to the species mass fractions.

Substituting the expression for $\bar{\mathbf{y}}$ from Equation (2.89) into Equation (2.87) gives

$$\mathbf{P}_p\mathbf{y} = \begin{pmatrix} 1 \\ \mathbf{0}_{(L-1)\times 1} \\ p_{min} \\ h_{min} \end{pmatrix} + \mathbf{P}_c \begin{pmatrix} 0 \\ \psi_2 \\ \vdots \\ \psi_{L+2} \end{pmatrix}. \tag{2.91}$$

Then applying the operator $\mathbf{P}_c^{-1}$ to Equation (2.91) gives

$$\mathbf{P}_c^{-1}\mathbf{P}_p\mathbf{y} = \begin{pmatrix} 1/L \\ -1/L \\ \vdots \\ -1/L \\ p_{min}/(p_{max} - p_{min}) \\ h_{min}/(h_{max} - h_{min}) \end{pmatrix} + \begin{pmatrix} 0 \\ \psi_2 \\ \vdots \\ \psi_{L+2} \end{pmatrix}. \tag{2.92}$$

Equation (2.92) can be written in a compact form as following

$$\mathbf{P}_z\mathbf{y} = \mathbf{\Omega} + \mathbf{\Psi}, \tag{2.93}$$

where the matrix $\mathbf{P}_z = \mathbf{P}_c^{-1}\mathbf{P}_p$ has dimensions $(L+2) \times (N+2)$, the constant vector $\mathbf{\Omega} = \left(\frac{1}{L}, \frac{-1}{L}, \ldots, \frac{-1}{L}, \frac{p_{min}}{(p_{max}-p_{min})}, \quad \frac{h_{min}}{(h_{max}-h_{min})}\right)^T$ is of length $L+2$ and the conserved parameters vector $\mathbf{\Psi} = (0, \psi_2, \ldots, \psi_{L+2})^T$ is of length $L+2$. The vector $\mathbf{\Omega}$ is constant for a given reactive mixture with L elements and for the given ranges of p and h. Note that the first entry of the conserved parameters vector $\mathbf{\Psi}$ is zero.

If the chemical equilibrium state is represented by $\mathbf{y}^e$, which is also the zero-dimensional ILDM $\mathbb{M}_0$, then using Equation (2.93), the following is obtained

$$\mathbf{P}_z\mathbf{y}^e = \mathbf{\Omega} + \mathbf{\Psi}^e, \tag{2.94}$$

where $\mathbf{\Psi}^e$ is the conserved parameters vector associated with $\mathbf{y}^e$. From here onwards in this chapter, any variable with superscript e will represent the value of that variable at the chemical equilibrium state. Subtracting Equation (2.94) from Equation (2.93) gives

$$\mathbf{P}_z(\mathbf{y} - \mathbf{y}^e) = \mathbf{\Psi} - \mathbf{\Psi}^e. \tag{2.95}$$

This formulation of the $L + 2$ parametric equations associated with the conserved quantities is useful as the ILDM construction is usually initiated from the chemical equilibrium state, $\mathbf{y}^e$, in the phase space. Note that the number of free parameters associated with the $L + 2$ parametric Equations (2.95) is $L + 1$ as the first element of the conserved parameters vector $\mathbf{\Psi}$ is zero. This reduction in degrees of freedom is because the sum of all the conserved element mass fractions is unity.

Sometimes it is not required to compute the ILDM for all ranges of conserved element mass fractions or the associated $L - 1$ conserved parameters, $\psi_l \in [0, 1]$, $(l = 2, \ldots, L)$. In some reactive systems as discussed in Appendix B where the mass diffusivity of all species are equal, all the element mass fractions are linear functions of the scalar mixture fraction. In a two stream reactive system, the mixture fraction [20] is a measure of the ratio of the amount of a mixture A, with species mass fractions Y_i^A, $i = 1, \ldots, N$, and the amount of a mixture B, with species mass fractions Y_i^B, $i = 1, \ldots, N$, which react with each other. Instead of computing the ILDM for different values of element mass fractions, it is computed for different values of mixture fraction. This will eventually reduce the dimension of the ILDM table. In a two stream reactive system with one stream of mixture A and the other stream of mixture B, the element mass fractions, $\hat{Y}_l, l = 1, \ldots, L$, are given by (see Appendix B)

$$\hat{Y}_l = \hat{Y}_l^A + \chi(\hat{Y}_l^B - \hat{Y}_l^A), \qquad (l = 1, \ldots, L), \tag{2.96}$$

where $\chi \in [0,1]$ represents the mixture fraction and $\hat{Y}_l^A$ and $\hat{Y}_l^B$ represent the mass fractions of element l in the mixtures A and B, respectively. Here onwards in this chapter, any variable with superscripts A or B will represent the value of that variable in the mixtures A and B, respectively.

As for the chemical equilibrium state in Equation (2.94), using Equation (2.93), the following is obtained for mixture A

$$\mathbf{P}_z \mathbf{y}^A = \mathbf{\Omega} + \mathbf{\Psi}^A, \tag{2.97}$$

where $\mathbf{y}^A$ represents the state of the mixture A and $\mathbf{\Psi}^A$ represents the conserved parameters vector associated with the mixture A. Subtracting Equation (2.97) from Equation (2.93) gives

$$\mathbf{P}_z(\mathbf{y} - \mathbf{y}^A) = \mathbf{\Psi} - \mathbf{\Psi}^A, \tag{2.98}$$

which, using Equation (2.96) and $\psi_l = \hat{Y}_l$, $(l = 1, \ldots, L)$ (see Equation (2.86)), can also be written as

$$\mathbf{P}_z(\mathbf{y} - \mathbf{y}^A) = \begin{pmatrix} 0 \\ \psi_2 - \psi_2^A \\ \vdots \\ \psi_L - \psi_L^A \\ \psi_{L+1} - \psi_{L+1}^A \\ \psi_{L+2} - \psi_{L+2}^A \end{pmatrix} = \begin{pmatrix} 0 \\ \chi(\psi_2^B - \psi_2^A) \\ \vdots \\ \chi(\psi_L^B - \psi_L^A) \\ \psi_{L+1} - \psi_{L+1}^A \\ \psi_{L+2} - \psi_{L+2}^A \end{pmatrix}, \tag{2.99}$$

and then in a compact form as following

$$\mathbf{P}_z(\mathbf{y} - \mathbf{y}^A) = \mathbf{\Gamma} \begin{pmatrix} \chi \\ \psi_{L+1} - \psi_{L+1}^A \\ \psi_{L+2} - \psi_{L+2}^A \end{pmatrix}, \tag{2.100}$$

where the matrix $\mathbf{\Gamma}$ has dimensions $(L+2)\times 3$ and is given by

$$\mathbf{\Gamma} = \begin{pmatrix} 0 & 0 & 0 \\ \psi_2^B - \psi_2^A & 0 & 0 \\ \vdots & \vdots & \vdots \\ \psi_L^B - \psi_L^A & 0 & 0 \\ 0 & 1 & 0 \\ 0 & 0 & 1 \end{pmatrix}. \tag{2.101}$$

The three column vectors of the matrix $\mathbf{\Gamma}$ are orthogonal to each other. The orthogonal complement to the matrix $\mathbf{\Gamma}$ can be obtained by the following singular value decomposition

$$\mathbf{\Gamma} = \mathbf{U}\mathbf{\Sigma}\mathbf{W}^T, \tag{2.102}$$

where the matrix $\mathbf{\Sigma}$ has dimensions $(L+2)\times 3$, and it has nonnegative diagonal elements and zero as the other elements. The matrix $\mathbf{U}$ has dimensions $(L+2)\times(L+2)$ and the matrix $\mathbf{W}$ has dimensions 3×3, both containing orthogonal column vectors. The matrix formed by the last $L+2-3$ column vectors of the matrix $\mathbf{U}$ is the orthogonal complement of the matrix $\mathbf{\Gamma}$, and it is represented by the matrix $\mathbf{\Gamma}^{\perp}$ with dimensions $(L+2)\times(L-1)$. The matrix represented by $\mathbf{\Upsilon}$ with dimensions $(L+2)\times(L+2)$ has the first $L-1$ columns as the matrix $\mathbf{\Gamma}^{\perp}$ and the last three columns as the matrix $\mathbf{\Gamma}$. Now Equation (2.100) can be written as

$$\mathbf{P}_z(\mathbf{y}-\mathbf{y}^A) = \mathbf{\Upsilon}\begin{pmatrix} \mathbf{0}_{(L-1)\times 1} \\ \chi \\ \psi_{L+1} - \psi_{L+1}^A \\ \psi_{L+2} - \psi_{L+2}^A \end{pmatrix}. \tag{2.103}$$

Equation (2.103) can be further simplified to

$$\mathbf{P}_{\chi}^{(1)}(\mathbf{y}-\mathbf{y}^{A}) = \begin{pmatrix} \mathbf{0}_{(L-1)\times 1} \\ \chi \\ \psi_{L+1}-\psi_{L+1}^{A} \\ \psi_{L+2}-\psi_{L+2}^{A} \end{pmatrix}, \tag{2.104}$$

where the matrix $\mathbf{P}_{\chi}^{(1)} = \boldsymbol{\Upsilon}^{-1}\mathbf{P}_{z}$ has dimensions $(L+2)\times(N+2)$. The inverse of the square matrix $\boldsymbol{\Upsilon}$ exists as it contains linearly independent column vectors. At the chemical equilibrium state, $\mathbb{M}_0$, Equation (2.104) can be written as

$$\mathbf{P}_{\chi}^{(1)}(\mathbf{y}^{e}-\mathbf{y}^{A}) = \begin{pmatrix} \mathbf{0}_{(L-1)\times 1} \\ \chi^{e} \\ \psi_{L+1}^{e}-\psi_{L+1}^{A} \\ \psi_{L+2}^{e}-\psi_{L+2}^{A} \end{pmatrix}. \tag{2.105}$$

Subtracting Equation (2.105) from Equation (2.104) gives

$$\mathbf{P}_{\chi}^{(1)}(\mathbf{y}-\mathbf{y}^{e}) = \begin{pmatrix} \mathbf{0}_{(L-1)\times 1} \\ \chi \\ \psi_{L+1} \\ \psi_{L+2} \end{pmatrix} - \begin{pmatrix} \mathbf{0}_{(L-1)\times 1} \\ \chi^{e} \\ \psi_{L+1}^{e} \\ \psi_{L+2}^{e} \end{pmatrix}, \tag{2.106}$$

which is written in a compact form as following

$$\mathbf{P}_{\chi}^{(1)}(\mathbf{y}-\mathbf{y}^{e}) = \boldsymbol{\Xi}_{(1)} - \boldsymbol{\Xi}_{(1)}^{e}, \tag{2.107}$$

where the vector $\boldsymbol{\Xi}_{(1)} = (0,\ldots,0,\chi,\psi_{L+1},\psi_{L+2})^{T}$ is of length $L+2$. This formulation of the $L+2$ parametric equations is useful as the ILDM construction is usually initiated from the chemical equilibrium state. Note that the number of free parameters associated with the $L+2$ parametric Equations (2.107) has been reduced to three as the first $L-1$ elements of the vector $\boldsymbol{\Xi}_{(1)}$ are zero.

Sometimes it is not required to compute the ILDM for all ranges of the conserved quantity, h, or the associated conserved parameter, ψ_{L+2}. In some reactive systems as discussed in Appendix B where the Lewis number $Le = 1$ or the thermal diffusivity is equal to the mass diffusivity, even the mixture enthalpy per unit mass becomes a linear function of the scalar mixture fraction. Now, instead of computing the ILDM for different values of element mass fractions and enthalpies, it is computed for different values of mixture fraction. This also reduces the dimension of the ILDM table. In a two stream reactive system, the mixture enthalpy per unit mass is the following linear function of χ (see Appendix B)

$$h = h^A + \chi(h^B - h^A), \tag{2.108}$$

where h^A and h^B represent the enthalpy per unit mass of the mixtures A and B, respectively. Then using Equation (2.108) with the following relations

$$h = h_{min} + \psi_{L+2}(h_{max} - h_{min}), \tag{2.109a}$$

$$h^A = h_{min} + \psi^A_{L+2}(h_{max} - h_{min}), \tag{2.109b}$$

$$h^B = h_{min} + \psi^B_{L+2}(h_{max} - h_{min}), \tag{2.109c}$$

the following is obtained

$$\psi_{L+2} = \psi^A_{L+2} + \chi(\psi^B_{L+2} - \psi^A_{L+2}). \tag{2.110}$$

Now using Equation (2.96) with $\psi_l = \hat{Y}_l$, $(l = 1, \ldots, L)$ (see Equation (2.86)), and

Equation (2.110), Equation (2.98) can be written as

$$\mathbf{P}_z(\mathbf{y}-\mathbf{y}^A) = \begin{pmatrix} 0 \\ \psi_2 - \psi_2^A \\ \vdots \\ \psi_L - \psi_L^A \\ \psi_{L+1} - \psi_{L+1}^A \\ \psi_{L+2} - \psi_{L+2}^A \end{pmatrix} = \begin{pmatrix} 0 \\ \chi(\psi_2^B - \psi_2^A) \\ \vdots \\ \chi(\psi_L^B - \psi_L^A) \\ \psi_{L+1} - \psi_{L+1}^A \\ \chi(\psi_{L+2}^B - \psi_{L+2}^A) \end{pmatrix}, \tag{2.111}$$

and then in a compact form as following

$$\mathbf{P}_z(\mathbf{y}-\mathbf{y}^A) = \mathbf{\Gamma} \begin{pmatrix} \chi \\ \psi_{L+1} - \psi_{L+1}^A \end{pmatrix}, \tag{2.112}$$

where now the matrix $\mathbf{\Gamma}$ has dimensions $(L+2)\times 2$ and is given by

$$\mathbf{\Gamma} = \begin{pmatrix} 0 & 0 \\ \psi_2^B - \psi_2^A & 0 \\ \vdots & \vdots \\ \psi_L^B - \psi_L^A & 0 \\ 0 & 1 \\ \psi_{L+2}^B - \psi_{L+2}^A & 0 \end{pmatrix}. \tag{2.113}$$

The corresponding orthogonal complement matrix $\mathbf{\Gamma}^\perp$ with dimensions $(L+2)\times L$ is obtained by performing singular value decomposition of the matrix $\mathbf{\Gamma}$, as described previously. Now Equation (2.112) can be written as

$$\mathbf{P}_z(\mathbf{y}-\mathbf{y}^A) = \mathbf{\Upsilon} \begin{pmatrix} \mathbf{0}_{L\times 1} \\ \chi \\ \psi_{L+1} - \psi_{L+1}^A \end{pmatrix}, \tag{2.114}$$

where the matrix $\mathbf{\Upsilon}$ with dimensions $(L+2)\times(L+2)$ is formed as described

previously. Finally, Equation (2.114) can be further simplified to

$$\mathbf{P}_{\chi}^{(2)}(\mathbf{y}-\mathbf{y}^{A}) = \begin{pmatrix} \mathbf{0}_{L\times 1} \\ \chi \\ \psi_{L+1}-\psi_{L+1}^{A} \end{pmatrix}, \tag{2.115}$$

where the matrix $\mathbf{P}_{\chi}^{(2)} = \boldsymbol{\Upsilon}^{-1}\mathbf{P}_{z}$ has dimensions $(L+2)\times(N+2)$. The inverse of the square matrix $\boldsymbol{\Upsilon}$ exists as it contains linearly independent column vectors. At the chemical equilibrium state, $\mathbb{M}_0$, Equation (2.115) can be written as

$$\mathbf{P}_{\chi}^{(2)}(\mathbf{y}^{e}-\mathbf{y}^{A}) = \begin{pmatrix} \mathbf{0}_{L\times 1} \\ \chi^{e} \\ \psi_{L+1}^{e}-\psi_{L+1}^{A} \end{pmatrix}. \tag{2.116}$$

Subtracting Equation (2.116) from Equation (2.115) gives

$$\mathbf{P}_{\chi}^{(2)}(\mathbf{y}-\mathbf{y}^{e}) = \begin{pmatrix} \mathbf{0}_{L\times 1} \\ \chi \\ \psi_{L+1} \end{pmatrix} - \begin{pmatrix} \mathbf{0}_{L\times 1} \\ \chi^{e} \\ \psi_{L+1}^{e} \end{pmatrix}, \tag{2.117}$$

which is written in a compact form as following

$$\mathbf{P}_{\chi}^{(2)}(\mathbf{y}-\mathbf{y}^{e}) = \boldsymbol{\Xi}_{(2)} - \boldsymbol{\Xi}_{(2)}^{e}, \tag{2.118}$$

where the vector $\boldsymbol{\Xi}_{(2)} = (0,\ldots,0,\chi,\psi_{L+1})^{T}$ is of length $L+2$. This formulation of the $L+2$ parametric Equations (2.118) is useful as the ILDM construction is usually initiated from the chemical equilibrium state. Note that the number of free parameters associated with the $L+2$ parametric Equations (2.118) has been reduced to two as the first L elements of the vector $\boldsymbol{\Xi}_{(2)}$ are zero.

To summarize, the general form of the $L+2$ parametric equations associated with the $L+2$ conserved quantities are given by

$$\mathbf{P}_{z}(\mathbf{y}-\mathbf{y}^{e}) = \boldsymbol{\Psi} - \boldsymbol{\Psi}^{e}, \tag{2.119}$$

and in the two special cases, the $L+2$ parametric equations are given by

$$\mathbf{P}_{\chi}^{(1)}(\mathbf{y}-\mathbf{y}^{e}) = \mathbf{\Xi}_{(1)} - \mathbf{\Xi}_{(1)}^{e}, \tag{2.120}$$

$$\mathbf{P}_{\chi}^{(2)}(\mathbf{y}-\mathbf{y}^{e}) = \mathbf{\Xi}_{(2)} - \mathbf{\Xi}_{(2)}^{e}. \tag{2.121}$$

In Equation (2.119) the number of free parameters are $L+1$, namely $\psi_2, \ldots, \psi_{L+2}$, while in Equation (2.120) the number of free parameters are three, namely χ, ψ_{L+1}, and ψ_{L+2}, while in Equation (2.121) the number of free parameters are two, namely χ, and ψ_{L+1}.

2.4.2 The m_d parametric equations associated with the m_d-dimensional ILDM

The additional $m_d = m - L - 2$ parametric equations associated with the m_d-dimensional ILDM are given by

$$\mathbf{P}_{s}(\mathbf{y}-\mathbf{y}^{e}) = \mathbf{s} - \mathbf{s}^{e}, \tag{2.122}$$

where the matrix $\mathbf{P}_s$ has dimensions $m_d \times (N+2)$, and the vector $\mathbf{s}$ is of length m_d. Unlike the parametric matrices, $\mathbf{P}_z$, $\mathbf{P}_{\chi}^{(1)}$, and $\mathbf{P}_{\chi}^{(2)}$, the parametric matrix $\mathbf{P}_s$ is user specified, and its m_d row vectors represent the parameterization directions in the phase space. Often the parameters $s_1, \ldots, s_{m_d}$ are chosen from the species mass fractions $y_3 = Y_1, \ldots, y_n = Y_N$ ($n > m = m_d + L + 2 > m_d$). In that case, the row vectors of the matrix $\mathbf{P}_s$ simply become the standard unit vectors, associated with the chosen species mass fractions, in the phase space $\mathbb{R}^n$. Typically the mass fractions of those species are chosen which are products in the reactive mixture, as they usually provide a single valued parameterization of the ILDM.

2.4.3 Final form of the $m = m_d + L + 2$ parametric equations

The parametric equation (2.119) or (2.120) or (2.121) can be combined with the parametric equation (2.122) to represent the m parametric equations as follows

$$\mathbf{P}_d(\mathbf{y} - \mathbf{y}^e) = \begin{pmatrix} \mathbf{0}_{l_1 \times 1} \\ \mathbf{d} \end{pmatrix}, \tag{2.123}$$

where the $m \times (N+2)$ dimensional matrix $\mathbf{P}_d = \begin{pmatrix} \mathbf{P}_z \\ \mathbf{P}_s \end{pmatrix}$ or $\begin{pmatrix} \mathbf{P}_\chi^{(1)} \\ \mathbf{P}_s \end{pmatrix}$ or $\begin{pmatrix} \mathbf{P}_\chi^{(2)} \\ \mathbf{P}_s \end{pmatrix}$, and the vector $\begin{pmatrix} \mathbf{0}_{l_1 \times 1} \\ \mathbf{d} \end{pmatrix} = \begin{pmatrix} \mathbf{\Psi} - \mathbf{\Psi}^e \\ \mathbf{s} - \mathbf{s}^e \end{pmatrix}$ or $\begin{pmatrix} \mathbf{\Xi}_{(1)} - \mathbf{\Xi}_{(1)}^e \\ \mathbf{s} - \mathbf{s}^e \end{pmatrix}$ or $\begin{pmatrix} \mathbf{\Xi}_{(2)} - \mathbf{\Xi}_{(2)}^e \\ \mathbf{s} - \mathbf{s}^e \end{pmatrix}$ is of length m. The vector on the right hand side of Equation (2.123) is composed of a null vector of length l_1 and a vector of free parameters, $\mathbf{d}$, of length $l_2 = m - l_1$. At the chemical equilibrium state $\mathbf{d} = \mathbf{0}$. For the most general case in Equation (2.119), $l_1 = 1$ and $l_2 = m - 1$ with $\mathbf{d} = (\psi_2 - \psi_2^e, \ldots, \psi_{L+2} - \psi_{L+2}^e, s_1 - s_1^e, \ldots, s_{m_d} - s_{m_d}^e)^T$. However, in some fully premixed reactive flow systems, the conserved quantities do not vary and hence, the ILDM is only computed for one fixed set of conserved quantities. In that case $l_1 = L + 2$ and $l_2 = m_d$ with $\mathbf{d} = (s_1 - s_1^e, \ldots, s_{m_d} - s_{m_d}^e)^T$. In the special case in Equation (2.120), $l_1 = L - 1$ and $l_2 = m_d + 3$ with $\mathbf{d} = (\chi - \chi^e, \psi_{L+1} - \psi_{L+1}^e, \psi_{L+2} - \psi_{L+2}^e, s_1 - s_1^e, \ldots, s_{m_d} - s_{m_d}^e)^T$, and in the other special case in Equation (2.120), $l_1 = L$ and $l_2 = m_d + 2$ with $\mathbf{d} = (\chi - \chi^e, \psi_{L+1} - \psi_{L+1}^e, s_1 - s_1^e, \ldots, s_{m_d} - s_{m_d}^e)^T$.

It is obvious from the previous discussion and Equation (2.123) that an m_d-dimensional ILDM is parameterized by $l_2 = m - l_1$ free parameters. Hence, the

following equations are required to be solved for *a priori* computation of the ILDM

$$\mathbf{P}_d(\mathbf{y}-\mathbf{y}^e) = \begin{pmatrix} \mathbf{0}_{l_1\times 1} \\ \mathbf{d} \end{pmatrix}, \qquad (m \text{ parametric equations}), \tag{2.124a}$$

$$\tilde{\mathbf{Z}}_f \mathbf{f}(\mathbf{y}) = \mathbf{0}, \qquad (n-m \text{ ILDM Equations}). \tag{2.124b}$$

Equations (2.124) can also be represented by the following explicit functional form

$$\mathbf{y} = \mathbf{f}_d(\mathbf{d}), \tag{2.125}$$

where the vector function $\mathbf{f}_d$ is a mapping of the form $\mathbf{f}_d : \mathbb{D} \to \mathbb{S}$, and $\mathbb{D} \subset \mathbb{R}^{l_2}$ is the domain of the ILDM functional form in the parametric space $\mathbb{R}^{l_2}$. All the user specified free parameters, which are $d_{(l_2-m_d+1)}, \ldots, d_{l_2}$ $(l_2 \geq m_d)$, are chosen such that the mapping $\mathbf{f}_d : \mathbb{D} \to \mathbb{S}$ is one to one, or in other words the ILDM has a single valued parameterization.

In the parametric space $\mathbb{R}^{l_2}$ the chemical equilibrium state is at the origin $\mathbf{d} = \mathbf{0}$. The ILDM is constructed for a l_2-dimensional polar grid system centered around the origin in the l_2-dimensional parametric space. Hence, Equation (2.123) is transformed to the following

$$\left(\begin{array}{c:c} \mathbf{I}_{l_1\times l_1} & \mathbf{0}_{l_1\times l_2} \\ \hdashline \mathbf{0}_{l_2\times l_1} & \mathbf{R}_{l_2\times l_2} \end{array}\right) \mathbf{P}_d(\mathbf{y}-\mathbf{y}^e) = \left(\begin{array}{c:c} \mathbf{I}_{l_1\times l_1} & \mathbf{0}_{l_1\times l_2} \\ \hdashline \mathbf{0}_{l_2\times l_1} & \mathbf{R}_{l_2\times l_2} \end{array}\right) \left(\begin{array}{c} \mathbf{0}_{l_1\times 1} \\ \hdashline \mathbf{d} \end{array}\right) = \begin{pmatrix} \mathbf{0}_{(m-1)\times 1} \\ r \end{pmatrix}, \tag{2.126}$$

where the rotation matrix $\mathbf{R}_{l_2\times l_2}$ has dimensions $l_2 \times l_2$ and its elements are given

by

$$R_{11} = -\sin(\theta_{l_2-1}), \tag{2.127a}$$

$$R_{i1} = R_{i-1\ 1}\cot(\theta_{l_2-i+1})\sin(\theta_{l_2-i}), \qquad (i = 2,\ldots,l_2-1), \tag{2.127b}$$

$$R_{l_2 1} = \prod_{j=1}^{l_2-1}\cos(\theta_j), \tag{2.127c}$$

$$R_{i2} = R_{i1}\tan(\theta_{l_2-1}), \qquad (i = 2,\ldots,l_2), \tag{2.127d}$$

$$R_{ij} = R_{i\ j-1}\frac{\tan(\theta_{l_2-j+1})}{\sin(\theta_{l_2-j+2})}, \qquad (j = 3,\ldots,i),\ (i = 3,\ldots,l_2), \tag{2.127e}$$

$$R_{i\ i+1} = \cos(\theta_{l_2-i}), \qquad (i = 1,\ldots,l_2-1), \tag{2.127f}$$

$$R_{ij} = 0, \qquad (j > i+1), \tag{2.127g}$$

with $\theta_i \in [-\pi/2, \pi/2]$, $i = 1,\ldots,l_2-2$, and $\theta_{l_2-1} \in [0, 2\pi]$. The vector on the extreme right hand side of Equation (2.126) is represented by $\mathbf{r} = \begin{pmatrix} \mathbf{0}_{(m-1)\times 1} \\ r \end{pmatrix}$ and is of length m. The vector $\mathbf{r}$ is composed of a null vector of length $m-1$ and an element r which is the radial distance from the chemical equilibrium state, $\mathbf{d} = \mathbf{0}$, in the parametric space. The rotation matrix $\mathbf{R}_{l_2\times l_2}$ depends on the l_2-1 polar angles, which are represented in a vector form as $\mathbf{\Theta} = (\theta_1,\ldots,\theta_{l_2-1})^T$. Each set of polar angles $\mathbf{\Theta}$ represents a direction within the parametric space along which a one-dimensional slice of the m_d-dimensional ILDM can be constructed by varying r and keeping $\mathbf{\Theta}$ fixed. A finite number of one-dimensional slices of the ILDM, in different directions, are constructed for uniformly discretized sets of values of the polar angles $\mathbf{\Theta}$. The parametric vector $\mathbf{d}$ is related to the polar parametric representation by the following functional form

$$\begin{aligned} d_1 &= r\prod_{i=1}^{l_2-1}\cos(\theta_i), \\ d_2 &= d_1\tan(\theta_{l_2-1}), \\ d_i &= d_{i-1}\frac{\tan(\theta_{l_2-i+1})}{\sin(\theta_{l_2-i+2})}, \qquad (i = 3,\ldots,l_2), \end{aligned} \tag{2.128}$$

which can be succinctly written as following

$$\mathbf{d} = \mathbf{p}_r(r, \mathbf{\Theta}), \tag{2.129}$$

with the vector function $\mathbf{p}_r$ being easily invertible. As in Equation (2.125), the ILDM can be represented by the following explicit functional form with polar parameterization

$$\mathbf{y} = \mathbf{f}_d(\mathbf{p}_r(r, \mathbf{\Theta})) = \mathbf{f}_r(r, \mathbf{\Theta}), \tag{2.130}$$

with the vector function $\mathbf{f}_d$ transformed to the vector function $\mathbf{f}_r$. However, Equation (2.130) is only an explicit representation of the actual implicit n algebraic equations in n unknowns which are to be solved for the construction of the ILDM, and are now given by

$$\mathbf{P}_r(\mathbf{y} - \mathbf{y}^e) = \mathbf{r}, \qquad (m \text{ parametric Equations}), \tag{2.131a}$$

$$\tilde{\mathbf{Z}}_f \mathbf{f}(\mathbf{y}) = \mathbf{0}, \qquad (n - m \text{ ILDM Equations}), \tag{2.131b}$$

where the matrix $\mathbf{P}_r = \left(\begin{array}{c:c} \mathbf{I}_{l_1 \times l_1} & \mathbf{0}_{l_1 \times l_2} \\ \hdashline \mathbf{0}_{l_2 \times l_1} & \mathbf{R}_{l_2 \times l_2} \end{array}\right) \mathbf{P}_d$ has dimensions $(L+2) \times (N+2)$ and has elements which are functions of the polar angles $\mathbf{\Theta}$. Equation (2.131) is used to compute one-dimensional slices of the ILDM by varying just one parameter r, the radial distance from the origin in the parametric space, and keeping the polar angles $\mathbf{\Theta}$ or the matrix $\mathbf{P}_r$ fixed. However, for each one-dimensional slice of the ILDM in a particular direction in the parametric space, the matrix $\mathbf{P}_r$ is changed as the rotation matrix $\mathbf{R}_{l_2 \times l_2}$ and the polar angles $\mathbf{\Theta}$ change.

2.4.4 Predictor corrector method of computing the ILDM

Equation (2.131) are solved in two steps, namely a predictor step and a corrector step. The chemical equilibrium state $\mathbf{y}^e$, which from now on is also represented by $\mathbf{y}_{c_0}$, lies on the m_d-dimensional ILDM. A sequence of points denoted by $\mathbf{y}_{c_k}$,

$(k = 0, 1, \ldots, K(\boldsymbol{\Theta}))$, are computed using Equation (2.131) along a one-dimensional slice of the m_d-dimensional ILDM, corresponding to a radial direction (with fixed polar angles $\boldsymbol{\Theta} = (\theta_1, \ldots, \theta_{l_2-1})^T$ and hence, fixed $\mathbf{R}_{l_2 \times l_2}$ and $\mathbf{P}_\mathbf{r}$) from the origin in the parametric space $\mathbb{R}^{l_2}$. Each point $\mathbf{y}_{c_k}$, on the ILDM slice, is at a radial distance of kr_p from the origin in the parametric space. The value of the integer $K(\boldsymbol{\Theta})$ is the number of points which can be computed along the one-dimensional slice of the ILDM, before it intersects the boundary of the physically accessible subspace, $\mathbb{S} \in \mathbb{R}^n$, defined in Equation (2.78). Hence, $K(\boldsymbol{\Theta})$ varies with $\boldsymbol{\Theta}$ as different one-dimensional slices of the ILDM may have different number of discrete points in $\mathbb{S}$. The discrete points on the one-dimensional ILDM slice are computed in a sequence, one after the other, starting from $k = 1$ until $k = K(\boldsymbol{\Theta})$, with $k = 0$ being the chemical equilibrium state which is already known.

A tangent predictor is used as a good initial guess for the corrector step. As discussed earlier and seen in Figure 2.3 the column vectors of the matrix $\mathbf{V}_s$ or the matrix $\mathbf{Z}_s$ approximate the local tangent space of the ILDM for a nonlinear $\mathbf{f}(\mathbf{y})$ in Equation (2.50). Before computing $\mathbf{y}_{c_k}$, a corresponding prediction $\mathbf{y}_{p_k}$ is evaluated along the the local tangent space at the previously computed $\mathbf{y}_{c_{k-1}}$. Hence, $\mathbf{y}_{p_k}$ should satisfy the following

$$\tilde{\mathbf{Z}}_{f_{k-1}}(\mathbf{y}_{p_k} - \mathbf{y}_{c_{k-1}}) = 0, \qquad (k = 1, \ldots, K(\boldsymbol{\Theta})), \tag{2.132}$$

with $\tilde{\mathbf{Z}}_{f_{k-1}}$ being the orthogonal complement of the approximate local tangent space $\mathbf{Z}_{s_{k-1}}$ at $\mathbf{y}_{c_{k-1}}$. Both, the predicted $\mathbf{y}_{p_k}$ and to be computed $\mathbf{y}_{c_k}$ should satisfy the parametric Equation (2.131a) and hence,

$$\mathbf{P}_r(\mathbf{y}_{p_k} - \mathbf{y}^e) = k\mathbf{r}_p, \qquad (k = 1, \ldots, K(\boldsymbol{\Theta})), \tag{2.133}$$

$$\mathbf{P}_r(\mathbf{y}_{c_k} - \mathbf{y}^e) = k\mathbf{r}_p, \qquad (k = 0, \ldots, K(\boldsymbol{\Theta})), \tag{2.134}$$

where $\mathbf{r}_p = \begin{pmatrix} \mathbf{0}_{m-1\times 1} \\ r_p \end{pmatrix}$, and both $\mathbf{y}_{p_k}$ and $\mathbf{y}_{c_k}$ correspond to a radial distance of kr_p from the origin in the parametric space. Equations (2.133) and (2.134) are combined to obtain the following recursive relation

$$\mathbf{P}_r(\mathbf{y}_{p_k} - \mathbf{y}_{c_{k-1}}) = \mathbf{r}_p, \qquad (k = 1, \ldots, K(\mathbf{\Theta})). \tag{2.135}$$

Following Maas [47] the following formulation for $\mathbf{y}_{p_k}$ will satisfy both Equations (2.132) and (2.135) on substitution

$$\mathbf{y}_{p_k} = \mathbf{y}_{c_{k-1}} + \mathbf{Z}_{s_{k-1}}[\mathbf{P}_r\mathbf{Z}_{s_{k-1}}]^{-1}\mathbf{r}_p, \qquad (k = 1, \ldots, K(\mathbf{\Theta})). \tag{2.136}$$

Finally, in the corrector step, the following equations

$$\mathbf{P}_r(\mathbf{y}_{c_k} - \mathbf{y}_{p_k}) = \mathbf{0}, \qquad (k = 1, \ldots, K(\mathbf{\Theta})), \tag{2.137a}$$

$$\tilde{\mathbf{Z}}_f\mathbf{f}(\mathbf{y}_{c_k}) = \mathbf{0}, \qquad (k = 1, \ldots, K(\mathbf{\Theta})), \tag{2.137b}$$

are solved for $\mathbf{y}_{c_k}$ using Newton's method with $\mathbf{y}_{p_k}$ being the initial guess. Equations (2.133) and (2.134) are again used to obtain Equation (2.137a). A damped Newton's method [49] is used as it is suitable for the numerical solution of the highly nonlinear algebraic equations (2.137).

The corrector step can also be performed by integrating the pseudo-transient ODEs [1] given by

$$\mathbf{P}_r\frac{d\mathbf{y}_{c_k}}{d\zeta} = \mathbf{0}, \qquad (k = 1, \ldots, K(\mathbf{\Theta})), \tag{2.138a}$$

$$\tilde{\mathbf{Z}}_f\frac{d\mathbf{y}_{c_k}}{d\zeta} = \tilde{\mathbf{Z}}_f\mathbf{f}(\mathbf{y}_{c_k}), \qquad (k = 1, \ldots, K(\mathbf{\Theta})), \tag{2.138b}$$

$$\mathbf{y}_{c_k}|_{\zeta=0} = \mathbf{y}_{p_k}, \qquad (k = 1, \ldots, K(\mathbf{\Theta})). \tag{2.138c}$$

Equation (2.138a) is obtained by differentiating Equation (2.137a) with respect to the pseudo-time variable ζ, with $\mathbf{y}_{p_k}$ being constant for the corrector step and $\mathbf{P}_r$

being constant for a particular one-dimensional slice of the ILDM. Equation (2.138b) is obtained by multiplying Equation (2.50) with the matrix $\tilde{\mathbf{Z}}_f$ and replacing the time variable by ζ. The initial condition used for the dependent variable $\mathbf{y}_{c_k}$ is $\mathbf{y}_{p_k}$, when integrating the pseudo-transient ODEs in the corrector step, as shown in Equation (2.138c). Equation (2.138) is then rewritten as following

$$\frac{d\mathbf{y}_{c_k}}{d\zeta} = \begin{pmatrix} \mathbf{P}_r \\ \tilde{\mathbf{Z}}_f \end{pmatrix}^{-1} \begin{pmatrix} \mathbf{0} \\ \tilde{\mathbf{Z}}_f \mathbf{f}(\mathbf{y}_{c_k}) \end{pmatrix}, \ \mathbf{y}_{c_k}|_{\zeta=0} = \mathbf{y}_{p_k}, \ (k = 1, \ldots, K(\mathbf{\Theta})), \quad (2.139)$$

and integrated using a backward difference formula (BDF) method of LSODE, [50] until steady state is achieved. The steady state solution for Equation (2.138) or (2.139) is same as the solution for Equation (2.137).

Sometimes the corrector step may not converge if r_p, the radial distance in the parametric space between consecutive points on the one-dimensional ILDM slice is too large, as it may result in a predicted $\mathbf{y}_{p_k}$ which is too far, in the phase space, from the corrected solution $\mathbf{y}_{c_k}$. In that case r_p should be reduced. Sometimes the corrector step may not converge because the ILDM does not exist in certain regions of the phase space where $\lambda(m) = \lambda(m+1)$ or $\lambda(m) \sim \lambda(m+1)$ or $\lambda(m)$ and $\lambda(m+1)$ become a complex conjugate pair, as discussed earlier in this chapter. In practice it was found that the corrector step converged more often when using Equation (2.139) than when using Equation (2.137).

The sequence of points $\mathbf{y}_{c_k}$, $(k = 1, \ldots, K(\mathbf{\Theta}))$, are computed by using the recursive Equation (2.136), in the predictor step, followed by a numerical solution of Equation (2.137), in the corrector step. Computation of each one-dimensional slice is initiated from the chemical equilibrium state $\mathbf{y}_{c_0} = \mathbf{y}^e$. Thus, a one-dimensional slice of the ILDM is constructed in the phase space corresponding to a fixed direction in the parametric space given by fixed $\mathbf{\Theta}$ and $\mathbf{P}_r$. The global ILDM is constructed in the phase space by computation of several one-dimensional ILDM slices for varying

$\mathbf{\Theta}$ and $\mathbf{P}_r$. Finally, the ILDM is stored as an l_2-dimensional table in a discrete form of the Equation (2.130) for discrete values of r and $\mathbf{\Theta}$. A multivariate linear interpolation is used for the intermediate values of r and $\mathbf{\Theta}$ which are not available in the discrete ILDM table. Some more details regarding the ILDM construction and the associated table will be given with respect to specific examples in the next section of this chapter. A FORTRAN code, based on the steps described in this chapter, was developed for construction of the ILDM for the dynamical system modeling the CASHPR.

2.5 Examples

In this section several examples for computation of the ILDM are given. The ILDMs are computed for various reaction mechanisms which govern the reactive processes within the CASHPR. Some of the peculiar cases encountered while constructing these ILDMs are demonstrated and discussed.

2.5.1 Ozone decomposition reaction mechanism

The ozone decomposition reaction mechanism is considered in the isobaric CASHPR. This reaction mechanism involves $N = 3$ species, $L = 1$ element, and $J = 14$ elementary reaction steps as depicted in Table A.1. The initial species mass fractions are taken to be $Y_{O_0} = 0.0$, $Y_{O_{2_0}} = 0.3333$, and $Y_{O_{3_0}} = 0.6667$, and hence, using Equation (2.10), the initial element mass fraction is given by $\hat{Y}_{O_0} = 1$, which remains constant. Note that the indices in the species and element mass fraction variables have been replaced by the respective symbols of the species and elements. The initial temperature and pressure is given by $T_0 = 300$ K and $p_0 = 0.832\times10^6$ dynes cm^{-2}, respectively. Since, the isobaric CASHPR is considered, the pressure and mixture enthalpy per unit mass remain constant (see Section 2.1.2). The constant mixture enthalpy per unit mass is obtained from the initial conditions

and is given by $h_0 = 0.9926 \times 10^{10}$ ergs g^{-1}. The highest dimensional ILDM, which is the complete physically accessible subspace of the phase space, has a dimensionality of $N - L = 2$, and it is given by

$$\mathbb{S} = \left\{ \mathbf{y} \in \mathbb{R}^n \;\middle|\; \begin{array}{l} p = p_0 > 0 \\ T > 0 \\ 0 \leq Y_O,\, Y_{O_2},\, Y_{O_3} \leq 1 \\ Y_O + Y_{O_2} + Y_{O_3} = 1 \\ h_O(T)Y_O + h_{O_2}(T)Y_{O_2} + h_{O_3}(T)Y_{O_3} = h = h_0 \end{array} \right\}, \tag{2.140}$$

where $\mathbf{y} = (h, p, Y_O, Y_{O_2}, Y_{O_3})^T$, $n = 5$, and the indices of the variables representing the species enthalpy per unit mass as a function of temperature have been replaced by the symbol of the respective species. The initial state of the reactive mixture can be represented by $\mathbf{y}_0 = (0.9926 \times 10^{10}, 0.832 \times 10^6, 0.0, 0.6667, 0.3333)^T$. The conserved quantities in the CASHPR can be represented by $\bar{\mathbf{y}} = (\hat{Y}_{O_0}, p_0, h_0)^T = (1, 0.832 \times 10^6, 0.9926 \times 10^{10})^T$. The species mass fractions and temperature at the chemical equilibrium state for the initial condition $\mathbf{y}_0$ are computed and given by $Y_O^e = 0.47041160501582 \times 10^{-7}$, $Y_{O_2}^e = 0.99999995256694$, $Y_{O_3}^e = 0.39191130110168 \times 10^{-9}$, and $T^e = 1255.68\, K$, respectively. Hence, the chemical equilibrium state which is the zero-dimensional ILDM, $\mathbb{M}_0$, can be represented by $\mathbf{y}^e = (0.9926 \times 10^{10}, 0.832 \times 10^6, 0.47041160501582 \times 10^{-7}, 0.99999995256694, 0.39191130110168 \times 10^{-9})^T$. The corresponding conserved parameters vector for the chemical equilibrium state is given by $\mathbf{\Psi}^e = (0, 0, 0)^T$, assuming that the range of the conserved quantities p and h, for any future computations of the ILDM, is given by $p \in [p_{min}, p_{max}] = [0.832 \times 10^6, 1.832 \times 10^6]$ dynes cm^{-2}, and $h \in [h_{min}, h_{max}] = [0.9926 \times 10^{10}, 1.9926 \times 10^{10}]$ ergs g^{-1}. Note that $\mathbf{\Psi}_0 = \mathbf{\Psi}^e$, where $\mathbf{\Psi}_0$ is the conserved parameters vector for the initial condition $\mathbf{y}_0$.

An $m_d = 1$-dimensional ILDM is computed in the $n = N + 2 = 5$-dimensional

phase space for a fixed set of values of the conserved quantities. Hence, $m = m_d + L + 2 = 4$ $(m < n)$, determines the segregation of the slow and fast time scales. A series of points are computed on the one-dimensional ILDM by using the predictor corrector steps in Equations (2.136-2.137). In this case there are four linear parametric equations (2.137a) and one nonlinear ILDM equation (2.137b). The one-dimensional ILDM is computed on either side of the chemical equilibrium state until it intersects the boundary of the physically accessible subspace $\mathbb{S}$ of the phase space. The parametric matrix $\mathbf{P}_r$ has dimensions 4×5, and for the one-dimensional ILDM with a fixed set of values of the conserved quantities, it is given by

$$\mathbf{P}_r = \mathbf{P}_d = \begin{pmatrix} \mathbf{P}_z \\ \mathbf{P}_s \end{pmatrix}, \tag{2.141}$$

where the matrix $\mathbf{P}_z$ has dimensions 3×5, and is given by

$$\mathbf{P}_z = \begin{pmatrix} 0 & 0 & 1 & 1 & 1 \\ 0 & \frac{1}{p_{max}-p_{min}} & 0 & 0 & 0 \\ \frac{1}{h_{max}-h_{min}} & 0 & 0 & 0 & 0 \end{pmatrix}, \tag{2.142}$$

while the user specified parametric matrix $\mathbf{P}_s$ has dimensions 1×5, and is given by

$$\mathbf{P}_s = \begin{pmatrix} 0 & 0 & 0 & 1 & 0 \end{pmatrix}, \tag{2.143}$$

as the one-dimensional ILDM is chosen to be parameterized by Y_{O_2}. Finally, for the one-dimensional ILDM with a fixed set of values of the conserved quantities, the vector $\mathbf{r}_p$ is given by

$$k\mathbf{r}_p = \begin{pmatrix} 0 \\ 0 \\ 0 \\ kr_p \end{pmatrix} = \begin{pmatrix} 0 \\ 0 \\ 0 \\ d_1 \end{pmatrix} = \begin{pmatrix} 0 \\ \psi_2 - \psi_2^e \\ \psi_3 - \psi_3^e \\ s_1 - s_1^e \end{pmatrix} = \begin{pmatrix} 0 \\ 0 \\ 0 \\ Y_{O_2} - Y_{O_2}^e \end{pmatrix} = k \begin{pmatrix} 0 \\ 0 \\ 0 \\ 1 \times 10^{-3} \end{pmatrix}. \tag{2.144}$$

Hence, $l_1 = 3$, and $l_2 = m - l_1 = 1$, where l_2 is the dimension of the parametric space associated with the ILDM.

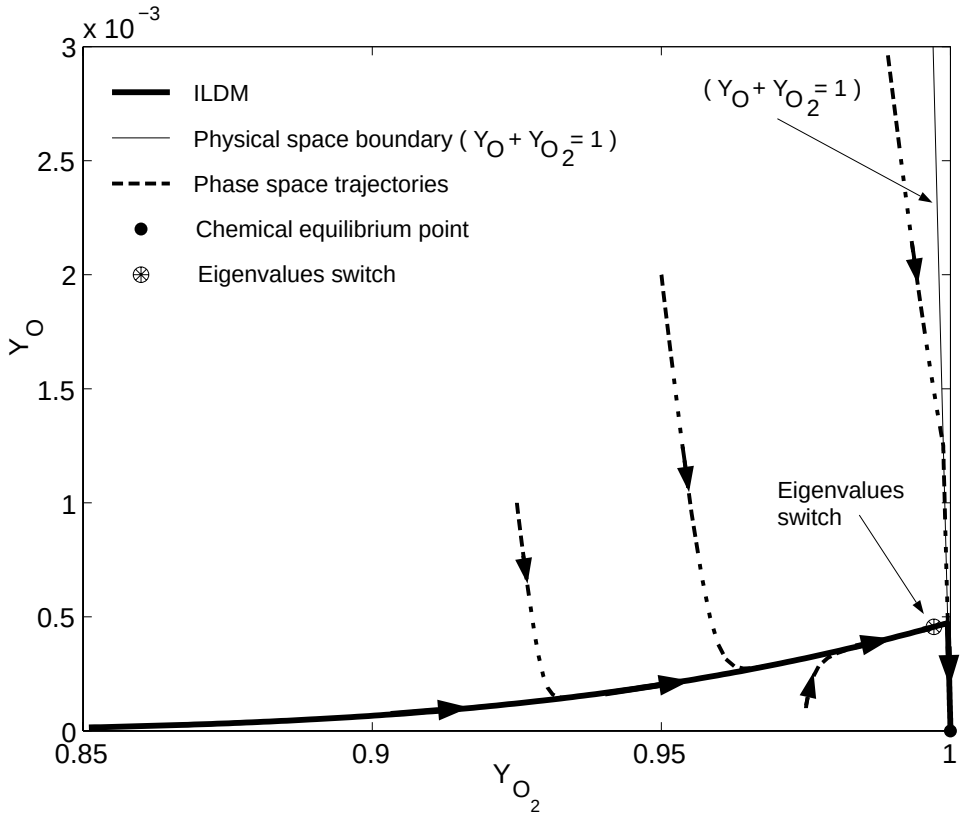

Figure 2.4. One-dimensional ILDM with fixed conserved quantities for ozone decomposition in the isobaric CASHPR for a reactive mixture of composition $Y_{O_0} = 0$, $Y_{O_{20}} = 0.6667$, $Y_{O_{30}} = 0.3333$ at a temperature $T_0 = 300$ K and pressure $p_0 = 0.832 \times 10^6$ dynes cm^{-2}.

Figure 2.4 depicts a projection of the one-dimensional ILDM, which exists in the $n = 5$-dimensional phase space. Also plotted are the phase space trajectories which relax to the ILDM and then move close to it until they reach the chemical equilibrium state. The phase space trajectories have been plotted for different initial conditions. However, the conserved parameters vector $\mathbf{\Psi}$ associated with all the initial conditions is equal to $\mathbf{\Psi}^e$ associated with the chemical equilibrium state $\mathbf{y}^e$ or $\mathbf{\Psi}_0$ associated with the original initial condition $\mathbf{y}_0$. Also plotted is one of the

boundaries of the physically accessible subspace $\mathbb{S}$ given by $Y_O + Y_{O_2} = 1$. A peculiar behavior of both the phase space trajectories and the ILDM, as seen in Figure 2.4, is that when they both reach the boundary, they move close to it until they reach the chemical equilibrium state, which also lies very close to the boundary. Hence, it is verified that the nonlinear dynamical system modeling the CASHPR is defined in such a way that it never leaves the physically accessible subspace $\mathbb{S}$. In this case the boundary defined by $Y_O + Y_{O_2} = 1$ also acts as a low dimensional manifold. The one-dimensional ILDM does not exist in that region of the phase space where the eigenvalues $\lambda_{(4)}$ and $\lambda_{(5)}$ ($m = 4$ for this case) have approximately equal values. The eigenvalue $\lambda_{(4)}$ switches from the slow set of eigenvalues to the fast set of eigenvalues, while the eigenvalue $\lambda_{(5)}$ switches from the fast set of eigenvalues to the slow set of eigenvalues, across this region of the phase space. A solution for Equation (2.137) fails to converge in this region of eigenvalue switch depicted in Figure 2.4. The two branches of the ILDM on either side of this region have been simply connected by the path taken by the phase space trajectories. There are $n - (L + 2) = 2$ nonzero eigenvalues for this system. The eigenvalue, $\lambda_{(5)}$, associated with the fast time scale, always has a negative real part along the ILDM, which is necessary for the ILDM to be attractive. However, the other nonzero eigenvalue, which is associated with the slow time scale, has a positive real part along the ILDM for $Y_{O_2} < 0.96$ approximately, while it has a negative real part along the ILDM otherwise. Once the ILDM has been computed, the species mass fractions and temperature along the ILDM are tabulated in the following functional forms

$$Y_i = Y(Y_{O_2}), \qquad (i = 1, \ldots, 3), \tag{2.145a}$$

$$T = T(Y_{O_2}), \tag{2.145b}$$

for discrete values of Y_{O_2}, which is the reference variable for the ILDM table. The

domain $\mathbb{D} = \{Y_{O_2} \in \mathbb{R} | 0 \leq Y_{O_2} \leq 1\}$ in the parametric space is mapped onto the one-dimensional ILDM in the phase space using Equation (2.145) (see Equation (2.125)). The ILDM table is single valued with respect to the reference variable Y_{O_2}, which is the major product species.

2.5.2 Syngas combustion reaction mechanism

The syngas combustion reaction mechanism is considered in the isobaric CASHPR. This reaction mechanism involves $N = 13$ species, $L = 4$ elements, and $J = 67$ elementary reaction steps as depicted in Table A.2. A syngas fuel mixture A of composition $Y_{CO}^A = 0.4517$, $Y_{H_2}^A = 0.03$, $Y_{N_2}^A = 0.5543$, with the remaining 10 species mass fractions being zero, reacts with an oxidizer mixture B of composition $Y_{O_2}^B = 0.2329$, $Y_{N_2}^B = 0.7671$, with the remaining 11 species mass fractions being zero. The reaction between the mixtures A and B is considered for two mixture fractions of $\chi = 0.70, 0.75$ at initial temperature and pressure of $T_0 = 298$ K and $p_0 = 1 \times 10^6$ dynes cm^{-2}, respectively. The element mass fractions, mixture fraction, pressure, and mixture enthalpy per unit mass remain constant in the isobaric CASHPR. The initial state of the reactive mixture for a certain mixture fraction is given by $\mathbf{y}_0 = (h_0, p_0, Y_{1_0}, \ldots, Y_{N_0})^T = (h^A + \chi(h^B - h^A), p_0, Y_1^A + \chi(Y_1^B - Y_1^A), \ldots, Y_N^A + \chi(Y_N^B - Y_N^A))^T$. The conserved quantities in the isobaric CASHPR for a certain mixture fraction are given by $\bar{\mathbf{y}} = (\hat{Y}_{1_0}, \ldots, \hat{Y}_{L_0}, p_0, h_0)^T = (\hat{Y}_1^A + \chi(\hat{Y}_1^B - \hat{Y}_1^A), \ldots, \hat{Y}_L^A + \chi(\hat{Y}_L^B - \hat{Y}_L^A), p_0, h^A + \chi(h^B - h^A))^T$. For $\chi = 0.75$, $Y_{CO_0} = 0.13858$, $Y_{H_{2_0}} = 7.48809 \times 10^{-3}$, $Y_{O_{2_0}} = 0.17474$, $Y_{N_{2_0}} = 0.67918$, with the remaining initial species mass fractions being zero, and $\hat{Y}_{H_0} = 0.74881 \times 10^{-2}$, $\hat{Y}_{C_0} = 0.59425 \times 10^{-1}$, $\hat{Y}_{O_0} = 0.25390$, $\hat{Y}_{N_0} = 0.67918$, and $h_0 = -0.54704 \times 10^{10}$ ergs g^{-1}. For $\chi = 0.70$, $Y_{CO_0} = 0.16630$, $Y_{H_{2_0}} = 8.98571 \times 10^{-3}$, $Y_{O_{2_0}} = 0.16310$, $Y_{N_{2_0}} = 0.66162$, with the remaining initial species mass fractions being zero, and

$\hat{Y}_{H_0} = 0.89857 \times 10^{-2}$, $\hat{Y}_{C_0} = 0.71310 \times 10^{-1}$, $\hat{Y}_{O_0} = 0.25808$, and $\hat{Y}_{N_0} = 0.66162$, and $h_0 = -0.65641 \times 10^{10}$ ergs g^{-1}. To initiate the ILDM computation, the chemical equilibrium state $\mathbf{y}^e$ is computed for each mixture fraction with $\chi^e = \chi_0 = 0.70, 0.75$.

An $m_d = 1$-dimensional ILDM is constructed in the $n = N + 2 = 15$-dimensional phase space for each mixture fraction. Hence, $m = m_d + L + 2 = 7$, determines the segregation of the slow and fast time scales. A series of points are computed on the one-dimensional ILDM by using the predictor corrector steps in Equations (2.136-2.137). In this case there are seven linear parametric equations (2.137a) and eight nonlinear ILDM equation (2.137b). The one-dimensional ILDM is computed on either side of the chemical equilibrium state until it intersects the boundary of the physically accessible subspace $\mathbb{S}$ of the phase space. The parametric matrix $\mathbf{P}_r$ has dimensions 7×15, and for the one-dimensional ILDM with a fixed mixture fraction, it is given by

$$\mathbf{P}_r = \mathbf{P}_d = \begin{pmatrix} \mathbf{P}_\chi^{(2)} \\ \mathbf{P}_s \end{pmatrix}, \tag{2.146}$$

where the matrix $\mathbf{P}_\chi^{(2)}$ has dimensions 6×15. Due to the large size of the matrix $\mathbf{P}_\chi^{(2)}$ all its elements are not listed here. The user specified parametric matrix $\mathbf{P}_s$ has dimensions 1×15, and is given by

$$\mathbf{P}_s = \begin{pmatrix} \mathbf{0}_{1\times 7} & 1 & \mathbf{0}_{1\times 7} \end{pmatrix}, \tag{2.147}$$

as the one-dimensional ILDM is chosen to be parameterized by Y_{CO_2}. Finally, for the one-dimensional ILDM with a fixed mixture fraction, the vector $\mathbf{r}_p$ is given by

$$k\mathbf{r}_p = \begin{pmatrix} \mathbf{0}_{6\times 1} \\ kr_p \end{pmatrix} = \begin{pmatrix} \mathbf{0}_{6\times 1} \\ d_1 \end{pmatrix} = \begin{pmatrix} \mathbf{0}_{4\times 1} \\ \chi - \chi^e \\ \psi_5 - \psi_5^e \\ s_1 - s_1^e \end{pmatrix} = \begin{pmatrix} \mathbf{0}_{6\times 1} \\ Y_{CO_2} - Y_{CO_2}^e \end{pmatrix} = k \begin{pmatrix} \mathbf{0}_{6\times 1} \\ 1 \times 10^{-3} \end{pmatrix}. \tag{2.148}$$

Hence, $l_1 = 6$, and $l_2 = m - l_1 = 1$, where l_2 is the dimension of the parametric space associated with the ILDM.

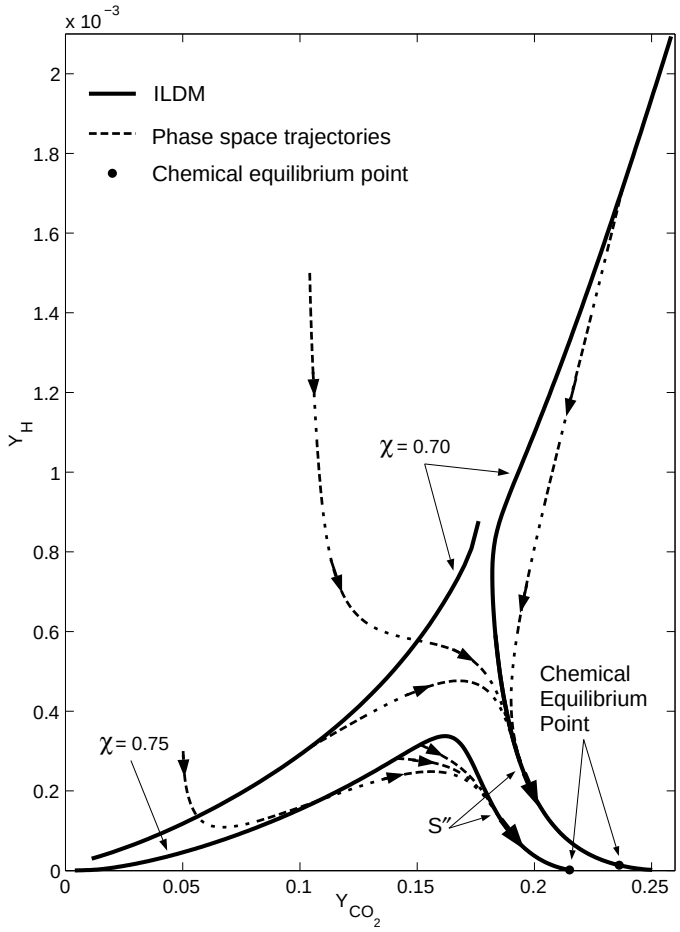

Figure 2.5. One-dimensional ILDM for combustion of a syngas fuel mixture A (Y^A_{CO} / $Y^A_{H_2}$ / $Y^A_{N_2} = 0.4517$ / 0.0300 / 0.5543) reacting with an oxidizer mixture B ($Y^B_{O_2}/Y^B_{N_2} = 0.2329/0.7671$), for mixture fractions of $\chi = 0.70, 0.75$, in the isobaric CASHPR at temperature $T_0 = 298$ K and pressure $p_0 = 1 \times 10^6$ dynes cm^{-2}.

Figure 2.5 depicts a projection of the one-dimensional ILDM, which exists in the $n = 15$-dimensional phase space, for mixture fractions of 0.70 and 0.75. Also plotted are the phase space trajectories which relax to the ILDM and then move close to it until they reach the chemical equilibrium state. For $\chi = 0.70$, the one-dimensional ILDM has two branches. The split occurs when $\frac{\lambda_{(7)}}{\lambda_{(8)}} \sim 1$. For one branch, the matrix $\mathbf{P}_s$ given in Equation (2.147) and the vector $\mathbf{r}_p$ given in Equation (2.148) are used.

For the other branch, $\mathbf{P}_s = (\mathbf{0}_{1\times 9}, 1, \mathbf{0}_{1\times 5})$, with the ILDM parameterized by Y_H, and $k\mathbf{r}_p = (\mathbf{0}_{1\times 6}, Y_H - Y_H^e)^T = k(\mathbf{0}_{1\times 6}, 1\times 10^{-5})^T$ are used. It is found that not all of the one-dimensional ILDM approximates the SIM well. It can be seen from Figure 2.5 that the phase space trajectories relax only to a subset, $\mathbb{S}''$, of the ILDM close to the chemical equilibrium state. On this attractive subset $\mathbb{S}''$ of the ILDM $\frac{\lambda_{(8)}}{\lambda_{(7)}} > 3$ approximately, and both $\lambda_{(7)}$ and $\lambda_{(8)}$ have negative real parts. Even if the phase space trajectories start exactly from other parts of the one-dimensional ILDM not in $\mathbb{S}''$, they do not stay close to the ILDM until they reach $\mathbb{S}''$. Hence, parts of the ILDM far from the chemical equilibrium state do not have an approximate invariant property as does $\mathbb{S}''$. Hence, only the attractive subset, $\mathbb{S}''$, of the ILDM is useful and should be computed and stored as a table. Similar behavior is depicted for the one-dimensional ILDM for $\chi = 0.75$. However, for $\chi = 0.75$, the ILDM is not discontinuous, and it does not split into two branches. All the species mass fractions and temperature along the subset $\mathbb{S}''$ of the one-dimensional ILDM are tabulated in the following functional form

$$Y_i = Y(Y_{CO_2}), \qquad (i = 1, \ldots, 13), \tag{2.149a}$$

$$T = T(Y_{CO_2}), \tag{2.149b}$$

for discrete values of Y_{CO_2}, which is the reference variable for the ILDM table. The domains $\mathbb{D} = \{Y_{CO_2} \in \mathbb{R} | 0.19 \leq Y_{CO_2} \leq 0.25\}$ for $\chi = 0.70$, and $\mathbb{D} = \{Y_{CO_2} \in \mathbb{R} | 0.17 \leq Y_{CO_2} \leq 0.21\}$ for $\chi = 0.75$, in the parametric space are mapped onto the subset $\mathbb{S}''$ of the respective one-dimensional ILDMs in the phase space using Equation (2.149). The ILDM table is single valued with respect to the reference variable Y_{CO_2} for the subset $\mathbb{S}''$ of the one-dimensional ILDM.

An $m_d = 2$-dimensional ILDM is constructed in the $n = N + 2 = 15$-dimensional phase space for $\chi = 0.70$. Hence, $m = m_d + L + 2 = 8$. Discrete points on

the two-dimensional ILDM are computed in the polar parametric space using the predictor corrector steps in Equations (2.136-2.137). In this case there are eight linear parametric equations (2.137a) and seven nonlinear ILDM equations (2.137b). The parametric matrix $\mathbf{P}_r$ has dimensions 8×15, and for the two-dimensional ILDM with a fixed mixture fraction, it is given by

$$\mathbf{P}_r = \left(\begin{array}{c:c} \mathbf{I}_{6\times6} & \mathbf{0}_{6\times2} \\ \hdashline \mathbf{0}_{2\times6} & \mathbf{R}_{2\times2} \end{array}\right) \mathbf{P}_d = \left(\begin{array}{c:c} \mathbf{I}_{6\times6} & \mathbf{0}_{6\times2} \\ \hdashline \mathbf{0}_{2\times6} & \mathbf{R}_{2\times2} \end{array}\right) \begin{pmatrix} \mathbf{P}_\chi^{(2)} \\ \mathbf{P}_s \end{pmatrix}, \tag{2.150}$$

where the matrix $\mathbf{P}_\chi^{(2)}$ has dimensions 6×15, $\mathbf{R}_{2\times2} = \begin{pmatrix} -\sin(\theta_1) & \cos(\theta_1) \\ \cos(\theta_1) & \sin(\theta_1) \end{pmatrix}$ is a two-dimensional rotation matrix, and the user specified parametric matrix $\mathbf{P}_s$ has dimensions 2×15, and its two rows can be represented by

$$\mathbf{P}_s = \begin{pmatrix} \mathbf{0}_{1\times6} & 1 & \mathbf{0}_{1\times8} \\ \mathbf{0}_{1\times7} & 1 & \mathbf{0}_{1\times7} \end{pmatrix}, \tag{2.151}$$

as the two-dimensional ILDM is chosen to be parameterized by Y_{H_2O} and Y_{CO_2}. Finally, for the two-dimensional ILDM with a fixed mixture fraction, the vector $\mathbf{r}_p$ is given by

$$k\mathbf{r}_p = \begin{pmatrix} \mathbf{0}_{7\times1} \\ kr_p \end{pmatrix} = \left(\begin{array}{c:c} \mathbf{I}_{6\times6} & \mathbf{0}_{6\times2} \\ \hdashline \mathbf{0}_{2\times6} & \mathbf{R}_{2\times2} \end{array}\right) \begin{pmatrix} \mathbf{0}_{6\times1} \\ d_1 \\ d_2 \end{pmatrix} = k \begin{pmatrix} \mathbf{0}_{7\times1} \\ 1\times10^{-3} \end{pmatrix}, \tag{2.152}$$

where

$$\begin{pmatrix} \mathbf{0}_{6\times1} \\ d_1 \\ d_2 \end{pmatrix} = \begin{pmatrix} \mathbf{0}_{4\times1} \\ \chi - \chi^e \\ \psi_5 - \psi_5^e \\ s_1 - s_1^e \\ s_2 - s_2^e \end{pmatrix} = \begin{pmatrix} \mathbf{0}_{6\times1} \\ Y_{H_2O} - Y_{H_2O}^e \\ Y_{CO_2} - Y_{CO_2}^e \end{pmatrix}. \tag{2.153}$$

Hence, $l_1 = 6$, and $l_2 = m - l_1 = 2$, where l_2 is the dimension of the parametric space associated with the ILDM.

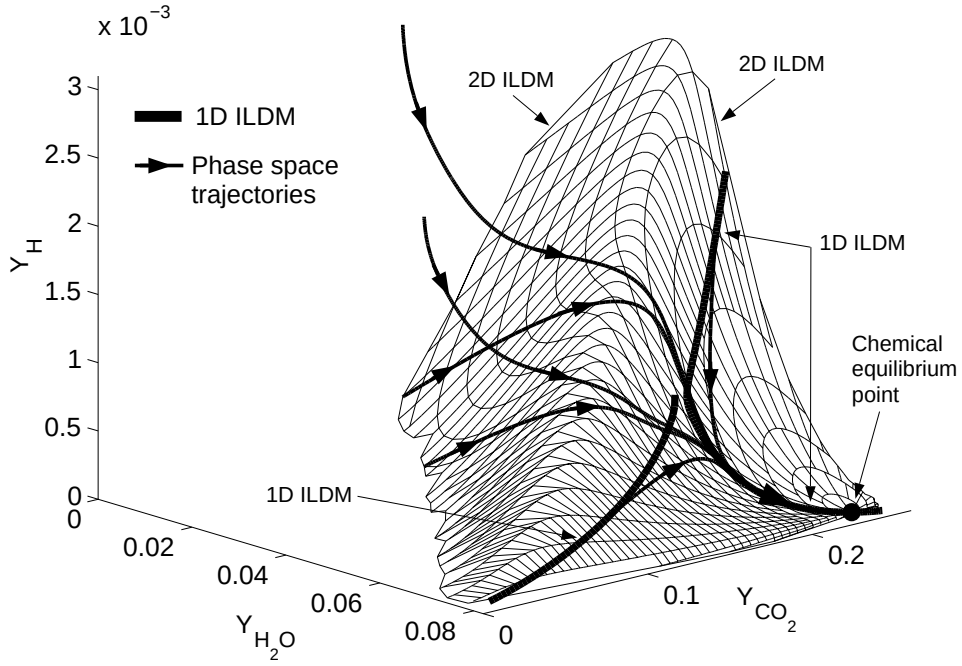

Figure 2.6. Two-dimensional ILDM for combustion of a syngas fuel mixture A (Y^A_{CO} / $Y^A_{H_2}$ / $Y^A_{N_2}$ = 0.4517 / 0.0300 / 0.5543) reacting with an oxidizer mixture B ($Y^B_{O_2}/Y^B_{N_2}$ = 0.2329/0.7671), for a mixture fraction of $\chi = 0.70$, in the isobaric CASHPR at temperature $T_0 = 298$ K and pressure $p_0 = 1 \times 10^6$ dynes cm^{-2}.

Figure 2.6 depicts a projection of the two-dimensional ILDM, which exists in the $n = 15$-dimensional phase space, for a mixture fraction of 0.70. Also plotted are the phase space trajectories which relax to the two-dimensional ILDM and then move close to it until they relax to the one-dimensional ILDM and then move close to it until they reach the chemical equilibrium state. It can be seen from Figure 2.6 that the one-dimensional ILDM lies completely within the two-dimensional ILDM subspace. Figure 2.7 depicts the polar parametric space associated with the two-dimensional ILDM. Note that all the points computed on the two-dimensional ILDM are not depicted in Figures 2.6 and 2.7 for plotting purposes, as they get too cluttered

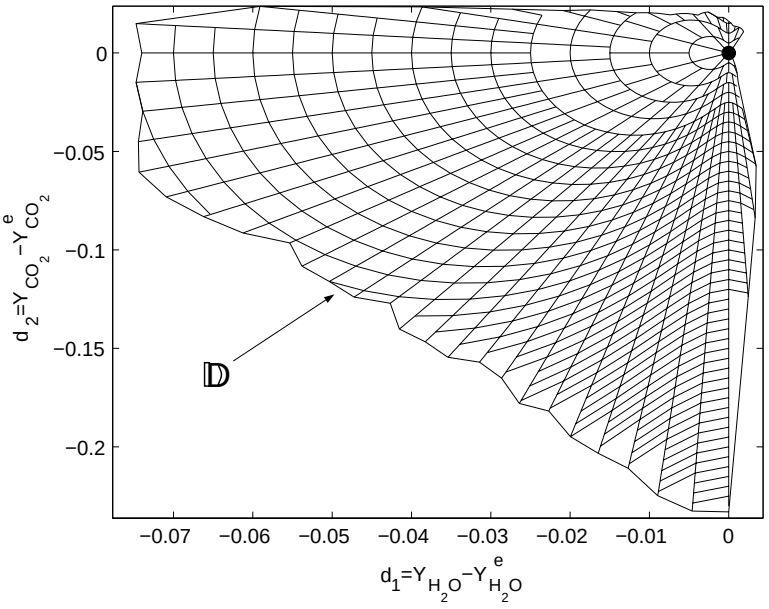

Figure 2.7. Parametric space associated with the two-dimensional ILDM in Figure 2.6 for syngas combustion.

near the chemical equilibrium point for the polar grid system. The species mass fractions and temperature are tabulated along the two-dimensional ILDM in the following functional forms

$$Y_i = Y(r, \theta_1), \qquad (i = 1, \ldots, 13), \tag{2.154a}$$

$$T = T(r, \theta_1), \tag{2.154b}$$

for discrete values of r and θ_1, which are given by

$$d_1 = Y_{H_2O} - Y^e_{H_2O} = r\cos(\theta_1), \tag{2.155a}$$

$$d_2 = Y_{CO_2} - Y^e_{CO_2} = r\sin(\theta_1). \tag{2.155b}$$

The domain $\mathbb{D}$ in the parametric space depicted in Figure 2.7 is mapped onto the two-dimensional ILDM in the phase space using Equation (2.154). Note that the chemical equilibrium state lies at the origin of the parametric space. The boundary of the two-dimensional ILDM and the domain $\mathbb{D}$ is not computed exactly, and hence,

appears to be crude. As soon as a point on the two-dimensional ILDM outside the boundary of the physically accessible subspace $\mathbb{S}$ is computed in a certain radial direction, the computation of the ILDM in that radial direction is terminated. The ILDM table is single valued with respect to the reference variables Y_{H_2O} and Y_{CO_2}, which are the major product species.

2.5.3 $H_2/O_2/Ar$ reaction mechanism

The $H_2/O_2/Ar$ reaction mechanism is considered in the isochoric CASHPR. This reaction mechanism involves $N = 9$ species, $L = 3$ elements, and $J = 37$ elementary reaction steps as depicted in Table A.3. The initial species mass fractions are taken to be $Y_{H_{2_0}} = 0.01277$, $Y_{O_{2_0}} = 0.10137$, and $Y_{Ar_0} = 0.88586$, with the remaining six initial species mass fractions being zero, and hence, using Equation (2.10), the initial element mass fractions are given by $\hat{Y}_{H_0} = 0.01277$, $\hat{Y}_{O_0} = 0.10137$, and $\hat{Y}_{Ar_0} = 0.88586$, which remain constant. Since, the isochoric CASHPR is considered, the mixture density and internal energy per unit mass remain constant (see Section 2.1.1). The reactions inside the isochoric CASHPR are considered at a constant mixture density of $\rho_0 = 0.5 \times 10^{-3}$ g cm^{-3}, and at a constant mixture internal energy per unit mass of $e_0 = 8 \times 10^9$ ergs g^{-1}. The initial state of the reactive mixture can be represented by $\mathbf{y}_0 = (e_0, \rho_0, Y_{1_0}, \ldots, Y_{N_0})^T = (8 \times 10^9, 0.5 \times 10^{-3}, 0, 0, 0.01277, 0.10137, 0, 0, 0, 0, 0.88586)^T$. The conserved quantities in the isochoric CASHPR can be represented by $\bar{\mathbf{y}} = (\hat{Y}_{1_0}, \ldots, \hat{Y}_{L_0}, \rho_0, e_0)^T = (0.01277, 0.10137, 0.88586, 0.5 \times 10^{-3}, 8 \times 10^9)^T$. The conserved parameters vector for the initial state is represented by $\mathbf{\Psi}_0 = (0, 0.10137, 0.88586, 0.33333, 0.77778)^T$, assuming that the ranges for the conserved quantities ρ and e, for any future computations of the ILDM, are given by $\rho \in [\rho_{min}, \rho_{max}] = [0.25 \times 10^{-3}, 1 \times 10^{-3}]$ g cm^{-1}, and $e \in [e_{min}, e_{max}] = [1 \times 10^9, 10 \times 10^9]$ ergs g^{-1}. To initiate

the computation of the ILDM, the chemical equilibrium state $\mathbf{y}^e$ is computed, with $\mathbf{\Psi}^e = \mathbf{\Psi}_0$.

An $m_d = 1$-dimensional ILDM is computed in the $n = N + 2 = 11$-dimensional phase space for a fixed set of values of the conserved quantities. Hence, $m = m_d + L + 2 = 6$ $(m < n)$, determines the segregation of the slow and fast time scales. A series of points are computed on the one-dimensional ILDM by using the predictor corrector steps in Equations (2.136-2.137). In this case there are six linear parametric equations (2.137a) and five nonlinear ILDM equation (2.137b). The parametric matrix $\mathbf{P}_r$ has dimensions 6×11, and for the one-dimensional ILDM with a fixed set of values of the conserved quantities, it is given by

$$\mathbf{P}_r = \mathbf{P}_d = \begin{pmatrix} \mathbf{P}_z \\ \mathbf{P}_s \end{pmatrix}, \tag{2.156}$$

where the matrix $\mathbf{P}_z$ has dimensions 5×11, while the user specified parametric matrix $\mathbf{P}_s$ has dimensions 1×11, and is given by

$$\mathbf{P}_s = \begin{pmatrix} \mathbf{0}_{1\times 7} & 1 & \mathbf{0}_{1\times 3} \end{pmatrix}, \tag{2.157}$$

as the one-dimensional ILDM is chosen to be parameterized by Y_{H_2O}. Finally, for the one-dimensional ILDM with a fixed set of values of the conserved quantities, the vector $\mathbf{r}_p$ is given by

$$k\mathbf{r}_p = \begin{pmatrix} \mathbf{0}_{5\times 1} \\ kr_p \end{pmatrix} = \begin{pmatrix} \mathbf{0}_{5\times 1} \\ d_1 \end{pmatrix} = \begin{pmatrix} 0 \\ \psi_2 - \psi_2^e \\ \vdots \\ \psi_5 - \psi_5^e \\ s_1 - s_1^e \end{pmatrix} = \begin{pmatrix} \mathbf{0}_{5\times 1} \\ Y_{H_2O} - Y_{H_2O}^e \end{pmatrix} = k \begin{pmatrix} \mathbf{0}_{5\times 1} \\ 2 \times 10^{-3} \end{pmatrix}. \tag{2.158}$$

Hence, $l_1 = 5$, and $l_2 = m - l_1 = 1$, where l_2 is the dimension of the parametric space associated with the ILDM.

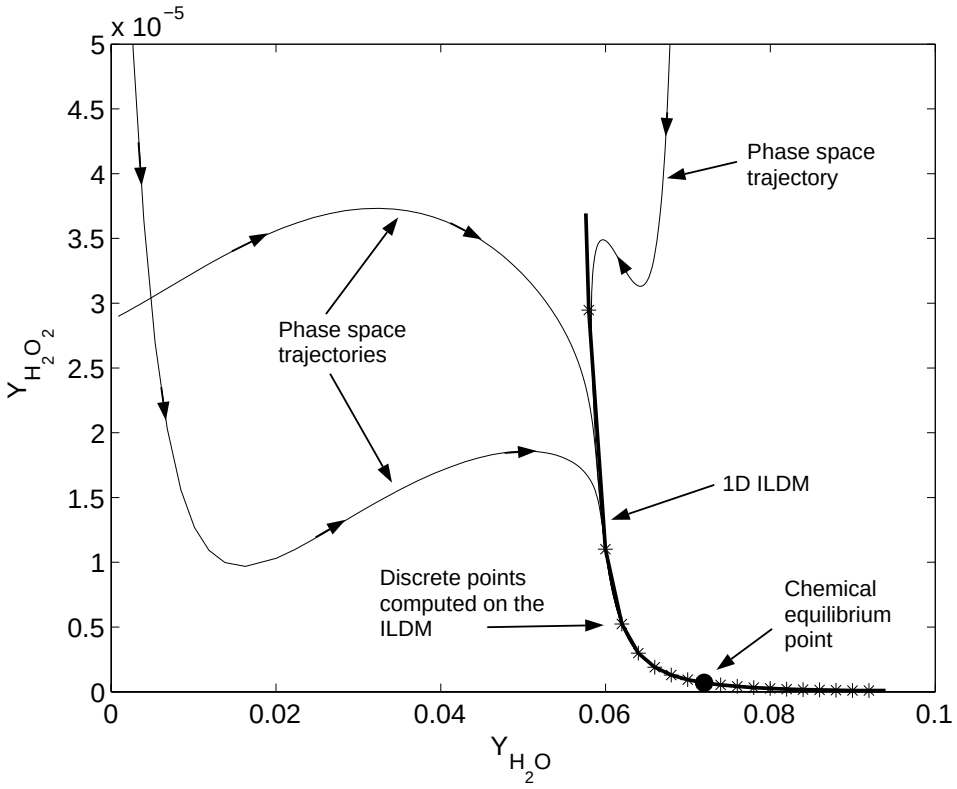

Figure 2.8. One-dimensional ILDM with fixed conserved quantities for $H_2/O_2/Ar$ reaction mechanism in the isochoric CASHPR for a reactive mixture of composition $Y_{H_{2_0}} = 0.01277$, $Y_{O_{2_0}} = 0.10137$, $Y_{Ar_0} = 0.88586$ at a constant mixture density of $\rho_0 = 0.5 \times 10^{-3}$ g cm^{-3} and a constant mixture internal energy per unit mass of $e_0 = 8 \times 10^9$ ergs g^{-1} (fixed parameterization).

Figure 2.8 depicts a projection of the one-dimensional ILDM, which exists in the $n = 11$-dimensional phase space. The one-dimensional ILDM is computed in the physically accessible subspace $\mathbb{S}$ for an additional constraint of $0 \leq Y_{H_2O_2} \leq 4.5 \times 10^{-3}$. Also plotted are the phase space trajectories which relax to the ILDM and then move close to it until they reach the chemical equilibrium state. A fixed parameterization matrix $\mathbf{P}_s$ in Equation (2.157) is used for computation of the one-dimensional ILDM. Note that in Figure 2.8, the successive points computed on the one-dimensional ILDM are spaced far apart as the ILDM becomes orthogonal to the fixed parameterization direction $\mathbf{P}_s$ or the Y_{H_2O}-axis. Also, with fixed

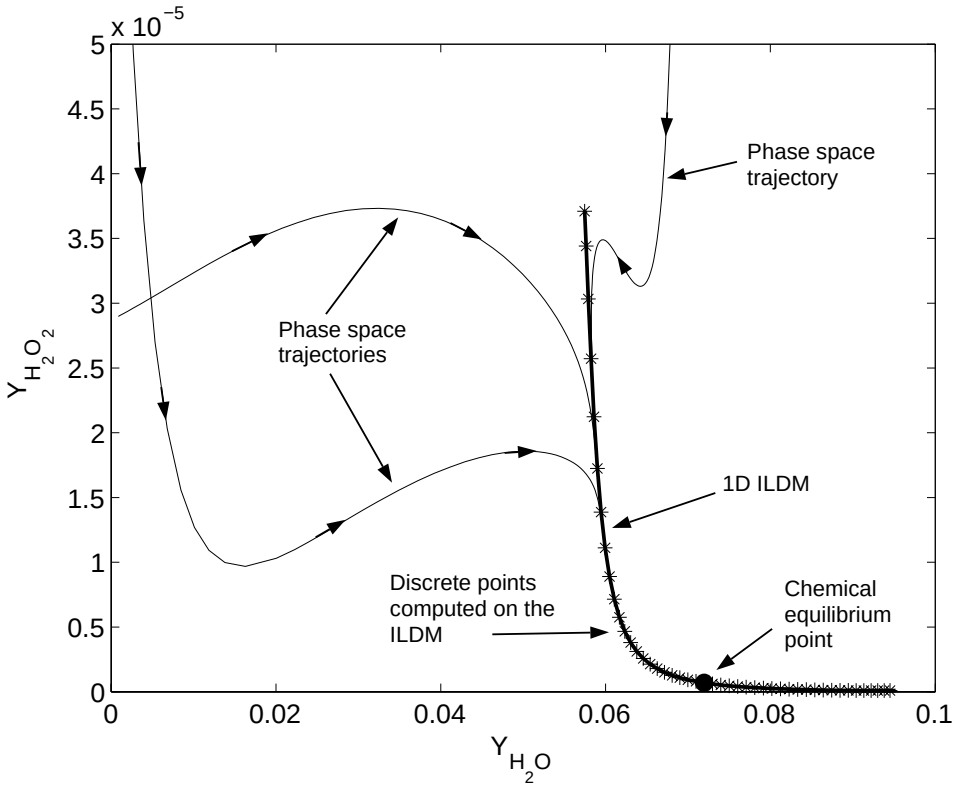

Figure 2.9. One-dimensional ILDM with fixed conserved quantities for $H_2/O_2/Ar$ reaction mechanism in the isochoric CASHPR for a reactive mixture of composition $Y_{H_{2_0}} = 0.01277$, $Y_{O_{2_0}} = 0.10137$, $Y_{Ar_0} = 0.88586$ at a constant mixture density of $\rho_0 = 0.5 \times 10^{-3}$ g cm^{-3} and a constant mixture internal energy per unit mass of $e_0 = 8 \times 10^9$ ergs g^{-1} (adaptive parameterization).

parameterization any turning points of the one-dimensional ILDM will not be captured. However, if the user specified parameterization matrix $\mathbf{P}_s$ is adapted, then these problems can be avoided. Following the adaptive parameterization method described by Maas [47], the matrix $\mathbf{P}_s$ is given by

$$\mathbf{P}_s = (\mathbf{y}_{c_{k-1}} - \mathbf{y}_{c_{k-2}})^T, \tag{2.159}$$

and the vector $\mathbf{r}_p$ for the kth point on the ILDM starting from the chemical equilibrium point, is given by

$$\mathbf{r}_{p_k} = \begin{pmatrix} \mathbf{0}_{5\times 1} \\ r_{p_k} \end{pmatrix} = \begin{pmatrix} \mathbf{0}_{5\times 1} \\ |\mathbf{y}_{c_{k-1}} - \mathbf{y}_{c_{k-2}}|^2 \end{pmatrix}, \tag{2.160}$$

with $d_1 = Y_{H_2O} - Y^e_{H_2O} = \sum_{i=1}^{k} r_{p_i}$. Figure 2.9 depicts the one-dimensional ILDM computed using adaptive parameterization. Even though in Figure 2.9, the successive points on the one-dimensional ILDM projection still appear to be far apart when the ILDM becomes orthogonal to the Y_{H_2O}-axis, the distances between the successive points on the ILDM are approximately equal in the eleven-dimensional phase space. This is not the case for fixed parameterization. Once the ILDM has been computed, the species mass fractions and temperature along the ILDM are tabulated in the following functional forms

$$Y_i = Y(Y_{H_2O}), \qquad (i = 1, \ldots, 11), \tag{2.161a}$$

$$T = T(Y_{H_2O}), \tag{2.161b}$$

for discrete values of Y_{H_2O}, which is the reference variable for the ILDM table. For fixed parameterization the discrete values of Y_{H_2O}, for which points along the ILDM are computed, are uniformly spaced along the Y_{H_2O}-axis. However, for adaptive parameterization these discrete values of Y_{H_2O} are nonuniformly spaced along the Y_{H_2O}-axis. The ILDM table for this one-dimensional ILDM is single valued with respect to the reference variable Y_{H_2O}.

An $m_d = 2$-dimensional ILDM is constructed in the $n = N + 2 = 11$-dimensional phase space for a fixed set of values of the conserved quantities. Hence, $m = m_d + L + 2 = 7$. Discrete points on the two-dimensional ILDM are computed in the polar parametric space using the predictor corrector steps in Equations (2.136-2.137). In this case there are seven linear parametric equations (2.137a) and four nonlinear ILDM equations (2.137b). The parametric matrix $\mathbf{P}_r$ has dimensions 7×11, and for the two-dimensional ILDM with a fixed set of values of the conserved

quantities, it is given by

$$\mathbf{P}_r = \left(\begin{array}{c:c} \mathbf{I}_{5\times5} & \mathbf{0}_{5\times2} \\ \hdashline \mathbf{0}_{2\times5} & \mathbf{R}_{2\times2} \end{array}\right) \mathbf{P}_d = \left(\begin{array}{c:c} \mathbf{I}_{5\times5} & \mathbf{0}_{5\times2} \\ \hdashline \mathbf{0}_{2\times5} & \mathbf{R}_{2\times2} \end{array}\right) \left(\begin{array}{c} \mathbf{P}_z \\ \\ \mathbf{P}_s \end{array}\right), \tag{2.162}$$

where the matrix $\mathbf{P}_z$ has dimensions 5×11, $\mathbf{R}_{2\times2}$ is a two-dimensional rotation matrix as described earlier, and the user specified parametric matrix $\mathbf{P}_s$ has dimensions 2×11, and its two rows can be represented by

$$\mathbf{P}_s = \left(\begin{array}{ccc} \mathbf{0}_{1\times7} & 1 & \mathbf{0}_{1\times3} \\ \\ \mathbf{0}_{1\times2} & 1 & \mathbf{0}_{1\times8} \end{array}\right), \tag{2.163}$$

as the two-dimensional ILDM is chosen to be parameterized by Y_{H_2O} and Y_H. Finally, for the two-dimensional ILDM with a fixed set of values of the conserved quantities, the vector $\mathbf{r}_p$ is given by

$$k\mathbf{r}_p = \left(\begin{array}{c} \mathbf{0}_{6\times1} \\ \\ kr_p \end{array}\right) = \left(\begin{array}{c:c} \mathbf{I}_{5\times5} & \mathbf{0}_{5\times2} \\ \hdashline \mathbf{0}_{2\times5} & \mathbf{R}_{2\times2} \end{array}\right) \left(\begin{array}{c} \mathbf{0}_{5\times1} \\ \\ d_1 \\ \\ d_2 \end{array}\right) = k \left(\begin{array}{c} \mathbf{0}_{6\times1} \\ \\ 1 \times 10^{-4} \end{array}\right), \tag{2.164}$$

where

$$\left(\begin{array}{c} \mathbf{0}_{5\times1} \\ \\ d_1 \\ \\ d_2 \end{array}\right) = \left(\begin{array}{c} 0 \\ \\ \psi_2 - \psi_2^e \\ \\ \vdots \\ \\ \psi_5 - \psi_5^e \\ \\ s_1 - s_1^e \\ \\ s_2 - s_2^e \end{array}\right) = \left(\begin{array}{c} \mathbf{0}_{5\times1} \\ \\ Y_{H_2O} - Y_{H_2O}^e \\ \\ Y_H - Y_H^e \end{array}\right). \tag{2.165}$$

Hence, $l_1 = 5$, and $l_2 = m - l_1 = 2$, where l_2 is the dimension of the parametric space associated with the ILDM.

Figure 2.10 depicts a projection of the two-dimensional ILDM and the phase space trajectories, which exists in the $n = 11$-dimensional phase space. It can be

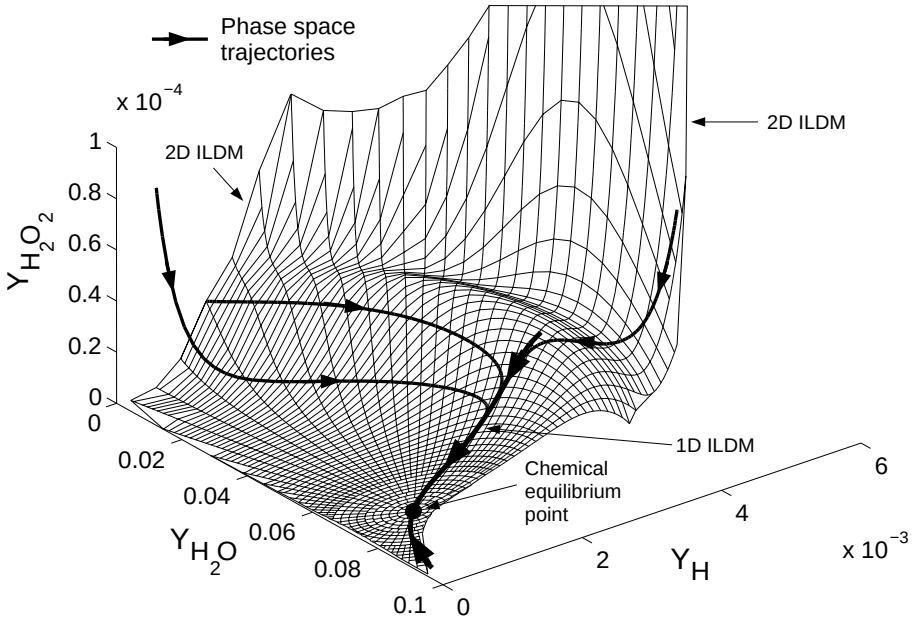

Figure 2.10. Two-dimensional ILDM with fixed conserved quantities for $H_2/O_2/Ar$ reaction mechanism in the isochoric CASHPR for a reactive mixture of composition $Y_{H_{2_0}} = 0.01277$, $Y_{O_{2_0}} = 0.10137$, $Y_{Ar_0} = 0.88586$ at a constant mixture density of $\rho_0 = 0.5 \times 10^{-3}$ g cm^{-3} and a constant mixture internal energy per unit mass of $e_0 = 8 \times 10^9$ ergs g^{-1}.

seen from Figure 2.10 that the one-dimensional ILDM lies completely within the two-dimensional ILDM subspace. The species mass fractions and temperature are tabulated along the two-dimensional ILDM in the following functional forms

$$Y_i = Y(r, \theta_1), \qquad (i = 1, \ldots, 11), \tag{2.166a}$$

$$T = T(r, \theta_1), \tag{2.166b}$$

for discrete values of r and θ_1, which are given by

$$d_1 = Y_{H_2O} - Y^e_{H_2O} = r\cos(\theta_1), \tag{2.167a}$$

$$d_2 = Y_H - Y^e_H = r\sin(\theta_1). \tag{2.167b}$$

The domain $\mathbb{D}$ in the parametric space depicted in Figure 2.11 is mapped onto the

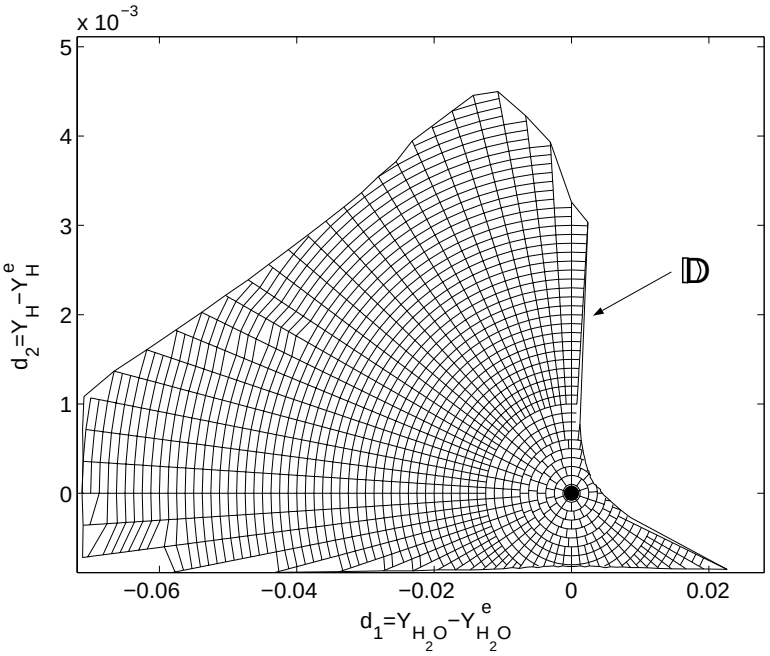

Figure 2.11. Parametric space associated with the two-dimensional ILDM in Figure 2.10 for $H_2/O_2/Ar$ reaction mechanism.

two-dimensional ILDM in the phase space using Equation (2.166). It is possible to use adaptive parameterization for computation of a one-dimensional slice of the two-dimensional ILDM in a radial direction.

An $m_d = 1$-dimensional ILDM is computed in the $n = N + 2 = 11$-dimensional phase space for fixed element mass fractions and mixture density but varying mixture internal energy per unit mass $e \in [e_{min}, e_{max}] = [1 \times 10^9, 10 \times 10^9]$ ergs g^{-1}. Hence, $m = m_d + L + 2 = 6$ $(m < n)$. Discrete points on the one-dimensional ILDM are computed in a polar parametric space using the predictor corrector steps in Equations (2.136-2.137). In this case there are six linear parametric equations (2.137a) and five nonlinear ILDM equation (2.137b). The parametric matrix $\mathbf{P}_r$ has dimensions 6×11, and for the one-dimensional ILDM with four fixed

conserved quantities and one varying conserved quantity e, it is given by

$$\mathbf{P}_r = \left(\begin{array}{c:c} \mathbf{I}_{4\times4} & \mathbf{0}_{4\times2} \\ \hdashline \mathbf{0}_{2\times4} & \mathbf{R}_{2\times2} \end{array}\right) \mathbf{P}_d = \left(\begin{array}{c:c} \mathbf{I}_{4\times4} & \mathbf{0}_{4\times2} \\ \hdashline \mathbf{0}_{2\times4} & \mathbf{R}_{2\times2} \end{array}\right) \left(\begin{array}{c} \mathbf{P}_z \\ \\ \mathbf{P}_s \end{array}\right), \tag{2.168}$$

where the matrix $\mathbf{P}_z$ has dimensions 5×11, $\mathbf{R}_{2\times2}$ is a two-dimensional rotation matrix described earlier, and the user specified parametric matrix $\mathbf{P}_s$ has dimensions 1×11, and is given by

$$\mathbf{P}_s = \left(\begin{array}{ccc} \mathbf{0}_{1\times7} & 1 & \mathbf{0}_{1\times3} \end{array}\right), \tag{2.169}$$

as the one-dimensional ILDM is chosen to be parameterized by Y_{H_2O} and e. Finally, for the one-dimensional ILDM with four fixed conserved quantities and one varying conserved quantity e, the vector $\mathbf{r}_p$ is given by

$$k\mathbf{r}_p = \left(\begin{array}{c} \mathbf{0}_{5\times1} \\ kr_p \end{array}\right) = \left(\begin{array}{c:c} \mathbf{I}_{4\times4} & \mathbf{0}_{4\times2} \\ \hdashline \mathbf{0}_{2\times4} & \mathbf{R}_{2\times2} \end{array}\right) \left(\begin{array}{c} \mathbf{0}_{4\times1} \\ d_1 \\ \\ d_2 \end{array}\right) = k \left(\begin{array}{c} \mathbf{0}_{5\times1} \\ 1 \times 10^{-3} \end{array}\right), \tag{2.170}$$

where

$$\left(\begin{array}{c} \mathbf{0}_{4\times1} \\ d_1 \\ d_2 \end{array}\right) = \left(\begin{array}{c} 0 \\ \psi_2 - \psi_2^e \\ \vdots \\ \psi_4 - \psi_4^e \\ \psi_5 - \psi_5^e \\ s_1 - s_1^e \end{array}\right) = \left(\begin{array}{c} \mathbf{0}_{4\times1} \\ \psi_5 - \psi_5^e \\ Y_{H_2O} - Y_{H_2O}^e \end{array}\right) = \left(\begin{array}{c} \mathbf{0}_{4\times1} \\ \frac{e-e^e}{e_{max}-e_{min}} \\ Y_{H_2O} - Y_{H_2O}^e \end{array}\right). \tag{2.171}$$

Hence, $l_1 = 4$, and $l_2 = m - l_1 = 2$, where l_2 is the dimension of the parametric space associated with the ILDM.

Figure 2.12 depicts a projection of the one-dimensional ILDM, which exists in the $n = 5$-dimensional phase space, for fixed element mass fractions and mixture density but varying mixture internal energy per unit mass. The one-dimensional ILDM is

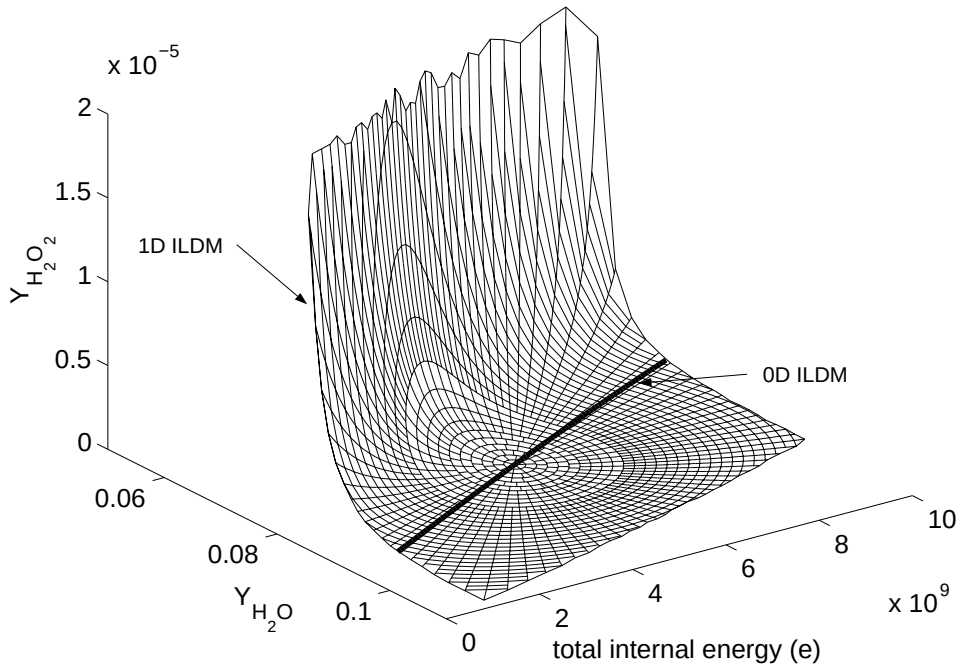

Figure 2.12. One-dimensional ILDM for $H_2/O_2/Ar$ reaction mechanism in the isochoric CASHPR for a reactive mixture of composition $Y_{H_{2_0}} = 0.01277$, $Y_{O_{2_0}} = 0.10137$, $Y_{Ar_0} = 0.88586$ for constant element mass fractions and constant mixture density of $\rho_0 = 0.5 \times 10^{-3}$ g cm^{-3} but a varying mixture internal energy per unit mass of $e \in [e_{min}, e_{max}] = [1 \times 10^9, 10 \times 10^9]$ ergs g^{-1}.

computed in the physically accessible subspace $\mathbb{S}$ for an additional constraint of $0 \leq Y_{H_2O_2} \leq 4.5 \times 10^{-3}$. The chemical equilibrium state $\mathbf{y}^e$ from which this ILDM computation is initiated, corresponds to a mixture density of $\rho = 0.5 \times 10^{-3}$ g cm^{-3} and mixture internal energy per unit mass of $e = 5 \times 10^9$ ergs g^{-1}. Also, plotted are the chemical equilibria or the zero-dimensional ILDM for fixed mixture density and varying mixture internal energy per unit mass. Note that the zero-dimensional ILDM lies completely within the one-dimensional ILDM. The species mass fractions and temperature are tabulated along the one-dimensional ILDM in the following

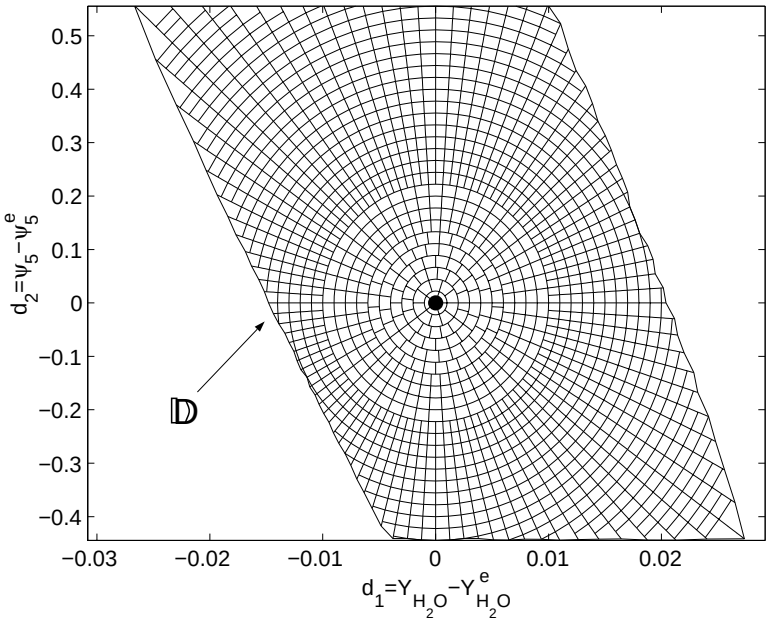

Figure 2.13. Parametric space associated with the one-dimensional ILDM in Figure 2.12 for $H_2/O_2/Ar$ reaction mechanism.

functional forms

$$Y_i = Y(r, \theta_1), \qquad (i = 1, \ldots, 11), \tag{2.172a}$$

$$T = T(r, \theta_1), \tag{2.172b}$$

for discrete values of r and θ_1, which are given by

$$d_1 = Y_{H_2O} - Y^e_{H_2O} = r\cos(\theta_1), \tag{2.173a}$$

$$d_2 = \psi_5 - \psi^e_5 = \frac{e - e^e}{e_{max} - e_{min}} = r\sin(\theta_1), \tag{2.173b}$$

The domain $\mathbb{D}$ in the parametric space depicted in Figure 2.13 is mapped onto the two-dimensional ILDM in the phase space using Equation (2.172). The ILDM table is single valued with respect to the reference variables Y_{H_2O} and e.

2.5.4 Methane combustion reaction mechanism

The methane combustion reaction mechanism is considered in the isobaric CASHPR. This reaction mechanism involves $N = 17$ species, $L = 4$ elements,

58 reversible elementary reaction steps, and hence, $J = 116$ irreversible elementary reaction steps as depicted in Table A.4. The initial species mass fractions are taken to be $Y_{CH_{4_0}} = 0.05515$, $Y_{O_{2_0}} = 0.22002$, and $Y_{N_{2_0}} = 0.72483$, with the remaining fourteen initial species mass fractions being zero, and hence, using Equation (2.10), the initial element mass fractions are given by $\hat{Y}_{H_0} = 0.01386$, $\hat{Y}_{O_0} = 0.22002$, $\hat{Y}_{C_0} = 0.04129$, and $\hat{Y}_{N_0} = 0.72483$, which remain constant. Since, the isobaric CASHPR is considered, the pressure and mixture enthalpy per unit mass remain constant (see Section 2.1.2). The reactions inside the isobaric CASHPR are considered at a constant pressure of $p_0 = 1.01325 \times 10^6$ dynes cm^{-2}, and at an initial temperature of $T_0 = 298$ K. Hence, the constant mixture enthalpy per unit mass, using the initial conditions, is given by $h_0 = -0.25761 \times 10^{10}$ erg g^{-1}. The initial state of the reactive mixture can be represented by $\mathbf{y}_0 = (h_0, p_0, Y_{1_0}, \ldots, Y_{N_0})^T = (-0.25761 \times 10^{10}, 1.01325 \times 10^6, 0.05515, 0, 0, 0, 0, 0, 0, 0, 0, 0, , 0.22002, 0, 0, 0, 0, 0, 0.72483)^T$. The conserved quantities in the isobaric CASHPR can be represented by $\bar{\mathbf{y}} = (\hat{Y}_{1_0}, \ldots, \hat{Y}_{L_0}, p_0, h_0)^T = (0.01386, 0.22002, 0.04129, 0.72483, 1.01325 \times 10^6, -0.25761 \times 10^{10})^T$. The conserved parameters vector for the initial state is given by $\mathbf{\Psi}_0 = (0, 0.22002, 0.04129, 0.72483, 0, 0)^T$, assuming that the range of the conserved quantities p and h, for any future computations of the ILDM, is given by $p \in [p_{min}, p_{max}] = [1.01325 \times 10^6, 2.01325 \times 10^6]$ dynes cm^{-2}, and $h \in [h_{min}, h_{max}] = [-0.25761 \times 10^{10}, -0.15761 \times 10^{10}]$ ergs g^{-1}. To initiate the ILDM computation, the chemical equilibrium state $\mathbf{y}^e$ is computed, with $\mathbf{\Psi}^e = \mathbf{\Psi}_0$.

An $m_d = 1$-dimensional ILDM is computed in the $n = N + 2 = 19$-dimensional phase space for a fixed set of values of the conserved quantities. Hence, $m = m_d + L + 2 = 7$ $(m < n)$, determines the segregation of the slow and fast time scales. A series of points are computed on the one-dimensional ILDM by using the predictor corrector steps in Equations (2.136-2.137). In this case there are seven

linear parametric equations (2.137a) and twelve nonlinear ILDM equation (2.137b). The one-dimensional ILDM is computed on either side of the chemical equilibrium state until it intersects the boundary of the physically accessible subspace $\mathbb{S}$ of the phase space. The parametric matrix $\mathbf{P}_r$ has dimensions 7×19, and for the one-dimensional ILDM with a fixed set of values of the conserved quantities, it is given by

$$\mathbf{P}_r = \mathbf{P}_d = \begin{pmatrix} \mathbf{P}_z \\ \mathbf{P}_s \end{pmatrix}, \tag{2.174}$$

where the matrix $\mathbf{P}_z$ has dimensions 6×19, while the user specified parametric matrix $\mathbf{P}_s$ has dimensions 1×19, and is given by

$$\mathbf{P}_s = \begin{pmatrix} \mathbf{0}_{1\times 8} & 1 & \mathbf{0}_{1\times 10} \end{pmatrix}, \tag{2.175}$$

as the one-dimensional ILDM is chosen to be parameterized by Y_{CO_2}. Finally, for the one-dimensional ILDM with a fixed set of values of the conserved quantities, the vector $\mathbf{r}_p$ is given by

$$k\mathbf{r}_p = \begin{pmatrix} \mathbf{0}_{6\times 1} \\ kr_p \end{pmatrix} = \begin{pmatrix} \mathbf{0}_{6\times 1} \\ d_1 \end{pmatrix} = \begin{pmatrix} 0 \\ \psi_2 - \psi_2^e \\ \vdots \\ \psi_6 - \psi_6^e \\ s_1 - s_1^e \end{pmatrix} = \begin{pmatrix} \mathbf{0}_{6\times 1} \\ Y_{CO_2} - Y_{CO_2}^e \end{pmatrix} = k \begin{pmatrix} \mathbf{0}_{6\times 1} \\ 1 \times 10^{-3} \end{pmatrix}. \tag{2.176}$$

Hence, $l_1 = 6$, and $l_2 = m - l_1 = 1$, where l_2 is the dimension of the parametric space associated with the ILDM.

Figure 2.14 depicts a projection of the one-dimensional ILDM, which exists in the $n = 19$. Also plotted are the phase space trajectories which relax to the ILDM and then move close to it until they reach the chemical equilibrium state. As observed for the syngas combustion case, it is found that not all of the one-dimensional ILDM

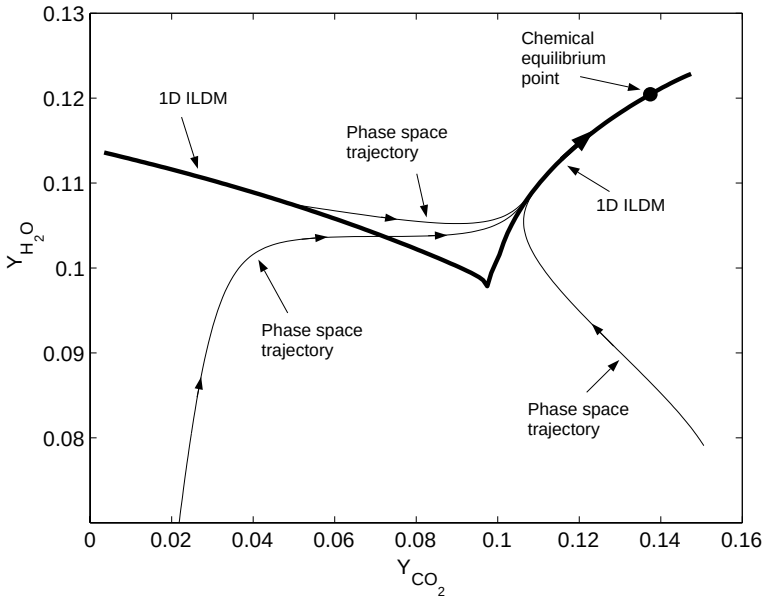

Figure 2.14. One-dimensional ILDM with fixed conserved quantities for methane combustion in the isobaric CASHPR for a reactive mixture of composition $Y_{CH_4 0}/Y_{O_2 0}/Y_{N_2 0} = 0.05515/0.22002/0.72483$ at a temperature $T_0 = 298K$ and pressure 1.01325×10^6 dynes cm^{-2}.

approximates the SIM well. It can be seen from Figure 2.14 that the phase space trajectories relax only to a subset, $\mathbb{S}''$, of the ILDM close to the chemical equilibrium state. Even if the phase space trajectories start exactly from other parts of the one-dimensional ILDM not in $\mathbb{S}''$, they do not stay close to the ILDM until they reach $\mathbb{S}''$. Hence, parts of the ILDM far from the chemical equilibrium state do not have an approximate invariant property as does $\mathbb{S}''$. Hence, only the attractive subset, $\mathbb{S}''$, of the ILDM is useful and should be computed and stored as a table. The species mass fractions and temperature along the subset $\mathbb{S}''$ of the one-dimensional ILDM are tabulated in the following functional form

$$Y_i = Y(Y_{CO_2}), \qquad (i = 1, \ldots, 17), \tag{2.177a}$$

$$T = T(Y_{CO_2}), \tag{2.177b}$$

for discrete values of Y_{CO_2}, which is the reference variable for the ILDM table. The

ILDM table is single valued with respect to the reference variable Y_{CO_2} for the subset $\mathbb{S}''$ of the one-dimensional ILDM.

An $m_d = 2$-dimensional ILDM is constructed in the $n = N + 2 = 19$-dimensional phase space for a fixed set of values of the conserved quantities. Hence, $m = m_d + L + 2 = 8$. Discrete points on the two-dimensional ILDM are computed in the polar parametric space using the predictor corrector steps in Equations (2.136-2.137). In this case there are eight linear parametric equations (2.137a) and eleven nonlinear ILDM equations (2.137b). The parametric matrix $\mathbf{P}_r$ has dimensions 8×19, and for the two-dimensional ILDM with a fixed set of values of the conserved quantities, it is given by

$$\mathbf{P}_r = \left(\begin{array}{c:c} \mathbf{I}_{6\times6} & \mathbf{0}_{6\times2} \\ \hdashline \mathbf{0}_{2\times6} & \mathbf{R}_{2\times2} \end{array}\right) \mathbf{P}_d = \left(\begin{array}{c:c} \mathbf{I}_{6\times6} & \mathbf{0}_{6\times2} \\ \hdashline \mathbf{0}_{2\times6} & \mathbf{R}_{2\times2} \end{array}\right) \left(\begin{array}{c} \mathbf{P}_z \\ \\ \mathbf{P}_s \end{array}\right), \tag{2.178}$$

where the matrix $\mathbf{P}_z$ has dimensions 6×19, $\mathbf{R}_{2\times2}$ is a two-dimensional rotation matrix described earlier, and the user specified parametric matrix $\mathbf{P}_s$ has dimensions 2×19, and its two rows can be represented by

$$\mathbf{P}_s = \left(\begin{array}{ccc} \mathbf{0}_{1\times8} & 1 & \mathbf{0}_{1\times10} \\ \\ \mathbf{0}_{1\times17} & 1 & 0 \end{array}\right), \tag{2.179}$$

as the two-dimensional ILDM is chosen to be parameterized by Y_{CO_2} and Y_{H_2O}. Finally, for the two-dimensional ILDM with a fixed set of values of the conserved quantities, the vector $\mathbf{r}_p$ is given by

$$k\mathbf{r}_p = \left(\begin{array}{c} \mathbf{0}_{7\times1} \\ \\ kr_p \end{array}\right) = \left(\begin{array}{c:c} \mathbf{I}_{6\times6} & \mathbf{0}_{6\times2} \\ \hdashline \mathbf{0}_{2\times6} & \mathbf{R}_{2\times2} \end{array}\right) \left(\begin{array}{c} \mathbf{0}_{6\times1} \\ \\ d_1 \\ \\ d_2 \end{array}\right) = k \left(\begin{array}{c} \mathbf{0}_{7\times1} \\ \\ 0.5 \times 10^{-3} \end{array}\right), \tag{2.180}$$

where

$$\begin{pmatrix} \mathbf{0}_{6\times 1} \\ d_1 \\ d_2 \end{pmatrix} = \begin{pmatrix} 0 \\ \psi_2 - \psi_2^e \\ \vdots \\ \psi_6 - \psi_6^e \\ s_1 - s_1^e \\ s_2 - s_2^e \end{pmatrix} = \begin{pmatrix} \mathbf{0}_{6\times 1} \\ Y_{CO_2} - Y_{CO_2}^e \\ Y_{H_2O} - Y_{H_2O}^e \end{pmatrix}. \tag{2.181}$$

Hence, $l_1 = 6$, and $l_2 = m - l_1 = 2$, where l_2 is the dimension of the parametric space associated with the ILDM.

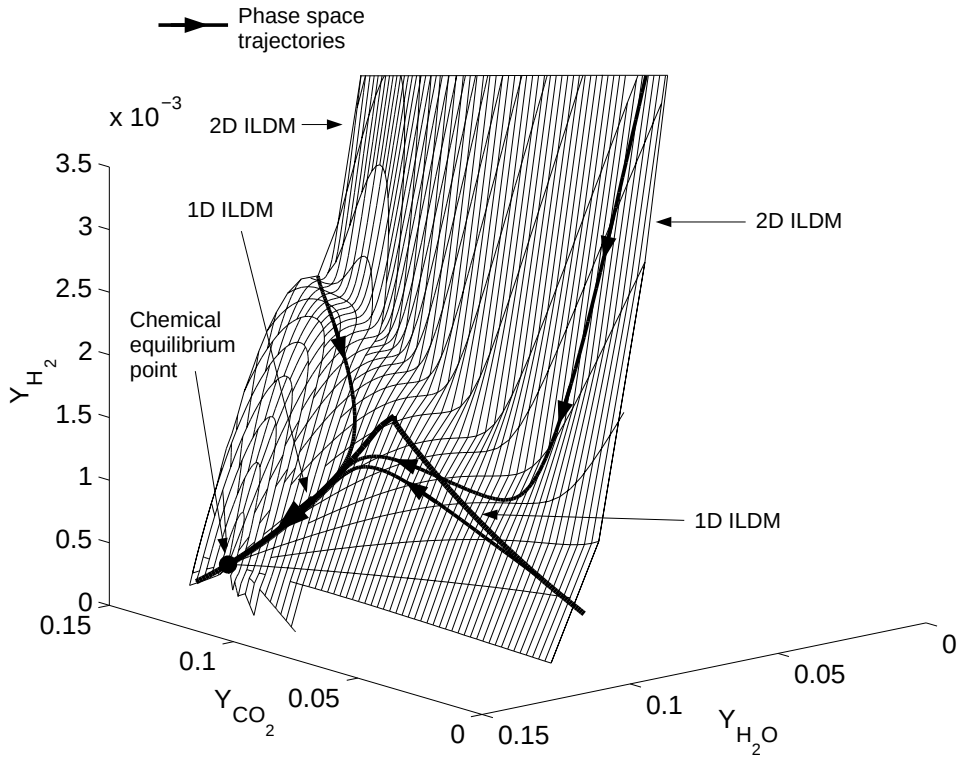

Figure 2.15. Two-dimensional ILDM with fixed conserved quantities for methane combustion in the isobaric CASHPR for a reactive mixture of composition $Y_{CH_{4_0}}/Y_{O_{2_0}}/Y_{N_{2_0}} = 0.05515/0.22002/0.72483$ at a temperature $T_0 = 298K$ and pressure 1.01325×10^6 dynes cm^{-2}.

Figure 2.15 depicts a projection of the two-dimensional ILDM and the phase space trajectories, which exists in the $n = 17$-dimensional phase space. It can be

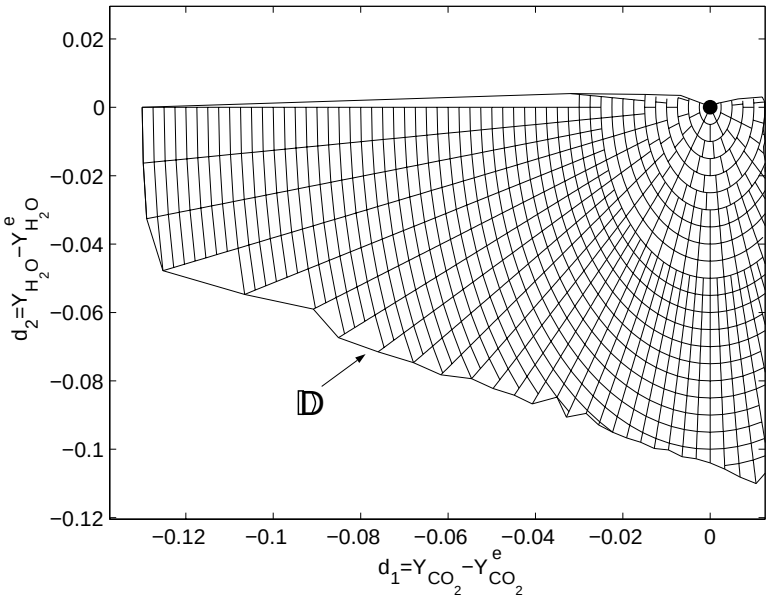

Figure 2.16. Parametric space associated with the one-dimensional ILDM in Figure 2.15 for methane combustion.

seen from Figure 2.15 that the one-dimensional ILDM lies completely within the two-dimensional ILDM subspace. The species mass fractions and temperature are tabulated along the two-dimensional ILDM in the following functional forms

$$Y_i = Y(r, \theta_1), \qquad (i = 1, \ldots, 17), \tag{2.182a}$$

$$T = T(r, \theta_1), \tag{2.182b}$$

for discrete values of r and θ_1, which are given by

$$d_1 = Y_{CO_2} - Y^e_{CO_2} = r\cos(\theta_1), \tag{2.183a}$$

$$d_2 = Y_{H_2O} - Y^e_{H_2O} = r\sin(\theta_1). \tag{2.183b}$$

The domain $\mathbb{D}$ in the parametric space depicted in Figure 2.16 is mapped onto the two-dimensional ILDM in the phase space using Equation (2.182). The ILDM table is single valued with respect to the reference variables Y_{CO_2} and Y_{H_2O}.

CHAPTER 3

VISCOUS DETONATION IN A REACTIVE MIXTURE OF $H_2/O_2/Ar$

In this chapter the standard ignition delay problem for a mixture of hydrogen/oxygen/argon ($H_2/O_2/Ar$) in a shock tube, extended to the viscous regime, is solved using the method of Intrinsic Low-Dimensional Manifolds (ILDM) coupled with a Wavelet Adaptive Multilevel Representation (WAMR) spatial discretization technique. An operator splitting method is used to separate the reaction part from the convection and diffusion part of the governing equations, and then the governing equations are solved in two steps. In the reaction step, the ILDM method, which rationally reduces detailed chemical kinetics, is used to eliminate the stiffness associated with the chemistry by decoupling chemical processes which evolve on fast and slow time scales. The fast time scale chemical processes are systematically equilibrated, thereby reducing the dimension of the phase space required to describe the reactive system. In the convection diffusion step, the WAMR is used to capture the detailed spatial structures automatically with a small number of basis functions thereby further reducing the number of variables required to describe the system. Additionally, the resolution of physical diffusion processes minimizes the effects of potentially reaction-inducing artificial entropy layers associated with numerical diffusion.

3.1 Problem description

The ignition delay problem considered is the viscous analog of the inviscid problem considered by Fedkiw, *et al.* [51] (see also [52]) and is as follows. As an initial condition, a shock is taken to be propagating to the right in a mixture of $H_2/O_2/Ar$. The shock is of insufficient strength to induce significant reaction over the length scales considered. After some time, the shock reflects from a wall at the right, inducing a reflected, left-propagating shock. This shock leaves the fluid adjacent to the wall in state of near zero velocity and a temperature which is sufficiently elevated to induce significant chemical reaction following a short ignition delay time. The problem considered in Ref. [51] is very similar to that studied by Oran, *et al.* [53], who, in a case they label "strong ignition," consider the same gaseous mixture at a reflected shock pressure which is roughly 10% higher and temperature which is roughly 10% lower than that considered in Ref. [51]. Additionally, there are small differences between the models used in Refs. [51] and [53].

A Strang [39] operator splitting technique is used for numerical simulation of the governing equations. This technique allows straightforward implementation of both ILDM and WAMR techniques. After initialization, the Strang splitting progresses in a series of two step processes. In the first step, convection and diffusion is suppressed. In this step, each point in physical space is treated as an isochoric closed adiabatic spatially homogeneous premixed reactor (CASHPR), and the associated ordinary differential equations (ODEs) at each spatial point are solved using the ILDM method. In Chapter 2 the ILDM method was developed such that it is applicable for solving the ODEs modeling the CASHPR under the rather general conditions which naturally arise from an operator splitting method applied to fully compressible, non-adiabatic, non-isobaric, diffusive reactive flow systems.

Such conditions are not fully discussed in most of the ILDM literature and must be considered if the ILDM method is to be used for general problems.

In the second step, the reaction source terms are deactivated such that the solution at each spatial point evolves only due to convection and diffusion, and the associated partial differential equations (PDEs) are solved using the WAMR method. Traditionally convection and diffusion in reactive flow problems are modeled by finite difference or finite element methods, which have difficulty modeling phenomena which have localization in physical and spectral space. The WAMR method is better suited for problems with physical and spectral localization. This technique, developed by Vasilyev and Paolucci [54], [55], projects the representation of the system onto a wavelet basis. This basis has been shown to be very efficient in representing systems with detailed spatial structures. The capturing of the details of the structure with a small number of basis functions dramatically reduces the number of equations which need to be solved, consequently reducing computational time.

While diffusion is typically not modeled in detonation studies, it is considered here for two reasons. First, as discussed in detail by Singh, *et al.* [56], physical diffusion is necessary to regularize predictions of flow variables downstream of the lead shock in simulations of multi-dimensional cellular instabilities in a propagating detonation wave. Whether or not this physically based regularization is crucial in determining wall tracings of a detonation wave in an open tube [57], is an open question. Second, as will be shown here, the use of resolved physical diffusion layers correctly captures entropy layers. As discussed by Menikoff [58], inviscid models using typical grid resolutions will introduce artificial entropy layers due to numerical diffusion. The coarser the grid, the more entropy introduced, and the more likely such a layer could falsely trigger temperature-sensitive chemical reaction.

3.2 Governing equations

The following equations describe the reactive flow system considered in this chapter, a one-dimensional viscous mixture of N ideal gases composed of L elements which undergo J reactions.

$$\frac{\partial \rho}{\partial t} + \frac{\partial}{\partial x}(\rho u) = 0, \tag{3.1}$$

$$\frac{\partial}{\partial t}(\rho u) + \frac{\partial}{\partial x}\left(\rho u^2 + p - \tau\right) = 0, \tag{3.2}$$

$$\frac{\partial}{\partial t}\left(\rho\left(e + \frac{u^2}{2}\right)\right) + \frac{\partial}{\partial x}\left(\rho u\left(e + \frac{u^2}{2}\right) + u\left(p - \tau\right) + J^q\right) = 0, \tag{3.3}$$

$$\frac{\partial}{\partial t}\left(\rho \hat{Y}_l\right) + \frac{\partial}{\partial x}\left(\rho u \hat{Y}_l + \hat{J}_l^m\right) = 0, \qquad (l = 1, \ldots, L-1), \tag{3.4}$$

$$\frac{\partial}{\partial t}(\rho Y_i) + \frac{\partial}{\partial x}(\rho u Y_i + J_i^m) = \dot{\omega}_i M_i, \qquad (i = 1, \ldots, N-L), \tag{3.5}$$

$$\tau = \frac{4}{3}\mu \frac{\partial u}{\partial x}, \tag{3.6}$$

$$J^q = -k\frac{\partial T}{\partial x} + \sum_{i=1}^{N} J_i^m \left(h_{fi}^{\circ} + \int_{T_s}^{T} c_{pi}(\hat{T}) d\hat{T}\right) - \Re T \sum_{i=1}^{N} \frac{\mathcal{D}_i^T}{M_i}\left(\frac{1}{X_i}\frac{\partial X_i}{\partial x} + \left(1 - \frac{M_i}{M}\right)\frac{1}{p}\frac{\partial p}{\partial x}\right), \tag{3.7}$$

$$J_i^m = \rho \sum_{j=1, j\neq i}^{N} \frac{M_i}{M} Y_j \mathcal{D}_{ij}\left(\frac{1}{X_j}\frac{\partial X_j}{\partial x} + \left(1 - \frac{M_j}{M}\right)\frac{1}{p}\frac{\partial p}{\partial x}\right) - \mathcal{D}_i^T \frac{1}{T}\frac{\partial T}{\partial x}, \qquad (i = 1, \ldots, N), \tag{3.8}$$

$$M = \sum_{i=1}^{N} M_i X_i, \tag{3.9}$$

$$X_i = \frac{M}{M_i} Y_i, \qquad (i = 1, \ldots, N), \tag{3.10}$$

$$\hat{Y}_l = \hat{M}_l \sum_{i=1}^{N} \frac{\varphi_{il}}{M_i} Y_i, \qquad (l = 1, \ldots, L-1), \tag{3.11}$$

$$\hat{J}_l^m = \hat{M}_l \sum_{i=1}^{N} \frac{\varphi_{il}}{M_i} J_i^m, \qquad (l = 1, \ldots, L-1), \tag{3.12}$$

$$\sum_{i=1}^{N} Y_i = 1, \tag{3.13}$$

$$\sum_{l=1}^{L} \hat{Y}_l = 1, \tag{3.14}$$

$$\dot{\omega}_i = \sum_{j=1}^{J} \alpha_j T^{\beta_j} \exp\left(\frac{-E_j}{\Re T}\right) \left(\nu''_{ij} - \nu'_{ij}\right) \prod_{k=1}^{N} \left(\frac{\rho Y_k}{M_k}\right)^{\nu'_{kj}}, \qquad (i = 1, \ldots, N-L), \tag{3.15}$$

$$p = \frac{\rho \Re T}{M}, \tag{3.16}$$

$$e = \sum_{i=1}^{N} Y_i \left(h_{fi}^{\circ} + \int_{T_s}^{T} c_{pi}(\hat{T}) d\hat{T}\right) - \frac{\Re T}{M}. \tag{3.17}$$

Equations (3.1-3.4) describe the conservation of mass, linear momentum, energy, and mass fraction of $L-1$ elements. Equation (3.5) is an evolution equation for $N-L$ of the N species. Equations (3.6-3.8) give constitutive relations for momentum, energy, and mass diffusion which are the Newtonian stress-strain rate relation, extended Fourier's law, and extended Fick's law. The form of both Fourier's and Fick's law given at this point is appropriate for a mixture of ideal gases, as detailed in a derivation by Merk [59] and summarized by Kee, *et al.* [60]. Equations (3.7)

and (3.8) account for multicomponent mass diffusion as well as Soret and DuFour effects, all of which are included at this stage for completeness. These will be later reduced to a simpler form which will be used in the analysis. Equation (3.9) defines the mean molecular mass, and Equation (3.10) defines the species mole fraction. Equations (3.11) and (3.12) define the mass fraction and diffusive mass flux, respectively, of element l. Equations (3.13) and (3.14) constrain the species and element mass fractions to sum to unity. Equation (3.15) is a constitutive equation for the evolution of species given by the law of mass action with Arrhenius kinetics. Equations (3.16) and (3.17) are, respectively, thermal and caloric state equations for a mixture of ideal gases with temperature dependent specific heats.

The $N+2$ PDEs (3.1-3.5) are taken to be fundamental equations for $N+2$ dependent variables, which are taken to be mass density, ρ; mass-averaged velocity, u; mass-averaged internal energy per unit mass, e; mass fraction of element l, $\hat{Y}_l$ $(l = 1, \ldots, L-1)$; and mass fraction of species i, Y_i $(i = 1, \ldots, N-L)$. These are supplemented by $3N + L + 5$ constitutive equations, equations of state, and supplementary algebraic equations (3.6-3.17) for the remaining $3N + L + 5$ intermediate variables which are taken to be pressure, p; viscous stress, τ; diffusive energy flux, J^q; mole fraction of species i, X_i $(i = 1, \ldots, N)$; mass fraction of element L, $\hat{Y}_L$; mass fraction of species i, Y_i $(i = N-L+1, \ldots, N)$; diffusive mass flux of element l, $\hat{J}_l^m$ $(l = 1, \ldots, L-1)$; diffusive mass flux of species i, J_i^m $(i = 1, \ldots, N)$; molar production rate per unit volume of species i, $\dot{\omega}_i$ $(i = 1, \ldots, N-L)$; mean molecular mass, M; and temperature, T. The independent variables are time t and position x. The specific heat at constant pressure of species i on a mass basis, c_{pi}, is taken to be a known function of temperature. The function is taken to be in the form of a standard polynomial curve fit found in the Chemkin III thermodynamic data base, [61].

Constant parameters in Equations (3.1-3.17) are M_i, $\hat{M}_l$, α_j, β_j, E_j, $\Re$, ν'_{ij}, ν''_{ij}, φ_{il}, $\mathcal{D}_{ij}$, $\mathcal{D}_i^T$, μ, k, and h°_{fi}. They represent the molecular mass of species i, the atomic mass of element l, the kinetic rate constant of reaction j, the temperature dependency exponent of reaction j, the activation energy of reaction j, the universal gas constant ($\Re = 8.31441 \times 10^7$ erg mol^{-1} K^{-1}), the stoichiometric coefficient of the ith species on the reactant and product sides in reaction j, respectively, the number of atoms of element l in species i, the multicomponent mass diffusion coefficient, the Soret/DuFour thermal diffusion coefficient, the dynamic viscosity, the thermal conductivity, and the standard enthalpy of formation per unit mass of species i. All reactions are treated as forward reactions with explicit reactions written for the actual reverse reactions. Following Maas and Warnatz [62], parameters for those reactions which could be written as reverse reactions are chosen to be consistent with thermodynamic equilibrium relations.

Many studies do not explicitly form Equation (3.4) and instead solve $N-1$ species equations. Equation (3.4) is included because it is critical in the implementation of the ILDM method within an operator splitting scheme. Equation (3.4), along with Equations (3.1) and (3.13), can be obtained by enforcing stoichiometric balances for the jth reaction $\sum_{i=1}^{N} \nu'_{ij}\varphi_{il} = \sum_{i=1}^{N} \nu''_{ij}\varphi_{il}$ for $l = 1, \ldots, L$, and the definition of molecular mass, $M_i = \sum_{l=1}^{L} \varphi_{il}\hat{M}_l$, along with Equation (3.11) and appropriate manipulations of Equation (3.5) when written in a form in which the evolution of all N species is considered.

It is straightforward to show that conditions exist which guarantee a constant element mass fraction for all time. Using Equation (3.1) and introducing the material derivative, $\frac{D}{Dt} \equiv \frac{\partial}{\partial t} + u\frac{\partial}{\partial x}$, Equation (3.4) transforms to

$$\rho \frac{D\hat{Y}_l}{Dt} = -\frac{\partial \hat{J}_l^m}{\partial x}, \qquad (l = 1, \ldots, L-1). \tag{3.18}$$

For general expressions of mass diffusion, such as that of Equation (3.8), the right

hand side of Equation (3.18) will be non-zero, and one can conclude that the element mass fraction of a fluid particle will change with time. Assuming now that 1) all multicomponent mass diffusion coefficients are equal, $\mathcal{D}_{ij} = \mathcal{D}$, 2) the molecular masses of each species are close to the mean molecular mass, $M_i \sim M$, and consequently mass fractions are roughly the same as mole fractions $Y_i \sim X_i$, and 3) Soret mass diffusion due to thermal effects is negligible, $\mathcal{D}_i^T \sim 0$, and consequently DuFour effects are negligible as well, a form of Fick's law is obtained, which is commonly used in the combustion community, e.g. Williams [63] and Merk [59], and which will be adopted from here on in this chapter

$$J_i^m = -\rho\mathcal{D}\frac{\partial Y_i}{\partial x}, \qquad (i = 1, \ldots N). \tag{3.19}$$

Note that for the problem considered in this chapter with the $H_2/O_2/Ar$ reaction mechanism, it can be shown, using a Maxwell diffusion formulation, that assumption 2) is not necessary.

Now using Equation (3.19), the Equation (3.12) reduces, using Equation (3.11), to

$$\hat{J}_l^m = -\rho\mathcal{D}\frac{\partial \hat{Y}_l}{\partial x}, \qquad (l = 1, \ldots, L-1)\,. \tag{3.20}$$

Then Equation (3.18) simplifies, through use of Equation (3.20), to

$$\rho\frac{D\hat{Y}_l}{Dt} = \mathcal{D}\frac{\partial}{\partial x}\left(\rho\frac{\partial \hat{Y}_l}{\partial x}\right), \qquad (l = 1, \ldots, L-1). \tag{3.21}$$

Consequently, for a system with a diffusive mass flux of the described character, no initial gradients of element mass fraction $\frac{\partial \hat{Y}_l}{\partial x}(x, t = 0) = 0$, and no fluxes at boundaries $\frac{\partial \hat{Y}_l}{\partial x}(x = 0, t) = \frac{\partial \hat{Y}_l}{\partial x}(x = L_x, t) = 0$ (where L_x is the domain length), Equations (3.21) and (3.14) insure there is no tendency for any element mass fraction to change from its uniform initial value, and each element mass fraction will remain constant for all x and t. The same conclusion obviously holds for systems with

no mass diffusion. For non-premixed flames with similar assumptions, the mixture fraction described by Warnatz, *et al.* [20] can be used to parameterize the $\hat{Y}_l$ values in a way that also simplifies the system.

It is recognized that the assumptions necessary to obtain Equation (3.21) are somewhat crude for the $H_2/O_2/Ar$ reactive mixture, and that this most likely induces small errors in zones in which mass fraction gradients are steep. While the methods used in this study to solve the governing equations can deal with the more complete system, these simplifications have been made for the following two reasons: 1) if preferential diffusion were allowed, a use of an ILDM of much higher dimension will be required in order to account for local non-conservation of element mass fractions, and 2) while the computational cost for adding such terms would be high, it is not clear that the effect of those terms in this problem is large.

The kinetic model, identical to that used in [51], was originally developed by Maas and Warnatz [62] and considers the reaction of $N = 9$ species (H, O, H_2, O_2, OH, H_2O, HO_2, H_2O_2, Ar) constituted from $L = 3$ elements (H, O, Ar), in $J = 37$ reactions. Coefficients for this mechanism are listed in Table 1. For this mechanism, the corrected value of third body efficiency for hydrogen, $f_{H_2} = 1.00$ as appears in Ref. [1], has been adopted. As reported in Ref. [62], no special tuning was imposed to match experimentally observed ignition delay times.

In order to verify the kinetic model, preliminary calculations were performed to simulate the experiments of Schott and Kinsey [64]. In their experiments, induction times, t_i, were measured in shock tubes for dilute, low pressure ($p \sim 3 \times 10^5$ dynes cm^{-2}) mixtures of H_2 and O_2 in Ar. The kinetic model under closed, adiabatic, isochoric, homogeneous premixed conditions predicted induction times which were within the experimental error bounds reported for conditions of Ref. [64]. A full simulation including the effect of spatial gradients proved impractical. This

is because the instrumentation in the experiment required at least a 1 ms induction time, rendering the ratio of the induction time to the reaction time sufficiently large to make its computation with full spatial details prohibitively expensive. The reflected shock pressure and temperature in Ref. [51] are 11.88×10^5 dynes cm^{-2} and 1196 K, Under these high pressure and temperature conditions, a closed, adiabatic, isochoric, homogeneous premixed calculation with the kinetic model for the reactive mixture of $H_2/O_2/Ar$ in a $2 : 1 : 7$ molar ratio, yields $t_i = 58.2$ μs. This is within the error bounds of an extrapolation of results of Ref. [64], which predicts $7.3 < t_i < 81.9$ μs at this state.

The values of the diffusion parameters are taken to be $\mathcal{D} = 5.6 \times 10^1$ cm^2 s^{-1}, $\mu = 1.0 \times 10^{-2}$ dynes s cm^{-2}, and $k = 8.3 \times 10^5$ erg cm^{-1} s^{-1} K^{-1}. It is noted that the viscosity is roughly one order of magnitude too large. Computations with a viscosity of the right magnitude would entail a much higher computational cost. There are two reasons for taking the larger value of viscosity. First, since the WAMR method captures all length scales present automatically, a smaller viscosity will require an increase in the number of degrees of freedom to do so. Second, subsequent calculations at resulting higher resolutions would necessitate quadruple precision computations because approximations of second derivatives on the finest scale using double precision are corrupted by machine roundoff! A discussion of the effect of this choice of viscosity on the results is given later.

A shock tube of length 12 cm filled initially with a reactive mixture of $H_2/O_2/Ar$ in a $2 : 1 : 7$ molar ratio, is considered. For $0 \leq x \leq 6$ cm, the gas is taken to be at $\rho = 0.18075 \times 10^{-3}$ g cm^{-3}, $u = 487.34 \times 10^2$ cm s^{-1}, and $p = 3.5594 \times 10^5$ dynes cm^{-2}. For $6 < x \leq 12$ cm, the gas is at $\rho = 0.072 \times 10^{-3}$ g cm^{-3}, $u = 0$ cm s^{-1}, and $p = 0.7173 \times 10^5$ dynes cm^{-2}. This state is consistent with Rankine-Hugoniot jump conditions for the inviscid equivalent of Equations (3.1-3.17). Knowledge of these

parameters allows determination of all other dependent variables at $t = 0$ s through the use of the governing equations. At $x = 12$ cm, a closed and adiabatic boundary is considered. Consequently $u = 0$ cm s^{-1}, and additionally diffusive mass and energy fluxes J_i^m $(i = 1, \ldots, N)$, and J^q must be zero. At $x = 0$ cm, inflow conditions of $u = 487.34 \times 10^2$ cm s^{-1}, $\rho = 0.18075 \times 10^{-3}$ g cm^{-3}, $p = 3.5594 \times 10^5$ dynes cm^{-2} are allowed.

3.3 Operator splitting

The governing equations (3.1-3.17) can be written in the following compact form

$$\frac{\partial \mathbf{y}}{\partial t} = \mathbf{f}(\mathbf{y}) - \frac{\partial}{\partial x}\mathbf{h}(\mathbf{y}), \tag{3.22}$$

where $\mathbf{y}$, representing the set of conserved dependent variables, $\mathbf{f}(\mathbf{y})$, representing the reaction source term, and $-\frac{\partial}{\partial x}\mathbf{h}(\mathbf{y})$ representing convection and diffusion, are given by

$$\mathbf{y} = \begin{pmatrix} \rho \\ \rho u \\ \rho\left(e + \frac{u^2}{2}\right) \\ \rho\hat{Y}_1 \\ \vdots \\ \rho\hat{Y}_{L-1} \\ \rho Y_1 \\ \vdots \\ \rho Y_{N-L} \end{pmatrix}, \mathbf{f}(\mathbf{y}) = \begin{pmatrix} 0 \\ 0 \\ 0 \\ 0 \\ \vdots \\ 0 \\ \dot{\omega}_1 M_1 \\ \vdots \\ \dot{\omega}_{N-L} M_{N-L} \end{pmatrix}, \mathbf{h}(\mathbf{y}) = \begin{pmatrix} \rho u \\ \rho u^2 + p - \tau \\ \rho u\left(e + \frac{u^2}{2}\right) + u\,(p - \tau) + J^q \\ \rho u\hat{Y}_1 + \hat{J}_1^m \\ \vdots \\ \rho u\hat{Y}_{L-1} + \hat{J}_{L-1}^m \\ \rho u Y_1 + J_1^m \\ \vdots \\ \rho u Y_{N-L} + J_{N-L}^m \end{pmatrix}. \tag{3.23}$$

Here the vectors $\mathbf{y}$, $\mathbf{f}$, and $\mathbf{h}$ are all of length $N+2$. Equation (3.22) is solved in two steps, a reaction step and a convection diffusion step, using Strang-splitting [39].

This splitting results in second order accuracy in time if both steps have the same accuracy in time.

3.3.1 Reaction step

In Step 1 or the reaction step, the following equation is solved at each spatial point

$$\frac{\partial \mathbf{y}}{\partial t} = \mathbf{f}(\mathbf{y}). \tag{3.24}$$

The first $2+L$ equations of Equation (3.24) are homogeneous and can be integrated exactly to give

$$\rho = \rho_0; \qquad u = u_0; \qquad e = e_0; \qquad \hat{Y}_l = \hat{Y}_{l_0}, \quad (l = 1, \ldots, L-1). \tag{3.25}$$

The remaining $N - L$ species evolution equations in Equation (3.24) reduce to the following PDEs, which are treated at each point in space as ODEs with ρ, u, e, and $\hat{Y}_l$ held constant to the values given in Equation (3.25) every time Step 1 is repeated:

$$\frac{\partial Y_i}{\partial t} = \frac{\dot{\omega}_i M_i}{\rho_0}, \qquad (i = 1, \ldots, N-L). \tag{3.26}$$

It is noted that even though during a single reaction step at each spatial point, the values of ρ_0, e_0, u_0, and $\hat{Y}_{l_0}$ do not change; because of convection and diffusion, in general, all vary in physical space and will change with time.

Equation (3.26) coupled with the algebraic equations (3.25), (3.11), (3.13), (3.14), (3.16), and (3.17) are solved in the reaction step at each spatial point to obtain the species and element mass fractions, pressure, temperature and density at the end of the reaction time step. These differential algebraic equations together are identical to the system of Equations (2.38-2.42) modeling the isochoric CASHPR as discussed in Chapter 2. Hence, in the reaction step each spatial point is treated as the isochoric CASHPR. Also these differential algebraic equations can be written in

a compact form as following

$$\frac{d\mathbf{Y}}{dt} = \mathbf{f}(\mathbf{Y}), \tag{3.27}$$

where $\mathbf{Y} = (Y_1, \ldots, Y_{N-L})^T$ and $\mathbf{f}(\mathbf{Y}) = \left(\frac{\dot{\omega}_1 M_1}{\rho_0}, \ldots, \frac{\dot{\omega}_{N-L} M_{N-L}}{\rho_0}\right)^T$. This can be accomplished by inverting and substituting all the algebraic equations into Equation (3.26). However, inversion of all the algebraic equations cannot be done algebraically; instead, it is done numerically. Equations (3.13) and (3.25) with (3.11) are appropriate to determine the remaining L mass fractions not included in vector $\mathbf{Y}$. Assuming all the gases in the reactive mixture are thermally perfect, the specific internal energy of each component, e_i, is at most a function of temperature. Hence, knowledge of the mass fractions and the constant (within a single reaction step at a spatial point) mass-averaged specific internal energy e_0, allows one to use Newton's method to invert Equation (3.17) to form $T = T(Y_1, \ldots, Y_{N-L}; \rho_0, e_0, \hat{Y}_{1_0}, \ldots, \hat{Y}_{(L-1)_0})$. Hence, $\dot{\omega}_i$, which is in general a function of temperature, density, and species mass fractions, can now be considered as a function of only $N - L$ of the species mass fractions for fixed values of ρ_0, e_0, and $\hat{Y}_{l_0}$:

$$\dot{\omega}_i = \dot{\omega}_i(Y_1, \ldots, Y_{N-L}; \rho_0, e_0, \hat{Y}_{1_0}, \ldots, \hat{Y}_{(L-1)_0}), \qquad (i = 1, \ldots, N-L). \tag{3.28}$$

Both $\dot{\omega}_i$ and e_i can be easily evaluated using the Chemkin III [42] package.

Equation (3.27) is well posed and can be solved in its entirety by any standard implicit or explicit technique at every point in space. Because these equations are stiff, the LSODE software package [50] in full implicit mode is used, when solving the full set of Equation (3.26). Alternatively, Equation (3.26) can be solved using the ILDM method, described in Chapter 2, which systematically removes the stiffness associated with reactions. When using the ILDM method, a simpler explicit Runge-Kutta method for time advancement is used, which is second order accurate in time.

The size of the time step is dictated by the convection diffusion time step restriction discussed in the next section.

3.3.2 Convection diffusion step

In Step 2 or the convection diffusion step, the following equation, which is a set of PDEs, is solved for the convection diffusion step:

$$\frac{\partial \mathbf{y}}{\partial t} = -\frac{\partial}{\partial x}\mathbf{h}(\mathbf{y}). \tag{3.29}$$

Again, Equation (3.29) can be solved by a variety of standard discretization techniques developed for inert fluid mechanics. Here the WAMR technique is used, as discussed in detail by Vasilyev and Paolucci [54], [55]. The method is summarized as follows. At any given time step, the temperature, density, pressure, species mass fractions and velocity fields are projected onto a multilevel wavelet basis. The amplitudes of the wavelet basis functions give a measure of the importance of a particular wavelet mode. Additionally, one has available *a priori* error estimates, in contrast to most gradient-based adaptive mesh refinement techniques. All wavelets whose amplitude are below a defined threshold are removed. Calculations are performed for each wavelet whose amplitude is above the threshold (essential wavelets) and for a certain number below the threshold (neighboring wavelets). If at the completion of a time step, an essential wavelet has its amplitude drop below the threshold, it is reclassified as a neighboring wavelet or eliminated, and the neighboring region is adjusted; similarly, if a wavelet in the neighboring region has its amplitude become sufficiently large, it is reclassified as an essential wavelet, and the neighboring region is adjusted. The method is based on a collocation strategy using the auto-correlation function of the Daubechies scaling function of order four as the basis. A linearized trapezoidal (implicit) scheme in conjunction with GMRES

iterations is used for time advancement. The size of the time step is chosen to satisfy a CFL condition associated with the fastest local velocity.

3.4 ILDM for the reaction step

In the reaction step of the operator splitting technique, each discrete point in physical space behaves as the isochoric CASHPR, thus enabling the use of the ILDM method which provides a systematic way to overcome the severe stiffness which is associated with full chemical kinetics models of gas phase combustion, and thus significantly improves computational efficiency. In a closed, adiabatic, isochoric and homogeneous premixed calculation, the full $H_2/O_2/Ar$ model predicts the ratio of the time scale of the slowest reaction mode to that of the fastest reaction mode to typically reach values near 10^5, which indicates severe stiffness is present. The ILDM method systematically eliminates most of this stiffness by equilibrating fast time scale chemical processes and describing parametrically a low-dimensional manifold close to which slow time scale chemical processes evolve.

The computation of the ILDM for the isochoric CASHPR has been discussed in detail in Chapter 2. The behavior of the isochoric CASHPR can be described by trajectories in an $(n = N + 2)$-dimensional composition (phase) space. The $N + 2$ dependent variables ρ, e, Y_i $(i = 1, \ldots, N)$ form the coordinates of this $(N + 2)$-dimensional composition space. Using the analysis in Section 2.4, an m_d-dimensional ILDM can be identified in the composition space for fixed values of ρ_0, e_0, $\hat{Y}_{1_0}, \ldots, \hat{Y}_{(L-1)_0}$. Close to this m_d-dimensional ILDM only the m_d slowest time scales evolve, while the remaining fast time scale processes have equilibrated. A different ILDM is required for a different set of densities, internal energies and element mass fractions. Since in general reactive flow calculations one can expect all of these quantities to vary, the actual relevant dimension of the ILDM table which

must be formed has dimension $m_d + L + 1$ and can be tabulated numerically to give

$$Y_i = Y_i(Y_1, \ldots, Y_{m_d}, \rho, e, \hat{Y}_1, \ldots, \hat{Y}_{L-1}), \qquad (i = m_d + 1, \ldots, N), \tag{3.30}$$

$$T = T(Y_1, \ldots, Y_{m_d}, \rho, e, \hat{Y}_1, \ldots, \hat{Y}_{L-1}), \tag{3.31}$$

$$p = p(Y_1, \ldots, Y_{m_d}, \rho, e, \hat{Y}_1, \ldots, \hat{Y}_{L-1}), \tag{3.32}$$

where $Y_1, \ldots, Y_{m_d}$ $(m_d + L + 1 < N + 2)$ are the chosen reference variables for the table, and ρ, e, $\hat{Y}_1, \ldots, \hat{Y}_{L-1}$ are the remaining parameters. This ILDM table for the species mass fraction, temperature and pressure is generated by solving the ILDM equation (2.58) coupled with the parametric equation (2.95), and the ideal gas thermal and caloric state equations (3.16) and (3.17) for discrete values of the $m_d + L + 1$ parameters. The reference variables are chosen in such a way that the ILDM is single valued with respect to these variables for easy lookup. While there is no guarantee of single-valuedness, in the problems studied, it has been found that this is the case.

It is the dimension of the table, $m_d + L + 1$, which is critically important in the ILDM method. Many previously reported calculations have been restricted to premixed conditions in the isobaric and/or adiabatic limits, thus reducing the dimension of the table. In the calculations presented here, variable density and energy are intrinsic features of the flow; and by choosing $m_d = 1$ for the $H_2/O_2/Ar$ system, which has $L = 3$, in principle a table which has dimension five must be used. Because a uniformly premixed reactive mixture is studied, and because the earlier described simplified diffusion model has been employed, $L - 1 = 2$ independent element mass fractions remain constant throughout the calculations at $\hat{Y}_H = 0.01277$, $\hat{Y}_O = 0.10137$, reducing the effective dimension of the table to three; the variables of table parameterization are chosen to be Y_{H_2O}, ρ, and e.

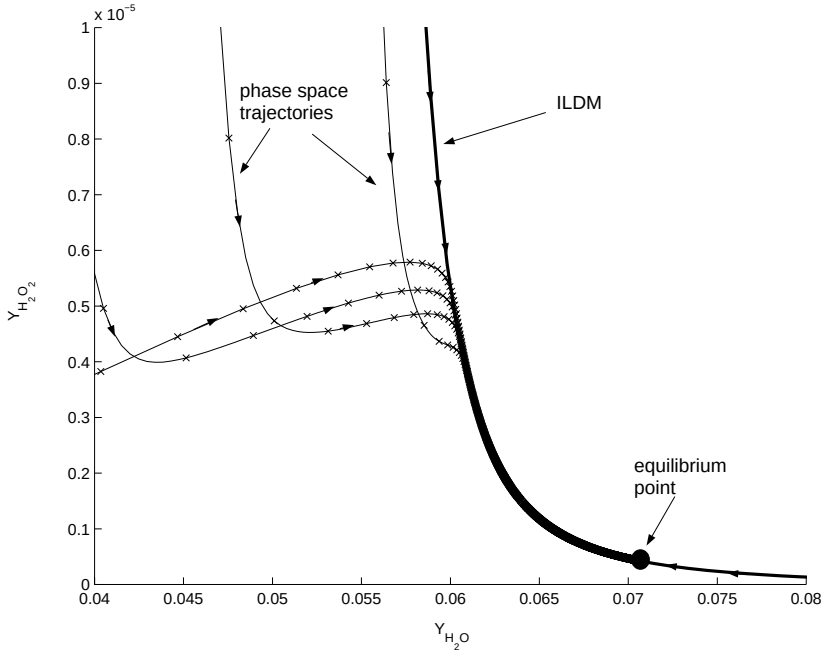

Figure 3.1. ILDM projection for 9 species 37 step reaction mechanism of $H_2/O_2/Ar$ combustion as function of Y_{H_2O} at constant values of $\rho = 0.5 \times 10^{-3}$ g cm^{-3}, $e = 8.0 \times 10^9$ erg g^{-1}. Element mass fractions fixed at $\hat{Y}_H = 0.01277$, $\hat{Y}_O = 0.10137$, $\hat{Y}_{Ar} = 0.88586$. Also plotted are trajectories from full time integration showing relaxation to the ILDM and equilibrium. The symbol 'x' denotes equally spaced 0.10 μs time intervals. Total time to relax to equilibrium is near 0.1 ms.

With $m_d = 1$, a projection of the ILDM for fixed density, internal energy, (as well as the always fixed element mass fractions), for the $H_2/O_2/Ar$ system is plotted in Figure 3.1 with Y_{H_2O} used as the reference independent variable for the ILDM and $Y_{H_2O_2}$ as the dependent variable. Mass fractions for all species, not shown here, are also available as functions of Y_{H_2O} for the same fixed density and internal energy. Also shown on the plot are projections of trajectories in this two-dimensional subspace for a variety of initial conditions. It is seen that all trajectories relax to the ILDM. As indicated on Figure 3.1, the relaxation from the initial state to the ILDM occurs on a relatively fast time scale on the order of microseconds, while once on the ILDM, the subsequent relaxation to final equilibrium occurs on a much slower

time scale on the order of 0.1 ms. The phase space trajectories appear to cross, but this is because they have been projected into a lower dimensional space.

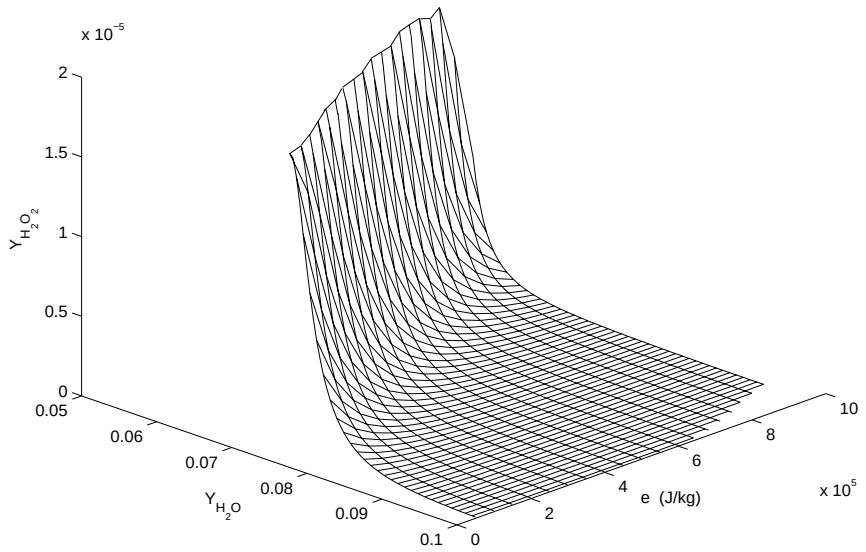

Figure 3.2. ILDM projection for 9 species 37 step mechanism of $H_2/O_2/Ar$ combustion giving $Y_{H_2O_2}$ as a function of Y_{H_2O} and e for constant $\rho = 0.5 \times 10^{-3}$ g cm^{-3}. Element mass fractions fixed at $\hat{Y}_H = 0.01277$, $\hat{Y}_O = 0.10137$, $\hat{Y}_{Ar} = 0.88586$.

A projection of the three-dimensional ILDM table for constant density and the same constant element mass fractions for the $H_2/O_2/Ar$ system is plotted in Figure 3.2, with Y_{H_2O} and e used as the reference independent variables and $Y_{H_2O_2}$ as the dependent variable. The portion of the ILDM depicted closely corresponds to values realized in the detonation calculation. Also, for the system studied here, the dependency of all variables on density was weak for the range of realized density values.

Instead of solving the full Equation (3.27) at each spatial point in the reaction step, only m_d of the species equations (3.26) for the reference species $Y_1, \ldots, Y_{m_d}$ are

solved, while the ILDM table depicted in Equations (3.30-3.32) is used to obtain all necessary secondary variables. However, this ILDM technique can only be used for those spatial points if the state of the reactive mixture at the corresponding spatial points in the reaction step is close to the ILDM subspace in the composition space.

When using ILDMs with $m_d = 1$, only one differential equation ($\frac{dY_1}{dt} = \frac{\dot{\omega}_1 M_1}{\rho_0}$) associated with the reference species is integrated. If the state of the reactive mixture is far from the ILDM subspace, it is important to incorporate the off-ILDM kinetics in some fashion. Here the full Equations (3.27) are integrated using LSODE in implicit mode. The integration is switched from full integration to the ILDM method, for a certain spatial location in the reactive flow system, when the $\mathbf{L}_2$ distance norm between the actual state of the reactive mixture in the composition space and the ILDM subspace is less than 1×10^{-6}. While this reduces the efficacy of the ILDM method, it is critical to avoid large phase errors associated with projecting onto the ILDM from a remote region of the composition space. In other words, while all processes are typically destined to reach the ILDM subspace, it is critical for the proper sequencing of events that they reach the ILDM subspace at the correct time, and reach the right point on the ILDM subspace. In practice, during calculations, it is found that the ILDM method can be used in cells or spatial points which have recently been shocked, have passed through the bulk of the induction zone, and are well within the thermal explosion region. The ILDM method is also applied to points in the trailing rarefaction wave.

The convection diffusion step results in to a perturbation off the ILDM. Subsequent to the perturbation, there is a fast relaxation to the ILDM corresponding to a new set of conserved parameters which are ρ_0 and e_0 in the premixed detonation problem. This is accomplished here by projection onto the ILDM while holding the reference variable, Y_{H_2O}, constant. This projection is allowed by the large time scale

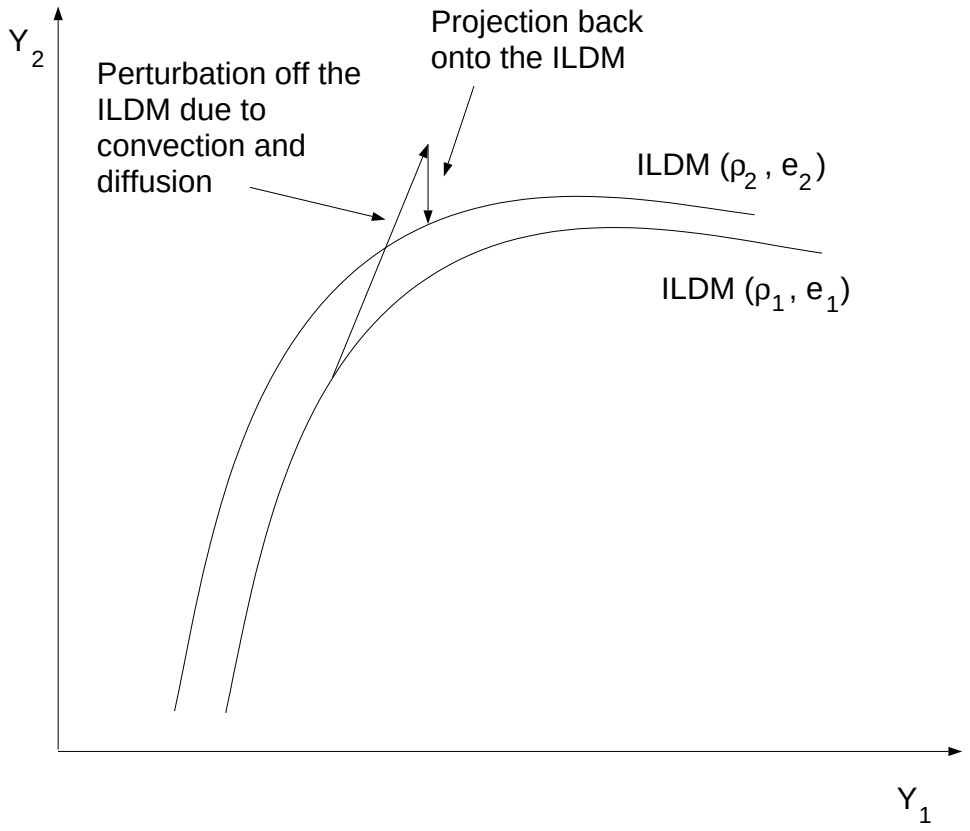

Figure 3.3. Sketch of projection back to the ILDM of new energy and density levels following perturbation due to convection and diffusion.

difference between slow chemical/fluid time scales and fast chemical time scales as long as convective and diffusive effects are not large. It is noted that for this reaction mechanism the fast directions are nearly orthogonal to the slow variable, Y_{H_2O}, on the ILDM. Figure 3.3 depicts how this projection is accomplished. A slightly more accurate alternative would be to project to the ILDM in the direction of the vectors associated with the local fast eigenmodes. In contrast to many implementations of the ILDM method for partial differential equations modeling reactive flow systems, all variables are convected and diffused, not just slow variables. While this comes at a cost of solving more equations, it is necessary to preserve the consistency of the Strang operator splitting method.

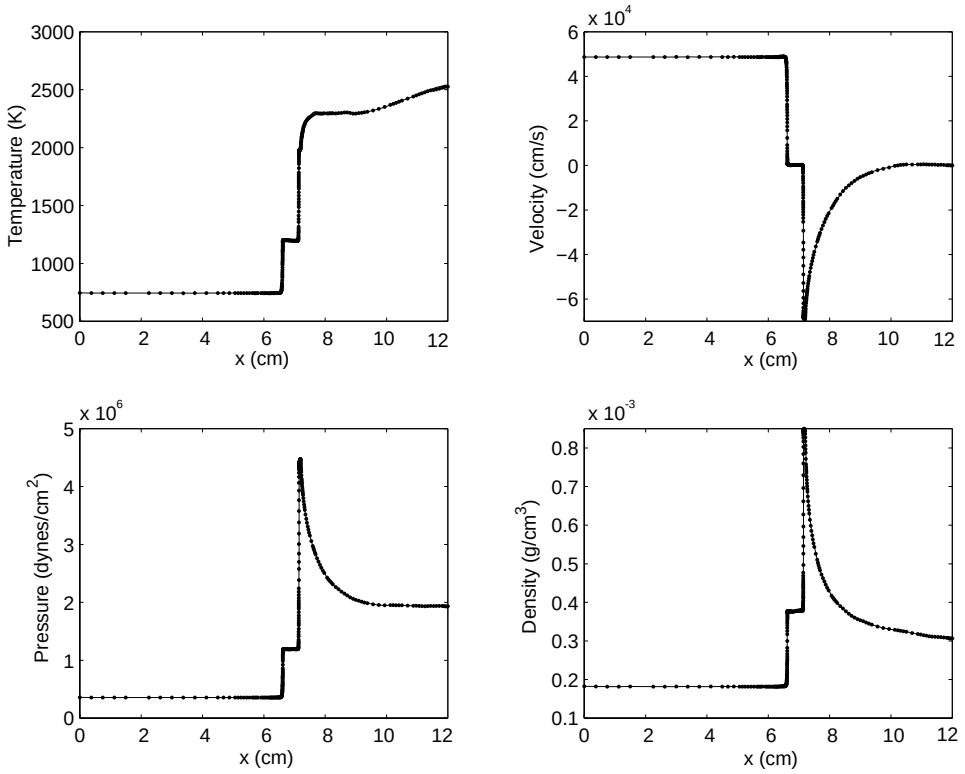

Figure 3.4. Predictions of temperature, velocity, pressure, and density vs. distance at $t = 195\ \mu s$ using a maximum of 300 collocation points, 15 wavelet scale levels for full chemical kinetics (solid lines) and ILDM kinetics (dots) for viscous $H_2/O_2/Ar$ detonation.

Results for the detonation calculations in a shock tube are given here. Figure 3.4 gives predictions of temperature, velocity, pressure, and density vs. distance at time $t = 195\ \mu$s. At this time, the lead right-traveling inert shock has reflected off the right wall and is propagating to the left with its head near $x = 6.5$ cm at a pressure and temperature of 11.88×10^5 dynes cm^{-2} and 1196 K, respectively. Close behind the lead shock is the much stronger, left-propagating ZND detonation wave, with its head near $x = 7.2$ cm. All of the usual salient features of a ZND detonation are predicted here. The von Neumann spike is predicted at a pressure of around 45.0×10^5 dynes cm^{-2}, and the pressure relaxes to near 20.0×10^5 dynes cm^{-2} at

the right boundary. The post-detonation temperatures are near 2500 K, and the velocity is seen to relax to a value of zero at the right boundary.

The solid lines show the predictions of the full chemical kinetics model. The dots show the results of the calculations using the ILDM method resolving only the slowest reaction time scale; this can be interpreted as one-step chemistry with a rational fidelity to full chemical kinetics. It is seen on this scale that the predictions are very similar Examination of the local eigenvalues indicates that use of the ILDM method suppresses temporal resolution of chemical processes which occur faster than times scales of the order of 0.1 μs. For a given ρ and e, the ILDM is constructed as described in Section 2.4. This is done for sixteen values of ρ ranging from 0.25×10^{-3} g cm^{-3} to 1.00×10^{-3} g cm^{-3} in steps of 0.05×10^{-3} g cm^{-3}. Similarly nineteen values of e ranging from 0.5×10^{9} erg g^{-1} to 9.5×10^{9} erg g^{-1} are used in steps of 0.5×10^{9} erg g^{-1}. Hence, 304 slices such as shown in Figure 3.1 were constructed. Finally each ILDM was stored with an equally spaced parameterization of 100 values of Y_{H_2O} for easy lookup. Thus, the ILDM table has a size of $16 \times 19 \times 100$. For easy lookup, a uniform grid has been used.

For this particular problem, use of the full integration technique requires three times as much computational time as the ILDM technique. It is noted however, that general conclusions regarding computational efficiency are difficult to draw as the savings realized will be model-dependent as well as initial condition-dependent. The bulk of the savings are realized near the end of the computation as more and more spatial cells have become chemically activated. At the beginning of the calculation, when most spatial cells are in a cold state far from equilibrium, there is no savings. The calculation itself took roughly ten hours on a 330 MHz Sun Ultra10 workstation.

Figure 3.5 shows similar results for the species mass fractions at the same time, $t = 195$ μs. Steep gradients in mass fractions are predicted near the detonation

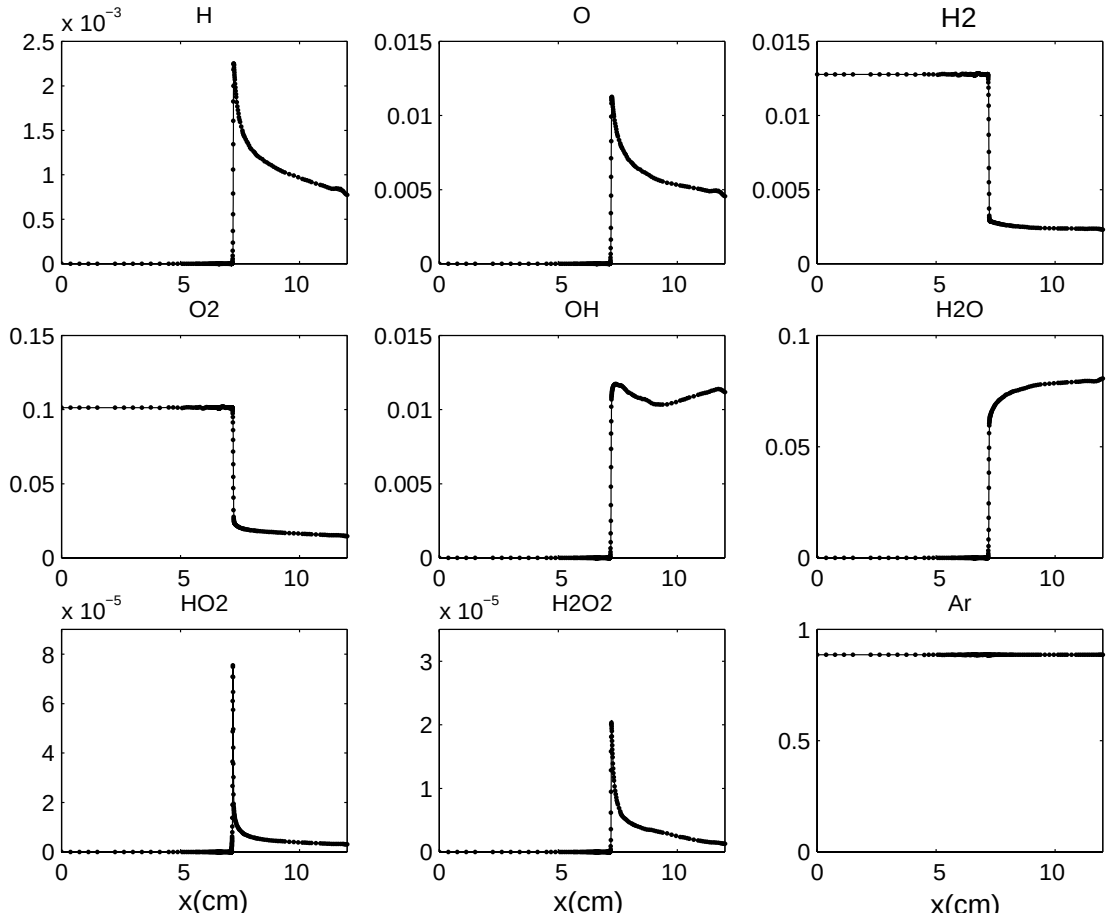

Figure 3.5. Predictions of species mass fractions vs. distance at $t = 195$ μs using a maximum of 300 collocation points, 15 wavelet scale levels for full chemical kinetics (solid lines) and ILDM kinetics (dots) for viscous $H_2/O_2/Ar$ detonation.

front. As expected, HO_2, H, and H_2O_2 mass fractions have relatively small values which peak at the detonation front. Under these conditions, the major product is H_2O. On the length scales shown in Figures 3.4 and 3.5, the results appear very similar to the inviscid predictions of Fedkiw, *et al.* [51].

The WAMR algorithm adapts to the features of the flow. Figure 3.6 depicts the distribution of the collocation points and their wavelet scale levels at two different times, first at $t = 180$ μs, when the lead shock and the approaching detonation are

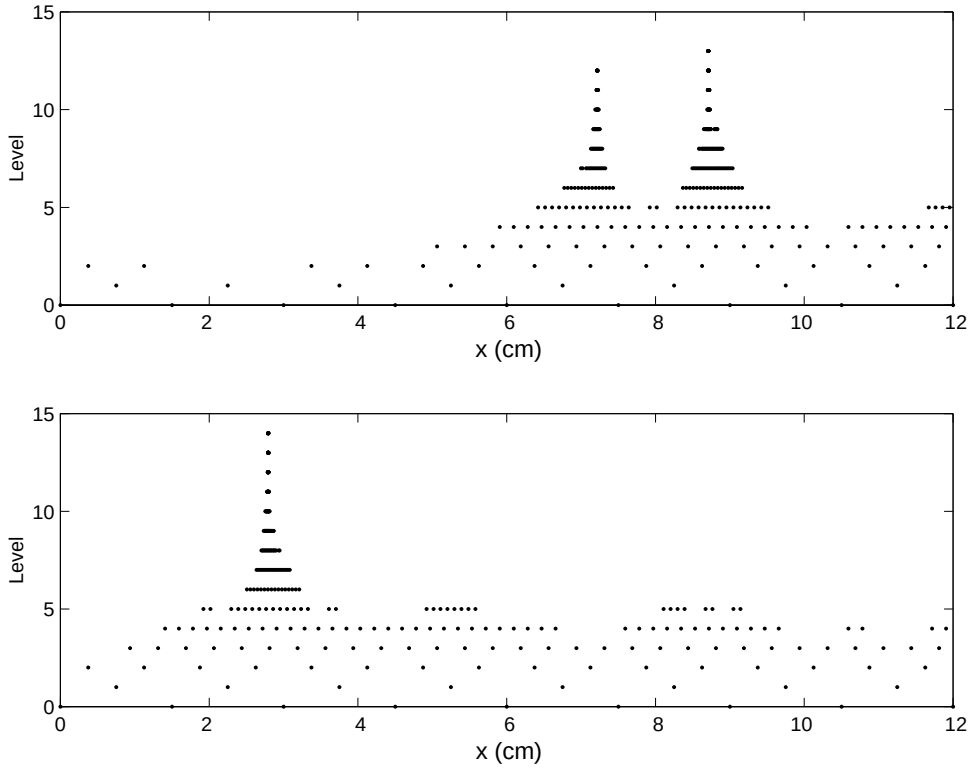

Figure 3.6. Spatial distribution of collocation points and wavelet levels at $t = 180$ μs (two shock structure), and $t = 230$ μs (single shock structure) demonstrating grid adaption.

present, and later at $t = 230$ μs, after they have merged. In both cases, at most three hundred collocation points and fifteen wavelet scale levels were sufficient to capture the flow features.

The effects of diffusion are clearly seen when one examines finer length scales. Figure 3.7 shows two views of pressure vs. distance at a somewhat later time, $t = 230$ μs, by which time the detonation wave has overtaken the reflected shock. In the second subfigure, the same length scale is shown as in Figure 3.4. The first subfigure shows a 120 factor spatial magnification near the lead shock. In this figure the dots represent the actual collocation points as chosen by the WAMR technique. It is clear

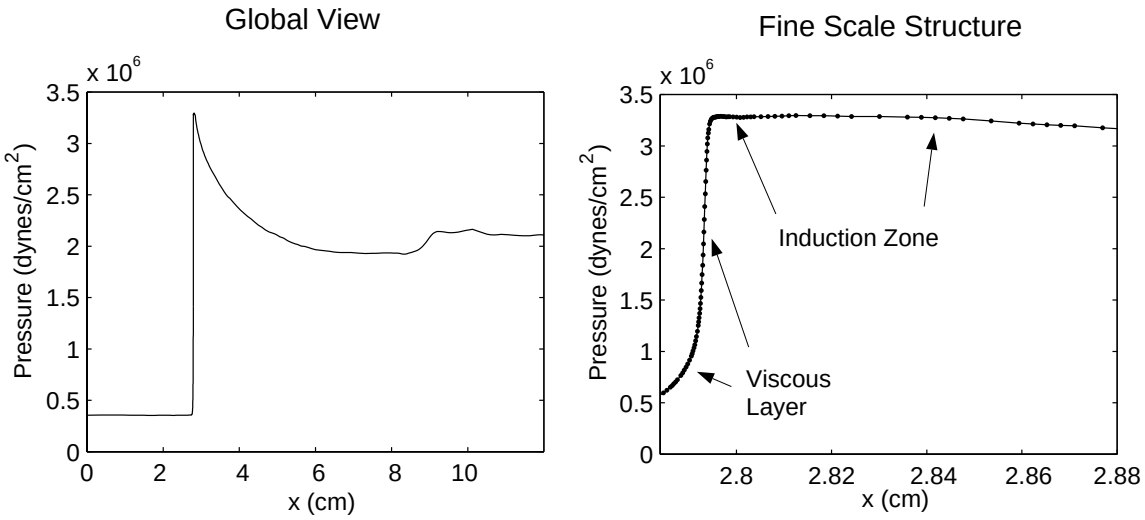

Figure 3.7. Predictions of pressure vs. distance at $t = 230$ μs on a coarse and fine length scales demonstrating the spatial resolution of viscous and induction zone structures.

on this scale that both the viscous shock and chemical induction zones have been resolved. Here it is predicted that the shock is essentially inert and has a thickness of roughly 5×10^{-3} cm.

The induction zone, a region of essentially constant pressure, temperature, and density, has a thickness of roughly 47×10^{-3} cm. In the induction zone many reactions are occurring, giving rise to a release of energy which, because of the extreme temperature sensitivity of reaction rates, accumulates to an extent that a thermal explosion occurs at the end of the induction zone. While the wavelet representation certainly has captured these thin layers, it is noted that because it was chosen not to use individual species mass fractions as part of the adaption criteria, some finer scale reaction zone structures have not been spatially resolved.

In the process of understanding the time scales associated with the kinetics of a spatially homogeneous reactive mixture, all time scales have been computed through an eigenvalue analysis. This analysis indicates that reaction time scales as small as sub-nanosecond are predicted by the standard models of Maas and Warnatz [62], and

Maas and Pope [1]. Such small time scales give rise to small reaction induced spatial scales which violate the continuum assumption. It is essentially for this reason that spatial grid is not adapted to capture the subsequent extremely fine length scales associated with individual species mass fraction variation. This issue is pervasive in most calculations involving detailed chemical kinetics, but it is not often addressed since standard spatial discretization algorithms are unable to resolve this range of scales.

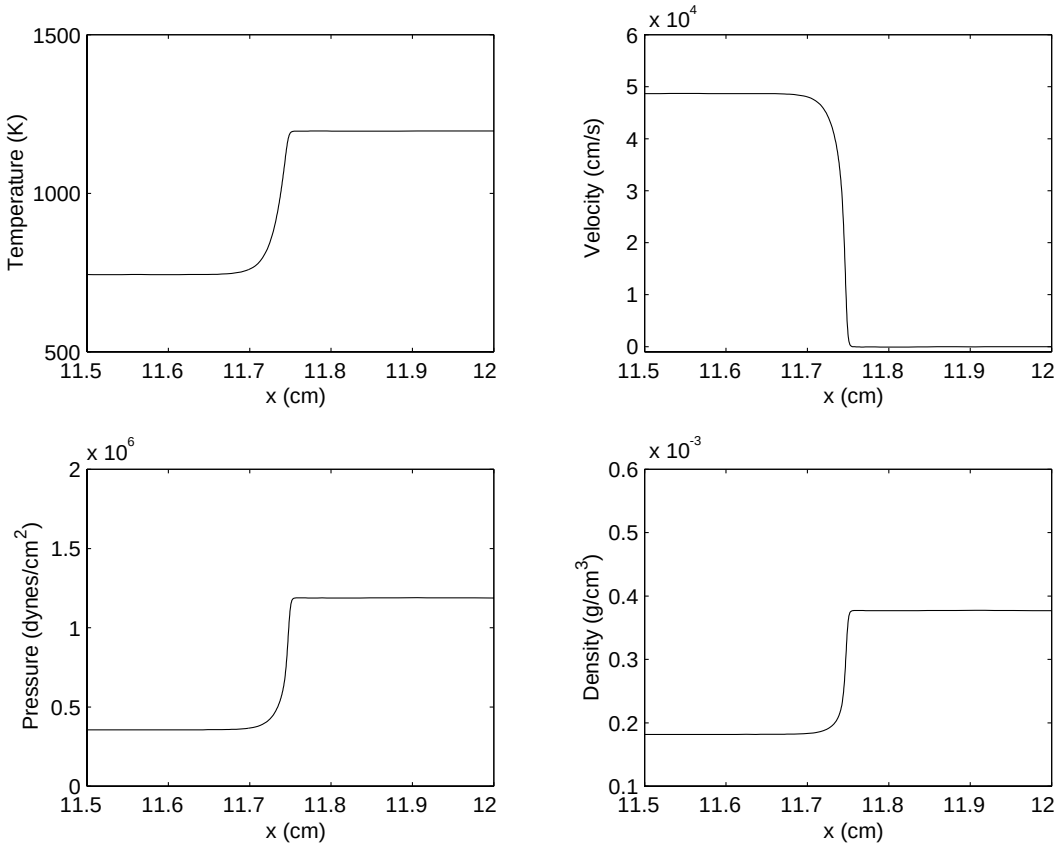

Figure 3.8. Predictions of temperature, velocity, pressure, and density vs. distance before commencement of significant reaction but after shock reflection using a reactive Navier-Stokes model ($t = 177$ μs).

As discussed by Menikoff [58], inviscid codes introduce pseudo-entropy layers near regions of wave-wave and wave-boundary interactions. These often appear as $O(1)$ anomalies in temperature and density near the wall in shock tube predictions.

Figure 3.8 shows the results of the viscous calculation in a spatial zone near the wall just after shock reflection. On this scale, there is no apparent entropy layer near the wall.

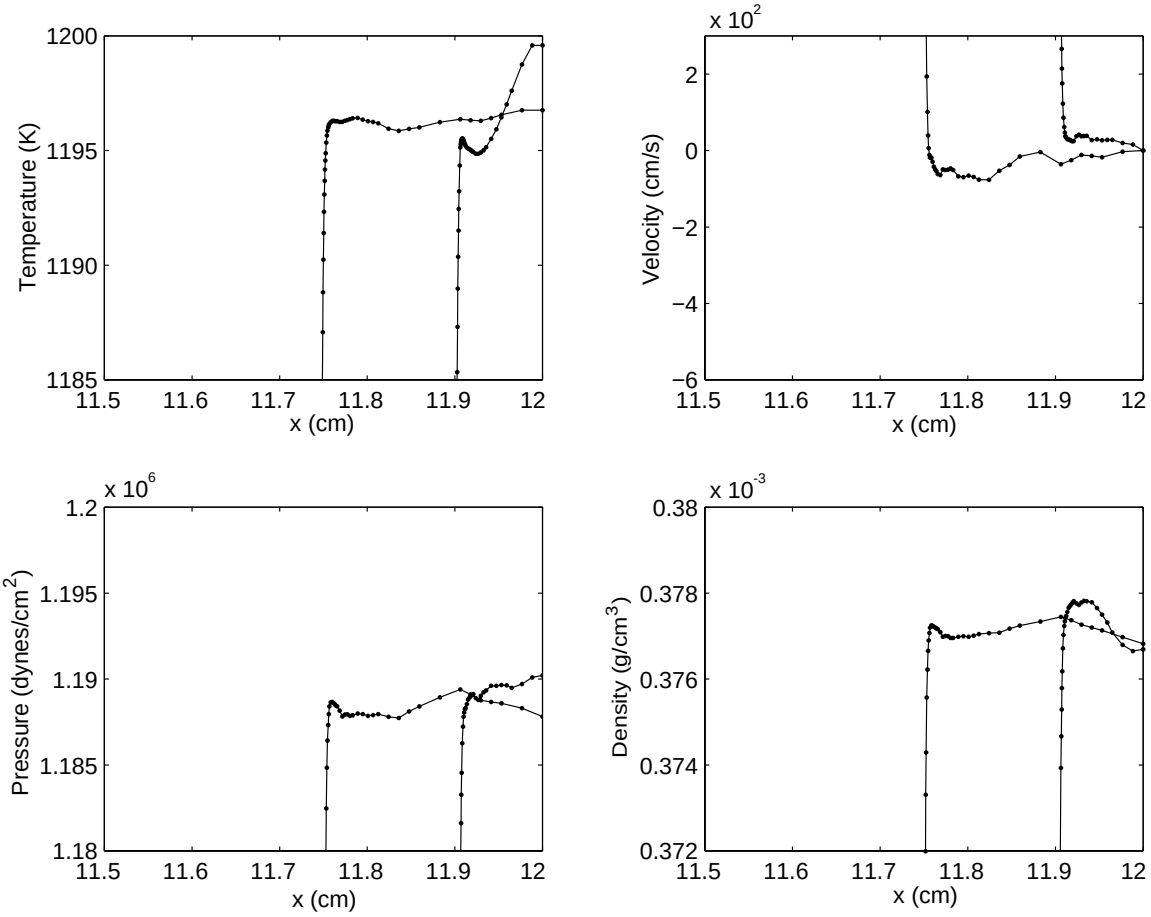

Figure 3.9. Close-up view of predictions of temperature, velocity, pressure, and density vs. distance before commencement of significant reaction but just after shock reflection ($t = 174$ μs) and slightly later ($t = 177$ μs).

A finer scale examination of the dependent variables, shown in Figure 3.9, reveals what is happening. It is evident from the temperature plot that there is a small entropy layer near the wall, here physically induced. The physical diffusion mechanisms rapidly smear the layer within a few microseconds. It may be possible

that the correct capturing of a temperature-sensitive ignition event near a wall could be critically dependent on having the correct physics in the model. For the viscous calculation, a temperature rise of roughly 5 K is predicted. Performing a similar calculation with an inviscid Godunov-based model with first order upwind spatial discretization near regions of steep gradients using 400 evenly spaced grid points induces a temperature rise of nearly 20 K, which persists. It might be expected that numerical diffusion would dissipate this temperature spike. However, as detailed by LeVeque [65], the leading order numerical diffusion coefficient for such methods is proportional to the local fluid particle velocity. As the fluid particle velocity at the wall and in the region downstream of the reflected shock is zero, the effects of numerical diffusion here are, at most, confined to higher order. This temperature rise, similar to that obtained by Fedkiw, *et al.* [51] [66], has been obtained by effectively imposing an adiabatic boundary condition done through extrapolation. It is noted that this type of condition is inconsistent with the inviscid governing equations.

In concluding, it is pointed out that decreasing the viscosity an order of magnitude to the more appropriate value does not change the results, as the viscous and induction length scales (which are the smallest and next to smallest length scales, respectively) are sufficiently segregated. A decrease of the viscosity would simply further segregate these scales. Because of the segregation, there is little interaction between these scales. Thus reducing viscosity will only reduce the shock thickness.

In addition, the value of viscosity, be it physical or numerical, has a substantial effect on the entropy layer resulting from shock reflection, as discussed above. In order to properly capture this entropy layer, one must have a numerical viscosity which is much smaller than the physical viscosity. This is the case in the viscous

calculations and is clearly not in inviscid calculations. In inviscid calculations, the dynamics of the entropy layers are dependent upon the particular discretization employed as well as artificial flux boundary conditions used.

The issues relating to scale segregation and entropy layer have been verified by performing calculations using a somewhat smaller value of viscosity without any noticeable changes from the results reported here.

CHAPTER 4

APPROXIMATE SLOW INVARIANT MANIFOLD FOR REACTIVE FLOW SYSTEMS

In this chapter a theoretical development of the Approximate Slow Invariant Manifold (ASIM) for reactive flow systems will be given. The ASIM approximately describes the slow dynamics of a reactive flow system once the fast dynamics has been equilibrated. The ASIM is then used to obtain reduced model equations for a simple reaction diffusion system and a premixed laminar flame for ozone decomposition. The ASIM is also compared with the Mass Pope Projection (MPP) method which is a strategy to extend the ILDM method to reactive flow systems.

4.1 Reactive flow equations

The governing equations for a one-dimensional reacting flow system can be written in the following compact form:

$$\frac{\partial \mathbf{y}}{\partial t} = \mathbf{f}(\mathbf{y}) - \frac{\partial}{\partial x}\left(\mathbf{h}(\mathbf{y})\right), \tag{4.1}$$

where $\mathbf{y} \in \mathbb{R}^n$ represents a set of dependent variables, the vector function $\mathbf{h}(\mathbf{y})$ represents the convective and diffusive fluxes, and the vector function $\mathbf{f}(\mathbf{y})$ represents the reaction source term. The independent time and space variables are t and x, respectively.

The reactive flow model equations are rewritten in terms of a new set of variables defined by $\mathbf{z} = \tilde{\mathbf{V}}\mathbf{y}$. The eigenvector matrix of the Jacobian, $\mathbf{J}$, of the source term

$\mathbf{f}(\mathbf{y})$ is represented by $\mathbf{V}$ and its is defined in Equation (2.51). Note that the basis, $\mathbf{V}$, is based only on the chemistry of a spatially homogeneous reactive system. A better basis on which to project would take account of the infinite-dimensional eigenfunctions associated with the convection diffusion operator. This, however, is difficult.

Equation (4.1) can be rewritten as

$$\frac{1}{\lambda_{(i)}}\left(\frac{\partial z_i}{\partial t}+\tilde{\mathbf{v}}_i\sum_{j=1}^{n}\frac{\partial \mathbf{v}_j}{\partial t}z_j\right)=z_i+\frac{1}{\lambda_{(i)}}\left(\tilde{\mathbf{v}}_i\mathbf{g}\right)-\frac{1}{\lambda_{(i)}}\left(\tilde{\mathbf{v}}_i\frac{\partial \mathbf{h}}{\partial x}\right),\quad (i=1,\ldots,n),\ (4.2)$$

where $\mathbf{g}=\mathbf{f}-\mathbf{J}\mathbf{y}$, and the right eigenvectors $\mathbf{v}_i$ and the left eigenvectors $\tilde{\mathbf{v}}_i$ are defined in Equation (2.51). It is assumed that only the dynamics of the processes occurring at time scales of $\mathcal{O}\left(\frac{1}{|\lambda_{(m)}|}\right)$ or slower are relevant, and that a spectral gap exists between $|\lambda_{(m)}|$ and $|\lambda_{(m+1)}|$.

The left hand side of Equation (4.2) is $\mathcal{O}\left(\frac{1}{|\lambda_{(m+1)}|}\right)$ for $i=m+1,\ldots,n$, while the right hand side of Equation (4.2) is $\mathcal{O}(1)$. By neglecting all the terms of $\mathcal{O}\left(\frac{1}{|\lambda_{(m+1)}|}\right)$ from the left hand side of Equation (2.55), the fast processes are effectively equilibrated, and the slow dynamics of the system can be approximated by the following set of partial differential algebraic equations

$$\frac{1}{\lambda_{(i)}}\left(\frac{\partial z_i}{\partial t}+\tilde{\mathbf{v}}_i\sum_{j=1}^{n}\frac{\partial \mathbf{v}_j}{\partial t}z_j\right)=z_i+\frac{1}{\lambda_{(i)}}\left(\tilde{\mathbf{v}}_i\mathbf{g}\right)-\frac{1}{\lambda_{(i)}}\left(\tilde{\mathbf{v}}_i\frac{\partial \mathbf{h}}{\partial x}\right),\qquad (i=1,\ldots,m),\ (4.3a)$$

$$0=z_i+\frac{1}{\lambda_{(i)}}\left(\tilde{\mathbf{v}}_i\mathbf{g}\right)-\frac{1}{\lambda_{(i)}}\left(\tilde{\mathbf{v}}_i\frac{\partial \mathbf{h}}{\partial x}\right),\qquad (i=m+1,\ldots,n).\ (4.3b)$$

In writing Equation (4.3b), it is assumed that $\|\mathbf{g}\|$ can be $\mathcal{O}\left(|\lambda_{(m+1)}|\right)$ or greater, and hence, the second term is not neglected. If convection and diffusion processes occur at time scales which are slower than the fast chemical time scales of $\mathcal{O}\left(\frac{1}{|\lambda_{(m+1)}|}\right)$, then the third term $\frac{1}{\lambda_{(i)}}\left(\tilde{\mathbf{v}}_i\frac{\partial \mathbf{h}}{\partial x}\right)$ in Equation (4.3b) can be neglected,

as it becomes $\mathcal{O}\left(\frac{1}{|\lambda_{(m+1)}|}\right)$ or smaller, and hence, Equation (2.58) is obtained. Instead, if convection and diffusion time scales are of the same order as the fast chemical time scales, then such an approximation cannot be made as the third term in Equation (4.3b) will become $\mathcal{O}(1)$. No robust analysis exists to determine convection and diffusion time scales *a priori*. It is assumed that convection and diffusion processes occur at time scales of $\mathcal{O}\left(\frac{1}{|\lambda_{(p)}|}\right)$ $(m < p < n)$ and slower. Then by equilibrating the fast dynamics, the slow dynamics of the system can be approximated by the following set of partial differential algebraic equations

$$\frac{1}{\lambda_{(i)}}\left(\frac{\partial z_i}{\partial t} + \tilde{\mathbf{v}}_i \sum_{j=1}^{n} \frac{\partial \mathbf{v}_j}{\partial t} z_j\right) = z_i + \frac{1}{\lambda_{(i)}}\left(\tilde{\mathbf{v}}_i \mathbf{g}\right) - \frac{1}{\lambda_{(i)}}\left(\tilde{\mathbf{v}}_i \frac{\partial \mathbf{h}}{\partial x}\right), \qquad (i = 1, \ldots, m), \tag{4.4a}$$

$$0 = z_i + \frac{1}{\lambda_{(i)}}\left(\tilde{\mathbf{v}}_i \mathbf{g}\right) - \frac{1}{\lambda_{(i)}}\left(\tilde{\mathbf{v}}_i \frac{\partial \mathbf{h}}{\partial x}\right), \qquad (i = m+1, \ldots, p), \tag{4.4b}$$

$$0 = z_i + \frac{1}{\lambda_{(i)}}\left(\tilde{\mathbf{v}}_i \mathbf{g}\right), \qquad (i = p+1, \ldots, n). \tag{4.4c}$$

These equations can be rewritten in a more convenient form as

$$\tilde{\mathbf{V}}_s \frac{\partial \mathbf{y}}{\partial t} = \tilde{\mathbf{V}}_s \mathbf{f} - \tilde{\mathbf{V}}_s \frac{\partial \mathbf{h}}{\partial x}, \tag{4.5a}$$

$$\mathbf{0} = \tilde{\mathbf{V}}_{fs} \mathbf{f} - \tilde{\mathbf{V}}_{fs} \frac{\partial \mathbf{h}}{\partial x}, \tag{4.5b}$$

$$\mathbf{0} = \tilde{\mathbf{V}}_{ff} \mathbf{f}, \tag{4.5c}$$

where now

$$\tilde{\mathbf{V}}_f = \left(\begin{array}{ccc} - & \tilde{\mathbf{v}}_{m+1} & - \\ & \vdots & \\ - & \tilde{\mathbf{v}}_p & - \\ \hline - & \tilde{\mathbf{v}}_{p+1} & - \\ & \vdots & \\ - & \tilde{\mathbf{v}}_n & - \end{array} \right) = \left(\begin{array}{c} \tilde{\mathbf{V}}_{fs} \\ \hline \tilde{\mathbf{V}}_{ff} \end{array} \right), \tag{4.6}$$

where the matrix $\tilde{\mathbf{V}}_{fs}$ has dimensions $(p-m)\times n$ and its row vectors contain the left eigenvectors associated with the time scales $\frac{1}{|\lambda_{(m+1)}|}, \ldots, \frac{1}{|\lambda_{(p)}|}$, and the matrix $\tilde{\mathbf{V}}_{ff}$ has dimensions $(n-p)\times n$ and its row vectors contain the left eigenvectors associated with the time scales $\frac{1}{|\lambda_{(p+1)}|}, \ldots, \frac{1}{|\lambda_{(n)}|}$. The matrices $\tilde{\mathbf{V}}_s$ and $\tilde{\mathbf{V}}_f$ are same as that used in Equation (2.57). The reduced PDEs in Equation (4.5a) describe the time evolution of the slow dynamics, and are solved in conjunction with Equations (4.5b) and (4.5c). The stiffness due to the reaction source term in Equation (4.1) is substantially reduced in Equations (4.5).

Hence, analogous to the ILDM for a spatially homogeneous reactive system, the *infinite-dimensional* Approximate Slow Invariant Manifold (ASIM) for the reactive flow system is given by

$$\tilde{\mathbf{V}}_{fs}\mathbf{f} - \tilde{\mathbf{V}}_{fs}\frac{\partial \mathbf{h}}{\partial x} = \mathbf{0}, \tag{4.7a}$$

$$\tilde{\mathbf{V}}_{ff}\mathbf{f} = \mathbf{0}. \tag{4.7b}$$

The ASIM is a slow manifold which accounts for the effects of convection and diffusion, and close to it slow dynamics occurs once all fast time scale processes have equilibrated. The system of differential algebraic equations representing the ASIM have to be solved in physical space dimensions together with the prescribed boundary conditions. It is obvious that for two- and three-dimensional reactive flow

equations the ASIM is described by a set of elliptic partial differential algebraic equations.

4.2 Simple example

The simple system in Equation (2.64) of Chapter 2 is extended by including diffusion effects in one spatial dimension so as to obtain an equation of the form of Equation (4.1). Specifically $\mathbf{y}$, $\mathbf{f}(\mathbf{y})$ and $\mathbf{h}(\mathbf{y})$ are chosen so as to obtain the following system of equations

$$\frac{\partial y_1}{\partial t} = -y_1 + \mathcal{D}\frac{\partial^2 y_1}{\partial x^2}, \tag{4.8a}$$

$$\frac{\partial y_2}{\partial t} = -\gamma y_2 + \frac{(\gamma-1)y_1 + \gamma y_1^2}{(1+y_1)^2} + \mathcal{D}\frac{\partial^2 y_2}{\partial x^2}. \tag{4.8b}$$

The chemical time scales are 1 and γ^{-1}, while the diffusion time scales depend on the parameter $\mathcal{D}$ and local spatial gradients. The ILDM for this system is given by Equation (2.68).

A spatial domain of $x \in [0,1]$ and the following boundary conditions, which lie on the ILDM, are chosen

$$\mathbf{y}(t,0) = \begin{pmatrix} 0 \\ \\ 0 \end{pmatrix}, \qquad \mathbf{y}(t,1) = \begin{pmatrix} 1 \\ \\ \frac{1}{2} + \frac{1}{4\gamma(\gamma-1)} \end{pmatrix}. \tag{4.9}$$

The reason for choosing the boundary conditions to lie on the ILDM will be clarified later. The following initial conditions are chosen which, for convenience only, linearly interpolate between the two boundary conditions

$$\mathbf{y}(0,x) = \begin{pmatrix} x \\ \\ \left(\frac{1}{2} + \frac{1}{4\gamma(\gamma-1)}\right) x \end{pmatrix}. \tag{4.10}$$

Figure 4.1 depicts results at time $t = 5$ for the integration of the full system of Equations (4.8), for $\mathcal{D} = 0.1$, 0.01 and $\gamma = 10$. The numerical computations are

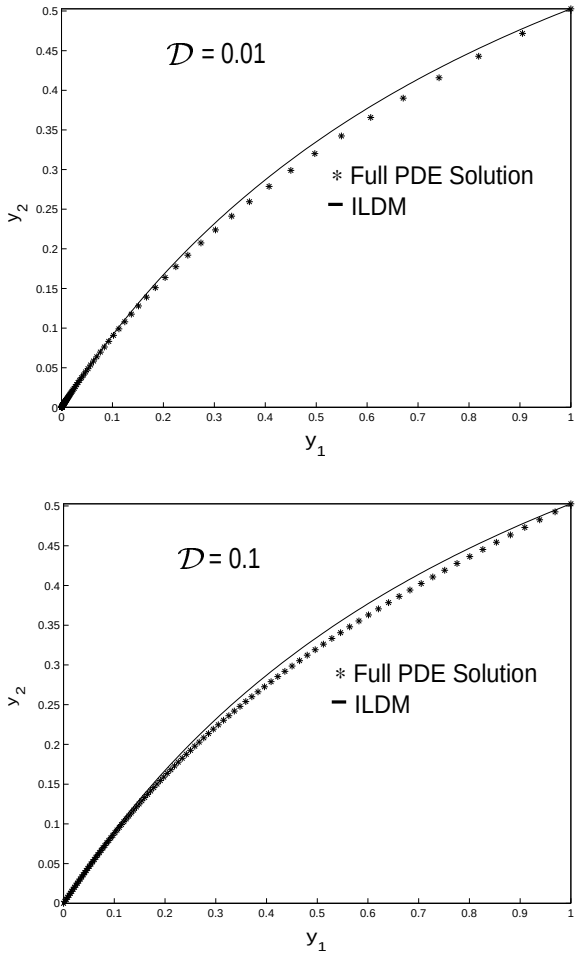

Figure 4.1. Comparison of solution of the full PDEs at $t = 5$ with the ILDM, for $\gamma = 10$ and $\mathcal{D} = 0.01$, 0.1, for Davis and Skodje's [36] model problem extended to include diffusion.

done using a uniform grid of 100 points in the spatial dimension x. A central difference approximation of second order is used for spatial discretization. A backward difference formula (BDF) of second order accuracy in time is used for time advancement with the aid of the LSODE [50] package. The solution is plotted in the two-dimensional phase space of the dependent variables. Stars represent the solution at various grid points in physical space. The time $t = 5$ is long enough for the fast time scales to equilibrate; in fact, the system is close to steady state. It can be seen from the figures that the steady state solution does not lie on the the ILDM.

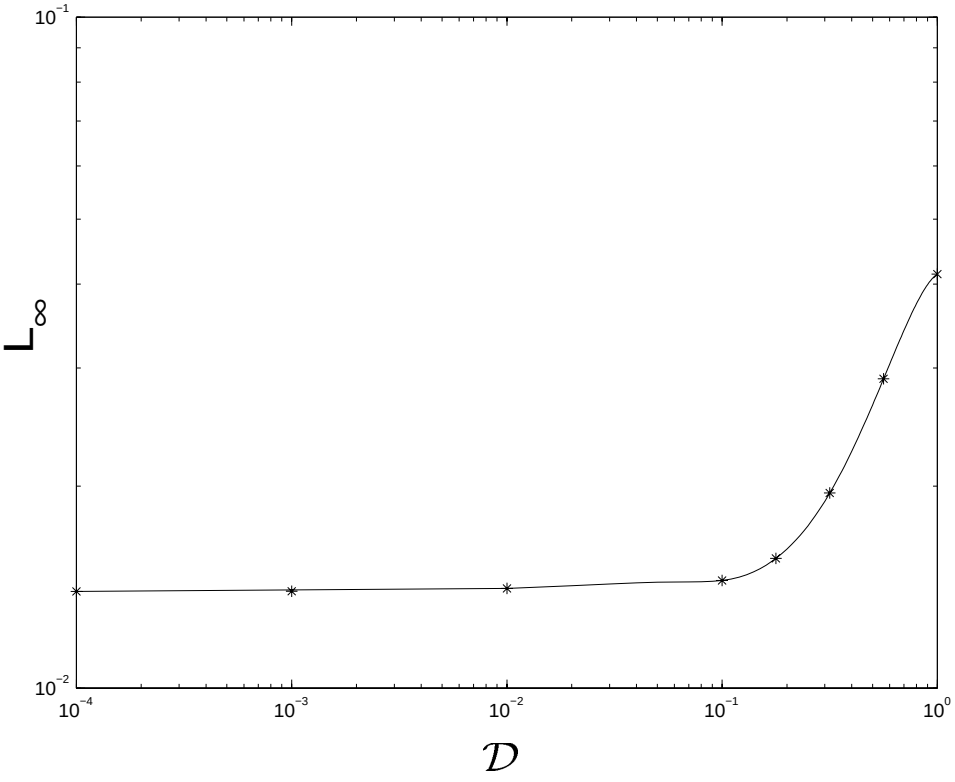

Figure 4.2. Maximum error ($\mathbf{L}_\infty[0,1]$) between solution of the full PDEs at $t = 5$ and the ILDM, for fixed $\gamma = 10$ and varying $\mathcal{D}$, for Davis and Skodje's [36] model problem extended to include diffusion. Stars indicate the values of $\mathcal{D}$ for which the computations were done.

Hence, forcing the solution onto the ILDM, or approximating the slow dynamics of Equations (4.8) by the ILDM, will lead to large errors. The effect of reducing the value of $\mathcal{D}$ is the appearance of sharper gradients in the solution in physical space. The maximum, or the $\mathbf{L}_\infty$ norm, of the difference between the full solution and the ILDM for fixed γ is seen in Figure 4.2 to remain large even when $\mathcal{D}$ is decreased.

Figure 4.3 depicts results at time $t = 5$, for the integration of the full system of Equations (4.8), for $\gamma = 100$ and $\mathcal{D} = 0.1$. It can be seen that for this case the solution is closer to the ILDM primarily because the diffusion term in Equation (4.3b) has a smaller contribution. Hence, the slow dynamics is better approximated by the ILDM for large γ. The $\mathbf{L}_\infty$ norm of the difference between the

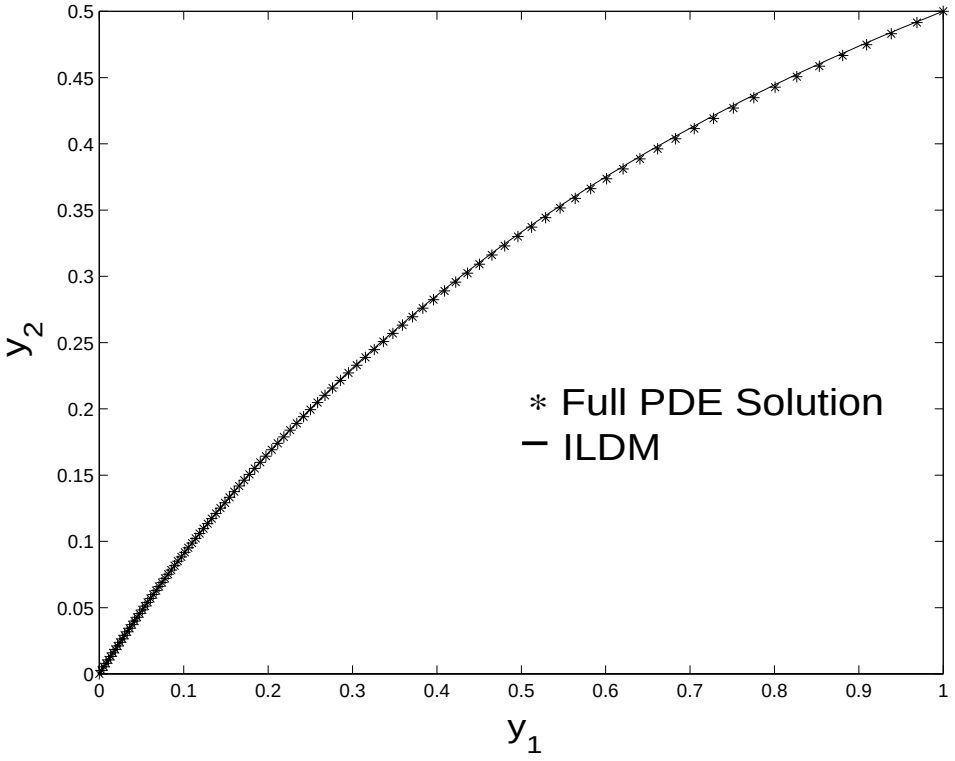

Figure 4.3. Comparison of solution of the full PDEs at $t = 5$ with the ILDM, for $\gamma = 100$ and $\mathcal{D} = 0.1$, for Davis and Skodje's [36] model problem extended to include diffusion.

full solution and the ILDM for fixed $\mathcal{D}$ is seen in Figure 4.4 to decrease as γ, or the stiffness due to the reaction source term $\mathbf{f}(\mathbf{y})$, increases.

The slow dynamics for Equations (4.8), obtained by using the ASIM as done in Equations (4.5), for $n = 2$, $m = 1$ and $p = n$, is given by

$$\frac{\partial y_1}{\partial t} = -y_1 + \mathcal{D}\frac{\partial^2 y_1}{\partial x^2}, \tag{4.11a}$$

$$0 = -y_2 + \frac{y_1}{1+y_1} + \frac{2y_1^2}{\gamma(\gamma-1)(1+y_1)^3} - \left(\frac{\gamma - 1 + (\gamma+1)y_1}{\gamma(\gamma-1)(1+y_1)^3}\right)\mathcal{D}\frac{\partial^2 y_1}{\partial x^2} + \frac{1}{\gamma}\mathcal{D}\frac{\partial^2 y_2}{\partial x^2}. \tag{4.11b}$$

The solution obtained by integrating Equations (4.11) will be compared to the solution obtained by integrating the full system of Equations (4.8). Note that the boundary conditions and initial condition for $y_1(t, x)$ are the same as before, but

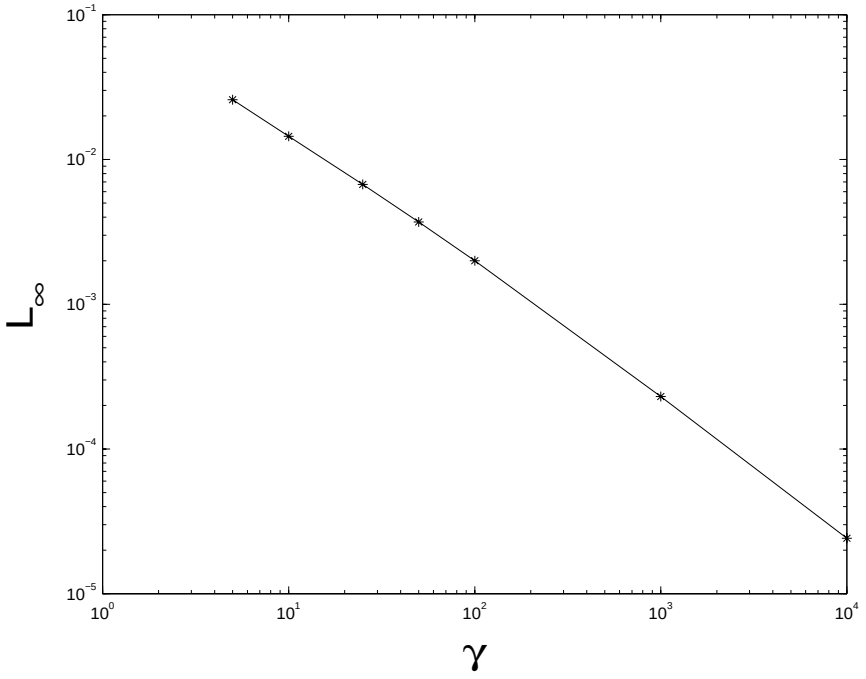

Figure 4.4. Maximum error ($\mathbf{L}_\infty[0,1]$) between solution of the full PDEs at $t = 5$ and the ILDM, for varying γ and fixed $\mathcal{D} = 0.1$, for Davis and Skodje's [36] model problem extended to include diffusion. Stars indicate the values of γ for which the computations were done.

the initial condition $y_2(0,x)$ must be chosen such that Equation (4.11b), which represents the ASIM for the system, is satisfied for given $y_1(0,x)$. That is, the initial condition is chosen so that it lies on the ASIM and minimizes the phase error that might occur if an arbitrary initial condition is used. Equation (4.11b) with boundary conditions given in Equation (4.9) constitute a two-point boundary value problem which can be written in the form

$$\mathbf{L}y_2 = F(y_1(t,x)), \qquad y_2(t,0) = 0, \quad y_2(t,1) = \frac{1}{2} + \frac{1}{4\gamma(\gamma-1)}, \tag{4.12}$$

where

$$\mathbf{L} = \frac{\partial^2}{\partial x^2} - \frac{\gamma}{\mathcal{D}}, \tag{4.13}$$

$$F(y_1(t,x)) = -\frac{\gamma}{\mathcal{D}}\left(\frac{y_1}{1+y_1} + \frac{2y_1^2}{\gamma(\gamma-1)(1+y_1)^3} - \left(\frac{\gamma-1+(\gamma+1)y_1}{\gamma(\gamma-1)(1+y_1)^3}\mathcal{D}\frac{\partial^2 y_1}{\partial x^2}\right)\right), \tag{4.14}$$

the solution of which is given by

$$y_2(t,x) = \left(\frac{1}{2} + \frac{1}{4\gamma\,(\gamma-1)}\right)\frac{\sinh\left(\sqrt{\frac{\gamma}{\mathcal{D}}}x\right)}{\sinh\left(\sqrt{\frac{\gamma}{\mathcal{D}}}\right)} + \int_0^1 G(x,s)F(y_1(t,s))\;ds, \tag{4.15}$$

where the Green's function $G(x,s)$ is given by

$$G(x,s) = \begin{cases} \frac{\sinh(\sqrt{\frac{\gamma}{\mathcal{D}}}(s-1))\sinh(\sqrt{\frac{\gamma}{\mathcal{D}}}x)}{\sqrt{\frac{\gamma}{\mathcal{D}}}\sinh(\sqrt{\frac{\gamma}{\mathcal{D}}})}, & 0 \le x \le s, \\ \frac{\sinh(\sqrt{\frac{\gamma}{\mathcal{D}}}(x-1))\sinh(\sqrt{\frac{\gamma}{\mathcal{D}}}s)}{\sqrt{\frac{\gamma}{\mathcal{D}}}\sinh(\sqrt{\frac{\gamma}{\mathcal{D}}})}, & s \le x \le 1. \end{cases} \tag{4.16}$$

Maas and Pope [38] have proposed a different projection (MPP) method when the diffusion time scales are of the order of the slow chemical time scales and much slower than the fast chemical time scales. They assume that diffusion processes perturb the system off the ILDM, but it rapidly relaxes back to the ILDM due to the fast chemistry. This procedure is implemented by the following projection of the convection diffusion term in Equation (4.1) along the local slow subspace on the reaction ILDM:

$$\frac{\partial \mathbf{y}}{\partial t} = \mathbf{f}(\mathbf{y}) - \mathbf{V}_s\tilde{\mathbf{V}}_s\frac{\partial}{\partial x}\left(\mathbf{h}(\mathbf{y})\right). \tag{4.17}$$

The corresponding equations for the system in Equation (4.8) are then given by

$$\frac{\partial y_1}{\partial t} = -y_1 + \mathcal{D}\frac{\partial^2 y_1}{\partial x^2}, \tag{4.18a}$$

$$\frac{\partial y_2}{\partial t} = -\gamma y_2 + \frac{(\gamma-1)y_1 + \gamma y_1^2}{(1+y_1)^2} - \left(\frac{\gamma-1+(\gamma+1)y_1}{\gamma(\gamma-1)(1+y_1)^3}\right)\mathcal{D}\frac{\partial^2 y_1}{\partial x^2}. \tag{4.18b}$$

One can then solve either of the Equations (4.18a) or (4.18b) along with the ILDM equation (2.68). Hence, the slow dynamics for the MPP method is described by

$$\frac{\partial y_1}{\partial t} = -y_1 + \mathcal{D}\frac{\partial^2 y_1}{\partial x^2}, \tag{4.19a}$$

$$y_2 = \frac{y_1}{1+y_1} + \frac{2y_1^2}{\gamma(\gamma-1)(1+y_1)^3}. \tag{4.19b}$$

The MPP method effectively chooses $n = 2$ and $m = p = 1$. Hence, the MPP method forces the solution onto the finite-dimensional ILDM, which will incur a large error for the cases depicted in Figure 4.1. Equation (4.19b) of the MPP method has as its analog Equation (4.15) of the ASIM method. It is clear that Equation (4.15) accounts for slow reaction and diffusion processes, and boundary conditions, while Equation (4.19b) only accounts for slow reaction processes.

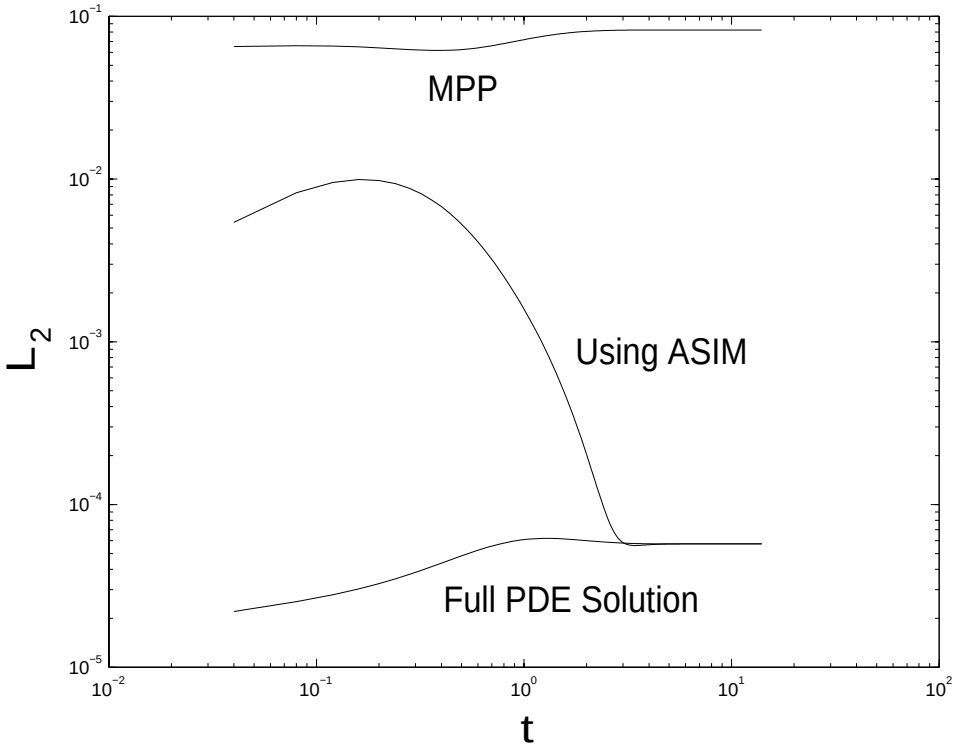

Figure 4.5. Comparison of errors incurred by the three methods at a resolution of 100 grid points relative to a baseline solution of full integration at a resolution of 10000 grid points, for $\gamma = 10$ and $\mathcal{D} = 0.1$, for Davis and Skodje's [36] model problem extended to include diffusion.

Figure 4.5 compares the solution obtained by full integration, use of the ASIM and the MPP method, all using a fixed grid of 100 points, with the baseline solution obtained by full integration at high spatial resolution of 10000 points. The computations are for $\gamma = 10$ and $\mathcal{D} = 0.1$. The numerical scheme used is

the same as described previously. Use of an implicit time stepping scheme is not required when using the ASIM or the MPP method. Also, larger time increments can be used for the solution of Equations (4.11a) and (4.15) when using the ASIM and the solution of Equations (4.19) when using the MPP method, than that for the solution of Equations (4.8), if explicit numerical methods are used, due to the reduced stiffness in the equations. However, since the accuracy of the three methods is to be compared, the numerical solutions of all the three methods are obtained using the same LSODE package with the same time increments until steady state is achieved. Note that a numerical quadrature of Equation (4.15) is done in the ASIM procedure. The $\mathbf{L}_2$ norm of the errors between the solutions obtained by the three methods and the baseline solution at various times have been plotted. When full integration is used, discretization error is incurred as the 100 grid points used for the computation are substantially fewer than those used for the computation of the baseline solution. At steady state, the error in the full integration method becomes constant. The initial error incurred when using the ASIM is due to the fact that the solution from the initial condition takes some time to relax to the ASIM. Near steady state the error incurred when using the ASIM and the error incurred by full integration are essentially identical. A large error is incurred by the MPP method in both transient and steady state periods. This is due to the fact that the MPP method forces the solution onto the finite-dimensional ILDM even though the solution does not lie on it. It can be seen that the overall error incurred when using the ASIM is substantially less than the error incurred when using the MPP method.

If the boundary conditions were not chosen on the ILDM, then the MPP method would incur larger errors, as that would further cause the solution to not lie on the ILDM. On the other hand, errors incurred when using the ASIM will not be affected by the choice of the boundary conditions. Figure 4.6 depicts the solutions in the

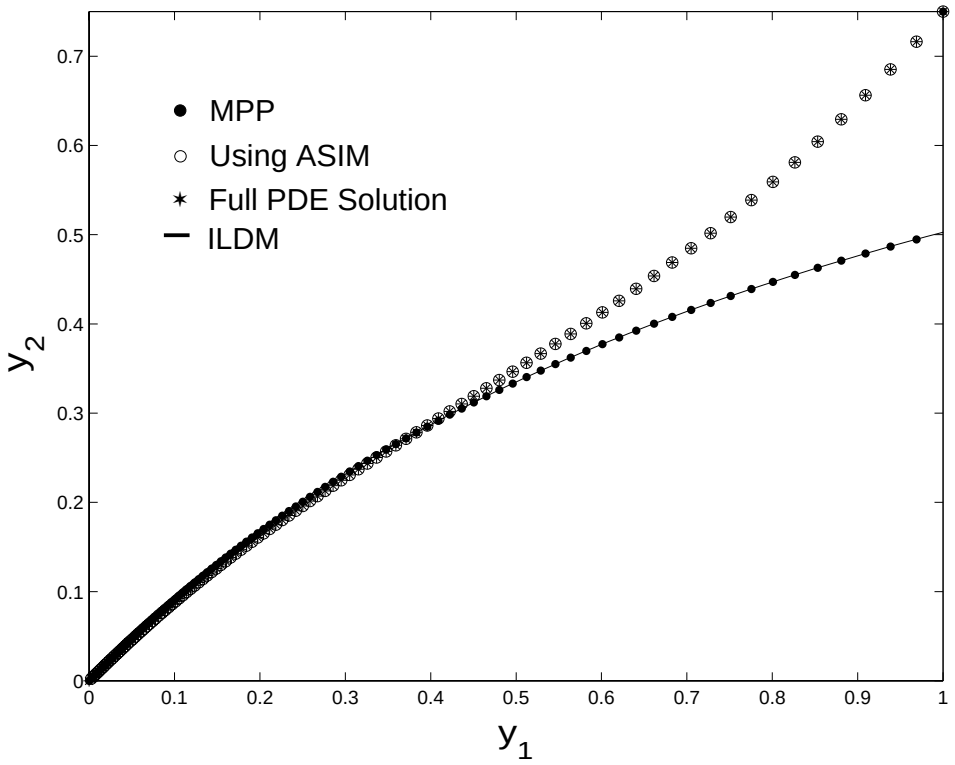

Figure 4.6. Comparison of solutions obtained by full integration, using the ASIM and the MPP method at $t = 5$, for $\gamma = 10$ and $\mathcal{D} = 0.1$, for a case where the boundary condition at $x = 1$ does not lie on the ILDM.

phase space at time $t = 5$, obtained using the three methods, for a case where one of the boundary condition, $\mathbf{y}(t, 1) = \begin{pmatrix} 1 \\ \\ \frac{3}{4} \end{pmatrix}$, does not lie on the ILDM. It can be seen that the error in the solution obtained by the MPP method will always remain large near the boundary at $x = 1$ which does not lie on the ILDM. In the earlier case for which the errors are plotted in Figure 4.5, the error due to the boundary condition in the MPP method is eliminated so as to separate the errors.

4.3 Premixed laminar flame for ozone decomposition

The governing equations which model the time-dependent, one-dimensional, isobaric, premixed laminar flame for ozone decomposition in Lagrangian coordinates

are derived from the Navier-Stokes equations under the assumptions of low Mach number [67],

$$\frac{\partial T}{\partial t} + \dot{m}_0 \frac{\partial T}{\partial \psi} = -\frac{1}{\rho c_p} \sum_{k=1}^{3} \dot{\omega}_k M_k h_k + \frac{1}{c_p} \frac{\partial}{\partial \psi} \left(\rho k \frac{\partial T}{\partial \psi} \right) + \sum_{k=1}^{3} \frac{c_{pk}}{c_p} \rho^2 \mathcal{D}_k \frac{\partial Y_k}{\partial \psi} \frac{\partial T}{\partial \psi}, \tag{4.20a}$$

$$\frac{\partial Y_k}{\partial t} + \dot{m}_0 \frac{\partial Y_k}{\partial \psi} = \frac{1}{\rho} \dot{\omega}_k M_k + \frac{\partial}{\partial \psi} \left(\rho^2 \mathcal{D}_k \frac{\partial Y_k}{\partial \psi} \right), \qquad k = 1, 2, 3, \tag{4.20b}$$

where the dependent variables are the fluid temperature T and the mass fractions in the fluid mixture, Y_1, Y_2 and Y_3, of oxygen atom O, oxygen molecule O_2 and ozone molecule O_3, respectively. The terms M_k and c_{pk} represent the molecular mass and the specific heat capacity at constant pressure, respectively, of species k. The mass averaged specific heat capacity at constant pressure of the fluid mixture is given by $c_p = \sum_{k=1}^{3} Y_k c_{pk}$. The specific enthalpy of species k is given by $h_k = h_{fk}^{\circ} + \int_{T_s}^{T} c_{pk} dT$, where h_{fk}° is the standard enthalpy of formation per unit mass of species k at the standard temperature $T_s = 298$ K. The mass diffusion coefficient of species k into the fluid mixture is $\mathcal{D}_k$, while the thermal conductivity of the fluid mixture is k. The mixture density is ρ. The independent variables are time t, and the Lagrangian coordinate ψ, where

$$\psi(t, x) = \int_0^x \rho(t, \tilde{x}) d\tilde{x}, \tag{4.21}$$

where x is the spatial coordinate. The inlet mass flow rate, $\dot{m}_0$, is given by

$$\dot{m}_0(t) = \rho u|_{x=0}, \tag{4.22}$$

where u is the flow velocity. The molar rate of production of species k per unit volume, $\dot{\omega}_k$, is given by the law of mass action with Arrhenius kinetics

$$\dot{\omega}_k = \sum_{j=1}^{J} \alpha_j T^{\beta_j} \exp\left(\frac{-E_j}{\Re T} \right) \left(\nu''_{kj} - \nu'_{kj} \right) \prod_{i=1}^{N} \left(\frac{\rho Y_i}{M_i} \right)^{\nu'_{ij}}, \qquad k = 1, \ldots, N, \tag{4.23}$$

where $J = 14$ is the number of elementary reaction steps and $N = 3$ is the number of species in the ozone decomposition reaction mechanism. The constant parameters

α_j, β_j, E_j, ν'_{kj}, ν''_{kj} and $\Re$ represent the kinetic rate constant of reaction j, the temperature dependence exponent of reaction j, the activation energy of reaction j, the stoichiometric coefficient of kth species on the reactant and product sides in reaction j, and the universal gas constant ($\Re = 8.31441 \times 10^7$ erg mol^{-1} K^{-1}), respectively. The elementary reaction steps in the ozone decomposition reaction mechanism, with the associated parameters, are given in Table A.1. The system of Equations (4.20) are closed using the ideal gas equation of state

$$p_0 = \rho \Re T \sum_{k=1}^{3} \frac{Y_k}{M_k}, \tag{4.24}$$

where $p_0 = 8.32 \times 10^5$ dynes/cm^2 is the constant pressure.

Following Margolis [67], the governing equations are simplified using the following assumptions and constants: $\mathcal{D}_1 = \mathcal{D}_2 = \mathcal{D}_3 = \mathcal{D}$, $\rho^2\mathcal{D} = 4.336 \times 10^{-7}$ g^2/(cm^4-s), $\rho k = 4.579$ g^2/(cm^2-s^3-K), $c_{p1} = c_{p2} = c_{p3} = c_p = 1.056 \times 10^7$ erg/(g-K), $M_1 = 16$ g/mol, $M_2 = 32$ g/mol, $M_3 = 48$ g/mol, $h^\circ_{f1} = 1.534 \times 10^{11}$ erg/g, $h^\circ_{f2} = 0$ erg/g, $h^\circ_{f3} = 3.011 \times 10^{10}$ erg/g. The initial and the boundary conditions are applied in a frame of reference in which the fluid is initially at rest. A semi-infinite computational domain is considered with the following boundary conditions

$$\frac{\partial T}{\partial \psi} = \frac{\partial Y_1}{\partial \psi} = \frac{\partial Y_2}{\partial \psi} = \frac{\partial Y_3}{\partial \psi} = 0, \quad \text{for} \quad \psi = 0, \infty \quad \text{and} \quad t \geq 0. \tag{4.25}$$

These conditions are equivalent to zero flux of thermal energy and species mass at $\psi = 0, \infty$, which also leads to $u(t, 0) = 0$, and hence, $\dot{m}_0 = 0$. Using these assumptions with a unity Lewis number and non-dimensionalization as done in Margolis [67], Equations (4.20) can be simplified to

$$\frac{\partial T^*}{\partial t^*} = -\frac{1}{\rho^*}\sum_{k=1}^{3}\dot{\omega}_k^* M_k^* h_k^* + \frac{\partial^2 T^*}{\partial {\psi^*}^2}, \tag{4.26a}$$

$$\frac{\partial Y_k}{\partial t^*} = \frac{1}{\rho^*}\dot{\omega}_k^* M_k^* + \frac{\partial^2 Y_k}{\partial {\psi^*}^2}, \qquad k = 1, 2, 3, \tag{4.26b}$$

where the star superscript denotes non-dimensional quantities.

The governing equations can be further simplified by replacing the species evolution equation for $k = 2$, in Equation (4.26b), by the following algebraic equation for the mass fractions

$$\sum_{k=1}^{3} Y_k = 1. \tag{4.27}$$

The mixture enthalpy h^*, in its non-dimensional form, is given by the following equation

$$h^* = \sum_{k=1}^{3} Y_k h_k^* = \sum_{k=1}^{3} Y_k h_{0_k}^* + T^* - T_s^*. \tag{4.28}$$

Using Equations (4.27) and (4.28) with Equations (4.26) and boundary conditions in Equation (4.25) the following is obtained

$$\frac{\partial h^*}{\partial t^*} = \frac{\partial^2 h^*}{\partial {\psi^*}^2}, \quad \text{with} \quad \frac{\partial h^*}{\partial \psi^*}(t^*, 0) = \frac{\partial h^*}{\partial \psi^*}(t^*, \infty) = 0. \tag{4.29}$$

If the initial conditions are chosen such that $h^*(0, \psi^*) = h_r^*$, where h_r^* is the specific enthalpy of the reactant mixture, then Equation (4.29) ensures that there is no tendency for the specific enthalpy of the fluid mixture to change from its uniform initial value, and thus remains constant for all ψ^* and t^*. Hence, Equation (4.26a) can be replaced by the following Schwab-Zeldovich relation

$$T^* = T_s^* + h_r^* - \sum_{k=1}^{3} Y_k h_{0_k}^*. \tag{4.30}$$

Therefore, the solution of only two PDEs from Equation (4.26b) is required, for $k = 1$ and 3 (O and O_3), coupled with algebraic Equations (4.27) and (4.30).

A computational domain of finite length is chosen from $\psi^* = 0$ to 2000. The following initial and boundary conditions are chosen

$$Y_1(0, \psi^*) = 0, \qquad 0 \leq \psi^* \leq 2000, \tag{4.31a}$$

$$Y_3(0, \psi^*) = 0.15, \qquad 0 \leq \psi^* \leq 300, \tag{4.31b}$$

$$Y_3(0, \psi^*) = 0.15 - 0.15 \cos^5 \left(\frac{\pi}{2} \frac{\psi^*}{2000} \right), \qquad 300 < \psi^* \leq 2000, \tag{4.31c}$$

$$\frac{\partial Y_1}{\partial \psi^*}(t^*, 0) = \frac{\partial Y_1}{\partial \psi^*}(t^*, 2000) = \frac{\partial Y_3}{\partial \psi^*}(t^*, 0) = \frac{\partial Y_3}{\partial \psi^*}(t^*, 2000) = 0. \tag{4.31d}$$

The initial conditions are chosen such that the computational domain near $\psi^* = 0$ has a small pocket of gas which has a composition close to that of the products at chemical equilibrium. The rest of the computational domain contains the reactant mixture. There is a reaction zone or a flame front of small initial thickness between the products and reactant mixture. After the flame front is fully developed, it propagates into the reactant mixture at a steady flame speed. The reactant mixture is at temperature $T = 300$ K, hence, $h_r^* = 1.432$.

Figure 4.7 depicts the steady state solution of the full PDEs, plotted in the two-dimensional Y_O-Y_{O_2} phase space. Stars represent the steady state solution at the actual grid points. One thousand equally spaced Lagrangian grid points were used, and for clarity every tenth grid point has been plotted. The numerical computations are done using second order central difference approximations for spatial discretization and second order BDF method in LSODE for time advancement. Also plotted is the one-dimensional ILDM as a curve in the same phase space. It can be seen from the figures that the steady solution does not lie on the ILDM. This is emphasized in Figure 4.7b which shows a close up of the region of phase space where the difference between the steady state solution and the ILDM is maximum.

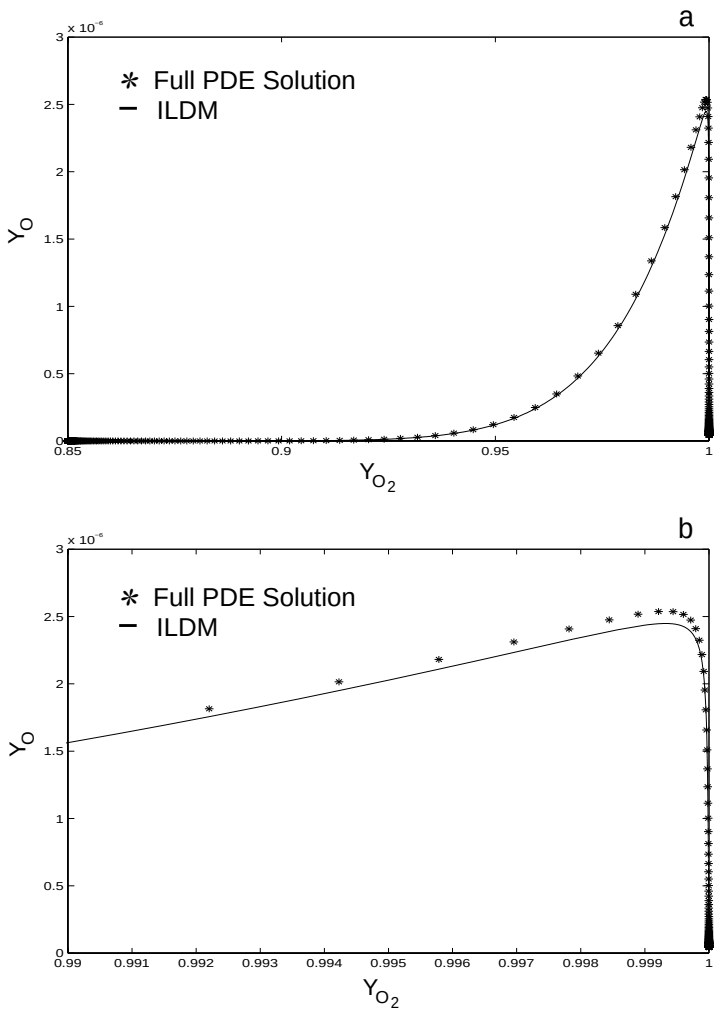

Figure 4.7. Comparison of the steady state solution of the full PDEs with the ILDM in the phase space for ozone decomposition laminar flame: a) global view b) close-up view.

Hence, forcing the solution onto the ILDM, as done in the MPP method, will lead to errors. The steady state temperature profile and mass fraction distribution of O, O_2 and O_3, in the premixed laminar flame of ozone decomposition, are plotted in Figure 4.8. The region of phase space depicted in Figure 4.7b corresponds to the flame front in physical space. Within the flame front the temperature gradients and the mass fraction gradients are large, hence, the effects of diffusion are large. Therefore, the steady solution deviates the most from the ILDM within the flame

front, as the ILDM is obtained from chemistry alone without incorporating the effects of diffusion.

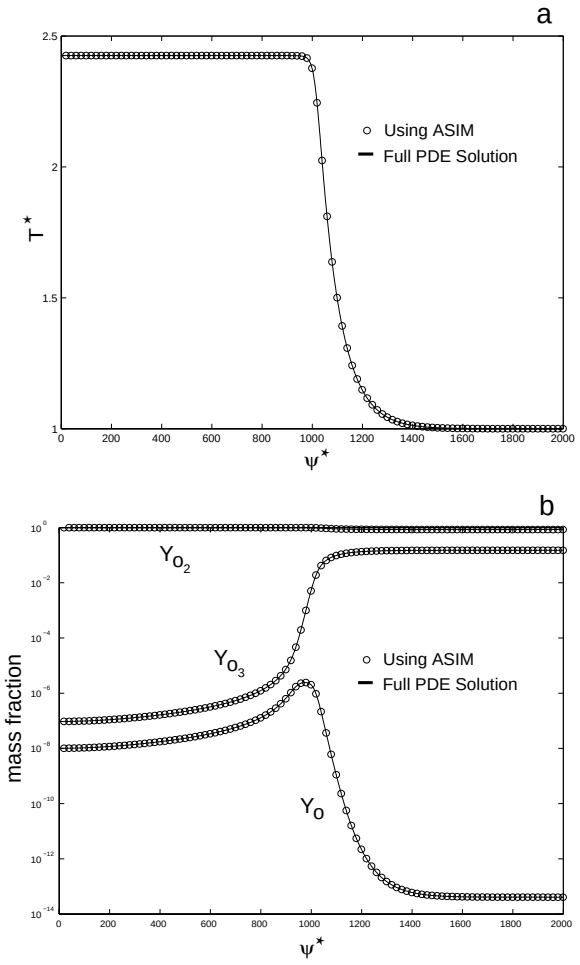

Figure 4.8. Ozone decomposition flame profile at $t^* = 70000$ for a) temperature, and b) species mass fractions.

It can be seen from Figure 4.8 that the steady profiles obtained when using the ASIM are nearly identical to those obtained by full integration. In this case, since the ASIM is given by the solution of a non-linear boundary value problem, the Green's function has not been constructed, but instead a discretized form of the partial differential algebraic equations (4.5) are solved.

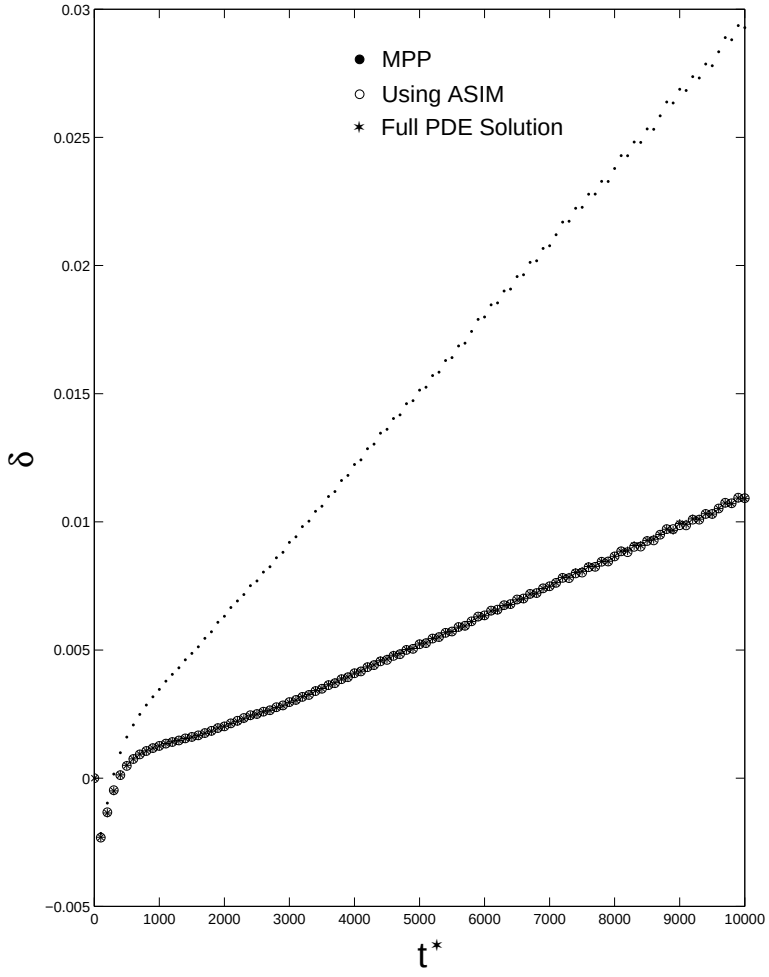

Figure 4.9. The phase error δ incurred in computations of the premixed laminar flame of ozone decomposition with the three methods, at a resolution of 1000 points, relative to computations using full integration at a resolution of 10000 points.

Figure 4.9 compares the phase error in the solutions obtained by full integration, use of the ASIM, and the MPP method, all using a spatial resolution of 1000 grid points, relative to the baseline solution obtained by full integration at a spatial resolution of 10000 grid points. The numerical computations are done using second order central difference approximations for spatial discretization and second order BDF method, in the differential algebraic solver DASSL [68], for time advancement. Use of DASSL is not required for full integration, but it is required when using the ASIM and for the MPP method for solving the resulting differential algebraic system

of equations from spatial discretization. For error analysis all the computations are done using the DASSL package with same time increments until steady state is achieved, in order to remove any numerical bias as done for the simple example in the previous section. The phase error δ is measured as the Lagrangian distance between the location within the flame front where the mass fraction of O_3 is 0.075, for the solution obtained by the three methods and the baseline solution. It is noted that there is a phase difference between the full integration using 1000 grid points and the baseline solution due to the inherent phase error in the BDF numerical method used. This is depicted in Figure 4.9 where stars represent the phase error in the full integration. At steady state the flame front propagates at a uniform speed, and the phase difference increases linearly, which signifies that different flame propagation speeds or burning rates are predicted at different grid resolutions. Near steady state, as can be seen from Figure 4.9, the phase errors incurred when using the ASIM and full integration with the same resolution, are essentially identical. On the other hand the phase error incurred by the MPP method is larger. Hence, there is also an error in the prediction of flame propagation speed or the burning rate by the MPP method. This is evident from the difference in slopes of the phase error curve for the MPP method and the slope of the phase error curve when the ASIM or full integration is used.

The amplitude error in the solutions obtained by the three methods relative to the baseline solution has also been computed. To estimate the amplitude error the phase error has to be eliminated. This is done by first estimating the difference in the flame front propagation speeds obtained by the three methods from that of the baseline solution. The flame propagation speed can be estimated from the slope of the linear part of the phase error curves at steady state. The flame profiles are then shifted to minimize the phase error at all times. Finally, the amplitude error

is estimated as the $\mathbf{L}_\infty$ norm of the error between the solution obtained by the three methods and the baseline solution. While not shown here, it is found that the error incurred when using the ASIM and the error incurred by full integration is essentially identical, and both relax to a constant value of 3.75×10^{-5} at steady state. On the other hand the error in the MPP method is slightly larger (4.5×10^{-5}) and increases slowly due to the fact that the solution is forced onto the ILDM when it does not lie there.

CHAPTER 5

CONCLUSIONS AND FUTURE WORK

The Intrinsic Low-Dimensional Manifolds (ILDM) method offers an effective way to rationally reduce the stiff ordinary differential equations modeling the Closed Adiabatic Spatially Homogeneous Premixed Reactor (CASHPR). The ILDM method equilibrates the fast time scale chemical processes and resolves only the slow time scale chemical processes. The advantage is that the reduced model is guaranteed to maintain fidelity to full kinetic models to within a time scale which is easily determined. The accuracy of the ILDM method was clarified, and it was shown that the ILDM approximates the Slow Invariant Manifold (SIM) well for dynamical systems with large stiffness or large time scale separations. The error in the ILDM approximation of the SIM increases in that region of the phase space where the manifold curvature is large. An algorithm for computation of the multi-dimensional ILDM in a polar parametric space was developed. The associated parametric equations were derived and described in detail. A FORTRAN code based on the algorithm was developed to compute the ILDM for various reaction mechanisms.

An operator splitting method was used to extend the use of the ILDM method for efficient simulation of a viscous $H_2/O_2/Ar$ detonation in a shock tube, which is modeled by a system of partial differential equations. The operator splitting method allows each spatial cell to be treated as an isochoric CASHPR in the

reaction step. The ILDM method was used for efficient solution of the stiff ODEs modeling the reactive processes at each spatial location. The Wavelet Adaptive Multilevel Resolution (WAMR) method used to solve the PDEs modeling the mixing processes in the convection-diffusion step, allows the attainment of dramatic spatial resolution for flows, such as viscous detonations, with widely disparate spatial scales. Thin viscous shocks, entropy layers, and induction zones were fully resolved along with phenomena which evolved on much larger laboratory scales. The detonation computations using the ILDM and WAMR methods were three times faster than the computations done by integrating the full model equations. It appears clear that these methods can be used effectively to solve problems with disparate length and time scales which are endemic in scientific computing.

Analogous to the ILDM for the CASHPR modeled by a system of ODEs, an infinite-dimensional Approximate Slow Invariant Manifold (ASIM) is developed for the reactive flow systems modeled by a system of PDEs. While no robust analysis exists to determine convection and diffusion time scales *a priori*, it is found that in reactive flow systems in which convection and diffusion have time scales comparable to those of reactions, the Mass and Pope projection (MPP) method can lead to large transient and steady state errors in numerical simulations. These errors occur because the MPP method projects the system onto the ILDM when it may not exist there. The error incurred when using the ASIM is much smaller than that in the MPP method. This is because when using the ASIM, reaction, convection and diffusion can be better coupled, while systematically equilibrating fast time scales. The ASIM is shown to be a good approximation for the long time dynamics of reactive flow systems. In this study, the improved accuracy in describing the slow dynamics of two simple reaction-diffusion systems by using the ASIM, has been illustrated with a concomitant decrease in computational cost.

Some future work of importance is required in the area of efficient computation of the multi-dimensional ILDM for various reaction mechanisms. It includes compression of the large data tables generated from *a priori* numerical computation of the high dimensional ILDMs. There is also a need for developing an improved storage system for these tables, possibly using data structures, so that data can be efficiently retrieved from the ILDM tables while they are being used for efficient numerical simulations of reactive systems.

Often an *a priori* computation of the the complete global ILDM in the phase space is not required because, usually only a small subset of the global ILDM is required for numerical simulation of a reactive system. The boundaries of this subset can be roughly estimated from initial conditions of the reactive system. Developing a method for an *in situ* computation of the ILDM may be beneficial. A subset of the global ILDM is computed and stored as a table in that region of the phase space where it is required during a numerical simulation of a reactive system. If that same subset of the global ILDM is required during the same or another numerical simulation of a reactive system, it is not recomputed and instead, retrieved from the stored ILDM table. However, if another subset of the global ILDM, which is not yet stored in the ILDM table, is required, then that subset of the global ILDM is computed and also added to the ILDM table. Hence, the size of the ILDM table grows. Another reason why the global ILDM should not be computed is because, it does not approximate the SIM well everywhere in the phase space. Only a subset of the global ILDM near the chemical equilibrium point, where the spectral gap condition holds, approximates the SIM well. This was shown for the examples in Chapter 2. Hence, only those subsets of the global ILDM, where the spectral gap condition holds, are useful and should be computed and stored in the ILDM table.

Another possible area of future work is obtaining an algebraic approximation of the multi-dimensional SIM using the functional iteration method [35]. A symbolic logic code was written to generate a polynomial series approximation of a one-dimensional SIM around the chemical equilibrium point for the dynamical system modeling the CASHPR. However, the polynomial approximation obtained worked well only close to the chemical equilibrium point and rapidly diverged away from it. It might be possible to use some algebraic functional form other than polynomials to better approximate the SIM. This possibility can be explored.

In this work, the ILDM method is used in conjunction with operator splitting method for numerical simulations of a viscous detonation. It is noted that the computational savings are problem dependent. A similar implementation of the ILDM and operator splitting methods with respect to a large scale commercial CFD code for solution of some real world reactive flow systems can give a better insight into the computational efficiency achieved.

The ASIM for reactive flow systems has been shown to work work well for a simple reaction diffusion system and ozone decomposition premixed laminar flame. By linearizing the ASIM about the ILDM, which lies close to it, the computation of the local fast and slow basis vectors can be avoided as they can also be stored in the ILDM tables. This can potentially make the computations of reactive flow systems with ASIM more efficient. A Green's function solution was obtained for the ASIM of the simple reaction diffusion system. Similarly, a numerical Green's function solution method for PDEs describing the ASIM can also be explored for more complicated reactive flow systems. At this point the fast and slow subspace decomposition is dependent only on reaction and should itself be modified to account for convection-diffusion effects.

APPENDIX A

REACTION MECHANISMS

The ozone decomposition, syngas combustion, hydrogen combustion, and methane combustion reaction mechanisms are represented in tabular forms. The species, elements and elementary reaction steps in the reaction mechanisms are listed in the tables. Third body (represented by M) collision efficiencies with respect to all the species are taken to be unity unless specified otherwise in a reaction step. Units of α_j are in appropriate combinations of cm, mol, s, and K, so that $\dot{\omega}_i$ has units of mol cm^{-3} s^{-1}; units of E_j are in erg mol^{-1}.

Table A.1. OZONE DECOMPOSITION REACTION MECHANISM

Species: O, O_2, O_3				
Elements: O				
j	Reaction	α_j	β_j	E_j
1	$O_3 + O \rightarrow O_2 + O + O$	6.76×10^6	2.50	1.01×10^{12}
2	$O_2 + O + O \rightarrow O_3 + O$	1.18×10^2	3.50	0.00
3	$O_3 + O_2 \rightarrow O_2 + O + O_2$	6.76×10^6	2.50	1.01×10^{12}
4	$O_2 + O + O_2 \rightarrow O_3 + O_2$	1.18×10^2	3.50	0.00
5	$O_3 + O_3 \rightarrow O_2 + O + O_3$	6.76×10^6	2.50	1.01×10^{12}
6	$O_2 + O + O_3 \rightarrow O_3 + O_3$	1.18×10^2	3.50	0.00
7	$O + O_3 \rightarrow O_2 + O_2$	4.58×10^6	2.50	2.51×10^{11}
8	$O_2 + O_2 \rightarrow O + O_3$	1.88×10^6	2.50	4.15×10^{12}
9	$O_2 + O \rightarrow O + O + O$	5.71×10^6	2.50	4.91×10^{12}
10	$O + O + O \rightarrow O_2 + O$	2.47×10^2	3.50	0.00
11	$O_2 + O_2 \rightarrow O + O + O_2$	5.71×10^6	2.50	4.91×10^{12}
12	$O + O + O_2 \rightarrow O_2 + O_2$	2.47×10^2	3.50	0.00
13	$O_2 + O_3 \rightarrow O + O + O_3$	5.71×10^6	2.50	4.91×10^{12}
14	$O + O + O_3 \rightarrow O_2 + O_3$	2.47×10^2	3.50	0.00

Table A.2. SYNGAS COMBUSTION REACTION MECHANISM

Species: N_2, CO, H_2, O_2, H_2O, CO_2, OH, H, O, HO_2, HCO, H_2O_2, CH_2O				
Elements: H, C, O, N				
j	Reaction	α_j	β_j	E_j
1	$O_2 + H \rightarrow OH + O$	2.00×10^{14}	0.0	16790.1
2	$OH + O \rightarrow O_2 + H$	1.47×10^{13}	0.0	501.6
3	$H_2 + O \rightarrow OH + H$	5.06×10^{04}	2.7	6281.3
4	$OH + H \rightarrow H_2 + O$	2.24×10^{04}	2.7	4394.6
5	$H_2 + OH \rightarrow H_2O + H$	1.00×10^{08}	1.6	3295.9
6	$H_2O + H \rightarrow H_2 + OH$	4.46×10^{08}	1.6	18414.1
7	$OH + OH \rightarrow H_2O + O$	1.50×10^{09}	1.1	95.5
8	$H_2O + O \rightarrow OH + OH$	1.51×10^{10}	1.1	17100.5
9	$H + H + M \rightarrow H_2 + M$	1.80×10^{18}	-1.0	0.0
10	$H_2 + M \rightarrow H + H + M$	6.98×10^{18}	-1.0	104131.8
11	$H + OH + M \rightarrow H_2O + M$	2.20×10^{22}	-2.0	0.0
12	$H_2O + M \rightarrow H + OH + M$	3.80×10^{23}	-2.0	119273.9
13	$O + O + M \rightarrow O_2 + M$	2.90×10^{17}	-1.0	0.0
14	$O_2 + M \rightarrow O + O + M$	6.78×10^{18}	-1.0	118557.4
15	$H + O_2 + M \rightarrow HO_2 + M$	2.30×10^{18}	-0.8	0.0
16	$HO_2 + M \rightarrow H + O_2 + M$	2.66×10^{18}	-0.8	49247.7
17	$HO_2 + H \rightarrow OH + OH$	1.50×10^{14}	0.0	1003.1
18	$OH + OH \rightarrow HO_2 + H$	1.63×10^{13}	0.0	37735.8
19	$HO_2 + H \rightarrow H_2 + O_2$	2.50×10^{13}	0.0	692.6
20	$H_2 + O_2 \rightarrow HO_2 + H$	8.39×10^{13}	0.0	55600.7
21	$HO_2 + H \rightarrow H_2O + O$	3.00×10^{13}	0.0	1719.6
22	$H_2O + O \rightarrow HO_2 + H$	3.29×10^{13}	0.0	55457.4
23	$HO_2 + O \rightarrow OH + O_2$	1.80×10^{13}	0.0	-406.0
24	$OH + O_2 \rightarrow HO_2 + O$	2.67×10^{13}	0.0	52615.2
25	$HO_2 + OH \rightarrow H_2O + O_2$	6.00×10^{13}	0.0	0.0
26	$H_2O + O_2 \rightarrow HO_2 + OH$	8.97×10^{14}	0.0	70026.3
27	$HO_2 + HO_2 \rightarrow H_2O_2 + O_2$	2.50×10^{11}	0.0	-1241.9
28	$OH + OH + M \rightarrow H_2O_2 + M$	3.25×10^{22}	-2.0	0.0
29	$H_2O_2 + M \rightarrow OH + OH + M$	2.11×10^{24}	-2.0	49391.0
30	$H_2O_2 + H \rightarrow H_2 + HO_2$	1.70×10^{12}	0.0	3749.7
31	$H_2 + HO_2 \rightarrow H_2O_2 + H$	9.35×10^{11}	0.0	21781.7
32	$H_2O_2 + H \rightarrow H_2O + OH$	1.00×10^{13}	0.0	3582.5
33	$H_2O + OH \rightarrow H_2O_2 + H$	2.66×10^{12}	0.0	73465.5
34	$H_2O_2 + O \rightarrow OH + HO_2$	2.80×10^{13}	0.0	6400.8
35	$OH + HO_2 \rightarrow H_2O_2 + O$	6.80×10^{12}	0.0	22546.0
36	$H_2O_2 + OH \rightarrow H_2O + HO_2$	5.40×10^{12}	0.0	1003.1
37	$H_2O + HO_2 \rightarrow H_2O_2 + OH$	1.32×10^{13}	0.0	34153.3

Continued on next page

Table A.2. *Continued from previous page*

j	Reaction	α_j	β_j	E_j
38	$CO + OH \rightarrow CO_2 + H$	4.40×10^{06}	1.5	-740.4
39	$CO_2 + H \rightarrow CO + OH$	6.12×10^{08}	1.5	22474.3
40	$CO + HO_2 \rightarrow CO_2 + OH$	1.50×10^{14}	0.0	23573.0
41	$CO_2 + OH \rightarrow CO + HO_2$	2.27×10^{15}	0.0	83520.4
42	$CO + O + M \rightarrow CO_2 + M$	7.10×10^{13}	0.0	-4537.9
43	$CO_2 + M \rightarrow CO + O + M$	1.69×10^{16}	0.0	120945.8
44	$CO + O_2 \rightarrow CO_2 + O$	2.50×10^{12}	0.0	47766.9
45	$CO_2 + O \rightarrow CO + O_2$	2.55×10^{13}	0.0	54693.1
46	$HCO + M \rightarrow CO + H + M$	7.10×10^{14}	0.0	16790.1
47	$CO + H + M \rightarrow HCO + M$	1.07×10^{15}	0.0	2054.0
48	$HCO + H \rightarrow CO + H_2$	2.00×10^{14}	0.0	0.0
49	$CO + H_2 \rightarrow HCO + H$	1.17×10^{15}	0.0	89419.6
50	$HCO + O \rightarrow CO + OH$	3.00×10^{13}	0.0	0.0
51	$CO + OH \rightarrow HCO + O$	7.72×10^{13}	0.0	87532.8
52	$HCO + O \rightarrow CO_2 + H$	3.00×10^{13}	0.0	0.0
53	$CO_2 + H \rightarrow HCO + O$	1.07×10^{16}	0.0	110747.6
54	$HCO + OH \rightarrow CO + H_2O$	1.00×10^{14}	0.0	0.0
55	$CO + H_2O \rightarrow HCO + OH$	2.60×10^{15}	0.0	104537.9
56	$HCO + O_2 \rightarrow CO + HO_2$	3.00×10^{12}	0.0	0.0
57	$CO + HO_2 \rightarrow HCO + O_2$	5.21×10^{12}	0.0	34511.6
58	$CH_2O + M \rightarrow HCO + H + M$	1.40×10^{17}	0.0	76427.0
59	$HCO + H + M \rightarrow CH_2O + M$	2.62×10^{15}	0.0	-13565.8
60	$CH_2O + H \rightarrow HCO + H_2$	2.50×10^{13}	0.0	3988.5
61	$HCO + H_2 \rightarrow CH_2O + H$	1.82×10^{12}	0.0	18151.4
62	$CH_2O + O \rightarrow HCO + OH$	3.50×10^{13}	0.0	3487.0
63	$HCO + OH \rightarrow CH_2O + O$	1.12×10^{12}	0.0	15763.1
64	$CH_2O + OH \rightarrow HCO + H_2O$	3.00×10^{13}	0.0	1194.2
65	$HCO + H_2O \rightarrow CH_2O + OH$	9.71×10^{12}	0.0	30475.3
66	$CH_2O + HO_2 \rightarrow HCO + H_2O_2$	1.00×10^{12}	0.0	8001.0
67	$HCO + H_2O_2 \rightarrow CH_2O + HO_2$	1.32×10^{11}	0.0	4131.8

Note: Third body collision efficiencies in all reaction steps involving M enhanced with respect to the following species: $f_{O_2} = 0.35$, $f_{H_2O} = 6.5$, $f_{N_2} = 0.5$, $f_{CO} = 1.5$, $f_{CO_2} = 1.5$.

Table A.3. HYDROGEN COMBUSTION REACTION MECHANISM

Species: H, O, H_2, O_2, OH, H_2O, HO_2, H_2O_2 Ar				
Elements: H, O, Ar				
j	Reaction	α_j	β_j	E_j
1	$O_2 + H \rightarrow OH + O$	2.00×10^{14}	0.00	70.30
2	$OH + O \rightarrow O_2 + H$	1.46×10^{13}	0.00	2.08
3	$H_2 + O \rightarrow OH + H$	5.06×10^{4}	2.67	26.30
4	$OH + H \rightarrow H_2 + O$	2.24×10^{4}	2.67	18.40
5	$H_2 + OH \rightarrow H_2O + H$	1.00×10^{8}	1.60	13.80
6	$H_2O + H \rightarrow H_2 + OH$	4.45×10^{8}	1.60	77.13
7	$OH + OH \rightarrow H_2O + O$	1.50×10^{9}	1.14	0.42
8	$H_2O + O \rightarrow OH + OH$	1.51×10^{10}	1.14	71.64
9	$H + H + M \rightarrow H_2 + M$	1.80×10^{18}	-1.00	0.00
10	$H_2 + M \rightarrow H + H + M$	6.99×10^{18}	-1.00	436.08
11	$H + OH + M \rightarrow H_2O + M$	2.20×10^{22}	-2.00	0.00
12	$H_2O + M \rightarrow H + OH + M$	3.80×10^{23}	-2.00	499.41
13	$O + O + M \rightarrow O_2 + M$	2.90×10^{17}	-1.00	0.00
14	$O_2 + M \rightarrow O + O + M$	6.81×10^{18}	-1.00	496.41
15	$H + O_2 + M \rightarrow HO_2 + M$	2.30×10^{18}	-0.80	0.00
16	$HO_2 + M \rightarrow H + O_2 + M$	3.26×10^{18}	-0.80	195.88
17	$HO_2 + H \rightarrow OH + OH$	1.50×10^{14}	0.00	4.20
18	$OH + OH \rightarrow HO_2 + H$	1.33×10^{13}	0.00	168.30
19	$HO_2 + H \rightarrow H_2 + O_2$	2.50×10^{13}	0.00	2.90
20	$H_2 + O_2 \rightarrow HO_2 + H$	6.84×10^{13}	0.00	243.10
21	$HO_2 + H \rightarrow H_2O + O$	3.00×10^{13}	0.00	7.20
22	$H_2O + O \rightarrow HO_2 + H$	2.67×10^{13}	0.00	242.52
23	$HO_2 + O \rightarrow OH + O_2$	1.80×10^{13}	0.00	-1.70
24	$OH + O_2 \rightarrow HO_2 + O$	2.18×10^{13}	0.00	230.61
25	$HO_2 + OH \rightarrow H_2O + O_2$	6.00×10^{13}	0.00	0.00
26	$H_2O + O_2 \rightarrow HO_2 + OH$	7.31×10^{14}	0.00	303.53
27	$HO_2 + HO_2 \rightarrow H_2O_2 + O_2$	2.50×10^{11}	0.00	-5.20
28	$OH + OH + M \rightarrow H_2O_2 + M$	3.25×10^{22}	-2.00	0.00
29	$H_2O_2 + M \rightarrow OH + OH + M$	2.10×10^{24}	-2.00	206.80
30	$H_2O_2 + H \rightarrow H_2 + HO_2$	1.70×10^{12}	0.00	15.70
31	$H_2 + HO_2 \rightarrow H_2O_2 + H$	1.15×10^{12}	0.00	80.88
32	$H_2O_2 + H \rightarrow H_2O + OH$	1.00×10^{13}	0.00	15.00
33	$H_2O + OH \rightarrow H_2O_2 + H$	2.67×10^{12}	0.00	307.51
34	$H_2O_2 + O \rightarrow OH + HO_2$	2.80×10^{13}	0.00	26.80
35	$OH + HO_2 \rightarrow H_2O_2 + O$	8.40×10^{12}	0.00	84.09
36	$H_2O_2 + OH \rightarrow H_2O + HO_2$	5.40×10^{12}	0.00	4.20
37	$H_2O + HO_2 \rightarrow H_2O_2 + OH$	1.63×10^{13}	0.00	132.71

Note: Third body collision efficiencies in all reaction steps involving M enhanced with respect to the following species: $f_{O_2} = 0.35$, $f_{H_2O} = 6.5$.

Table A.4. METHANE COMBUSTION REACTION MECHANISM

Species: CH_4, CH_3, CH_2, CH, CH_2O, HCO, CO_2, CO, H_2, H, O_2, O, OH, HO_2, H_2O_2, H_2O, N_2				
Elements: H, C, O, N				
j	Reaction	α_j	β_j	E_j
1	$CH_3 + H + M \rightleftharpoons CH_4 + M$	8.00×10^{26}	-3.0	0.0
2	$CH_4 + O_2 \rightleftharpoons CH_3 + HO_2$	7.90×10^{13}	0.0	56000.0
3	$CH_4 + H \rightleftharpoons CH_3 + H_2$	2.20×10^{04}	3.0	8750.0
4	$CH_4 + O \rightleftharpoons CH_3 + OH$	1.60×10^{06}	2.4	7400.0
5	$CH_4 + OH \rightleftharpoons CH_3 + H_2O$	1.60×10^{06}	2.1	2460.0
6	$CH_3 + O \rightleftharpoons CH_2O + H$	6.80×10^{13}	0.0	0.0
7	$CH_3 + OH \rightleftharpoons CH_2O + H_2$	1.00×10^{12}	0.0	0.0
8	$CH_3 + OH \rightleftharpoons CH_2 + H_2O$	1.50×10^{13}	0.0	5000.0
9	$CH_3 + H \rightleftharpoons CH_2 + H_2$	9.00×10^{13}	0.0	15100.0
10	$CH_2 + H \rightleftharpoons CH + H_2$	1.40×10^{19}	-2.0	0.0
11	$CH_2 + OH \rightleftharpoons CH_2O + H$	2.50×10^{13}	0.0	0.0
12	$CH_2 + OH \rightleftharpoons CH + H_2O$	4.50×10^{13}	0.0	3000.0
13	$CH + O_2 \rightleftharpoons HCO + O$	3.30×10^{13}	0.0	0.0
14	$CH + O \rightleftharpoons CO + H$	5.70×10^{13}	0.0	0.0
15	$CH + OH \rightleftharpoons HCO + H$	3.00×10^{13}	0.0	0.0
16	$CH + CO_2 \rightleftharpoons HCO + CO$	3.40×10^{12}	0.0	690.0
17	$CH_2 + CO_2 \rightleftharpoons CH_2O + CO$	1.10×10^{11}	0.0	1000.0
18	$CH_2 + O \rightleftharpoons CO + H + H$	3.00×10^{13}	0.0	0.0
19	$CH_2 + O \rightleftharpoons CO + H_2$	5.00×10^{13}	0.0	0.0
20	$CH_2 + O_2 \rightleftharpoons CO_2 + H + H$	1.60×10^{12}	0.0	1000.0
21	$CH_2 + O_2 \rightleftharpoons CH_2O + O$	5.00×10^{13}	0.0	9000.0
22	$CH_2 + O_2 \rightleftharpoons CO2 + H_2$	6.90×10^{11}	0.0	500.0
23	$CH_2 + O_2 \rightleftharpoons CO + H_2O$	1.90×10^{10}	0.0	-1000.0
24	$CH_2 + O_2 \rightleftharpoons CO + OH + H$	8.60×10^{10}	0.0	-500.0
25	$CH_2 + O_2 \rightleftharpoons HCO + OH$	4.30×10^{10}	0.0	-500.0
26	$CH_2O + OH \rightleftharpoons HCO + H_2O$	3.43×10^{09}	1.2	-447.0
27	$CH_2O + H \rightleftharpoons HCO + H_2$	2.19×10^{08}	1.8	3000.0
28	$CH_2O + M \rightleftharpoons HCO + H + M$	3.31×10^{16}	0.0	81000.0
29	$CH_2O + O \rightleftharpoons HCO + OH$	1.81×10^{13}	0.0	3082.0
30	$HCO + OH \rightleftharpoons CO + H_2O$	5.00×10^{12}	0.0	0.0
31	$HCO + M \rightleftharpoons H + CO + M$	1.60×10^{14}	0.0	14700.0
32	$HCO + H \rightleftharpoons CO + H_2$	4.00×10^{13}	0.0	0.0
33	$HCO + O \rightleftharpoons CO_2 + H$	1.00×10^{13}	0.0	0.0
34	$HCO + O_2 \rightleftharpoons HO_2 + CO$	3.30×10^{13}	-0.4	0.0
35	$CO + O + M \rightleftharpoons CO_2 + M$	3.20×10^{13}	0.0	-4200.0
36	$CO + OH \rightleftharpoons CO_2 + H$	1.51×10^{07}	1.3	-758.0

Continued on next page

Table A.4. *Continued from previous page*

j	Reaction	α_j	β_j	E_j
37	$CO + O_2 \rightleftharpoons CO_2 + O$	1.60×10^{13}	0.0	41000.0
38	$HO_2 + CO \rightleftharpoons CO_2 + OH$	5.80×10^{13}	0.0	22934.0
39	$H_2 + O_2 \rightleftharpoons 2OH$	1.70×10^{13}	0.0	47780.0
40	$OH + H_2 \rightleftharpoons H_2O + H$	1.17×10^{09}	1.3	3626.0
41	$H + O_2 \rightleftharpoons OH + O$	5.13×10^{16}	-0.8	16507.0
42	$O + H_2 \rightleftharpoons OH + H$	1.80×10^{10}	1.0	8826.0
43	$H + O_2 + M \rightleftharpoons HO_2 + M$	3.61×10^{17}	-0.7	0.0
	Third body collision efficiencies enhanced for reaction step 43: $f_{H_2O} = 18.6$, $f_{CO_2} = 4.2$, $f_{H_2} = 2.86$, $f_{CO} = 2.11$, $f_{N_2} = 1.26$			
44	$OH + HO_2 \rightleftharpoons H_2O + O_2$	7.50×10^{12}	0.0	0.0
45	$H + HO_2 \rightleftharpoons 2OH$	1.40×10^{14}	0.0	1073.0
46	$O + HO_2 \rightleftharpoons O_2 + OH$	1.40×10^{13}	0.0	1073.0
47	$2OH \rightleftharpoons O + H_2O$	6.00×10^{08}	1.3	0.0
48	$H + H + M \rightleftharpoons H_2 + M$	1.00×10^{18}	-1.0	0.0
49	$H + H + H_2 \rightleftharpoons H_2 + H_2$	9.20×10^{16}	-0.6	0.0
50	$H + H + H_2O \rightleftharpoons H_2 + H_2O$	6.00×10^{19}	-1.2	0.0
51	$H + H + CO_2 \rightleftharpoons H_2 + CO_2$	5.49×10^{20}	-2.0	0.0
52	$H + OH + M \rightleftharpoons H_2O + M$	1.60×10^{22}	-2.0	0.0
	Third body collision efficiencies enhanced for reaction step 52: $f_{H_2O} = 5.0$			
53	$H + O + M \rightleftharpoons OH + M$	6.20×10^{16}	-0.6	0.0
	Third body collision efficiencies enhanced for reaction step 53: $f_{H_2O} = 5.0$			
54	$H + HO_2 \rightleftharpoons H_2 + O_2$	1.25×10^{13}	0.0	0.0
55	$HO_2 + HO_2 \rightleftharpoons H_2O_2 + O_2$	2.00×10^{12}	0.0	0.0
56	$H_2O_2 + M \rightleftharpoons OH + OH + M$	1.30×10^{17}	0.0	45500.0
57	$H_2O_2 + H \rightleftharpoons HO_2 + H_2$	1.60×10^{12}	0.0	3800.0
58	$H_2O_2 + OH \rightleftharpoons H_2O + HO_2$	1.00×10^{13}	0.0	1800.0

Note: All the reversible reaction steps are treated as two irreversible reaction steps. The forward reaction rates are evaluated using the parameters given in the table, while the backward reaction rates are evaluated using the package CHEMKIN [42].

APPENDIX B

MIXTURE FRACTION

It is shown in Chapter 3 that the element conservation equations in a reactive flow system can be simplified to the following

$$\rho \frac{D\hat{Y}_l}{Dt} = \mathcal{D} \frac{\partial}{\partial x} \left(\rho \frac{\partial \hat{Y}_l}{\partial x} \right), \qquad (l = 1, \ldots, L), \tag{B.1}$$

by using a form of Fick's law given in Equation (3.19). This form of Fick's law is obtained by assuming that all the multicomponent mass diffusion coefficients are equal ($\mathcal{D}_{ij} = \mathcal{D}$), the molecular masses of each species are close to the mean molecular mass ($M_i \sim M$), and the Soret and DuFour effects are negligible ($\mathcal{D}_T = 0$).

If in a reactive flow system, a stream of mixture A with species mass fractions represented by Y_i^A, $(i = 1, \ldots, N)$, reacts with a stream of mixture B with species mass fractions represented by Y_i^B, $(i = 1, \ldots, N)$, then a choice of initial conditions for species mass fractions may be given by

$$Y_i(x, t = 0) = \left\{ \begin{array}{ll} Y_i^A, & 0 \leq x \leq \frac{L_x}{2} \\ Y_i^B, & \frac{L_x}{2} \leq x \leq L_x \end{array} \right\}, \qquad (i = 1, \ldots, N), \tag{B.2}$$

implying that initially there is only mixture A in first half of the domain and only mixture B in second half of the domain. The length of the domain is represented by L_x. The two streams mix and react at future time. Zero gradient boundary conditions are chosen for all the species mass fractions

$$\frac{\partial Y_i}{\partial x}(x = 0, t) = \frac{\partial Y_i}{\partial x}(x = L_x, t) = 0, \qquad (i = 1, \ldots, N). \tag{B.3}$$

Using Equation (2.10), the initial and boundary conditions for element mass fractions are then given by

$$\hat{Y}_l(x, t=0) = \left\{ \begin{array}{ll} \hat{Y}_l^A, & 0 \leq x \leq \frac{L_x}{2} \\ \hat{Y}_l^B, & \frac{L_x}{2} \leq x \leq L_x \end{array} \right\}, \qquad (l = 1, \ldots, L), \tag{B.4}$$

$$\frac{\partial \hat{Y}_l}{\partial x}(x = 0, t) = \frac{\partial \hat{Y}_l}{\partial x}(x = L_x, t) = 0, \qquad (l = 1, \ldots, L), \tag{B.5}$$

where $\hat{Y}_l^A = \hat{M}_l \sum_{i=1}^{N} \varphi_{il} \frac{Y_i^A}{M_i}$ and $\hat{Y}_l^B = \hat{M}_l \sum_{i=1}^{N} \varphi_{il} \frac{Y_i^B}{M_i}$ represent the mass fractions of element l in mixtures A and B, respectively.

If the element mass fraction $\hat{Y}_l$ is normalized as follows

$$\chi_l = \frac{\hat{Y}_l - \hat{Y}_l^A}{\hat{Y}_l^B - \hat{Y}_l^A}, \tag{B.6}$$

then the conservation equation (B.1) and the initial and boundary conditions in Equations (B.4-B.5) for the element mass fraction $\hat{Y}_l$ can be simplified to

$$\rho \frac{D\chi_l}{Dt} = \mathcal{D} \frac{\partial}{\partial x} \left(\rho \frac{\partial \chi_l}{\partial x} \right), \tag{B.7}$$

$$\chi_l(x, t=0) = \left\{ \begin{array}{ll} 0, & 0 \leq x \leq \frac{L_x}{2} \\ 1, & \frac{L_x}{2} \leq x \leq L_x \end{array} \right\}, \tag{B.8}$$

$$\frac{\partial \chi_l}{\partial x}(x = 0, t) = \frac{\partial \chi_l}{\partial x}(x = L_x, t) = 0. \tag{B.9}$$

Note that by using the normalization in Equation (B.6) for the two stream reactive flow system, the conservation equations and the initial and boundary conditions for all element mass fractions become identical and are given in Equations (B.7-B.9). Hence, $\chi_l(x, t) = \chi(x, t)$, which is also known as mixture fraction. Even though this simplification has been done for particular forms of initial and boundary conditions for demonstration purposes, it can also be done for other forms of linear initial and boundary conditions in multidimensional reactive flow systems.

The element mass fractions in a reactive flow system do not change due to the reactive processes. This can be deduced from the element conservation equation (B.1), which has no reactive source term. Instead, the element mass fractions change only due to the mixing processes. Since, all the mass diffusion coefficients are equal, all the elements mix alike (see Equation (3.20)). Hence, by solving the conservation equation (B.7) for a single scalar mixture fraction, $\chi(x,t) = \chi_l(x,t)$, and then using Equation (B.6), all the element mass fractions, $\hat{Y}_l(x,t)$, $(l = 1, \ldots, L)$, can be tracked in space and time.

For the simplified mass diffusion models in Equations (3.19-3.20), the numerical simulation of a reactive flow system can be done by solving the mass, momentum and energy conservation equations (3.1-3.3), the species evolution equation (3.5), the mixture fraction conservation equation (B.7), and Equation (B.6). The main advantage of this formulation is that the dimension of the ILDM table required for efficient simulation of the reactive flow model equations is reduced by $L - 2$ (see Section 2.4.1). Instead of tabulating the ILDM for different values of element mass fractions, it needs to be tabulated only for different values of mixture fraction, $\chi \in [0, 1]$.

For an isobaric, low Mach number laminar flame, where the effects of fluid viscosity are assumed to be negligible, the simple mass diffusion model in Equation (3.19) is used, and the Lewis number is assumed to be unity ($Le = \frac{k}{\rho c_p \mathcal{D}} = 1$) or in other words thermal and mass diffusivities are assumed to be equal, the energy conservation equation (3.3) can be simplified to

$$\rho \frac{Dh}{Dt} = \mathcal{D} \frac{\partial}{\partial x} \left(\rho \frac{\partial h}{\partial x} \right). \tag{B.10}$$

In the two stream reactive flow system described previously with initial conditions given in Equation (B.2), the initial condition for mixture enthalpy per unit mass is

given by

$$h(x, t=0) = \left\{ \begin{array}{ll} h^A, & 0 \leq x \leq \frac{L_x}{2} \\ h^B, & \frac{L_x}{2} \leq x \leq L_x \end{array} \right\}, \tag{B.11}$$

where $h^A = \sum_{i=1}^{N} h_i(T) Y_i^A$ and $h^B = \sum_{i=1}^{N} h_i(T) Y_i^B$ represent the enthalpy per unit mass of mixtures A and B, respectively. Zero gradient boundary conditions are chosen for the mixture enthalpy per unit mass

$$\frac{\partial h}{\partial x}(x=0,t) = \frac{\partial h}{\partial x}(x=L_x,t) = 0. \tag{B.12}$$

By using the following normalization for h

$$\chi = \frac{h - h^A}{h^B - h^A}, \tag{B.13}$$

the conservation equation (B.10) and the initial and boundary conditions in Equations (B.11-B.12) for the mixture enthalpy per unit mass h also become identical to those given in Equations (B.7-B.9) with $\chi_l = \chi$.

Hence, for the the assumptions described earlier, the numerical simulation of the isobaric, low Mach number laminar flame can be done by solving the mass conservation equation (3.1), the species evolution equation (3.5), the mixture fraction conservation equation (B.7), Equation (B.6), and Equation (B.13). The momentum conservation equation (3.2) reduces to the constant pressure condition when fluid viscosity is neglected. The element and energy conservation equations have been replaced by Equations (B.7), (B.6), and (B.13). However, this simplification can be done only if the boundary conditions for the element and energy conservation equations are similar in form. This is the case in the laminar flame problem where a zero flux boundary condition is used for both. The main advantage of this formulation is that the dimension of the ILDM table required for efficient simulation of the laminar flame model equations is reduced by $L - 1$ (see Section 2.4.1). Instead of tabulating the ILDM for different values of element mass

fractions and enthalpies, it needs to be tabulated only for different values of mixture fraction, $\chi \in [0, 1]$.

APPENDIX C

ELEMENT CONSERVATION IN THE CASHPR

The species evolution equations in the CASHPR are given by

$$\frac{dY_i}{dt} = \frac{\dot{\omega}_i M_i}{\rho}, \qquad (i = 1, \ldots, N). \tag{C.1}$$

Using the following relationship between element mass fractions and species mass fractions

$$\hat{Y}_l = \hat{M}_l \sum_{i=1}^{N} \varphi_{il} \frac{Y_i}{M_i}, \qquad (l = 1, \ldots, L), \tag{C.2}$$

with Equation (C.1), the element conservation equations can be written as

$$\frac{d\hat{Y}_l}{dt} = \frac{\hat{M}_l}{\rho} \sum_{i=1}^{N} \varphi_{il} \dot{\omega}_i, \qquad (l = 1, \ldots, L). \tag{C.3}$$

Since, the molar rate of evolution per unit volume of species i is given by

$$\dot{\omega}_i = \sum_{j=1}^{J} \left(\nu''_{ij} - \nu'_{ij} \right) r_j, \qquad (i = 1, \ldots, N), \tag{C.4}$$

Equation (C.3) can be rewritten as follows

$$\frac{d\hat{Y}_l}{dt} = \frac{\hat{M}_l}{\rho} \sum_{i=1}^{N} \varphi_{il} \sum_{j=1}^{J} \left(\nu''_{ij} - \nu'_{ij} \right) r_j, \qquad (l = 1, \ldots, L), \tag{C.5}$$

which can be further modified to

$$\frac{d\hat{Y}_l}{dt} = \frac{\hat{M}_l}{\rho} \sum_{j=1}^{J} r_j \sum_{i=1}^{N} \varphi_{il} \left(\nu''_{ij} - \nu'_{ij} \right), \qquad (l = 1, \ldots, L). \tag{C.6}$$

The stoichiometric balances of elementary reactions give the following relations

$$\sum_{i=1}^{N} \nu'_{ij} \varphi_{il} = \sum_{i=1}^{N} \nu''_{ij} \varphi_{il}, \qquad (l = 1, \ldots, L), \tag{C.7}$$

which when used with Equation (C.6), simplifies the element conservation equations to

$$\frac{d\hat{Y}_l}{dt} = \frac{\hat{M}_l}{\rho} \sum_{j=1}^{J} r_j \underbrace{\sum_{i=1}^{N} \varphi_{il} \left(\nu''_{ij} - \nu'_{ij}\right)}_{=0} = 0, \qquad (l = 1, \ldots, L). \tag{C.8}$$

Hence, the element mass fractions in the CASHPR remain constant for all times.

BIBLIOGRAPHY

[1] U. Maas and S. B. Pope. Simplifying chemical kinetics: Intrinsic low-dimensional manifolds in composition space. *Combustion and Flame*, 88(3-4):239–264, 1992.

[2] W. C. Reynolds. The element potential method for chemical equilibrium analysis: implementation in the interactive program stanjan. Stanford University Report, ME 270 HO no 7, 1986.

[3] W. G. Vincenti and C. H. Kruger Jr. *Introduction to Physical Gas Dynamics*. John Wiley and Sons, Inc., New York, London, Sydney, 1967.

[4] J. F. Griffiths. Reduced kinetics models and their application to practical combustion systems. *Progress in Energy and Combustion Science*, 21(1):25–107, 1995.

[5] M. S. Okino and M. L. Mavrovouinotis. Simplification of mathematical models of chemical reaction systems. *Chemical Reviews*, 98(2):391–408, 1998.

[6] J. D. Buckmaster and G. S. S. Ludford. *Theory of Laminar Flames*. Cambridge University Press, New York, Cambridge, 1982.

[7] M. Smooke, editor. *Reduced Kinetic Mechanisms and Asymptotic Approximations for Methane-Air Flames : A Topical Volume*. Springer-Verlag, Berlin, New York, 1991.

[8] J. D. Buckmaster. The structure and stability of laminar flames. *Annual Review of Fluid Mechanics*, 25:21–53, 1993.

[9] A. M. Khokhlov, E. S. Oran, A. Y. Chtchelkanova, and J. C. Wheeler. Interaction of a shock with a sinusoidally perturbed flame. *Combustion and Flame*, 117(1-2):99–116, 1999.

[10] T. Turanyi, T. Berces, and S. Vajda. Reaction rate analysis of complex kinetic systems. *International Journal of Chemical Kinetics*, 21:83–99, 1989.

[11] S. Vajda, P. Valko, and T. Turanyi. Principal component analysis of kinetic models. *International Journal of Chemical Kinetics*, 17:55–81, 1985.

[12] L. Petzold and W. Zhu. Model reduction for chemical kinetics: An optimization approach. *American Institute of Chemical Engineers Journal*, 45(4):869–886, 1999.

[13] K. Edwards and T. F. Edgar. Reaction set simplification using variable selection techniques. *Chemical Engineering Science*, 55:551–572, 2000.

[14] I. P. Androulakis. Kinetic mechanism reduction based on an integer programming approach. *American Institute of Chemical Engineers Journal*, 46:361–371, 2000.

[15] G. Li and H. Rabitz. A general analysis of exact lumping in chemical kinetics. *Chemical Engineering Science*, 44:1413–1430, 1989.

[16] G. Li and H. Rabitz. A general analysis of approximate lumping in chemical kinetics. *Chemical Engineering Science*, 45:977–1002, 1990.

[17] G. Li, A. Tomlin, H. Rabitz, and J. Toth. A general analysis of approximate nonlinear lumping in chemical kinetics. I. unconstrained lumping. *Journal of Chemical Physics*, 101:1172–1187, 1994.

[18] G. Li, A. Tomlin, H. Rabitz, and J. Toth. A general analysis of approximate nonlinear lumping in chemical kinetics. II. constrained lumping. *Journal of Chemical Physics*, 101:1188–1201, 1994.

[19] N. Peters and B. Rogg, editors. *Reduced Kinetic Mechanisms for Applications in Combustion Systems*. Lecture Notes in Physics Vol. 15, Springer-Verlag, Berlin, New York, 1993.

[20] J. Warnatz, U. Maas, and R. W. Dibble. *Combustion*. Springer, Berlin, New York, 1996.

[21] S. H. Lam and D. A. Goussis. Understanding complex chemical kinetics with computational singular perturbation. In *Proceedings of the Combustion Institute*, volume 22, pages 931–941, Pittsburgh, 1988.

[22] S. H. Lam. Using CSP to understand complex chemical kinetics. *Combustion Science and Technology*, 89(5-6):375–404, 1993.

[23] T. Blasenbrey, D. Schmidt, and U. Maas. Automatically simplified chemical kinetics and molecular transport and its applications in premixed and non-premixed laminar flame calculations. In *Proceedings of the Combustion Institute*, volume 27, pages 505–515, Pittsburgh, 1997.

[24] R. L. G. M. Eggels, J. J. J. Louis, J. B. W. Kok, and L. P. H. DeGoey. Comparison of conventional and low-dimensional manifold methods to reduce reaction mechanisms. *Combustion Science and Technology*, 123(1-6):347–362, 1997.

[25] D. Schmidt, J. Segatz, U. Riedel, J. Warnatz, and U. Maas. Simulation of laminar methane-air flames using automatically simplified chemical kinetics. *Combustion Science and Technology*, 114:3–16, 1996.

[26] B. Yang and S. B. Pope. An investigation of the accuracy of manifold methods and splitting schemes in the computational implementation of combustion chemistry. *Combustion and Flame*, 112(1-2):16–32, 1998.

[27] C. Rhodes, M. Morari, and S. Wiggins. Identification of low order manifolds: Validating the algorithm of Maas and Pope. *Chaos*, 9(1):108–123, 1999.

[28] R. Lowe and A. Tomlin. Low-dimensional manifolds and reduced chemical models for tropospheric chemistry simulations. *Atmospheric Environment*, 34(15):2425–2436, 2000.

[29] O. Gicquel, D. Thevenin, M. Hilka, and N. Darabiha. Direct numerical simulations of turbulent premixed flames using intrinsic low-dimensional manifolds. *Combustion Theory and Modeling*, 3(3):479–502, 1999.

[30] C. Correa, H. Niemann, B. Schramm, J. Warnatz, J. W. Daily, and B. Zamuner. Reaction mechanism reduction for higher hydrocarbons by the ILDM method. In *Proceedings of the Combustion Institute*, volume 28, pages 1607–1614, Pittsburgh, 2000.

[31] H. Kaper and T. Kaper. Asymptotic analysis of two reduction methods for systems of chemical reactions. *Physica D*, 165:66–93, 2002.

[32] N. Fenichel. Geometric singular perturbation theory for ordinary differential equations. *Journal of Differential Equations*, 31(15):53–98, 1979.

[33] A. N. Yannacopoulos, A. S. Tomlin, J. Brindley, J. H. Merkin, and M. J. Pilling. The use of algebraic sets in the approximation of inertial manifolds and lumping in chemical kinetic systems. *Physica D*, 83(4):421–449, 1995.

[34] S. J. Fraser. The steady state and equilibrium approximations: A geometric picture. *Journal of Chemical Physics*, 88:4732–4738, 1988.

[35] M. R. Roussel and S. J. Fraser. On the geometry of transient relaxation. *Journal of Chemical Physics*, 94(11):7106–7113, 1991.

[36] M. J. Davis and R. T. Skodje. Geometric investigation of low-dimensional manifolds in systems approaching equilibrium. *Journal of Chemical Physics*, 111(3):859–874, 1999.

[37] M. Hadjinicolaou and D. A. Goussis. Asymptotic solution of stiff PDEs with the csp method: The reaction diffusion equations. *SIAM Journal on Scientific Computing*, 20(3):781–810, 1999.

[38] U. Maas and S. B. Pope. Laminar flame calculations using simplified chemical kinetics based on intrinsic low-dimensional manifolds. In *Proceedings of the Combustion Institute*, volume 25, Pittsburgh, 1994. 1349-1359.

[39] G. Strang. On the construction and comparison of difference schemes. *SIAM Journal on Numerical Analysis*, 5:506–517, 1968.

[40] S. Singh, Y. Rastigejev, S. Paolucci, and J. M. Powers. Viscous detonation in $H_2/O_2/Ar$ using intrinsic low dimensional manifolds and wavelet adaptive multilevel representation. *Combustion Theory and Modeling.*, 5:163–184, 2001.

[41] R. J. LeVeque and H. C. Yee. A study of numerical methods for hyperbolic conservation laws with stiff source terms. *Journal of Computational Physics*, 86:187, 1990.

[42] Reaction Design, Inc., San Diego, California. *Chemkin: A Software Package for the Analysis of Gas-Phase Chemical and Plasma Kinetics*, chemkin collection release 3.6 edition, 2000.

[43] J. Carr and R. G. Muncaster. The application of center manifolds to amplitude expansions.1. Ordinary differential equations. *Journal of Differential Equations*, 50:260–279, 1983.

[44] M. R. Roussel. Forced-convergence iterative schemes for the approximation of invariant manifolds. *Journal of Mathematical Chemistry*, 21:385–393, 1997.

[45] M. R. Roussel and S. J. Fraser. Invariant manifold methods for metabolic model reductions. *Chaos*, 11:196–206, 2001.

[46] E. Anderson, Z. Bai, C. Bischof, S. Blackford, J. Demmel, J. Dongarra, J. Du Croz, A. Greenbaum, S. Hammarling, A. McKenney, and D. Sorensen. *LAPACK User's Guide*. 3rd edition, SIAM, Philadelphia, PA, 1999.

[47] U. Maas. Efficient calculation of intrinsic low-dimensional manifolds for the simplification of chemical kinetics. *Computing Visualization Science*, 1(2):69–81, 1998.

[48] G. H. Golub and C. F. Van Loan. *Matrix Computations*. Johns Hopkins, Baltimore, MD, 1996.

[49] P. Deuflhard. *A Relaxation Strategy for the Modified Newton Method,* edited by I. Burlisch and O. Stoer, Springer Lecture Notes Vol. 477, Springer-Verlag, Berlin, New York, 1975.

[50] A. C. Hindmarsh. Odepack, a systematized collection of ODE solvers. In R. S. Stepleman *et al.*, editor, *Scientific computing : applications of mathematics and computing to the physical sciences*, pages 55–64. North-Holland Publication Company, Amsterdam, New York, 1983.

[51] R. P. Fedkiw, B. Merriman, and S. Osher. High accuracy numerical methods for thermally perfect gas flows with chemistry. *Journal of Computational Physics*, 132:175–190, 1997.

[52] R. P. Fedkiw, B. Merriman, and S. Osher. Simplified discretization of systems of hyperbolic conservation laws containing advection equations. *Journal of Computational Physics*, 157:302–326, 2000.

[53] E. S. Oran, T. R. Young, J. P. Boris, and A. Cohen. Weak and strong ignition. I. numerical simulations of shock tube experiments. *Combustion and Flame*, 48:135–148, 1982.

[54] O. V. Vasilyev and S. Paolucci. A dynamically adaptive multilevel wavelet collocation method. *Journal of Computational Physics*, 125:498–512, 1996.

[55] O. V. Vasilyev and S. Paolucci. A fast adaptive wavelet collocation algorithm for multidimensional PDEs. *Journal of Computational Physics*, 138:16–56, 1997.

[56] S. Singh, J. M. Powers, and S. Paolucci. Detonation solutions from reactive Navier-Stokes equations. AIAA 99-0966, Reno, 1999.

[57] W. Fickett and W. C. Davis. *Detonation*. University of California Press, Berkley, 1979.

[58] R. Menikoff. Errors when shock-waves interact due to numerical shock width. *SIAM Journal of Scientific Computation*, 15:1227–1242, 1994.

[59] H. J. Merk. The macroscopic equations for simultaneous heat and mass transfer in isotropic, continuous and closed systems. *Applied Scientific Research*, A8:73–99, 1959.

[60] Reaction Design, Inc., San Diego, California. *Transport: a software package for the evaluation of gas-phase, multicomponent transport properties*, CHEMKIN collection release 3.6 edition, 2000.

[61] Reaction Design, Inc., San Diego, California. *The chemkin thermodynamic database*, CHEMKIN collection release 3.6 edition, 2000.

[62] U. Maas and J. Warnatz. Ignition processes in hydrogen-oxygen mixtures. *Combustion and Flame*, 74:53–69, 1988.

[63] F. A. Williams. *Combustion*. Benjamin/Cummings, Menlo Park, California, 1985.

[64] G. L. Schott and J. L. Kinsey. Kinetic studies of hydroxyl radicals in shock waves. ii. induction times in the hydrogen-oxygen reaction. *Journal of Chemical Physics*, 29:1177–1182, 1958.

[65] R. J. LeVeque. *Numerical Methods for Conservation Laws*. Birkhäuser, Basel, 1992.

[66] R. P. Fedkiw, A. Marquina, and B. Merriman. An isobaric fix for the overheating problem in multimaterial compressible flows. *Journal of Computational Physics*, 148:545–578, 1999.

[67] S. B. Margolis. Time-dependent solution of a premixed laminar flame. *Journal of Computational Physics*, 27:410–427, 1978.

[68] L. R. Petzold. A description of DASSL: A differential/algebraic system solver. In R. S. Stepleman *et al.*, editor, *Scientific computing : applications of mathematics and computing to the physical sciences*, page 65. North-Holland Publication Company, Amsterdam, New York, 1983.